INJECTION MOLDING OF THERMOPLASTICS

INJECTION MOLDING OF THERMOPLASTICS

by

S. Kenig, B.Sc.

Department of Chemical Engineering
McGill University

A Thesis Submitted to the Faculty of Graduate Studies and Research in Partial Fulfilment of the Requirements for the Degree of Doctor of Philosophy

McGill University

March 1972

ABSTRACT

A mathematical model is proposed for the quantitative treatment of the injection molding of thermoplastics as it relates to the behavior of the polymer in the cavity. The model is based on setting up the equations of continuity, motion and energy for the system during each of the stages of the injection molding cycle (filling, packing and cooling) and the coupling of these equations with practical boundary conditions. The treatment takes into consideration the non-Newtonian behavior of the melt, the effect of temperature on density and viscosity, the latent heat of solidification, and the differences in thermal properties between the solid and the melt. Numerical solutions have been obtained for the case of a spreading radial flow in a semi-circular cavity. The theoretical results yield data on the filling,packing and cooling times as well as velocity pressure and temperature profiles throughout the filling,packing and cooling stages.

Experimental studies have been conducted with a 2 1/3 oz. reciprocating screw injection molding machine to check the validity of the proposed theoretical model. Results show that theoretical predictions are in good agreement with experimental data for all stages.

ACKNOWLEDGEMENTS

The author wishes to express his utmost appreciation and sincere gratitude for the guidance and encouragement received from Dr. M.R. Kamal during the course of this research and for his critical review of this thesis.

Acknowledgement is also extended to the:

National Research Council of Canada for financial assistance.

Dr. J.L. Lewis for his help in the photographic work.

Dr. M.E. Weber and Mr. S. Sourour for helpful comments during their participation in the author's research group.

Finally, the author wishes to express his appreciation to his wife and family for their patience and constant encouragement.

TABLE OF CONTENTS

	Page
ABSTRACT	
ACKNOWLEDGEMENTS	i
TABLE OF CONTENTS	ii
LIST OF TABLES	v
LIST OF ILLUSTRATIONS	vi
1. INTRODUCTION	1
1.1 General Introduction	1
1.2 Injection Molding: Background	6
1.2.1 Filling Stage	7
1.2.2 Packing Stage	14
1.2.3 Cooling Stage	15
2. EXPERIMENTAL	16
2.1 Equipment	16
2.2 Transducer System and Its Calibration	21
2.3 Experimental Procedure	28
2.4 Materials and Properties	33
3. FILLING STAGE	37
3.1 Theoretical Analysis	37
3.1.1 Equations and Boundary Conditions	37
3.1.2 Dimensional Analysis	45
3.1.3 Difference Equations	48
3.1.4 Numerical Procedure	54
3.1.5 Stability, Convergence and Uniqueness	58

		Page
3.2	Results and Discussion	64
3.2.1	General	67
3.2.2	Boundary Conditions	70
3.2.3	Filling Times	74
3.2.4	Velocity Profiles	93
3.2.5	Temperature Profiles	100
3.2.6	Pressure Profiles	110
3.2.7	Short Shot	124
3.2.8	Melt Fracture	129
3.2.9	Summary	130
4.	PACKING STAGE	132
4.1	Theoretical Analysis	132
4.1.1	Equations and Boundary Conditions	132
4.1.2	Dimensional Analysis	135
4.1.3	Difference Equations	138
4.1.4	Stability, Convergence and Uniqueness	139
4.1.5	Numerical Procedure	142
4.2	Results and Discussion	144
4.2.1	General	144
4.2.2	Packing Profiles	146
4.2.3	Flow Rate Variation	162
4.2.4	Temperature Profiles	169
4.2.5	Summary	169
5.	COOLING STAGE	170
5.1	Theoretical Analysis and Computational Procedure	170
5.2	Results and Discussion	171
5.2.1	General	171
5.2.2	Pressure Variation	172
5.2.3	Residual Pressure	186
5.2.4	Temperature Profiles	189
5.2.5	Remarks on Pressure Measurements in the Cooling Stage	189
5.2.6	Summary	196

		Page
6.	COMPOSITE CYCLE	197
7.	REPRODUCIBILITY, ACCURACY AND ERROR ANALYSIS	201
8.	CONCLUSION	209
	8.1 Conclusions	209
	8.2 Recommendations	211
	8.3 Claims for Original Work	212
	LIST OF SYMBOLS	214
	REFERENCES	220
9.	APPENDICES	
	9.1 APPENDIX 1: CONSTITUTIVE EQUATION AND VISCOSITY	224
	9.2 APPENDIX 2: ANALYTICAL SOLUTION OF A SIMPLIFIED RADIAL FLOW PROBLEM	232
	9.3 APPENDIX 3: COMPUTER PROGRAM - FILLING STAGE	240
	9.4 APPENDIX 4: COMPUTER PROGRAM - PACKING AND COOLING STAGES	248
	9.5 APPENDIX 5: NUMERICAL TREATMENT OF LATENT HEAT	256
	9.6 APPENDIX 6: EXTENSIONAL STRESSES	259
	9.7 APPENDIX 7: ESTIMATE OF DIFFERENT TERMS IN THE MOMENTUM EQUATION	264

LIST OF TABLES

Table		Page
1-1	Sales of Plastics Processed in Canada in 1966 and 1970	5
3-1	Comparison Between Analytical and Numerical Velocity Profile: $n = 0.5$, $\Delta z^* = 0.1$	61
3-2	Comparison Between Analytical and Numerical Solutions for Pressure Profile: $P_f = 500$ psi, $n = 0.5$	63
3-3	Injection Conditions for Experimental Program	65
7-1	Error Analysis: Filling Stage	204
7-2	Error Analysis: Packing Stage	205
7-3	Error Analysis: Cooling Stage	206
9-1	Magnitudes of Different Terms in the Momentum Equation: Polyethylene, Case 3	265
9-2	Magnitudes of Different Terms in the Momentum Equation: Polystyrene, Case 11	266

LIST OF ILLUSTRATIONS

Figure		Page
1-1	Pressure Variation in Injection Molding	8
1-2	Radial Flow in Various Molds	11
2-1	Injection Molding Machine	17
2-2	Experimental Apparatus	18
2-3	Arrangement of Transducer in the Cavity Wall	20
2-4	Schematic Diagram of Transducer TG-M-6G(T)	22
2-5	Transducer Calibration Apparatus	24
2-6	Calibration Curve for Pressure Transducer	26
2-7	Schematic Diagram of Electrical Circuit for the Transducer	27
2-8	Temperature-Time Curve for Thermo-couple Calibration	29
2-9	Temperature-Time Plot for First Order System	30
2-10	P-V-T Diagram for Polyethylene	34
2-11	P-V-T Diagram for Polystyrene	35
3-1	Finite Difference Net	50
3-2	Computer Flow Diagram - Filling Stage	55
3-3	Spreading Radial Flow in Semi-Circular Cavity - Case 2	68

Figure		Page
3-4	Spreading Radial Flow in Semi-Circular Cavity - Case 10	69
3-5	Variation of Entrance Pressure During Filling - Polyethylene	71
3-6	Variation of Entrance Pressure During Filling - Polystyrene	72
3-7	Progression of Melt Front - Case 1	75
3-8	Progression of Melt Front - Case 2	76
3-9	Progression of Melt Front - Case 3	77
3-10	Progression of Melt Front - Case 4	78
3-11	Progression of Melt Front - Case 5	79
3-12	Progression of Melt Front - Case 6	80
3-13	Progression of Melt Front - Case 7	81
3-14	Progression of Melt Front - Case 8	82
3-15	Progression of Melt Front - Case 9	83
3-16	Progression of Melt Front - Case 10	84
3-17	Progression of Melt Front - Case 11	85
3-18	Progression of Melt Front - Case 12	86
3-19	Comparison Between Different Solutions - Case 1	91
3-20	Comparison Between Different Solutions - Case 9	92
3-21	Velocity Profiles at $r^* = 0.20$ - Case 1	94

Figure		Page
3-22	Velocity Profiles at r* = 0.20 - Case 3	95
3-23	Velocity Profiles at r* = 0.20 - Case 6	96
3-24	Velocity Profiles at r* = 0.20 - Case 8	97
3-25	Velocity Profiles at r* = 0.20 - Case 10	98
3-26	Velocity Profiles at r* = 0.20 - Case 12	99
3-27	Temperature Profiles at the End of Filling - Case 2	101
3-28	Temperature Profiles at the End of Filling - Case 4	102
3-29	Temperature Profiles at the End of Filling - Case 5	103
3-30	Temperature Profiles at the End of Filling - Case 7	104
3-31	Temperature Profiles at the End of Filling - Case 9	105
3-32	Temperature Profiles at the End of Filling - Case 11	106
3-33	Temperature Profiles at the Wall - Case 2	107
3-34	Temperature Profiles at the Wall - Case 6	108
3-35	Temperature Profiles at the Wall - Case 10	109

Figure		Page
3-36	Pressure Profiles at the End of Filling - Case 1	111
3-37	Pressure Profiles at the End of Filling - Case 2	112
3-38	Pressure Profiles at the End of Filling - Case 3	113
3-39	Pressure Profiles at the End of Filling - Case 4	114
3-40	Pressure Profiles at the End of Filling - Case 5	115
3-41	Pressure Profiles at the End of Filling - Case 6	116
3-42	Pressure Profiles at the End of Filling - Case 7	117
3-43	Pressure Profiles at the End of Filling - Case 8	118
3-44	Pressure Profiles at the End of Filling - Case 9	119
3-45	Pressure Profiles at the End of Filling - Case 10	120
3-46	Pressure Profiles at the End of Filling - Case 11	121
3-47	Pressure Profiles at the End of Filling - Case 12	122
3-48	Progression of Melt Front - Short Shot Case 13	125
3-49	Progression of Melt Front - Short Shot Case 14	126

Figure		Page
3-50	Temperature Profiles at the End of Filling - Case 13	127
3-51	Temperature Profiles at the End of Filling - Case 14	128
4-1	Comparison Between Analytical and Numerical Solutions for Heat Conduction in a Slab	141
4-2	Computer Flow Diagram - Packing Stage	143
4-3	Packing Curves - Case 1	147
4-4	Packing Curves - Case 2	148
4-5	Packing Curves - Case 3	149
4-6	Packing Curves - Case 4	150
4-7	Packing Curves - Case 5	151
4-8	Packing Curves - Case 6	152
4-9	Packing Curves - Case 7	153
4-10	Packing Curves - Case 8	154
4-11	Packing Curves - Case 9	155
4-12	Packing Curves - Case 10	156
4-13	Packing Curves - Case 11	157
4-14	Packing Curves - Case 12	158
4-15	Packing Curves - Case 2	160
4-16	Packing Curves - Case 6	161

Figure		Page
4-17	Temperature Profiles at the End of Packing - Case 2	163
4-18	Temperature Profiles at the End of Packing - Case 4	164
4-19	Temperature Profiles at the End of Packing - Case 5	165
4-20	Temperature Profiles at the End of Packing - Case 7	166
4-21	Temperature Profiles at the End of Packing - Case 9	167
4-22	Temperature Profiles at the End of Packing - Case 11	168
5-1	Pressure Variation During Cooling - Case 1	173
5-2	Pressure Variation During Cooling - Case 2	174
5-3	Pressure Variation During Cooling - Case 3	175
5-4	Pressure Variation During Cooling - Case 4	176
5-5	Pressure Variation During Cooling - Case 5	177
5-6	Pressure Variation During Cooling - Case 6	178
5-7	Pressure Variation During Cooling - Case 7	179
5-8	Pressure Variation During Cooling - Case 8	180
5-9	Pressure Variation During Cooling - Case 9	181

Figure		Page
5-10	Pressure Variation During Cooling - Case 10	182
5-11	Pressure Variation During Cooling - Case 11	183
5-12	Pressure Variation During Cooling - Case 12	184
5-13	Temperature Profiles at the End of Cooling - Case 2	190
5-14	Temperature Profiles at the End of Cooling - Case 4	191
5-15	Temperature Profiles at the End of Cooling - Case 5	192
5-16	Temperature Profiles at the End of Cooling - Case 7	193
5-17	Temperature Profiles at the End of Cooling - Case 9	194
5-18	Temperature Profiles at the End of Cooling - Case 11	195
6-1	Composite Pressure-Time Curve - Case 2	198
6-2	Composite Pressure-Time Curve - Case 10	199
9-1	Viscosity as Function of Shear Rate and Temperature - Polyethylene E.P. 245	228
9-2	Viscosity as Function of Shear Rate and Temperature - Polystyrene Styron 683	229
9-3	Unsteady-State Velocity Profiles for Analytical Solution	238

1. INTRODUCTION

1.1 GENERAL INTRODUCTION

The purpose of most plastics processing operations is to transform a resin which consists of random particles into a commercial product of predetermined shape and dimensions. Thus, powder, beads, or pellets are converted to film, sheet, pipe, monofilament, coating, special profiles and to a variety of articles like cups, toys, bottles, bottle caps, gasoline tanks, auto-body parts, furniture parts and a multitude of other components. In general, processing or fabricating operations have the following three basic steps in common:

1) Heating and melting of the resin.
2) Forming the desired shape by filling a mold or pumping the melt through a die.
3) Cooling of the formed article to a solid mass.

Some processes, like cold forming, do not require the formation of a high-temperature melt as an essential part of the fabricating process. Also, the processing of thermosetting resins, which are excluded from this study, requires a delicate balance between the thermal and flow conditions and their variation with time as a result of the reactivity of these systems.

The present study is concerned only with the processing of thermoplastic resins.

The three stages of plastics fabrication may be accomplished by continuous steady state operations or by unsteady-state batch or semi-batch processes.

In the extrusion operation, the solid polymer in the form of pellets or powder is melted with the help of a plasticating screw and pumped through a die which controls the cross section. Then the shaped product is cooled to a solid state. Since extrusion is a continuous steady-state process, only two dimensional control of the shape of the extruded product is possible. In the molding operation, the solid polymer is converted to the liquid state. If the melt is not formed inside the mold cavity, it is necessary to transfer it to a mold, where the plastic solidifies. Molding is an unsteady state operation, and thus three-dimensional control of the shape is achieved.

Various types of molding operations are used commercially depending on the resin used, the final product requirements, and economic feasibility.

In compression molding, material in the form of loose powder or a preheated preform, is placed in an open heated mold cavity. Then the mold is closed. The combination of heat and pressure softens the material and causes it to flow and

fill the cavity. Then the mold is cooled till solidification is achieved.

In transfer molding, the operation starts with the mold in the closed position. Then, the plastic melt is forced into the mold from an auxiliary chamber. Transfer molding is generally accomplished with a single ram press where the same force that closes the mold is used to transfer the melt. In this respect the process is similar to compression molding.

In rotational molding, a plastic charge is placed inside a hollow mold. The mold and charge are rotated and heated to the melting point of the polymer. The mold is then cooled, solidifying the plastic and finally the molded part is unloaded.

In blow molding, an extruded tube parison is introduced into a cooled mold where it is inflated by air pressure until the walls of the parison assume the shape of the walls of the mold. The shaped parison is then cooled to structural rigidity. Blow molding is an example of combined steady state (extrusion) and unsteady state (molding) operations.

In injection molding, the raw material is melted, then it is injected under pressure into a cold mold where it solidifies to a point when it can be ejected from the mold without mechanical damage.

Most of the theoretical work published in connection with the processing of thermoplastics deals with the extrusion operation (1,2,3,4,5). Much less published work is available on the various molding operations, mainly as a result of the complexity of the equations describing these systems. In most instances, researchers have dealt with isolated problems or small parts of the overall process (6,7,8,9,10).

In the present work, an attempt is made to develop a model for the theoretical treatment of the overall injection molding process, excluding the plastication step, which may be handled adequately by available extrusion theory. Injection molding has been selected for two reasons. Firstly, the problems of heat transfer and fluid flow which are encountered in injection molding are typical of those encountered with other molding operations. Thus the treatment may be modified or extended to handle processes like compression molding and transfer molding. Secondly, injection molding is not only the most widely used plastics molding technique but is also one of the most common plastics processing operations, second only to extrusion, as shown in Table 1-1(11). Polyethylene accounts for more than half of the injection molding volume in both Canada and the United States (11,12).

TABLE 1-1

SALES OF PLASTICS PROCESSED IN CANADA

IN 1966 AND 1970

PROCESS	SALES IN $ MILLION 1966	1970
EXTRUSION		
FILM	67	80
PIPE	11	27
PROFILE	14	19
MOLDING		
INJECTION	44	74
COMPRESSION	8	9
BLOW	14	20
ROTATION	5	16
VACUUM FORMING	3	5
REINFORCED PLASTICS	19	26
HIGH PRESSURE LAMINATING	18	18
PLASTIC FOAMS	17	32
MISCELLANEOUS	55	83
TOTAL	275	409

1.2 INJECTION MOLDING: BACKGROUND

Injection molding is accomplished in an injection molding machine which consists of two basic components - the injection unit and the clamping unit. The injection unit serves to heat the raw material to a molten state and to transfer it under pressure into the mold which is held by the clamping unit. Melting is achieved with the help of external heaters and, in some cases, by mechanical heating produced when the granular raw material is compressed and worked.

The earliest injection molding machines employed a plunger unit. With units of this type, raw material is fed volumetrically from the hopper into the plasticating chamber, which is mounted between the plunger and the nozzle. Each stroke of the plunger froces unmelted material into the chamber through a spreader (called also torpedo) from which plastic melt is forced out through a nozzle into the mold. Later, two-stage plungers were developed, with plastication and injection performed in two separate units.

Most of the injection molding machines produced today are built with reciprocating-screw injection units. In these units, the extruder chamber is utilized to achieve both plastication and injection. A typical operating sequence may be described as follows. Starting with the reciprocating screw in the forward position, material is gravity fed from

the hopper. The rotation of the screw plasticizes the material and conveys it forward in the screw barrel. Accumulation of the plasticized material at the front of the barrel forces the screw to move backwards and the melt collects in the front of the injection chamber, ahead of the screw tip. Material back flow over the screw flights is prevented by a check valve. When the injection unit is activated the screw moves forward, as a ram, forcing the melt from the injection chamber through the nozzle into the mold. The hot polymer melt flows into an empty cold cavity. When filling is complete more polymer is packed into the cavity at high pressure in order to compensate for shrinkage by cooling. Cooling is continued until sufficient solidification is achieved so that the polymer may be ejected from the mold without damage.

It is reasonable, in attempting to develop a model for the injection molding operation, to divide the process into three major stages: filling, packing and cooling. Schematically, the three stages are best described by the pressure time curve, shown in Figure 1-1.

1.2.1 Filling Stage

The filling stage is represented by the unsteady flow of a hot non-Newtonian compressible melt into an empty cold cavity, which is held at a temperature below the solidification

FIGURE 1-1

PRESSURE VARIATION IN INJECTION MOLDING

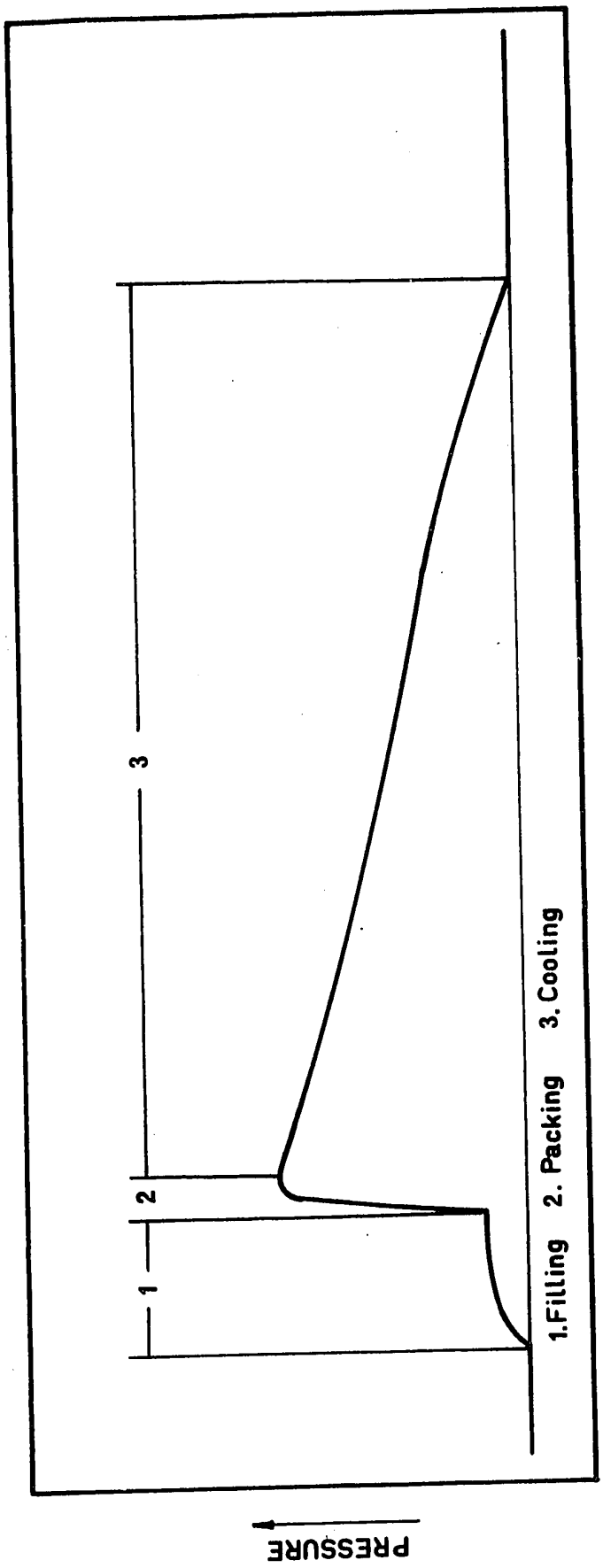

temperature of the polymer. The problem has to do with simultaneous unsteady flow and heat transfer.

Earlier theoretical and experimental results have been reported for the cases of spiral or very long molds. Ballman, Shusman and Toor (13) studied the flow of molten polyethylene and polystyrene in a cold long cavity. The cavity consisted of parallel plates, one inch wide and twelve inches long with varying thickness between 0.050 and 0.150 inches. By a set of simplifying assumptions, they reached empirical correlations for the distance traversed by the polymer as a function of time, and the maximum length of flow as a function of operating conditions. By assuming isothermal conditions, they were able to explain the experimental results. However, they agreed that the relationship between the experimental results, material properties and system parameters must depend strongly upon the heat transfer in the cavity.

Kazankov and Basov (14) attempted to calculate the maximum flow length in a long two plate mold for polystyrene. They assumed unidirectional flow and included only the conduction terms in the Energy equation. By assuming a Power Law fluid, they were able to obtain an analytical solution that consisted of the first term of an infinite series.

Grinblat (15) worked also with a rectangular cavity. He employed the heat conduction equation to calculate the thickness of the solidifying layer. Thus, he treated the melt as two regions: a stationary layer and an isothermal flowing core. From experimental results he was able to obtain an empirical equation describing the velocity of the melt front as a function of time and the total length of flow.

The main disadvantage of the above treatments results from poor and unspecified correlation between the behaviour in the model molds and actual molding conditions. A more practical geometry for studying the filling stage would employ "Spreading Radial Flow", which resembles more closely injection molding conditions, where the melt emerges from the gate and spreads to the outer boundaries of the cavity.

Spencer and Gilmore (16) and Beyer and Spencer (6) photographed the flow pattern of polystyrene in a disc shaped cavity, Figure 1-2a. They described the polymer front as a circular segment of continuously increasing radius with the gate at the centre. In the early stages of filling, the wall exerts a retarding force, and the polymer front in the vicinity of the wall bends back toward the gate. If the wall were not present, the polymer would flow radially into the cavity from the gate. During the later stages of filling the curved boundary deflects the material, which would otherwise strike it in radial flow. As a result, the front eventually becomes

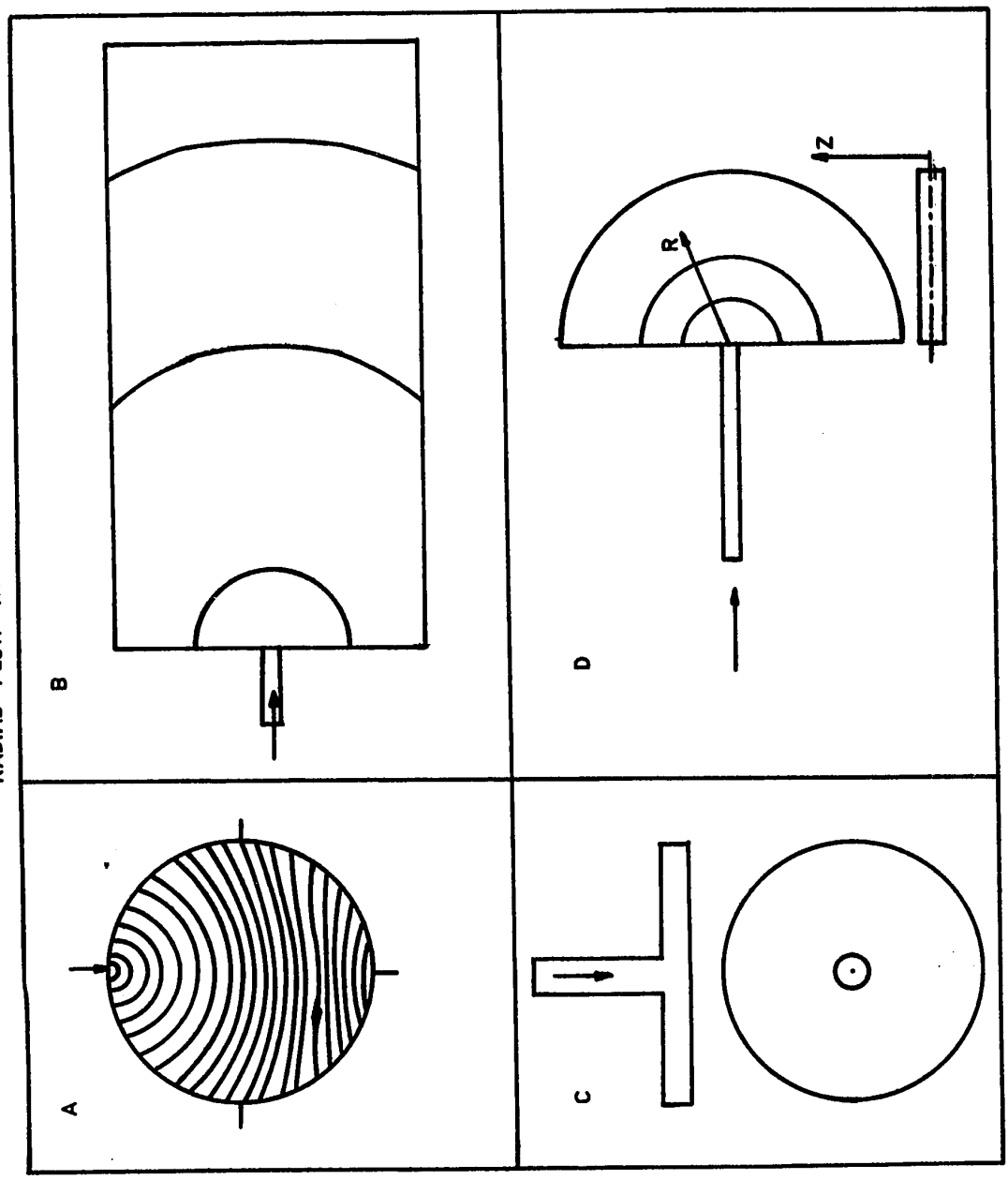

FIGURE 1-2
RADIAL FLOW IN VARIOUS MOLDS

linear and then curves away from the gate just before completion of the filling operation.

Bauer (17) has reported experimental and empirical results on the filling of a rectangular thin mold with low density polyethylene, Figure 1-2b. He attempts to describe the progression of the melt front in terms of wave propagation, where the injection point is considered to be the centre of the wave. From this point, spherical waves propagate, thus generating the circular front. The wave front position may be determined experimentally by registering the mold surface temperature.

More recently, Barrie (18) employed the disc shaped cavity shown in Figure 1-2c. The objective of his work was to measure and analyze the melt pressure distribution in the cavity. By using an empirical approach he was able to correlate the pressure profile obtained experimentally using pressure transducers at different radial locations. In a second paper (19) Barrie attempted to calculate the "solid skin" content of the polymer at the end of filling. He applied the pure heat conduction equation,and found that experimental results did not fit the calculations. The predicted values were higher than the experimental ones.

Harry and Parrott (20,21) suggested a numerical simulation of the injection mold filling. They considered flow in a thin rectangular cavity with a gate that occupied the

whole cross-section of the cavity. Thus, the problem was reduced to flow in one dimension. They assumed constant polymer properties and linear pressure drop.

Pearson (9) proposed a model for filling the mold shown in Figure 1-2c, by radial flow. He also assumed a linear pressure drop across the circular mold and constant thermal properties. More recently, Berger and Gogos (10) simulated the filling of a circular mold by treating the channel leading to the cavity and the cavity itself as one flow system under the effect of the pressure at the injection end. In their treatment, they assumed constant density and thermal properties for the melt.

The present work is conducted to study the filling stage for spreading radial flow in the cavity shown in Figure 1-2d. This geometry has been chosen in order to permit the study of radial flow in a simple geometry, without interference from the walls of the mold as observed by some of the above studies. The parallel feed from the gate was employed to avoid a 90^{o} diversion in the direction of flow, and to allow high speed photography.

1.2.2 Packing Stage

Polymer flow into the cavity does not cease when the melt front reaches the outer boundaries of the cavity. It is desirable to introduce more polymer to the cavity during the packing stage. Such packing is necessary in order to compensate for shrinkage of the polymer, as a result of cooling.

Two factors compete with regard to pressure variation in the cavity during the packing stage. The first is the flow of the polymer into the mold which leads to an increase of pressure corresponding to the increase of the density of the polymer in the cavity. The second factor is the cooling of the polymer which continues during the entire process. Cooling tends to reduce the pressure in the cavity.

Very little work is reported in the literature regarding the analysis of the packing stage. The main contribution is an attempt by Spencer and Gilmore (16) to calculate the maximum pressure in the mold by means of an equation of state and an empirical relation for filling time. The bulk of the other work deals with the thermodynamics of the packing stage, especially as it relates to shrinkage (6,7,8).

In the present work, a mathematical model is proposed to treat both the dynamics and thermodynamics of the packing stage in the same semicircular cavity which has been employed for the study of the filling stage.

1.2.3 Cooling Stage

After filling and packing are complete, cooling of the plastic continues by virtue of the lower temperature of the mold. Cooling without flow continues until the plastic has reached a sufficient level of solidification. Ideally solidification in molding operations occur under conditions of constant mass and volume, so that the molded article retains the shape and dimensions of the mold.

Some work is reported in the literature regarding the cooling of polymer melts. Gloor (22) has solved the heat conduction equation, with change of phase, for various crystalline polymers. He assumes that cooling is achieved under atmospheric pressure and employs constant average properties for the polymers over the whole temperature field. Kenig and Kamal (23,24) calculated temperature profiles and pressure as function of time for pressurized high density polyethylene and polystyrene. They included in their solution the dependence of polymer properties on temperature and the effects of pressure and rates of cooling on the solidification temperature.

In the present study, the same approach is used as in (24). Both temperature and pressure are calculated for the cooling stage by employing the heat conduction equations with change of phase together with an equation of state.

2. EXPERIMENTAL

2.1 EQUIPMENT

Experiments were conducted on a Model 60-SR 2 1/3 oz. reciprocating-screw injection molding machine, which is manufactured by Metalmec, see Figure 2-1. The melt temperature at the injection end was controllable to within $\pm 5^{o}F$. Automatic controls and timers were available for injection pressure, hold pressure, injection time, hold time and cycle time. The machine could be operated in the automatic, semi-automatic or manual modes. In this work only the semi-automatic and manual modes were used, as will be described later.

The injection pressure during filling is regulated by the injection speed and injection pressure valves. These valves regulate the pressure at the injection end, thus the pressure of the melt, as it enters the cavity depends on the dimensions of the nozzle and channel that lead from the injection end to the cavity and on the material properties.

The maximum pressure in the packing stage is regulated by the shot size and the hold pressure valve.

A schematic diagram of the semi-circular mold is shown in Figure 2-2. The cavity dimensions have been governed by the maximum shot size of the injection molding machine (2 1/3 oz.) and space available in the clamping system. The clamping force was obtained from twelve 5/8 inch screws. The mold was used in two different modes. In the first mode, the

FIGURE 2-1

INJECTION MOLDING MACHINE

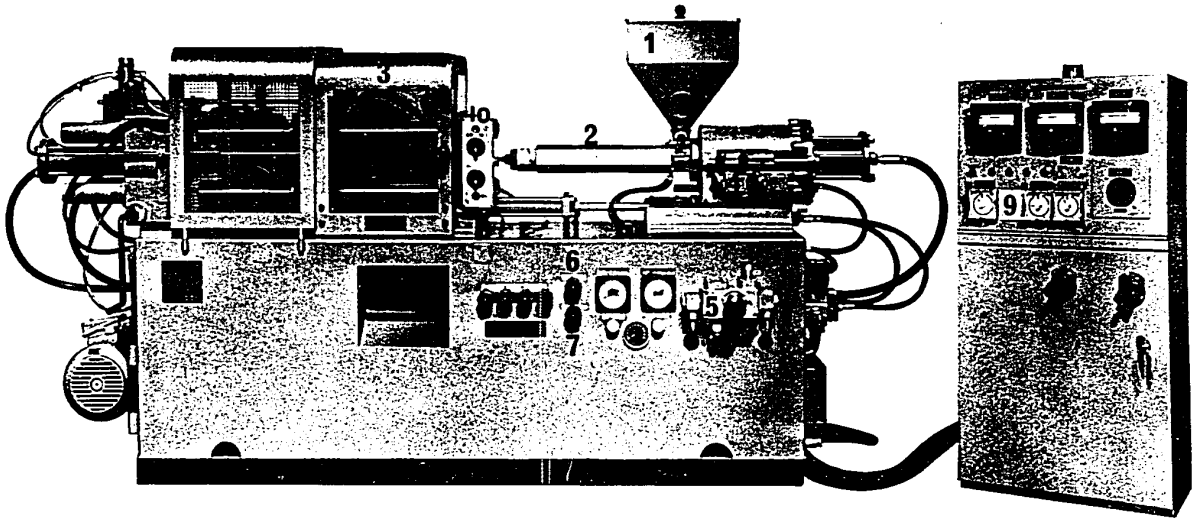

1. HOPPER
2. SCREW BARREL
3. CLAMPING UNIT
4. SHOT SIZE SWITCHES
5. INJECTION SPEED VALVE
6. INJECTION PRESSURE VALVE
7. HOLD PRESSURE VALVE
8. TEMPERATURE CONTROL
9. AUTOMATIC TIMERS
10. MANUAL INJECTION SWITCHES

FIGURE 2-2

EXPERIMENTAL APPARATUS

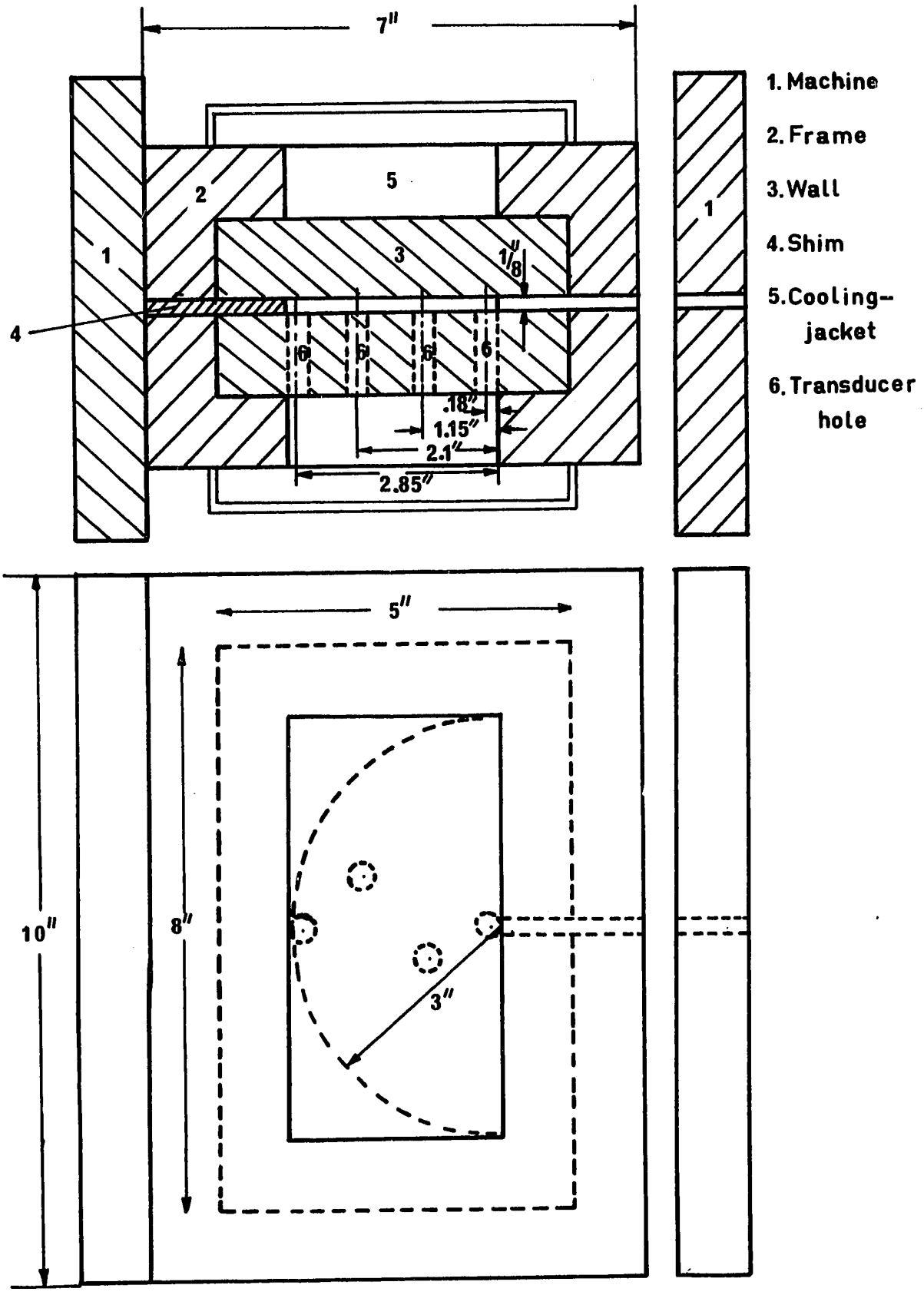

walls of the mold were made of transparent, especially tempered 1 1/8 inch pyrex 7720 glass, prepared by John's Scientific. Flow patterns and filling times were observed with the aid of a 16 mm. high speed camera. The camera used was a rotating-prism type "Hycam" Model K20S4E, manufactured by Red Lake Labs. Inc. Movies were taken at 200 frames per second. In the second mode, the glass walls were replaced by 1 1/4 inch steel walls. Four holes were drilled in one of the walls, as shown in Figure 2-2 for the insertion of a pressure transducer with a built-in thermocouple. The holes were plugged when the transducer was not used. The way in which the transducer was mounted in the wall of the cavity is shown in Figure 2-3. Special care was taken to ensure that the surface of the transducer was flush with the inside surface of the cavity, to avoid any interference with the flow of the melt.

In addition to measuring the pressure, the transducer was used to indicate the time required for the melt to travel from one position to the other. Since the response of the transducer was effectively instantaneous, it would start to indicate pressure as soon as the melt touched it. Thus measurements taken with the transducer placed at different points indicated the time required for the melt to reach the corresponding radii.

FIGURE 2-3

ARRANGEMENT OF TRANSDUCER IN THE CAVITY WALL

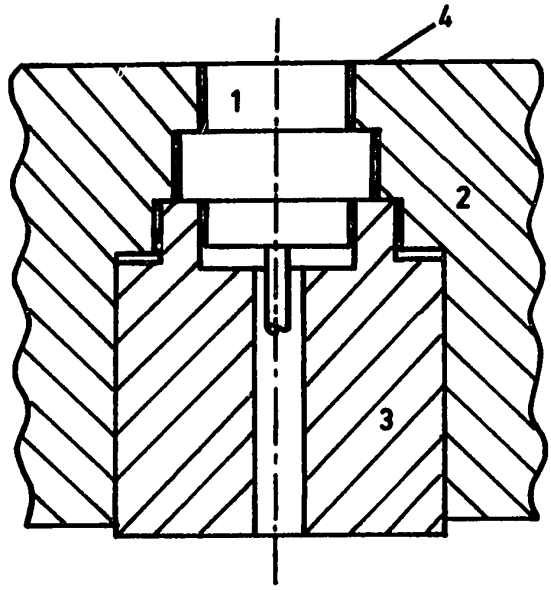

1. Transducer

2. Cavity wall

3. Plug

4. Cavity surface

In order to ensure that atmospheric pressure was attained at the melt front, during the filling stage, shims of 0.003 inch thickness were placed between parts 3 and 4 (Figure 2-2) in order to allow air to escape.

Water was circulated over the outside surface of the steel cavity. The temperature of the circulating water was controlled at 80 $\pm 5^{o}$F. This was achieved by employing a Sterlco heating-cooling unit, Model 7000. Water was circulated only during the experiments involving the steel walls. An attempt was made to circulate water during the experiments with the glass walls. The motion of the flowing water, small particles and air bubbles interfered with the clarity of the films, thus air at room temperature 75 $\pm 5^{o}$F was used instead.

2.2 TRANSDUCER SYSTEM AND ITS CALIBRATION

The pressure transducer used in this study is Model TG-M-6G(T) manufactured by Sensotec for measuring pressures up to 20,000 psi and temperature up to 425^{o}F, see Figure 2-4. The active diameter of the transducer is 0.19 inch. It is of a force collecting type, utilizing four arm foil strain gauges, connected in a conventional Wheatestone Bridge arrangement. It uses an excitation voltage of 3.0 volts D.C., and has an input impedance of 117.0 ohms, and an output inpedance 117.1 ohms. Temperature compensation resistors are included to compensate for the effects of temperature variation.

FIGURE 2-4

SCHEMATIC DIAGRAM OF TRANSDUCER TG-M-6G(T)

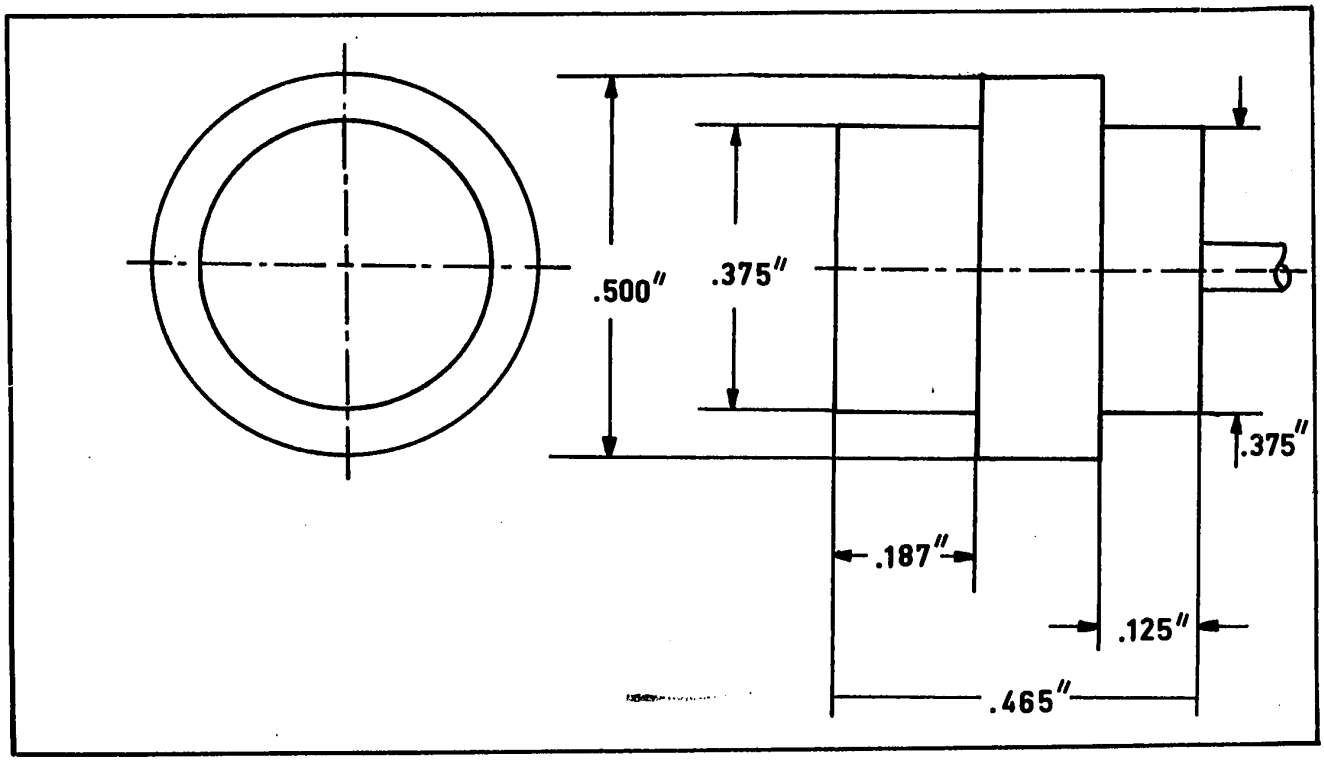

However, the thermal error of the transducer used is -1 psi/^{o}F.

An iron-constantan thermocouple is built in the transducer to give a simultaneous measurement of the surface temperature. The pressure transducer is equipped with a signal conditioning unit, Model SCA-4 manufactured by Sensotec. The unit consists of the following components:

a) Transducer power supply with three available voltages: 3, 5 and 10 volts D.C.

b) A set of variable resistors capable of balancing the transducer bridge.

c) Gain control for varying the amplification of the signal.

d) A fixed shunt resistor for calibration purposes.

Pressure and temperature-time curves have been obtained with the aid of a Sanborn 7702 oscillographic recorder, operating at various chart speeds. Two speeds were used: 20 and 100 mm. per second. The frequency response of the recorder is 125 Hz. Thus the recorder response is the limiting factor, since the frequency response of the transducer is of the order of 20,000 Hz. while that of the signal conditioning unit is 2,000 Hz.

A special calibration apparatus was built, as shown in Figure 2-5. It consists of a cylindrical reservoir connected to a pressure gauge Model M manufactured by Foxboro that could measure pressures up to 3,000 psi. For the purpose

FIGURE 2-5

TRANSDUCER CALIBRATION APPARATUS

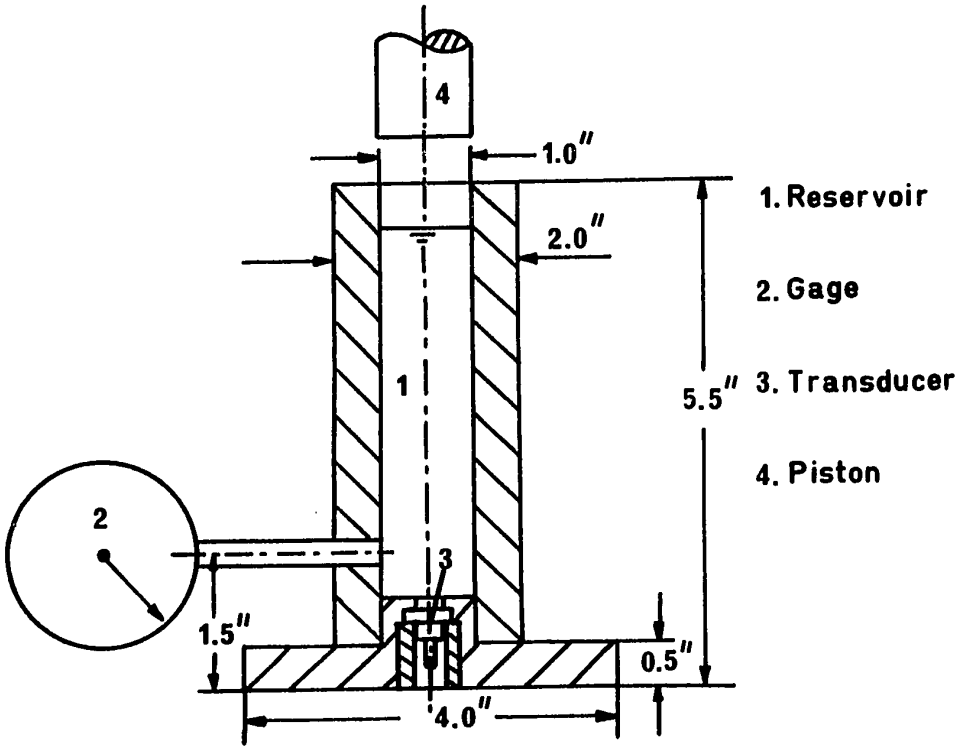

of calibration, the transducer was fixed in the bottom part of the cylinder, in the same arrangement used in the mold cavity, see Figure 2-3. The cylindrical reservoir was filled with silicone oil 710R to the appropriate level, and the piston was placed inside the cylinder. The load was supplied, to the piston by the Instron Mechanical Tester. The transducer was connected to the signal conditioning unit and the latter was connected to the Sanborn recorder. Various loads were applied and the corresponding simultaneous readings were taken from the pressure gauge and the recorder. The transducer showed a linear increase of voltage with load as shown in Figure 2-6.

In order to calibrate the transducer permanently, so that the pressure would be known regardless of the amplification used both in the recorder and the signal conditioning unit, a special procedure was followed: If a resistor is keyed across a leg of the transducer bridge as shown in Figure 2-7, a deflection in the output circuit results, which simulates the effect of the combined resistance changes of the active leg due to a change of pressure. In this way calibration of the transducer could be made, before every experiment and regardless of the amplification of the signal, without the necessity of applying a physical quantity, provided that the equivalent of the change in pressure units is known. For this purpose, a precision resistor is supplied in the signal con-

FIGURE 2-6

CALIBRATION CURVE FOR PRESSURE TRANSDUCER

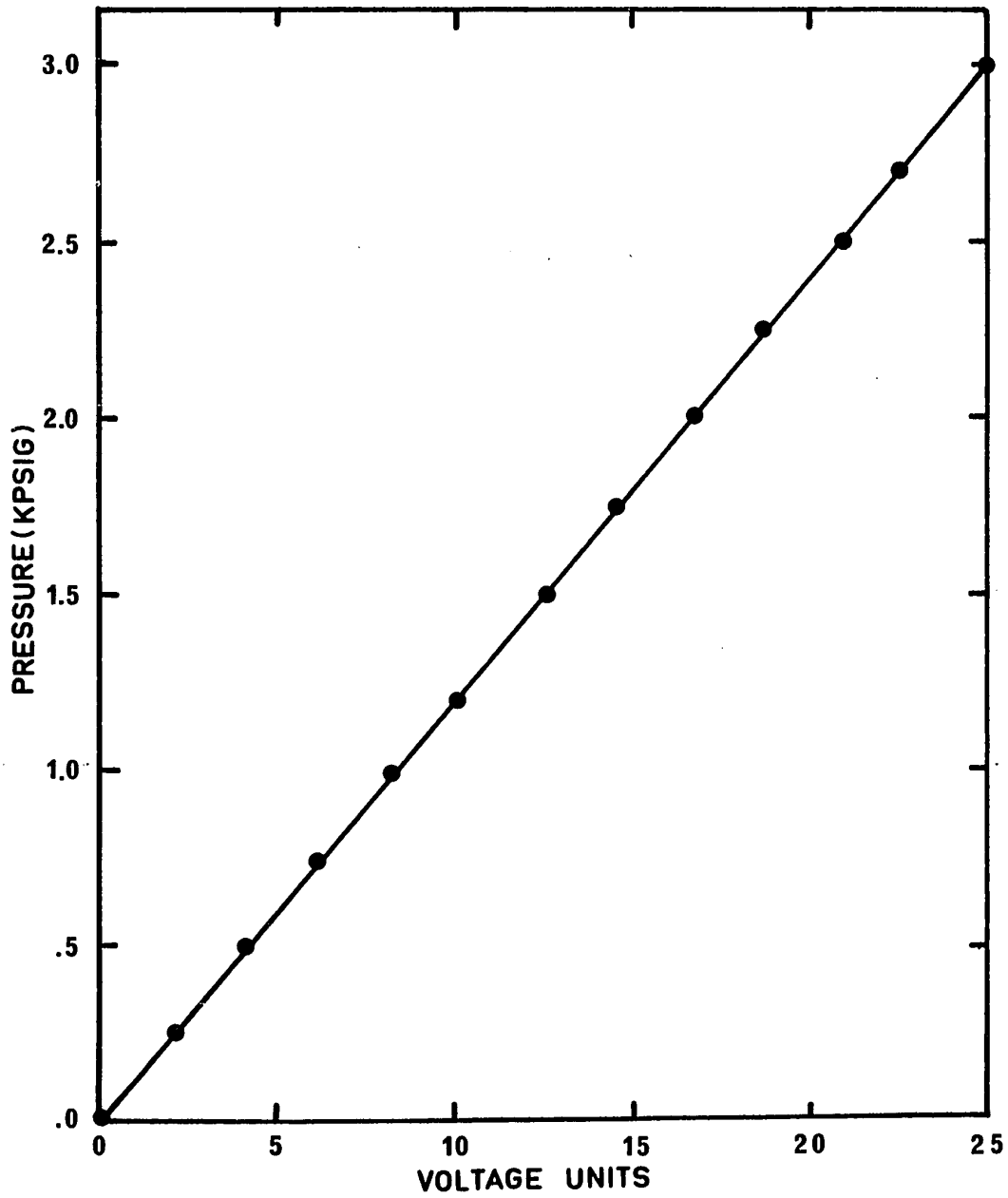

FIGURE 2-7

SCHEMATIC DIAGRAM OF ELECTRICAL CIRCUIT FOR THE TRANSDUCER

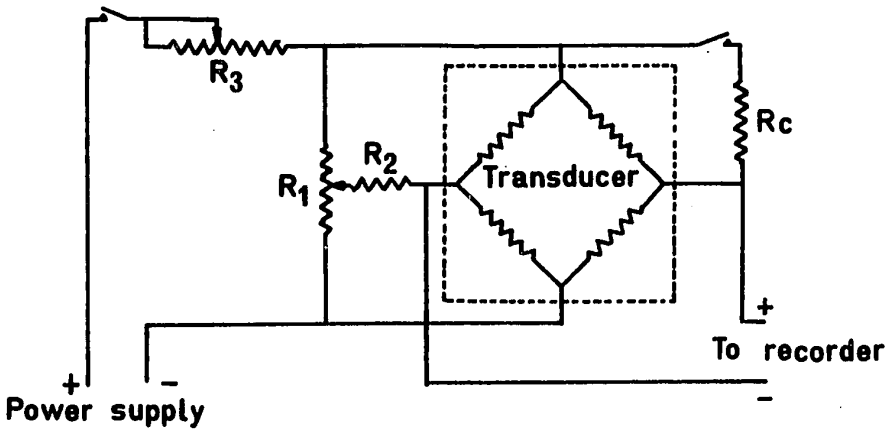

R_1 – Zero adjustment
R_2 – Padder
R_3 – Input rheostat
Rc – Calibration resistor

ditioning unit. By shunting the resistor over a leg in the bridge a resultant voltage change is recorded. The equivalence of the resistor was found to be 7200 ± 50 psi. Although the calibration was done in the range of 0-3000 psig, the calibration specifications of the manufacturer gave a deviation of 0.1% in the linearity of the output voltage versus pressure applied over the range of 0-20,000 psig.

The calibration of the Iron-Constantan thermocouple was checked by inserting the probe in ice-distilled water mixture and in distilled boiling water, and found to agree with the charts supplied by the manufacturer. In addition, the time constant of the thermocouple was obtained by inserting the probe in boiling water from room temperature. The temperature-time curve is given in Figure 2-8. The thermocouple was found to obey approximately a first order system, since a plot of the logarithm of the temperature versus time resulted in a straight line (25), see Figure 2-9. The time constant was found to be 4.1 seconds.

2.3 EXPERIMENTAL PROCEDURE

At the beginning of each run, the temperature controllers were fixed at the desired melt temperature. About 20-30 minutes were needed for the temperature to reach its final value. When temperature was sufficiently high, polymer pellets were placed in the hopper and the screw was rotated in order to

FIGURE 2-8

TEMPERATURE-TIME CURVE FOR
THERMOCOUPLE CALIBRATION

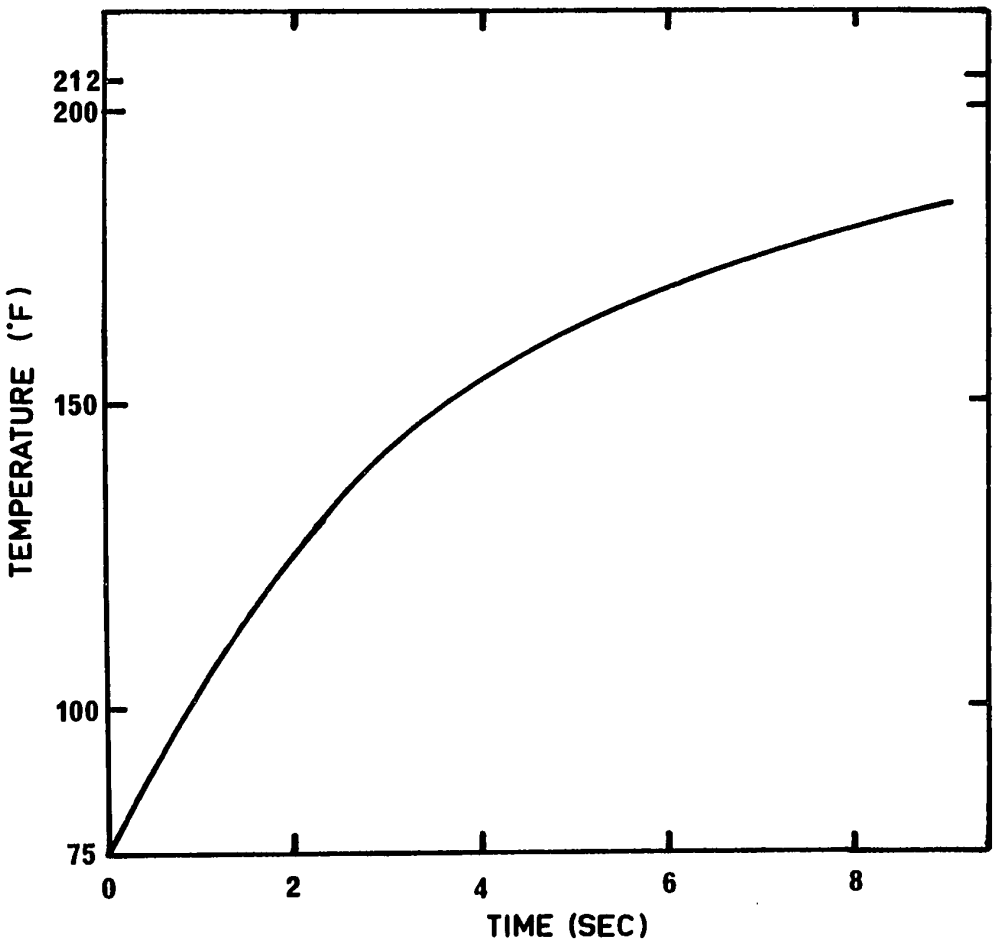

FIGURE 2-9

TEMPERATURE-TIME PLOT FOR
FIRST ORDER SYSTEM

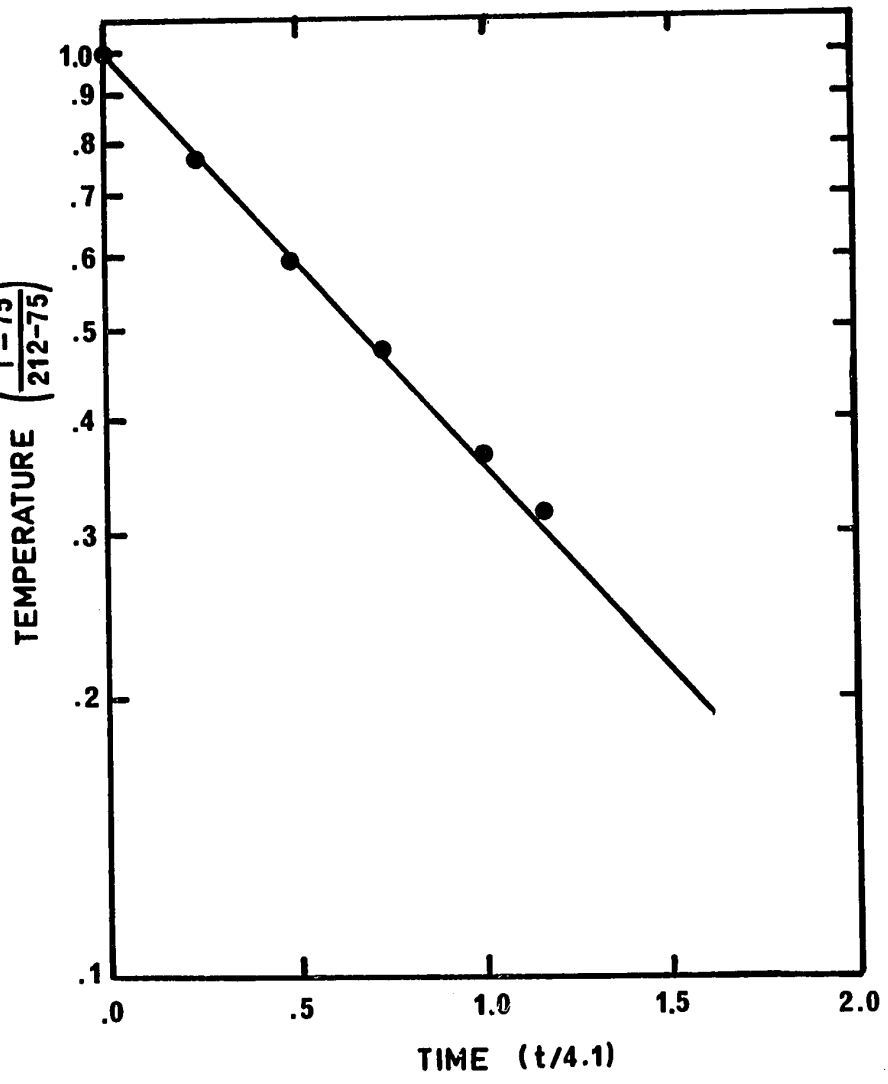

plasticize and convey the polymer melt to the reservoir section. The melt was injected a few times into the open air in order to clean the barrel from old material that could be degraded. At this point, the recorder and the signal conditioning unit were switched on to allow one hour of warming up as recommended by the manufacturer. Water was circulated and about half an hour was needed for the temperature of the mold to reach the 80°F mark, as indicated by the thermocouple and an additional thermometer.

When all the components were ready, the settings for the pressure control valves and the shot size were fixed at the desired values. The recorder was run at the appropriate speed and the melt was injected manually. Pressure was applied during the entire cycle, till the recorded pressure decreased to atmospheric. Then the mold was opened and the molded article was ejected and marked.

Subsequently, experiments were conducted for the same melt temperature, shot size, and transducer position but at different injection pressures. Then, the melt temperature was changed and the whole sequence was repeated. In order to change the position of the pressure transducer, water circulation was stopped, the mold was taken apart, and the position was changed. The whole procedure was repeated for the same melt temperatures and the same pressure valve settings as above. In this way results were obtained for the four transducer positions at different melt temperatures

and different injection pressure settings, for the same shot size. After this sequence was completed, the shot size was changed, in order to check the model for the packing stage.

In the movie experiments, the injection pressure and temperature conditions were the same as those employed in the corresponding transducer experiments. Thus each set of conditions was employed twice: once with the steel cavity for transducer measurements and once with the glass cavity for photographic analysis.

Each run was repeated two or three times, in order to check reproducibility of the results and to emphasize different stages in the injection molding process. For example, since the packing stage was relatively short, the speed of the chart was increased to the maximum velocity of 100 mm per second in some runs. In addition the amplification of the recorded signal in the filling stage was increased in order to allow accurate readings of the relatively low pressures during the stage.

The semi-automatic mode was used in order to show with actual moldings that radial flow existed in the parallel feeding injection system. This was done by setting the injection timer to different injection durations, at the same injection pressure conditions. Thus the filling stage was frozen at different stages.

2.4 MATERIALS AND PROPERTIES

Experimental results and theoretical calculations have been carried out for two polymers: one crystalline and the other amorphous.

The crystalline category is represented by Dow Chemical High Density Polyethylene E.P. 245 which has a density of 0.953 corresponding to crystallinity of about 72%. Thermal diffusivities for the solid and melt phases have been calculated from the thermal conductivity given by Nagler (26) for high density polyethylene. Specific heat and density are given by Bernhardt (27). For the solid phase, the average properties are : thermal conductivity k_s = 0.260 Btu/hr/ft/^oF; specific heat C_{ps} = 0.55 Btu/lb/^oF and density ρ_s = 57.0 lb/ft^3. For the melt region the average properties are: thermal conductivity k_m = 0.130 Btu/hr/ft/^oF; specific heat C_{pm} = 0.70 Btu/lb/^oF and density ρ_m = 46.0 lb/ft^3. The latent heat portion of the freezing enthalpy for polyethylene is 95 Btu/lb as given by references (22) and (28). The PVT diagram used is given by Bernhardt (27) and shown in Figure 2-10. The constants for the equation of state are: ω = 47,600 psi; b = 0.875 cc/gm; R_c = 43.0 in units consistent with T in ^oK; V in cc/gm and P in psi.

The amorphous group is represented by Dow Chemical Polystyrene Styron 683C. Thermal diffusivity is taken from Shoulberg (29) $\alpha = 3.1 \times 10^{-3}$ ft^2/hr. Thermal conductivity is calculated from thermal diffusivity, specific heat and

FIGURE 2-10

P-V-T DIAGRAM FOR POLYETHYLENE

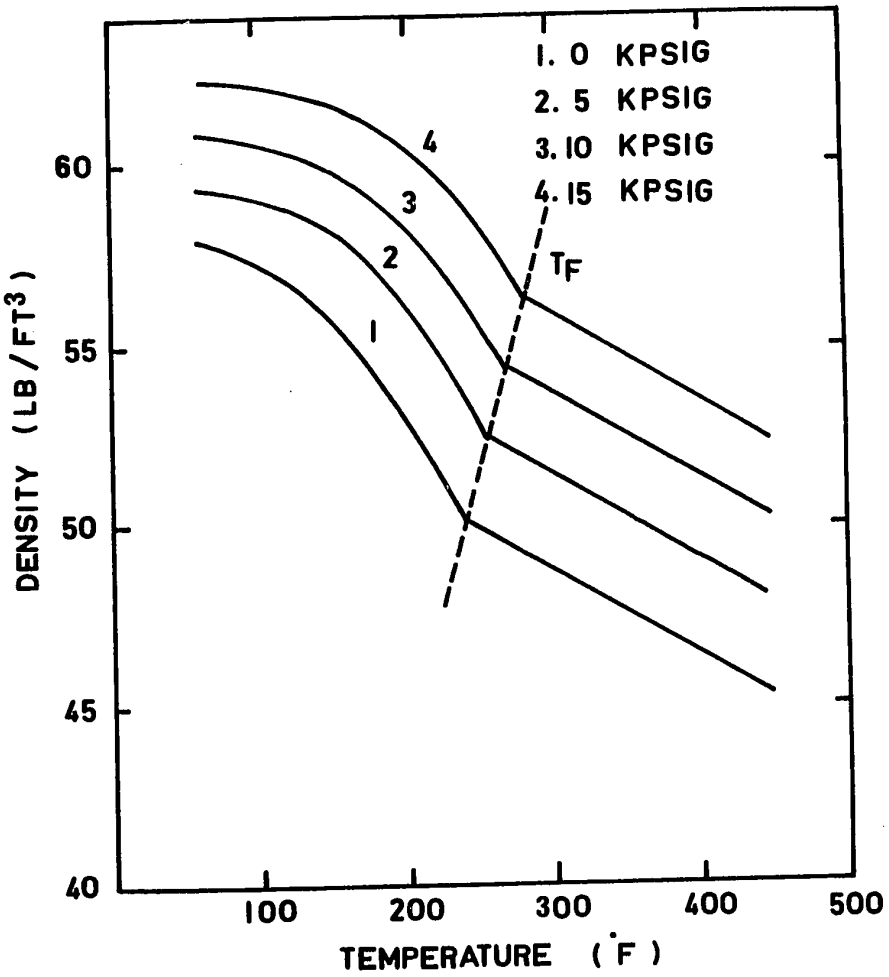

FIGURE 2-11

P-V-T DIAGRAM FOR POLYSTYRENE

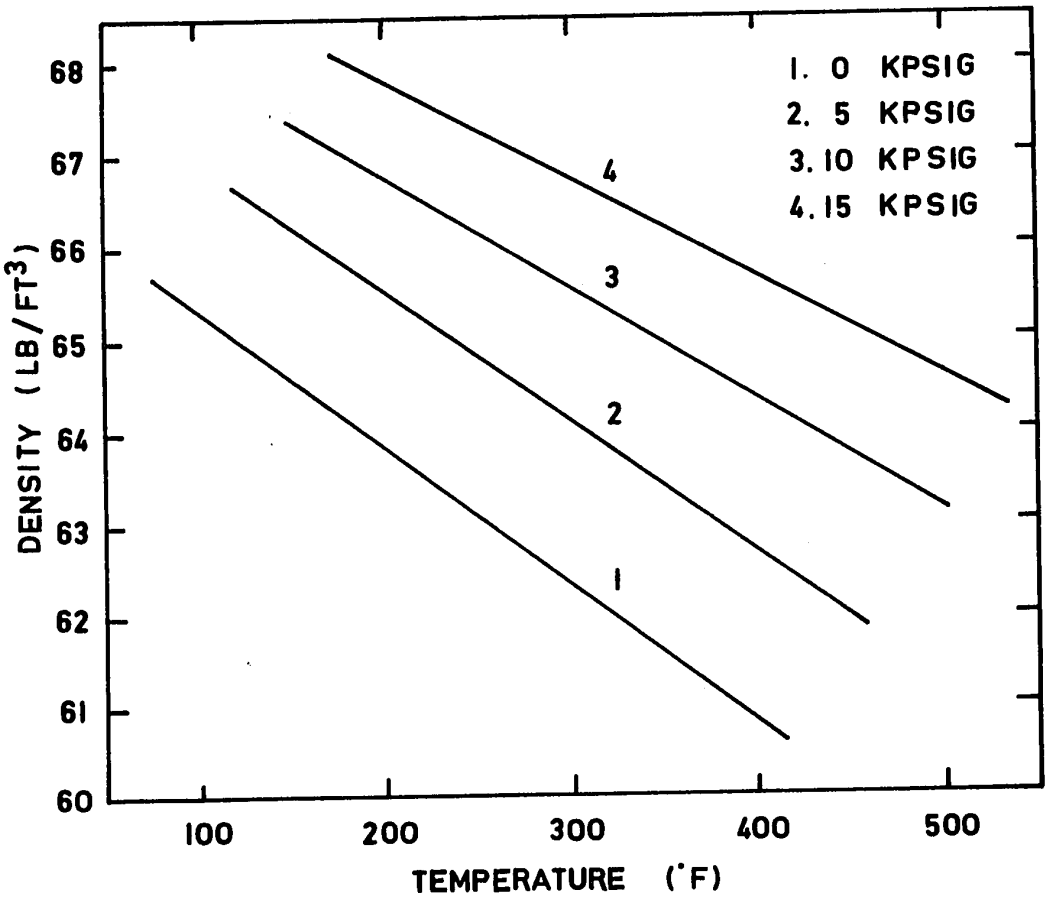

density at 400°F as given by Bernhardt (30), k_t = 0.06 Btu/ft/hr/°F. The PVT diagram used is given by Bernhardt (30) and shown in Figure 2-11. The corresponding constants for the equation of state are: ω = 27,000 psi; b = 0.822 cc/gm; R_c = 11.6 in the same units as above.

The effective heat transfer coefficient, H, between the polymer and the cavity wall are taken to be 50-150 Btu/ft^2/hr/°F as pointed by Jepson (31) and Carley (32).

For rheological properties see Appendix 1.

3. FILLING STAGE

In the treatment of injection molding, the process will be divided to three stages: filling, packing and cooling. It is not intended, however, to imply that these three stages are independent of each other. In fact, it is essential to preserve the continuity of the process and to recognize that in the complete treatment of the injection molding cycle, the conditions that exist at the end of one stage prevail at the beginning of the following stage. The division into three stages is intended mainly for purposes of discussion and mathematical analysis. At the end of the treatment, the three stages will be recombined to evaluate the validity of the proposed approach for the overall integrated injection molding process.

3.1 THEORETICAL ANALYSIS

3.1.1 Equations and Boundary Conditions

The filling stage is concerned with the unsteady-state non-isothermal flow of a hot, non-Newtonian, compressible fluid, partially solidifying during flow, as the cavity walls are kept below the freezing temperature of the polymer. In this study, spreading radial flow of the plastic melt is of interest.

Qualitatively, the problem of mold filling may be summarized as follows: A polymer melt at a uniform temperature is contained in a reservoir. At zero time, pressure is applied to the melt (pressure may be constant or variable with time). Then , the polymer starts to flow through a capillary into a semicircular cavity. Flow continues in a spreading radial flow pattern until the advancing front hits the outer boundary of the cavity.

In order to describe this qualitative picture mathematically, one starts from the basic equations of change (33,34). Assuming that the only non-zero velocity component is in the radial direction, V_r, and that symmetry with respect to the axial direction exists, the equations of change take the following forms (using cylindrical co-ordinates):

Continuity: $$\frac{\partial \rho}{\partial t} + \frac{1}{r}\frac{\partial}{\partial r}(\rho . r . V_r) = 0 \qquad \ldots\ldots (3\text{-}1)$$

Momentum: $$\rho\left(\frac{\partial V_r}{\partial t} + V_r \frac{\partial V_r}{\partial r}\right) = -\frac{\partial P}{\partial r} - \left[\frac{1}{r}\frac{\partial}{\partial r}(r . \tau_{rr}) - \frac{\tau_{\theta\theta}}{r} + \frac{\partial \tau_{rz}}{\partial z}\right] + \rho g_r \qquad \ldots\ldots\ldots (3\text{-}2)$$

Energy: $$\rho C_p \left(\frac{\partial T}{\partial t} + V_r \frac{\partial T}{\partial r}\right) = k_t\left[\frac{1}{r}\frac{\partial}{\partial r}\left(r \frac{\partial T}{\partial r}\right) + \frac{\partial^2 T}{\partial z^2}\right] + - \tau_{rr}\frac{\partial V_r}{\partial r} - \tau_{00}\frac{V_r}{r} - \tau_{rz}\frac{\partial V_r}{\partial z} \qquad \ldots (3\text{-}3)$$

Where P and T are the pressure and temperature, respectively, at time t and at a point which has radial and axial co-ordinates r and z, respectively, as in Figure 1-2d. The time elapsed from the beginning of injection is t, while ρ is the density, C_p is the specific heat, k_t is the thermal conductivity, and τ_{rr}, τ_{rz} and $\tau_{\theta\theta}$ are components of the stress tensor at the point of interest.

The following simplifying assumptions are made in obtaining a solution to the filling problem:

1. Viscoelastic and entrance effects are not included.
2. τ_{rr} and $\tau_{\theta\theta}$ are neglected due to the lack of rheological data and simplicity (see Appendix 1 and Appendix 7). Thus the only shear stress τ_{rz} is included.
3. It is assumed that the melt obeys the Power Law, see Appendix 1.
4. The unsteady state terms in the momentum and continuity equations are neglected, in view of the comparatively long duration of flow. At any instant, $\frac{\partial V_r}{\partial t}$ is very small compared to other terms in these equations. However, the velocity at any point in the cavity changes with time; see Appendix 2.

5. The polymer is assumed to be a compressible fluid only for the purpose of solving the continuity equation. It is assumed to be an incompressible fluid for the energy and momentum equations.

6. Creeping flow is assumed. Thus, the nonlinear term $V_r \times \frac{\partial V_r}{\partial r}$, in the equation of motion is omitted. This term is of some importance in the entrance region, since both the velocity and its derivative are quite large. However, due to computational difficulties this term is omitted in the present treatment (see Appendix 7).

7. Heat conduction in the direction of flow (r) is negligible in comparison to convected heat transfer.

8. In the case of crystalline polymers (like polyethylene), the specific heat, thermal conductivity and thermal diffusivity are assumed to be constant but having different values, depending on whether the melt is above or below the freezing temperature. In the case of amorphous polymers (like polystyrene) only one constant is assigned to these properties (24).

By employing the above assumptions, the equations of change take the following forms:

Continuity: $$\frac{\partial}{\partial r}(\rho \cdot r \cdot V_r) = 0 \qquad \text{.....(3-4)}$$

Motion: $$\frac{\partial P}{\partial r} = \frac{\partial}{\partial z}\left[M \left(\frac{\partial V_r}{\partial z}\right)^n\right] \qquad \text{.....(3-5)}$$

Energy: $$\rho C_p \left(\frac{\partial T}{\partial t} + V_r \frac{\partial T}{\partial r}\right) = k_t \frac{\partial^2 T}{\partial z^2} + M \left(\frac{\partial V_r}{\partial z}\right)^{n+1} \qquad \text{...(3-6)}$$

Where M is the consistency index, and n is the flow index.

The following boundary conditions were employed in conjunction with the above equations of change.

a) There is no slip at the wall

$$V_r(r, \pm h, t) = 0 \qquad \text{.....(3-7)}$$

Where h is half of the thickness of the cavity.

b) The velocity profile is symmetrical around z=0.

$$\frac{\partial V_r}{\partial z}(r, o, t) = 0 \qquad \text{.....(3-8)}$$

c) At the cavity walls, a constant heat transfer coefficient H is assumed, thus

$$k_t\left(\frac{\partial T}{\partial z}\right)_{z=\pm h} = H[T_o - T(r, \pm h, t)] \qquad \text{.....(3-9)}$$

Where T_o is the wall temperature.

d) The melt temperature at the entrance to the cavity, where r = a, is constant at T_I.

$$T(a, z, t) = T_I \qquad \text{.....(3-10)}$$

Also the effects of viscous heating and cooling in the runner are ignored, so, that the temperature T_I is the same as the melt temperature in the injection reservoir (see section 3.2.2).

e) The temperature profile is symmetrical around z=0.

$$\frac{\partial T}{\partial z}(r, o, t) = 0 \qquad \text{.....(3-11)}$$

f) The radial temperature gradient is zero in a newly formed volume increment near the melt front, R.

$$\frac{\partial T}{\partial r}(R, z, t) = 0 \qquad \text{.....(3-12)}$$

g) In the regions where the temperature is below the solidification temperature, T_F, the velocity of the polymer is zero.

$$V_r(r,z,t) = 0 \quad \text{for} \quad T(r,z,t) \leq T_F \qquad (3\text{-}13)$$

h) In the regions where the temperature reaches the solidification temperature, T_F, heat of freezing is evolved only in the case of crystalline polymers. In the solidifying layer, the following equations hold (35).

$$k_s\left(\frac{\partial T_s}{\partial z}\right)_{z=\epsilon} - k_m\left(\frac{\partial T_m}{\partial z}\right)_{z=\epsilon} = \rho_s L \frac{d\epsilon}{dt} \qquad \text{....(3-14)}$$

$$T_m = T_s = T_F \quad \text{at} \quad z = \epsilon \qquad \text{.....(3-15)}$$

Where s and m refer to the solid and melt, respectively; ϵ is the axial co-ordinate of the freezing front, and L is the latent heat of freezing

i) The variation of pressure with time is known at the entrance to the cavity:

$$P(a,t) = P_o(t) \qquad \text{.....(3-16)}$$

$P_o(t)$ is obtained experimentally with the help of the transducer when it is positioned at the entrance to the cavity. The entrance radius, a, is equal to the radial distance between the centre of the cavity and the centre of the transducer at the entrance position.

j. The pressure at the melt front, R, is equal to atmospheric pressure:

$$P(R,t) = P_{atm} \qquad \text{.....(3-17)}$$

The volumetric flow rate is defined as follows:

$$Q(r,t) = 2 \int_o^h \pi r V_r(r,z,t)dz \qquad \text{.....(3-18)}$$

Also, the incremental time, Δt, that is required for the advancement of the front from R_1 to R_2 is given by:

$$\Delta t = \frac{\pi(R_2^2 - R_1^2) \times h}{Q(R_1, t)} \qquad \text{.....(3-19)}$$

In the cases where the melt is treated as a compressible fluid, either an equation of state or a P-V-T diagram is used to relate temperature, pressure and density. The equation of state has the form (36):

$$(P + \omega)(V - b) = R_c T \qquad \text{.....(3-20)}$$

Where ω, b and R_c are constants characteristic of the polymer and V is the specific volume. Equation (3-20) is valid only for the melt region. In order to extend the compressible fluid treatment to the regions close to the freezing temperature and below it, a P-V-T diagram is employed (27,30).

The above analysis of the filling stage may be applied to any plastic material. If the polymer is amorphous, boundary conditions (3-14) and (3-15) are omitted. If the polymer is assumed to be an incompressible fluid, the density in equation (3-4) is omitted, and the equation of state (3-20) is not used. Otherwise, for the general case of a crystalline compressible fluid, all the equations are needed.

The filling stage, as analyzed above, results in a mixed problem, with moving boundaries. The continuity equation (3-4), momentum equation (3-5) with boundary conditions (3-7) and (3-8) result in a boundary value problem in the axial

direction (z), and a two point boundary value problem in the radial direction as a result of boundary conditions (3-16) and (3-17). The energy equation (3-6) and boundary conditions (3-9, (3-10), (3-11) and (3-12) result in an initial value problem in the axial and radial directions. As the melt advances in the cavity the flow boundary in the radial direction moves, in addition the solidification that takes place results in another moving boundary in the axial direction.

The mathematical complexity inherent in the above equations and the fact that these equations are coupled through the dependence of the material properties on temperature, makes the analytical solution to the filling stage impossible, thus numerical methods were employed with the help of a digital computer.

3.1.2 Dimensional Analysis

For the sake of generality, a dimensional analysis has been carried out. The following dimensionless terms are defined:

$$r^* = r/R_o \qquad V^* = V/V_e$$

$$z^* = z/h \qquad P^* = P/P_f$$

$$t^* = \frac{t \cdot V_e}{h} \qquad T^* = \frac{T - T_o}{T_l - T_o}$$

$$V_e = (P_f/\rho_m)^{\frac{1}{2}} \qquad A_r = h/R_o$$

Where R_o is the radius of the cavity, h is half thickness of the cavity, P and T are the pressure and temperature, respectively, P_f is the experimentally measured pressure at the entrance to the cavity at the end of filling, and ρ_m is a reference density. T_o and T_1 are the wall temperature and the temperature at the entrance to the cavity, respectively. It should be emphasized that since compressibility is taken into account only in the continuity equation, this analysis is valid also for the case of a compressible fluid, in spite of the fact that a reference density is involved in the definition of V_e. By employing the above definitions, the equations of change take the following forms:

Continuity: $$\frac{\partial}{\partial r^*}(\rho . V^* . r^*) = 0 \qquad \text{.....(3-21)}$$

Motion: Since $\frac{\partial P^*}{\partial r^*} \neq f(z^*)$, the equation of motion is integrated to give:

$$A_r \frac{\partial P^*}{\partial r^*} = \frac{1}{Re} \frac{1}{z^*} \left[\left(\frac{\partial V^*}{\partial z^*}\right)^n\right] \qquad \text{.....(3-22)}$$

Energy: $$\frac{\partial T^*}{\partial t^*} + A_r V^* \frac{\partial T^*}{\partial r^*} = \frac{1}{Pr \cdot Re} \frac{\partial^2 T^*}{\partial z^{*2}} + \frac{Br}{Pr \times Re} \left(\frac{\partial V^*}{\partial z^*}\right)^{n+1} \qquad \text{.....(3-23)}$$

In the above equations, the following dimensionless groups have to be defined:

$$Re = \frac{V_e^{2-n} \rho_m h^n}{M}$$

$$Pr = \frac{M C_p h^{1-n}}{k_t V_e^{1-n}}$$

$$Br = \frac{M V_e^{1+n} h^{1-n}}{k_t (T_1 - T_o)}$$

The boundary conditions take the following forms:

a) $$V^* (r, \pm 1, t^*) = 0 \qquad \text{.....(3-24)}$$

b) $$\frac{\partial V^*}{\partial z^*} (r^*, 0, t^*) = 0 \qquad \text{.....(3-25)}$$

c) $$\left(\frac{\partial T^*}{\partial z^*}\right)_{z^* = \pm 1} = \frac{H \times h}{k_t} [-T^*(r^*, \pm 1, t^*)] \qquad \text{.....(3-26)}$$

d) $$T^* (a^*, z^*, t^*) = 1 \qquad \text{.....(3-27)}$$

e) $$\frac{\partial T^*}{\partial z^*} (r^*, 0, t^*) = 0 \qquad \text{.....(3-28)}$$

f) $$\frac{\partial T^*}{\partial r^*} (R^*, z^*, t^*) = 0 \qquad \text{.....(3-29)}$$

g) $$V^*(r^*, z^*, t^*) = 0 \quad \text{for} \quad T^*(r^*, z^*, t^*) \leq T_F^* \qquad \text{....(3-30)}$$

h) $$\left(\frac{\partial T^*}{\partial z^*}\right)_{z^* = \epsilon^*} - \frac{k_m}{k_s} \left(\frac{\partial T_m^*}{\partial z^*}\right)_{z^* = \epsilon^*} = \frac{\rho_s \cdot L \cdot V_e \cdot h}{k_s (T_1 - T_o)} \frac{d\epsilon^*}{dt^*}$$

$$\text{.....(3-31)}$$

i) $$T_s^* = T_m^* = T_F^* \quad \text{at} \quad z^* = \epsilon^* \qquad \text{.....(3-32)}$$

j) $$P^*(a^*, t^*) = P_o^*(t^*) \qquad \text{.....(3-33)}$$

k) $$P^*(R^*, t^*) = P_{atm}^* \qquad \text{.....(3-34)}$$

$$Q^*(r^*,t^*) = 2 \int_0^{1.0} \pi r^* V^*(r^*,z^*,t^*)\, dz^* \qquad \text{.....(3-35)}$$

$$\Delta t^* = \frac{\pi(R_2^{*2} - R_1^{*2})}{A_r\, Q^*(R_1^*, t^*)} \qquad \text{.....(3-36)}$$

3.1.3 Difference Equations

The set of partial differential equations (3-21), (3-22), (3-23) together with the boundary conditions and other equations(3-24)-(3-36) are solved simultaneously by numerical techniques. The standard finite difference representation is used for this purpose. Briefly, the method replaces partial derivatives by finite difference approximations. Thus the set of differential equations is replaced by a set of algebraic equations, which may be solved simultaneously with the aid of a digital computer (37,38). Finite difference representation may be accomplished by either an explicit or an implicit scheme,with varying degrees of accuracy. In

general, implicit schemes are stable in nature but expensive to use, since iteration procedures are usually involved. Explicit schemes have the disadvantage of limited stability. Various methods have been used in order to improve the stability of explicit schemes.

The first step, in the numerical solution, is the construction of a network as in Figure 3-1. It consists of I points in r direction and J points in z direction. A radial increment, Δr, and axial and time increments Δz and Δt are defined, respectively. Finite difference equations are written for each point in the net. Since the energy equation (3-23) represents an unsteady-state situation, one may write all second derivatives in Saul'yev's manner (39). Thus it is possible to employ an explicit and stable scheme for computation. All other derivatives have been centered,whenever possible. For the derivatives in the radial direction the average of the forward and backward differences have been used.

Equations (3-21) and (3-22) are written in different forms for the convenience of computation. First, equation (3-22) is integrated with respect to z* to give:

$$V^*(r^*,z^*,t^*) = \left(\frac{\partial P^*}{\partial r^*}\right)^{1/n} \times I_1 \quad \cdots\cdots\cdots\cdots (3\text{-}37)$$

FIGURE 3-1

FINITE DIFFERENCE NET

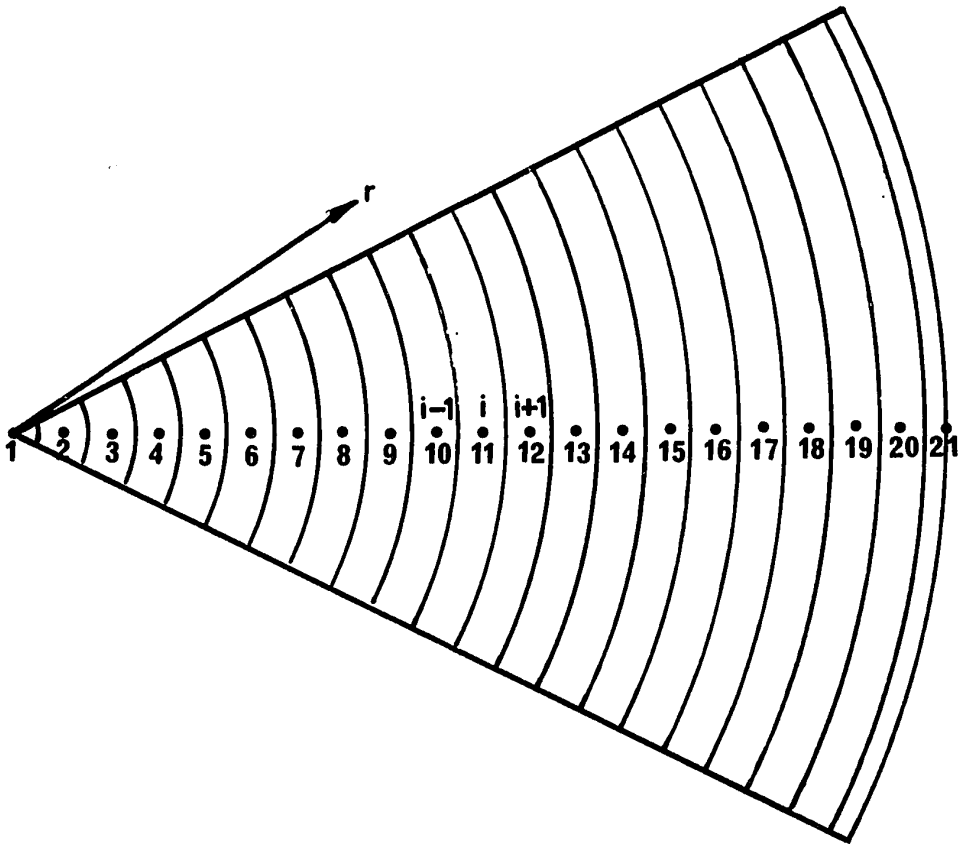

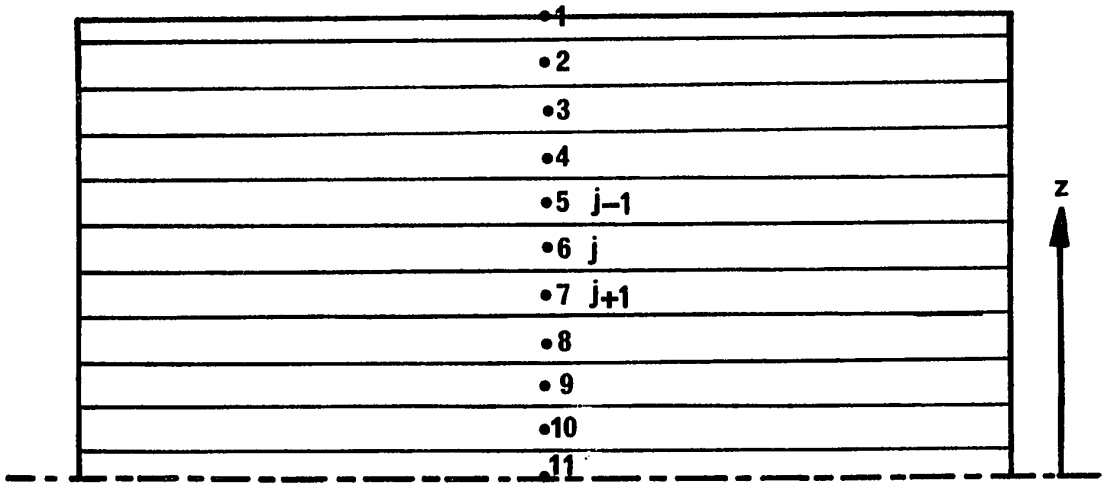

Where $$I_1 = \int_{z^*=1.0}^{z^*} (z^* \cdot A_r \cdot Re)^{1/n} \, dz^*$$

From equation (3-21) one may write the mass flow rate, Q_m, as follows:

$$Q_m(r^*,t^*) = 2 \int_{z^*=0}^{z^*=1.0} \pi r^* \rho(P,T) V^* \, dz^* \qquad \ldots\ldots(3\text{-}38)$$

Substitution of (3-37) results in:

$$Q_m(r^*,t^*) = 2\pi r^* \times \left(\frac{\partial P^*}{\partial r^*}\right)^{1/n} \times \int_{z^*=0}^{z^*=1.0} \rho(P,T) \times I_1 \times dz^* \qquad \ldots\ldots(3\text{-}39)$$

and finally:

$$\frac{\partial P^*}{\partial r^*} = \left[\frac{Q_m(r^*, t^*)}{2\pi r^* \int_{z^*=0}^{z^*=1.0} \rho(P,T) \times I_1 \times dz^*}\right]^n \qquad \ldots\ldots(3\text{-}40)$$

The integrals that appear in equations (3-37), (3-39) have been obtained numerically by employing the "Extended Trapezoidal Rule" (40). Equation (3-40) is written in the following difference form:

$$P^*_{(i)} = P^*_{(i-1)} - \left\{\left[\frac{Q_m}{I_{2(i)}}\right]^n + \left[\frac{Q_m}{I_{2(i-1)}}\right]^n\right\} \Delta r^*/2 \qquad \ldots\ldots(3\text{-}41)$$

This equation has been obtained by writing the forward difference for point (i-1) and a backward difference for point (i) and averaging the results (see Figure 3-1). I_2 is defined in the following equation:

$$I_2 = 2\pi r^* \int_{z^*=0}^{z^*=1} \rho(P,T) \times I_1 \times dz^*$$

The energy equation has been written in the following finite difference form:

$$T^*(i,j,k+1) = T^*(i,j,k) \times \frac{1-A}{1+A} - [V^*(i,j,k+1)+V^*(i-1,j,k+1)]/2$$

$$\times \frac{A_r \times \Delta t^*}{\Delta r^*(1+A)} \times [T(i,j,k) - T^*(i-1,j,k)]$$

$$+ \frac{A}{1+A} [T^*(i,j-1,k+1) + T^*(i,j+1,k)]$$

$$+ \frac{Br}{Pr \cdot Re\,(1+A)} \Delta t^* \times \left[\frac{V^*(i,j+1,k+1)-V^*(i,j-1,k+1)}{2 \times \Delta z^*}\right]^{n+1} \quad \text{.....(3-42)}$$

Where $A = \dfrac{\Delta t^*}{\Delta z^{*2} \cdot Pr \cdot Re}$, i and j as defined in Figure 3-1 and k is the number of time increments elapsed from the beginning of injection.

The boundary conditions are expressed in difference form as follows:

a) $V^*(i, \pm J, k) = 0$ .....(3-43)

b) $V^*(i, 1, k) = V^*(i,2,k)$ .....(3-44)

c) $T^*(i,\pm J,k) = T^*(i,\pm J-1,k)/(1 + \frac{\Delta z^* \cdot H}{k_t} \cdot h)$ ..(3-45)

In this expression a backward difference has been used.

d) $T^*(3, j, k) = 1.0$ .....(3-46)

e) $T^*(i, 11, k) = T^*(i, 10, k)$ .....(3-47)

f) $T^*(i_R, j, k) = T^*(i_R-1, j, k)$ .....(3-48)

Where i_R is the radial increment to which the melt front has reached.

g) $V^*(i, j, k) = 0$ for $T^*(i, j, k) \leq T_F^*$ ....(3-49)

h) See numerical solution in Appendix 5 .....(3-50)

i) See numerical solution in Appendix 5 .....(3-51)

j) $P^*(3, k) = P_o^*(k)$ .....(3-52)

k) $P^*(i_R, k) = P^*atm$ .....(3-53)

$$Q^*(i,k) = 2 \times \pi \times [\frac{h_{(1)}}{2} + h_{(2)} + ... + h_{(J-1)} + \frac{h_{(J)}}{2}] \times \Delta z^* \quad .....(3-54)$$

Where $h_{(j)} = r^* \cdot V^*(i,j,k)$ using the "Trapezoidal Rule".

$$\Delta t^* = \frac{\pi \left[R^{*2}_{(i)} - R^{*2}_{(i-1)}\right]}{A_r \, Q^* \left(i_{R-1}, k\right)} \qquad \text{.....(3-55)}$$

3.1.4 Numerical Procedure

A computer program was set up to solve the set of difference equations and boundary conditions, see Figure 3-2.

At the beginning of each time increment, the first and second integrals I_1 and I_2, respectively, were calculated for all points occupied by the flowing melt. To be exact, I_2 should be calculated within the iteration loop by employing the pressure values based on the corrected pressure profile for the density. However, it was found that the calculations could be simplified, with no loss of accuracy, by employing the pressures based on the pressure profile which prevailed when the melt front was at the last radial position. Thus, when the melt front was at the ith radial position, I_2 was based on the pressure profile prevailing when the front was at the (i-1) position. Such a simplification was valid because the pressure variation in the cavity during the filling stage is small. The main contribution to density variation in this stage arises from the temperature gradients.

The first set of calculations was conducted over three radial rings. These calculations were started by assuming a pressure drop in the first ring based on a linear

FIGURE 3-2

COMPUTER FLOW DIAGRAM-FILLING STAGE

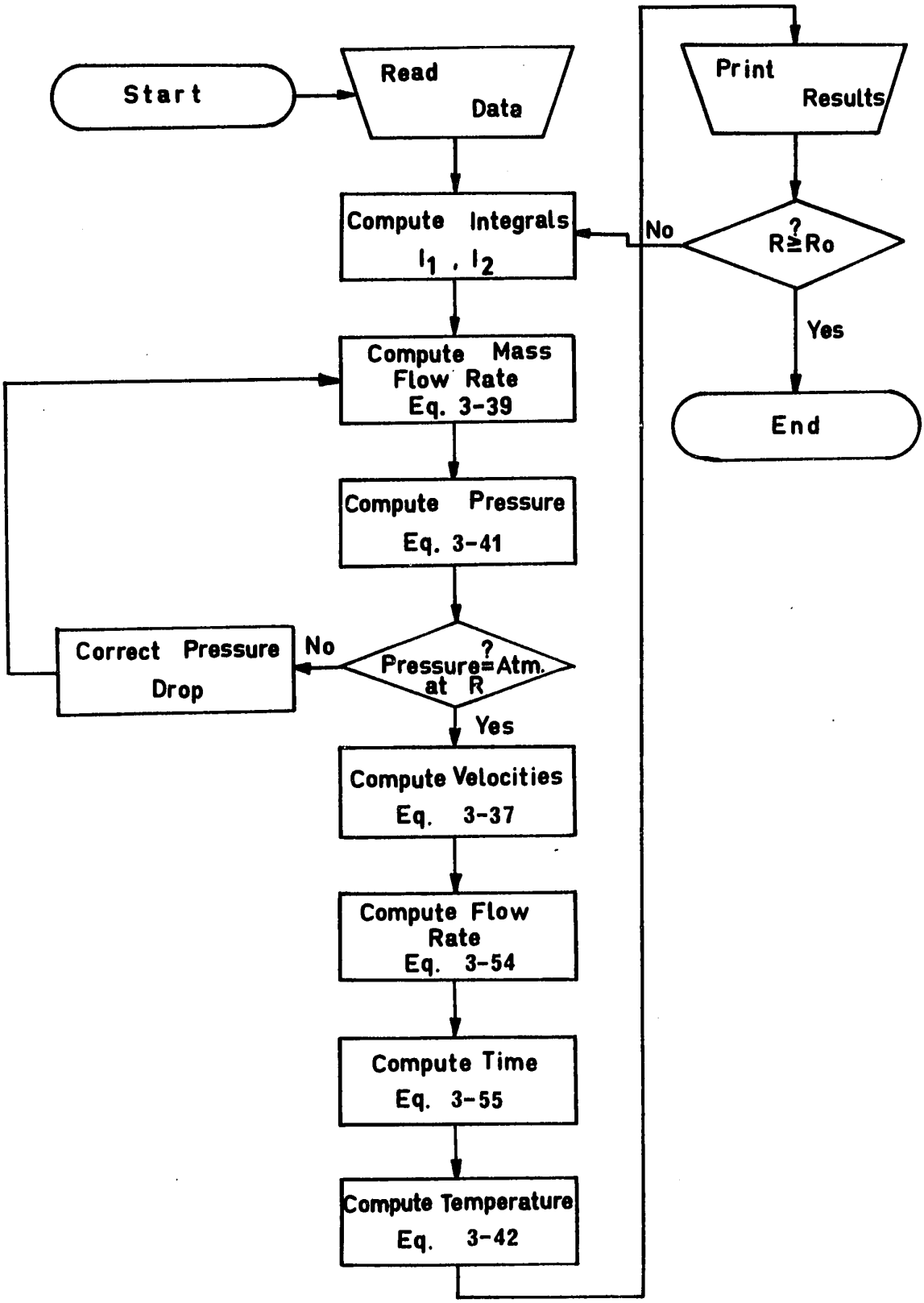

pressure profile between the entrance radius and the melt front. Thus, the mass flow rate at the first radial ring was calculated by equation (3-39). This mass flow rate was then employed sequentially in equation (3-41) by coupling with the available corresponding values of I_2 to calculate the pressure at the remaining radial positions. When the melt front was reached, the pressure value was compared to boundary condition (3-53) - atmospheric pressure. If the pressure was off, a new pressure gradient was assumed for the first radial ring. The procedure was continued until the pressure at the melt front agreed with atmospheric pressure to two decimal places.

The sequence in which the pressure drop in the first ring was selected was as follows. In the first calculation, a linear pressure profile was assumed as outlined above. For the second trial, the profile was modified by adding or subtracting the absolute difference between the calculated pressure and atmospheric pressure to the third power, depending on whether the calculated pressure was lower or higher than atmospheric, respectively. Thus

$$\Delta P_{12} = \Delta P_{11} \pm (\Delta P_d)^3 \qquad .....(3\text{-}56)$$

where ΔP_{11} is the assumed pressure drop in the first ring during the first calculation, ΔP_{12} is the assumed pressure drop in the same ring during the second calculation, and ΔP_d

is the deviation between the calculated pressure at the melt front and atmospheric pressure. The one-third power was selected since it gave the fastest convergence. The third trial was a linear interpolation between the first and second trials. The fourth trial was a third order interpolation and so on. It was found that an average of 3-4 iterations were needed. In all these procedures the properties were chosen to be the same as those prevailing for the temperature and pressure distributions established in the previous cycle.

After the pressure profile was calculated, the corresponding pressure gradients were substituted in equation (3-37) and the velocities at each point were obtained. The velocity profiles were integrated at the melt front to calculate the volumetric flow rate by equation (3-54). Equation (3-55) gave the time needed for the front to traverse the corresponding ring. At this point, velocities were substituted in the energy equation (3-42). Thus, the new temperature profile was calculated for all points occupied by the melt.

As the melt advanced to a new radial ring, the procedure was repeated, while previous calculated temperatures and pressures served as the "initial conditions" at each point and for calculation of the integral I_2. This procedure was continued till the melt front hit the boundary of the semi-

circular cavity. Filling was started from the fourth radial ring, as the entrance radius was located at the second ring and since at least three points are needed for the iteration procedure. However, calculations were started from the entrance radius of the cavity.

The output of the computer program, gave the pressure, velocity and temperature profiles, time elapsed, position of the front and flow rates.

Berger and Gogos (10) and Gee and Lyon (41) solved numerically a two-point boundary value problem. They iterated on the flow rate, as they solved the simultaneous difference equations by "Gauss Seidel Iterative Method" (42). It was felt that the present iterative method employing successive higher iterpolation polynomial for the unknown pressure directly, was simpler to use.

3.1.5 Stability, Convergence and Uniqueness

Finite difference approximations, which replace partial derivatives, are subject to uncertainty as a result of factors relating to the stability, convergence and uniqueness of the mathematical scheme (43). However, it is difficult sometimes to distinguish completely between these three terms.

Since the set of equations (3-4), (3-5) and (3-6) are nonlinear in nature, and since the system has moving boundaries, it is not possible to follow the analysis that is

applicable for cases where the coefficients and boundaries are constant (44) in order to obtain the relations for the time and space increments that lead to a stable numerical scheme. Consequently, the trial and error method has been used. Examination of the difference equation (3-42) would suggest that the dimensionless coefficient A plays a role in the stability problem. As indicated earlier, Saulyev's representation of the second derivatives has been employed. It can be shown (39) that Saul'yev's method is unconditionally stable for the case of a pure parabolic partial differential equation. However, this is not true for the present problem, where additional terms of convection and viscous heating are present. Since these terms are large in comparison with the conduction term, instabilities are encountered. In order to overcome these difficulties it has been found that the condition:

$$N = \frac{\Delta t^* \cdot V^*(a^*)\, A_r}{(1 + A)\, \Delta r^*} < 1.0 \qquad .....(3\text{-}57)$$

must be satisfied, as the convection term is the largest one. To achieve this, the time already determined by equation (3-55) is divided into additional time increments to satisfy (3-57).

No instabilities have been detected in the pressure iteration procedure, unless the velocities computed during the iteration are bigger than unity. This situation will not arise due to physical impossibility.

Convergence of the numerical solution can be tested by varying Δz^*, Δr^*, $\beta = \frac{\Delta t^*}{\Delta z^{*2}}$, $\gamma = \frac{\Delta t^*}{\Delta r^*}$. A valid solution must converge as these values decrease. The effect of the space increment Δz^* was tested in equation (3-37) and compared with the analytical solution for the isothermal flow of a Power Law fluid with n = 0.5. Three sizes of space increments were used 0.2, 0.1, 0.05. It was found that the difference between the analytical and the numerical solutions varied only in the third significant figure as can be seen in Table 3-1.

The convergence of the pressure iteration procedure was tested on the analytical solution for the pressure profiles of an isothermal flow of an incompressible Power Law fluid between circular discs. The analytical solution is given by the following equation:

$$P^*(r^*) = P^*_{atm} + (1 - P^*_{atm}) \times \left(\frac{1 - r^{*1-n}}{1 - a^{*1-n}}\right) \qquad \ldots\ldots(3\text{-}58)$$

Two different numerical schemes were tested, the average of the forward and backward differences as given by equation (3-41) and the backward difference given by:

$$P^*_{(i)} = P^*_{(i-1)} - \left[\frac{Q_m}{I_2(i)}\right]^n \cdot \Delta r^* \qquad \ldots\ldots(3\text{-}59)$$

TABLE 3-1

COMPARISON BETWEEN ANALYTICAL AND NUMERICAL VELOCITY PROFILE

$n = 0.5, \quad \Delta Z^* = 0.1$

Z*	Analytical*	Numerical*
.000	0.000	.000
.100	.271	.270
.200	.488	.487
.300	.657	.657
.400	.784	.784
.500	.875	.874
.600	.936	.937
.700	.973	.974
.800	.992	.992
.900	.999	.999
1.000	1.000	1.000

* All values are normalized

Table (3-2) shows the results given by these two schemes compared with the analytical ones. As can be seen from Table (3-2) the average representation gave a faster convergence. In all cases 10 increments were used in the axial direction. Uniqueness was established, as the calculated pressure profiles with $\Delta r^* = 0.025$ ($I = 41$) agreed to two significant figures with those predicted by the analytical solution. Convergence was achieved by increasing the number of the radial increments. As can be seen from Table (3-2), the pressure gradients calculated numerically are greater than the analytical ones at large radii and are smaller at radii close to the entrance. As a result flow rates calculated from the entrance pressure profile will be smaller than those calculated from the melt front region profile. This may have an effect on the calculated filling times, as the flow rate is introduced through equation (3-55). Thus a few runs have been made using flow rates calculated on basis of the entrance region and the melt front, respectively. Results have indicated that the differences in the filling diagram (see section 3.2.3) deviate by less than 1%.

Convergence of the energy equation was tested by varying the value for $N = 1, \frac{1}{2}, \frac{1}{4}$. The results for $N = 1$ and $\frac{1}{4}$ agreed to within 2 decimal places.

Since it was found that the computing time was squared when the number of mesh points was doubled, a compromise is needed between convergence properties and accuracy

TABLE 3-2

COMPARISON BETWEEN ANALYTICAL AND NUMERICAL SOLUTIONS FOR PRESSURE PROFILES

P_f = 500 psi, n = 0.5

r*		0.1	0.2	0.3	0.4	0.5	0.6	0.7	0.8	0.9	1.0
ANALYTICAL		.914	.745	.615	.505	.409	.322	.241	.167	.0960	.030
$\Delta r^*=0.2$	A^1		.772		.532		.337		.174		.030
	B^2		.791		.547		.345		.179		.030
$\Delta r^*=0.1$	A^1	.932	.758	.627	.515	.418	.329	.247	.170	.0975	.030
	B^2	.943	.761	.634	.524	.425	.335	.251	.173	.0990	.030
$\Delta r^*=0.05$	A^1	.923	.751	.620	.509	.412	.324	.243	.168	.0970	.030
	B^2	.930	.757	.628	.517	.419	.330	.248	.171	.0985	.030
$\Delta r^*=0.025$	A^1	.915	.746	.615	.506	.409	.322	.241	.167	.0964	.030
	B^2	.917	.751	.622	.512	.414	.326	.245	.169	.0974	.030

A^1 - average of backward and forward differences

B^2 - backward difference

desired. Following this reasoning, 20 increments in radial direction, 10 in axial direction and a value of N = 1.0 were chosen as an optimal compromise. All results were based on these values.

The proof of uniqueness of the numerical solution is always difficult, when introducing a new numerical solution to a problem which does not have an analytical solution. Usually the standard procedure is to compare a numerical solution to the closest analytical one available. As shown earlier, the numerical solution to the momentum equation alone gives a unique solution for the velocity and pressure profiles, see Tables 3-1 and 3-2. The uniqueness in the physical sense can be tested by experiments which is the objective of the present work.

3.2 RESULTS AND DISCUSSION

Theoretical and experimental results were obtained for high density polyethylene (H.D.P.E.) and polystyrene at different injection pressures and melt temperatures. In all cases, the mold temperature was kept at $80^{o}F$. Twelve cases will be analyzed in detail, eight for polyethylene and four for polystyrene. In addition, two short shots are demonstrated, one for each resin. The injection conditions employed are given in Table 3-3.

TABLE 3-3

INJECTION CONDITIONS FOR EXPERIMENTAL PROGRAM

Case	Resin	Melt Temperature (°F)	Pressure P_f* (psi)
1	P.E.	350	350
2	P.E.	350	450
3	P.E.	350	500
4	P.E.	350	650
5	P.E.	400	250
6	P.E.	400	300
7	P.E.	400	400
8	P.E.	400	450
9	P.S.	450	475
10	P.S.	450	550
11	P.S.	450	525
12	P.S.	450	500
13	P.E.	350	300
14	P.S.	450	600

*P_f - pressure at the entrance to the cavity at the end of the filling stage, as determined experimentally.

The lower limit of injection pressure was selected so that the filling time did not exceed two seconds. It was found that a filling time of more than three seconds resulted in a rough and rippled surface, a situation that could introduce inaccuracies in the theoretical treatment due to disturbed heat transfer at the interface between the polymer and the wall. The upper limit for pressure was determined by the characteristics of the injection molding machine. The cavity could not be filled in less than 0.45 seconds. The temperature range for molding was determined by the flow properties of the resins. Two melt temperatures were chosen for polyethylene 350 and 400°F, the common temperatures for the injection molding of polyethylene. One melt temperature of 450°F was chosen for polystyrene. At a temperature of 400°F, polystyrene exhibited melt fracture at relatively low shear rates, as could be seen also in Appendix 1, section 9.1. At a temperature close to 500°F, the resin employed in this study exhibited discoloration (yellowing) apparently due to degradation. The mold temperature of 80°F was chosen, since the corresponding high speed photography experiments were performed at room temperature for reasons discussed earlier.

3.2.1 General

In the theoretical analysis of the filling stage it was assumed that a "Spreading Radial Flow" takes place in a parallel feed situation. Although Spencer et al (16) and Bauer (17) showed that a radial flow was realized in parallel feeding, they also noticed some deviations in their particular geometries. Therefore, it was necessary from the early stages of this study in a semicircular cavity to determine if a spreading radial flow existed and to what extent the front deviated from a perfect semicircle. This was achieved by employing the automatic controls of the injection molding machine, so that the polymer was frozen while the cavity was only partially filled. As a result, different sizes of semicircular pieces were obtained. Although the moldings were rough, due to cooling without packing, the frontier was a perfect semicircle, except for some deviation due to the wall effect close to the entrance plane at $r = 0$. In order to obtain direct experimental observation of the front during filling, high speed photography was employed. The films showed that the melt front travelled in a perfect radial spreading pattern, except for a small edge effect. Figures 3-3 and 3-4 show photographs of the melt front position at different stages of filling for polyethylene and polystyrene for cases 2 and 10, respectively.

FIGURE 3-3

SPREADING RADIAL FLOW IN SEMICIRCULAR CAVITY

CASE 2

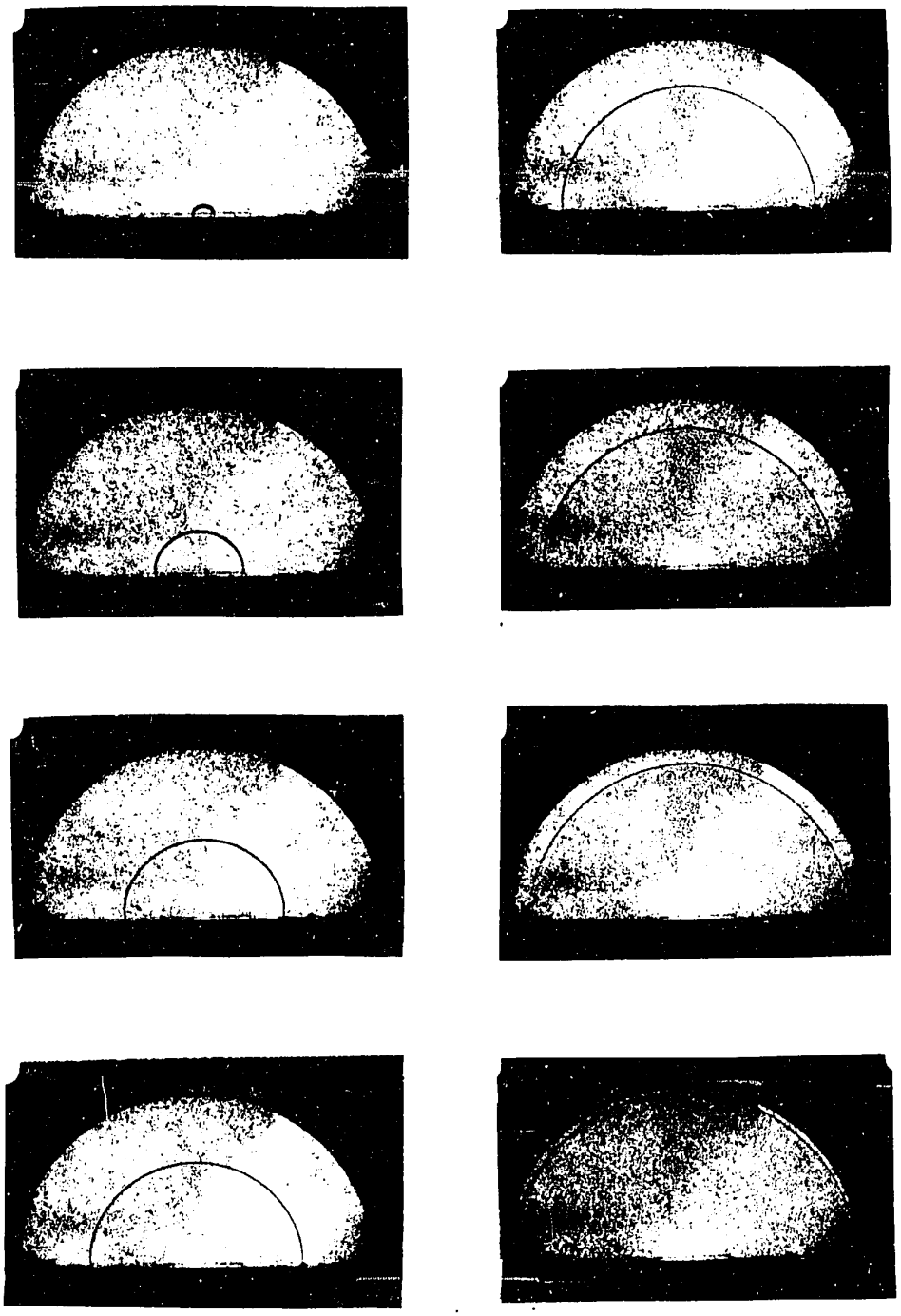

FIGURE 3-4

SPREADING RADIAL FLOW IN SEMICIRCULAR CAVITY

CASE 10

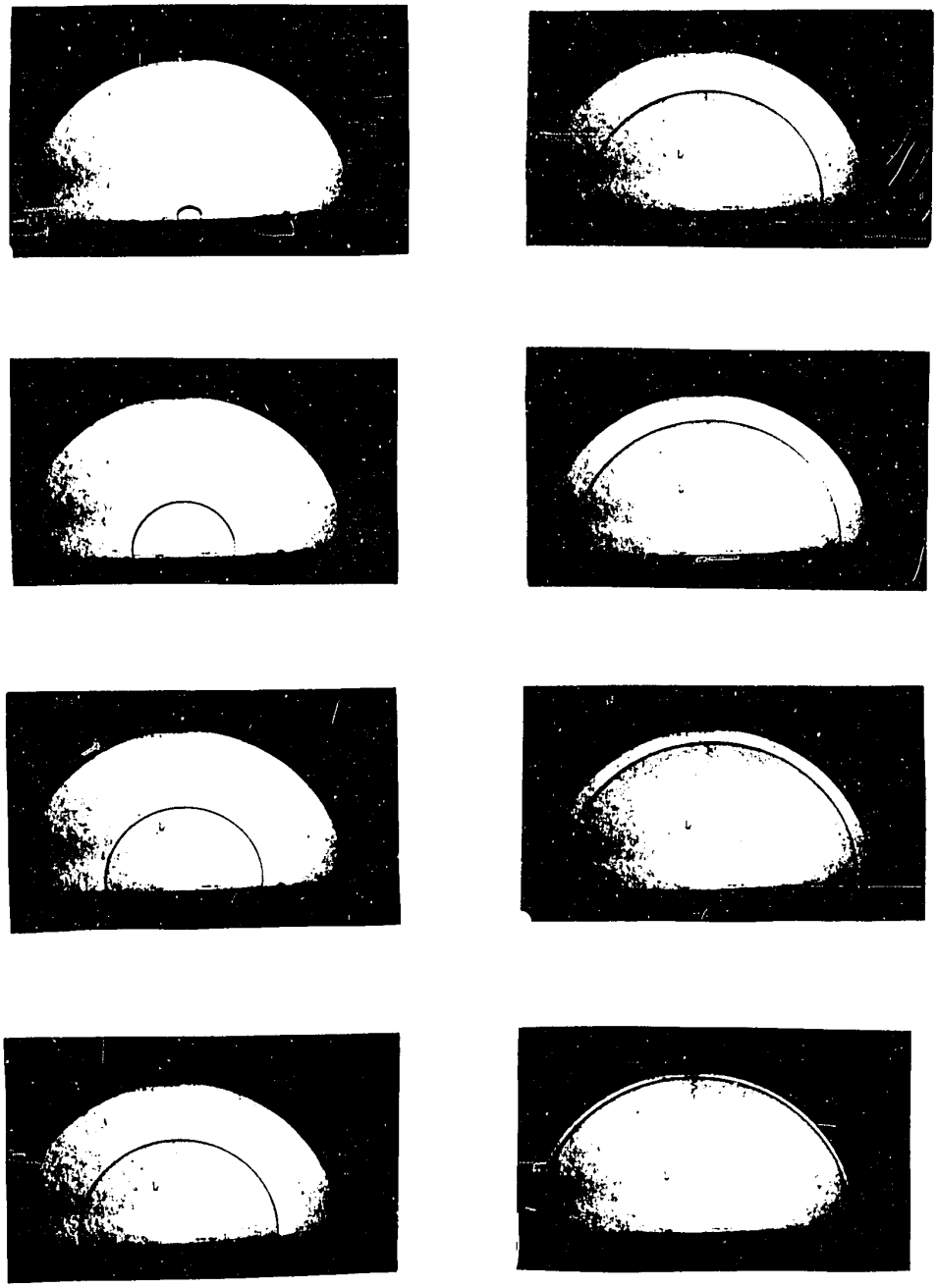

3.2.2 Boundary Conditions

An important factor for the relevance of the proposed theoretical model and numerical procedure is the assignment of accurate and practical values for the boundary conditions.

It has been shown in the experimental measurements by Bauer (17) that it is not possible to obtain a constant injection pressure at the injection end throughout the filling stage,due to the start-up time required before a constant pressure can be reached. Furthermore, the presence of the nozzle, channels, sprues and gate between the reservoir and the cavity causes substantial pressure losses before the melt reaches the cavity. Barrie (45) points out that these losses may exceed 50% of the pressure at the injection end. The complexity of these effects, coupled with swelling and other viscoelastic effects at the entrance to the cavity, makes it difficult at this stage to treat the cavity, nozzle, channel and gate as one system in the manner proposed by Berger et al (10). In an attempt to test the proposed filling model while avoiding the above complications, the boundary conditions relating to pressure at the entrance, equation (3-33), have been based on actual pressure values as measured experimentally at the entrance to the cavity. Experimental pressure time curves for the entrance are shown in Figure 3-5 for polyethylene and Figure 3-6 for polystyrene.

FIGURE 3-5

VARIATION OF ENTRANCE PRESSURE DURING FILLING

POLYETHYLENE

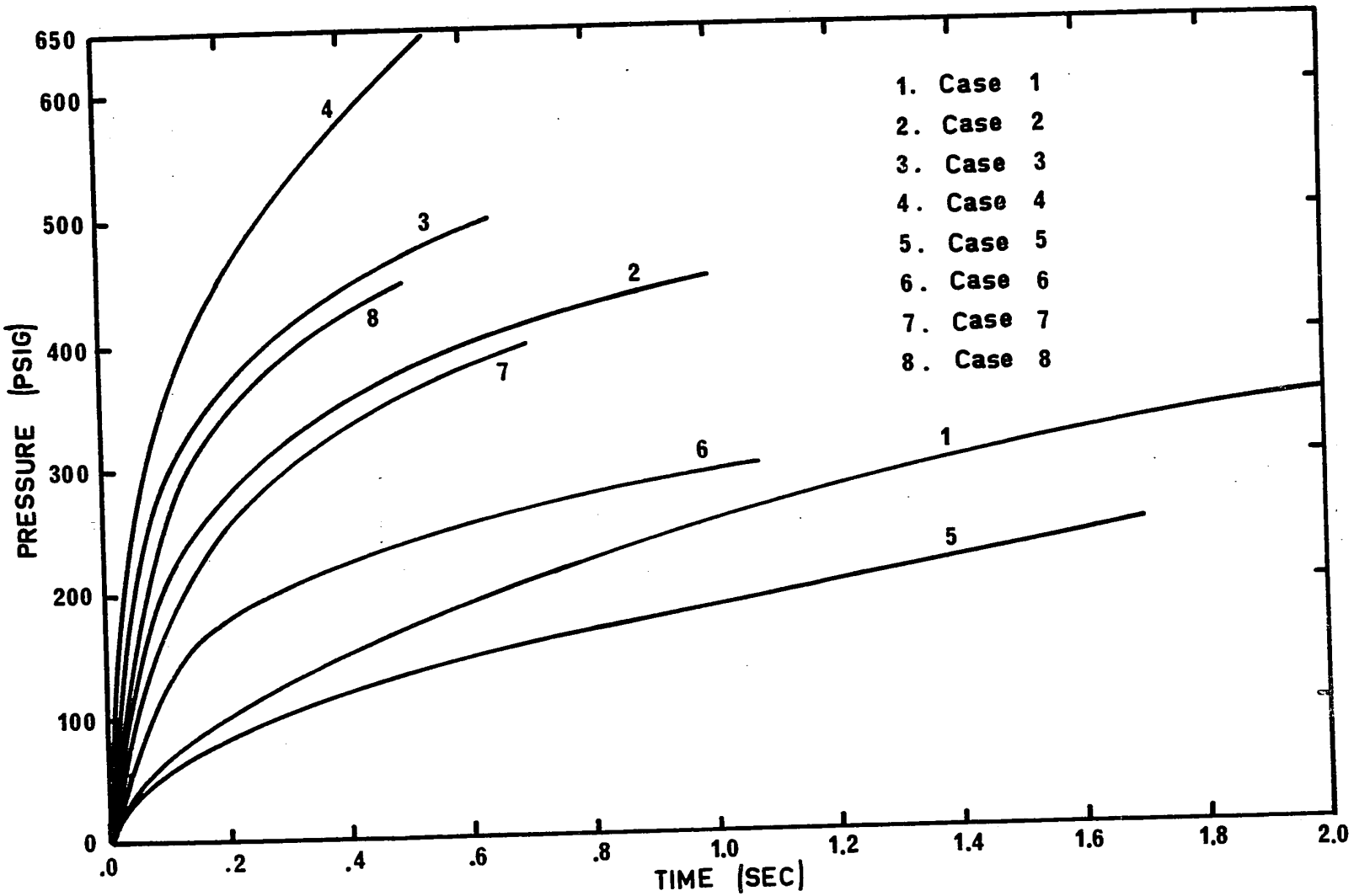

FIGURE 3-6

VARIATION OF ENTRANCE PRESSURE DURING FILLING

POLYSTYRENE

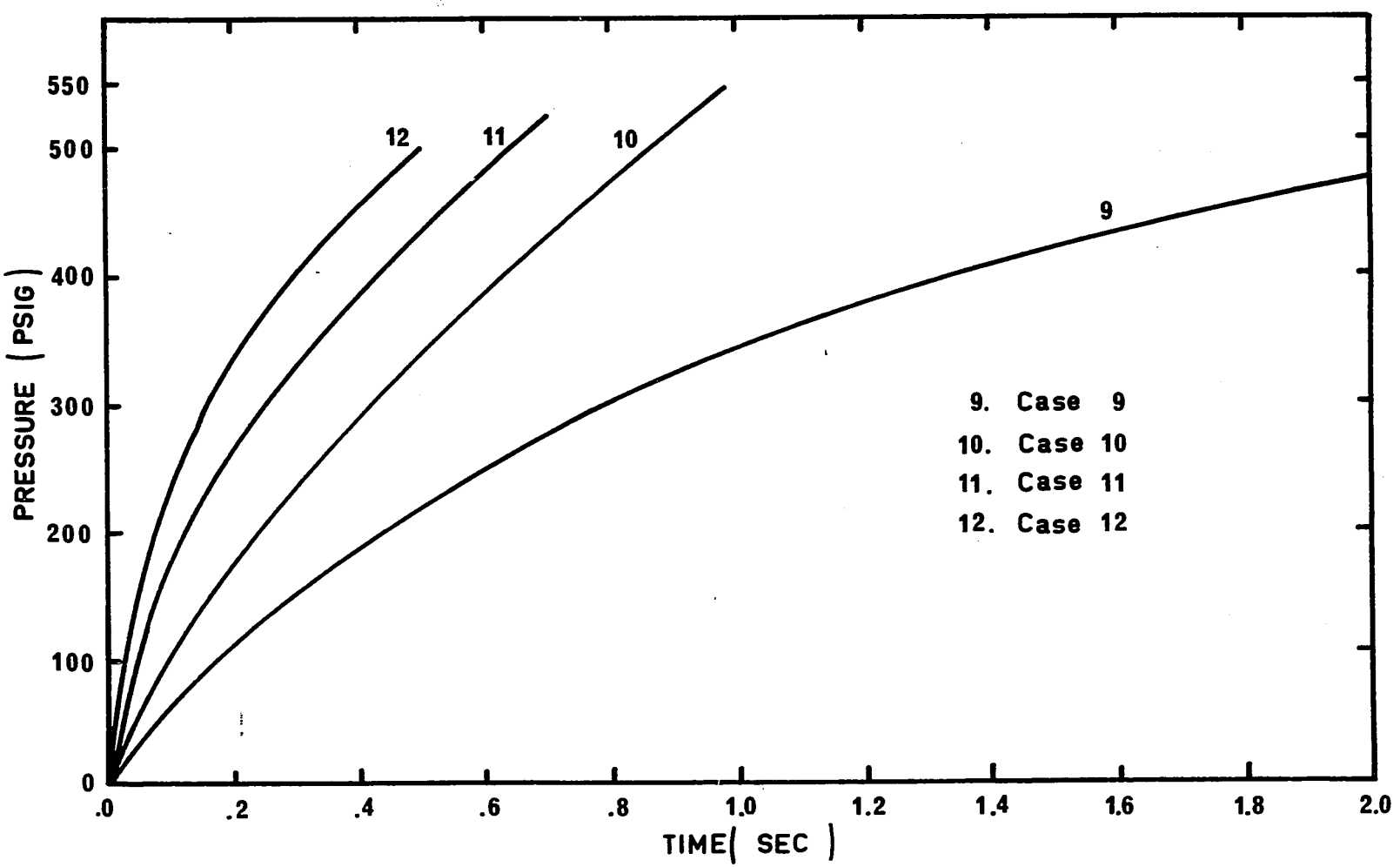

For reasons of convenience in the calculation procedure, the time axis has been converted to a distance (radial) axis in the computer program, using the experimental filling time curve.

Some inaccuracies may be associated with boundary condition (3-27) which assumes that the melt temperature at the entrance to the cavity is constant and equals the melt temperature at the nozzle. Some cooling may take place during the flow of the melt in the cooled channel. The effects of this cooling may be at least partially offset by the viscous heating effect due to high shear rates. However these effects are not considered to change the temperature of the melt to a large extent, since the residence time of the melt in the channel is very short, as the volume of the channel is only 2% of the cavity volume. The effect of the melt temperature on the filling time is discussed in Chapter 7.

The validity of boundary condition (3-26) which assumes a constant heat transfer coefficient between the melt and the wall is discussed in Chapter 7.

The assumption of a constant wall temperature has been checked by the thermocouple installed in the transducer. It has been found that the average maximum temperature rise of the wall is 20^{o}F. Such an increase is not expected to change the results to a large extent, as will be shown in Chapter 7.

Atmospheric pressure at the melt front, boundary condition (3-34) was maintained by installing thin shims of 0.003 inch thickness between parts 3 and 4, see Figure 2-2, and checked by the pressure transducer. The recorded pressure curves indicated that atmospheric pressure prevailed from the beginning of the filling stage until the melt touched the transducer.

3.2.3 Filling Times

Figures 3-7 to 3-14 give the distance travelled by the melt as a function of time for polyethylene, and Figure 3-15 to 3-18 give the same representation for polystyrene. The experimental curves were obtained as explained earlier by the pressure transducer. For comparison, the results obtained from high speed photography are given for the same injection conditions, when available. In all cases, the filling time obtained by the photographic technique is shorter than that obtained from the pressure transducer results. This is attributed to the different thermal properties of glass and steel. The thermal conductivity of steel is 11.7 Btu/^{o}F/ft/hr (46) while that of glass is only 0.55 Btu/^{o}F/ft/hr (47), thus higher temperatures and lower viscosities tend to prevail in the high speed experiments.

FIGURE 3-7

PROGRESSION OF MELT FRONT

CASE 1

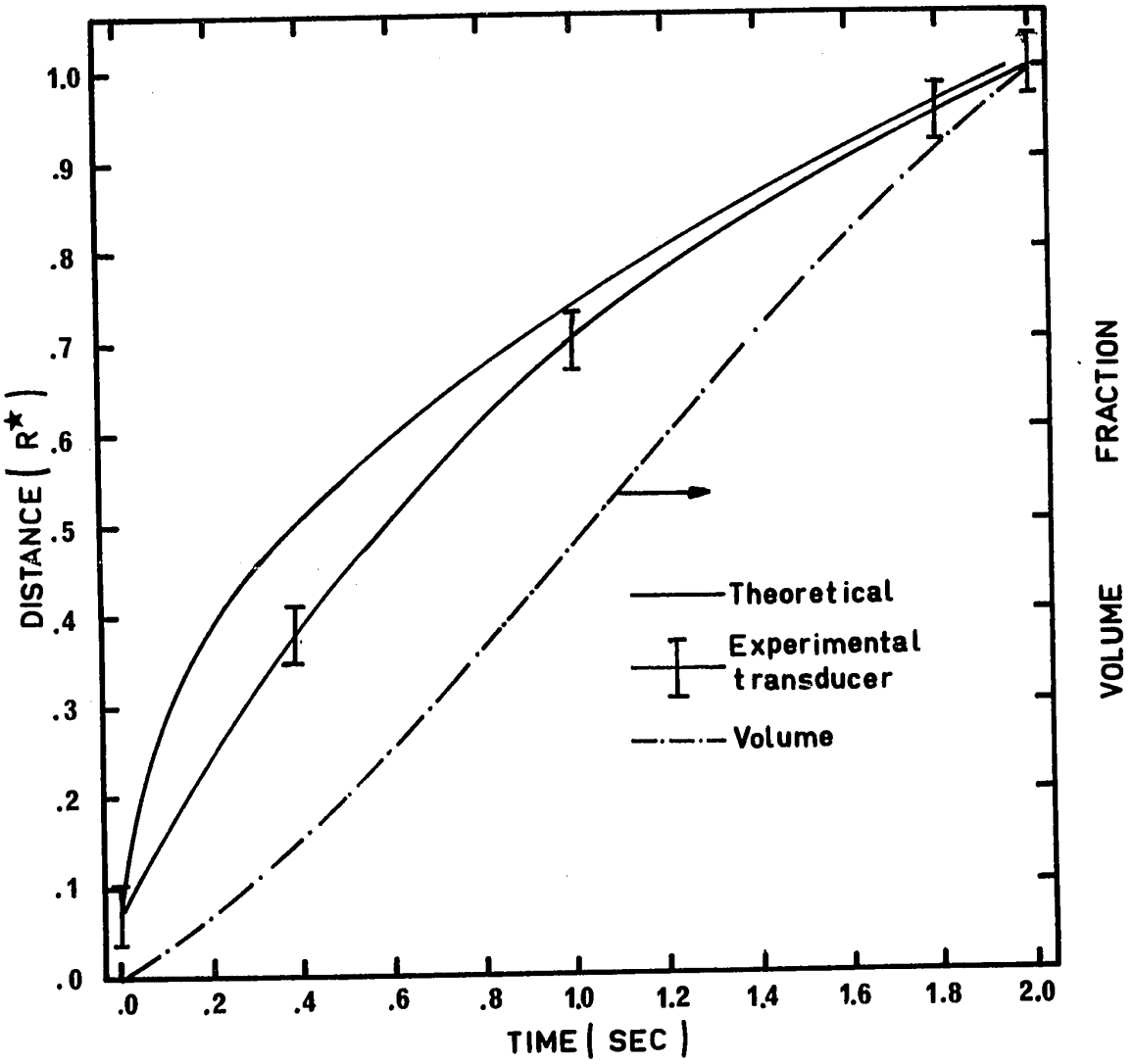

FIGURE 3-8

PROGRESSION OF MELT FRONT
CASE 2

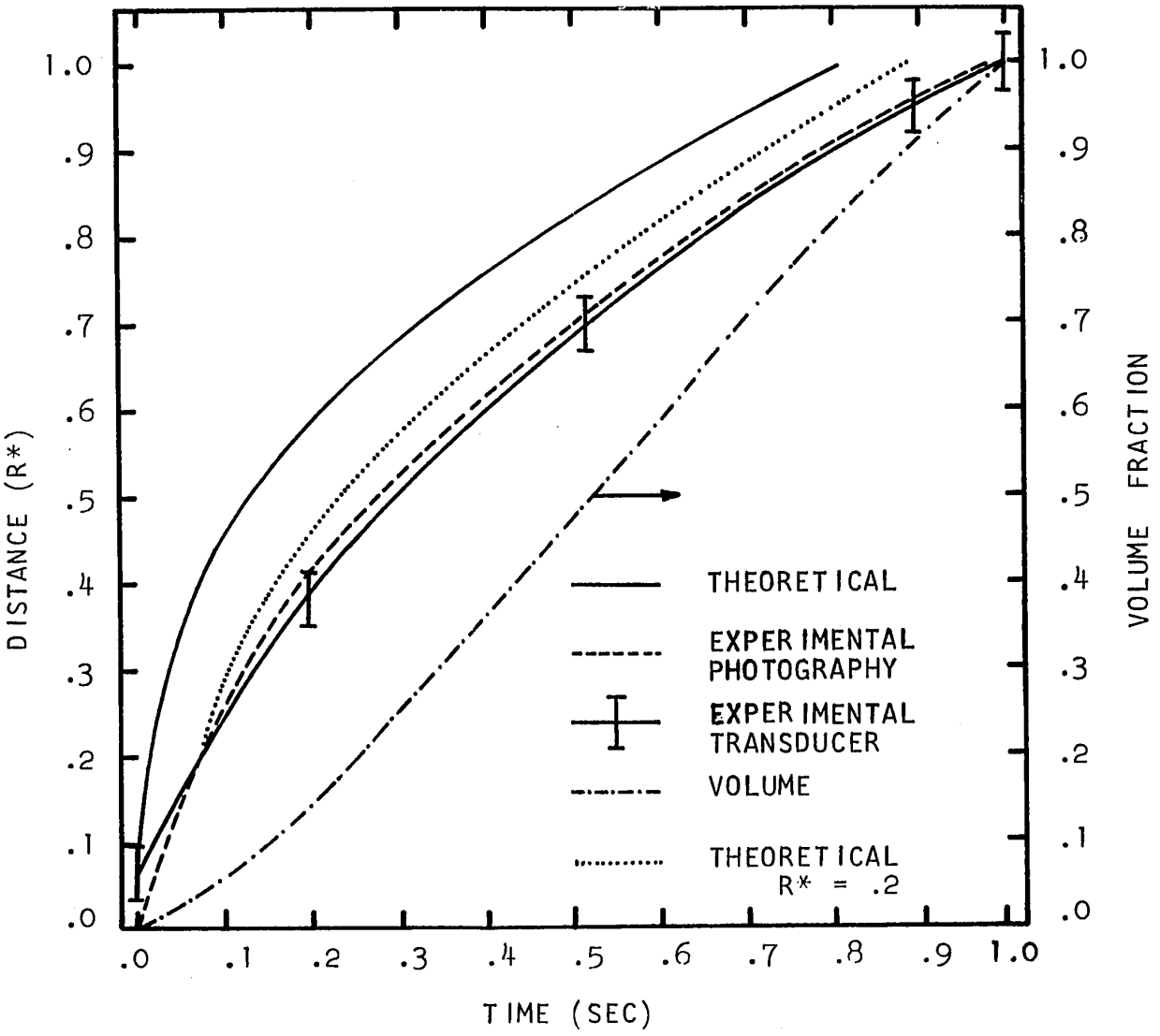

FIGURE 3-9

PROGRESSION OF MELT FRONT

CASE 3

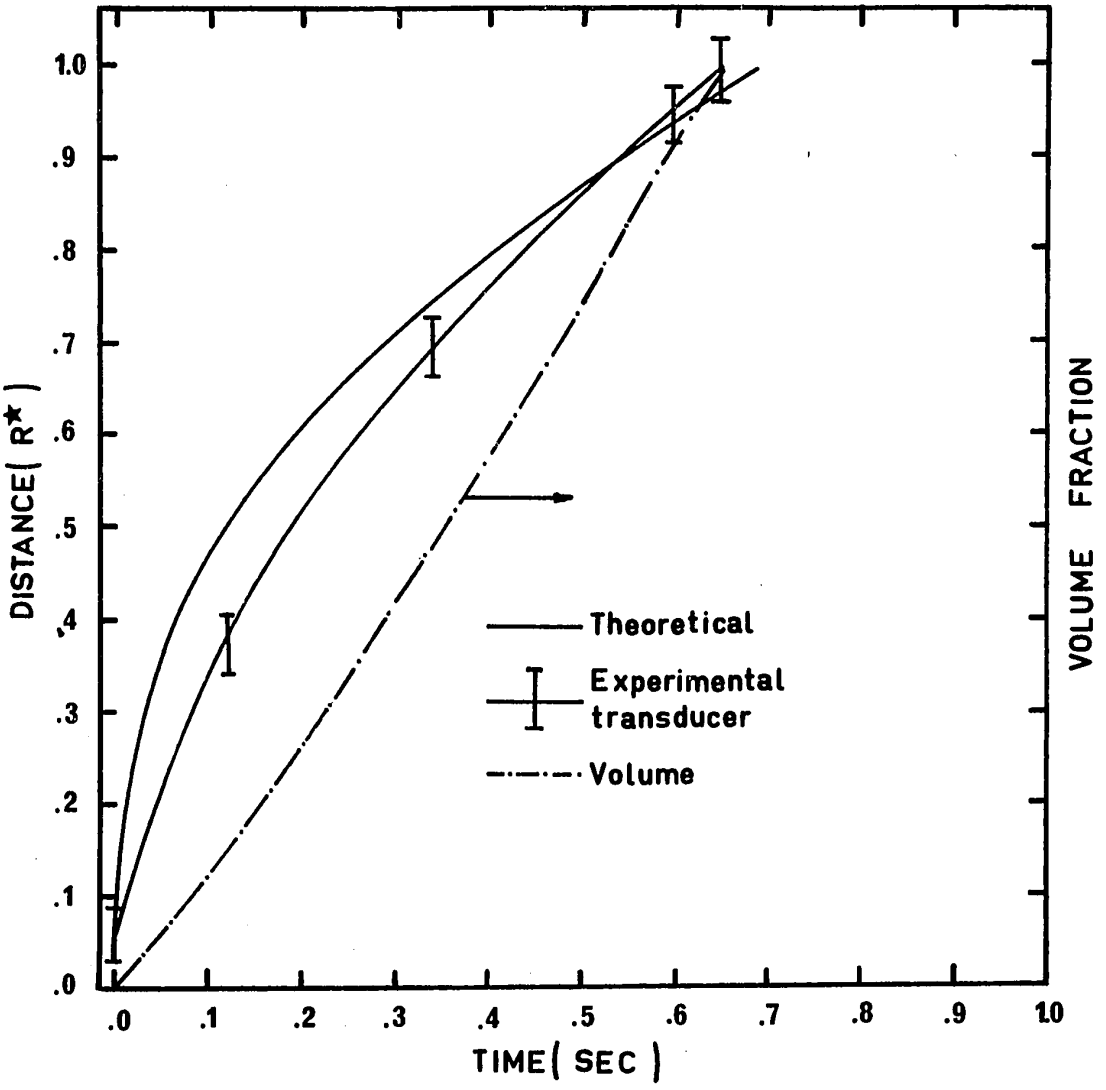

FIGURE 3-10

PROGRESSION OF MELT FRONT

CASE 4

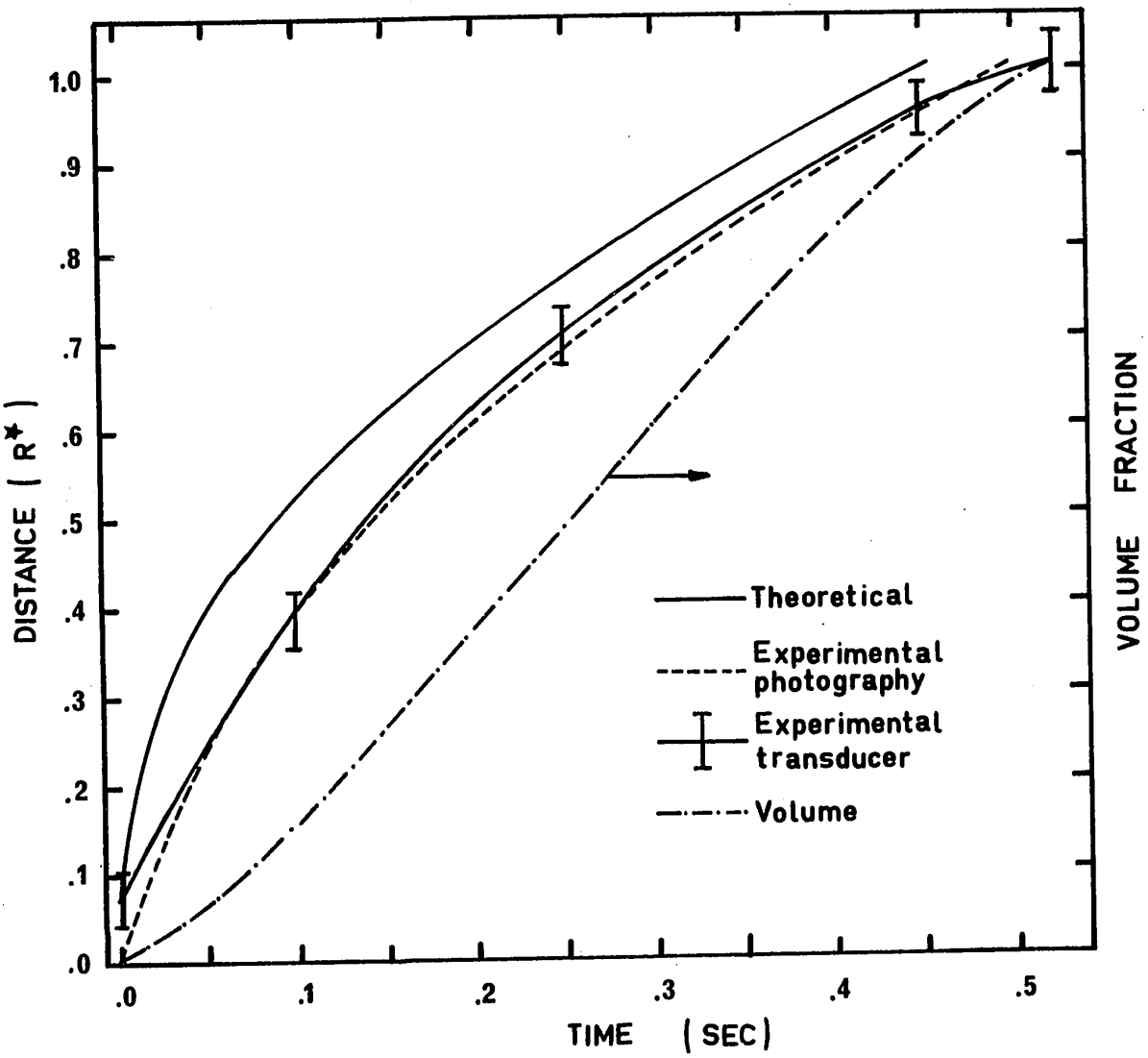

FIGURE 3-11

PROGRESSION OF MELT FRONT
CASE 5

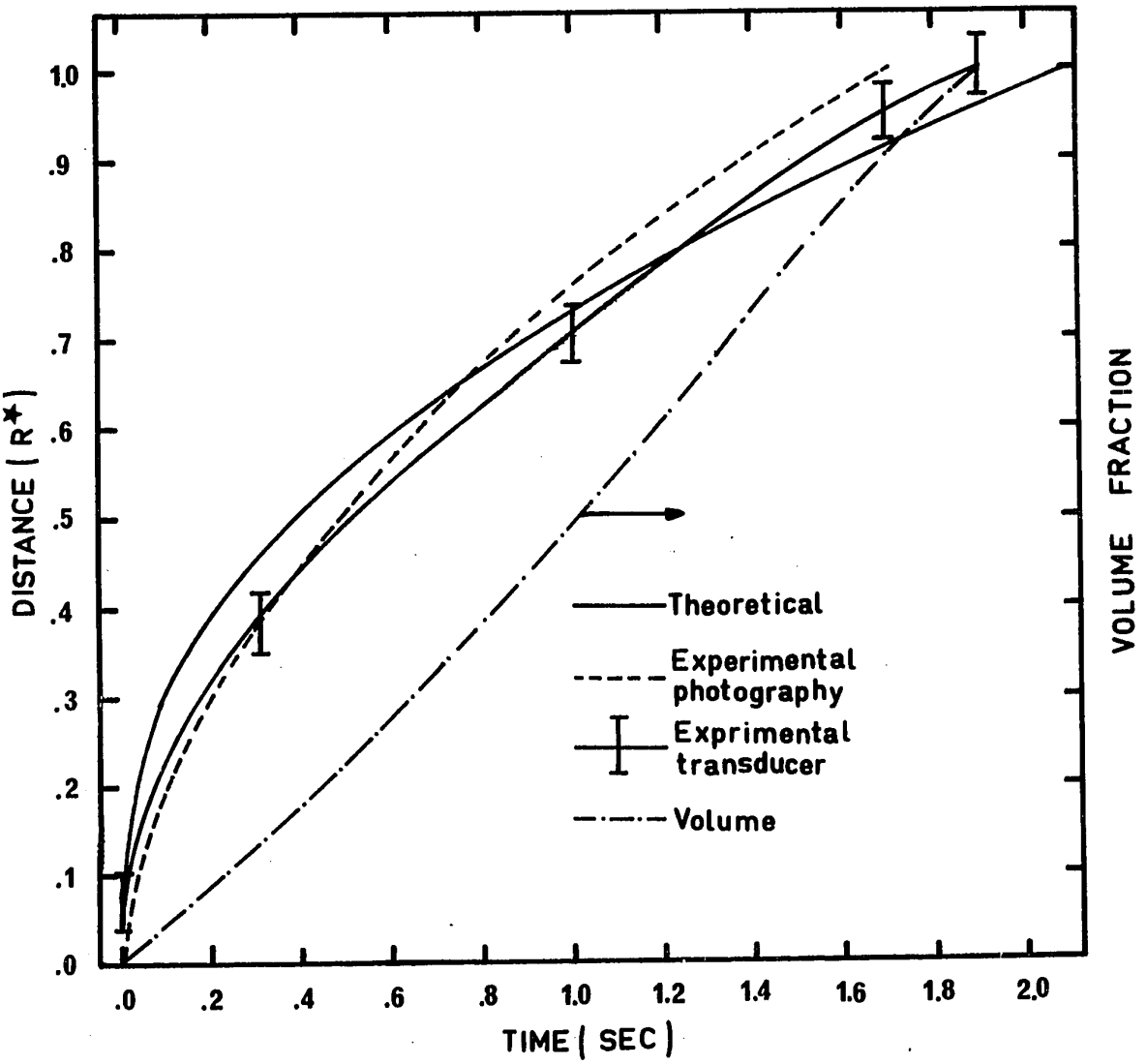

FIGURE 3-12

PROGRESSION OF MELT FRONT

CASE 6

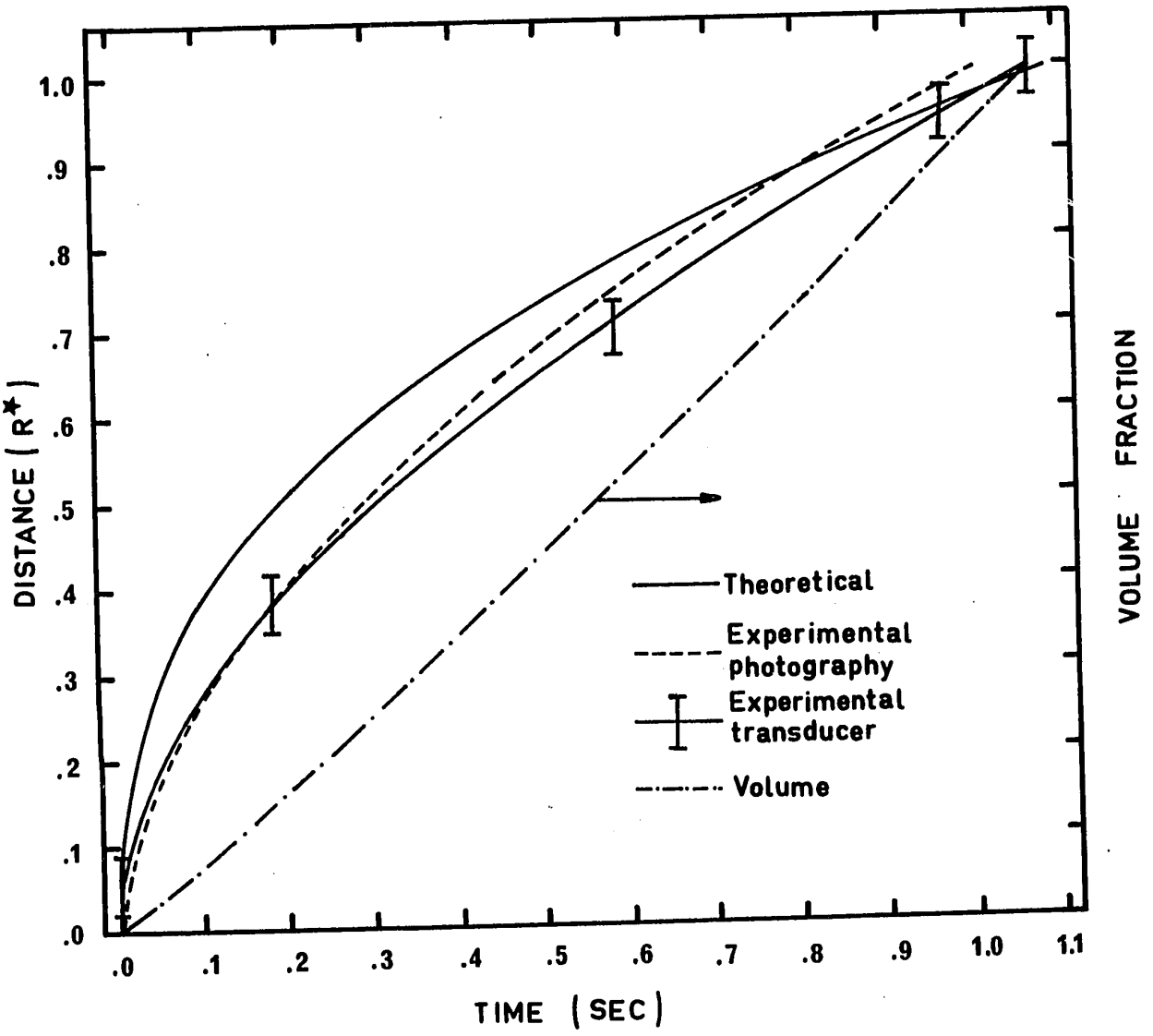

FIGURE 3-13

PROGRESSION OF MELT FRONT

CASE 7

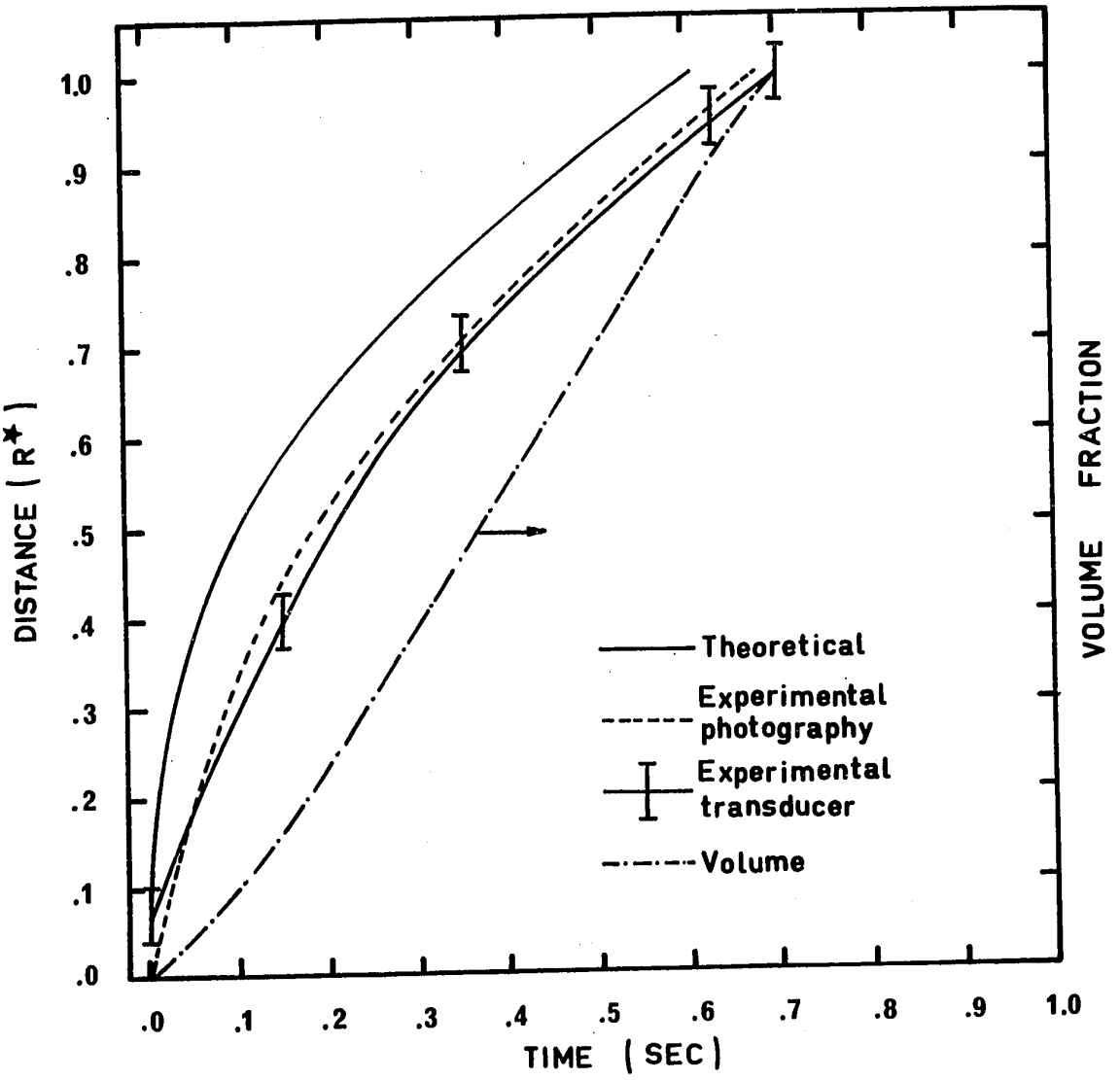

FIGURE 3-14

PROGRESSION OF MELT FRONT

CASE 8

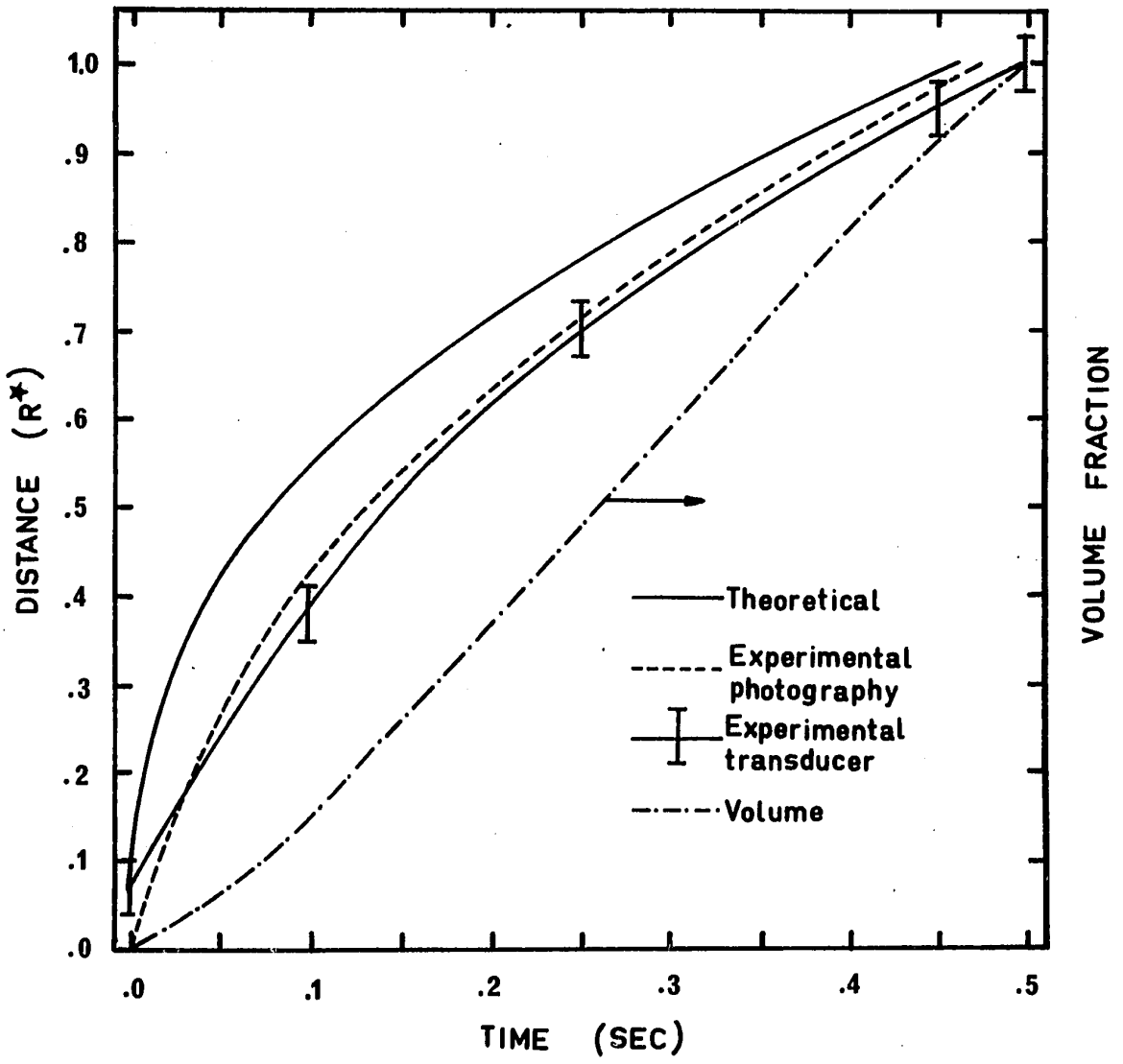

FIGURE 3-15

PROGRESSION OF MELT FRONT

CASE 9

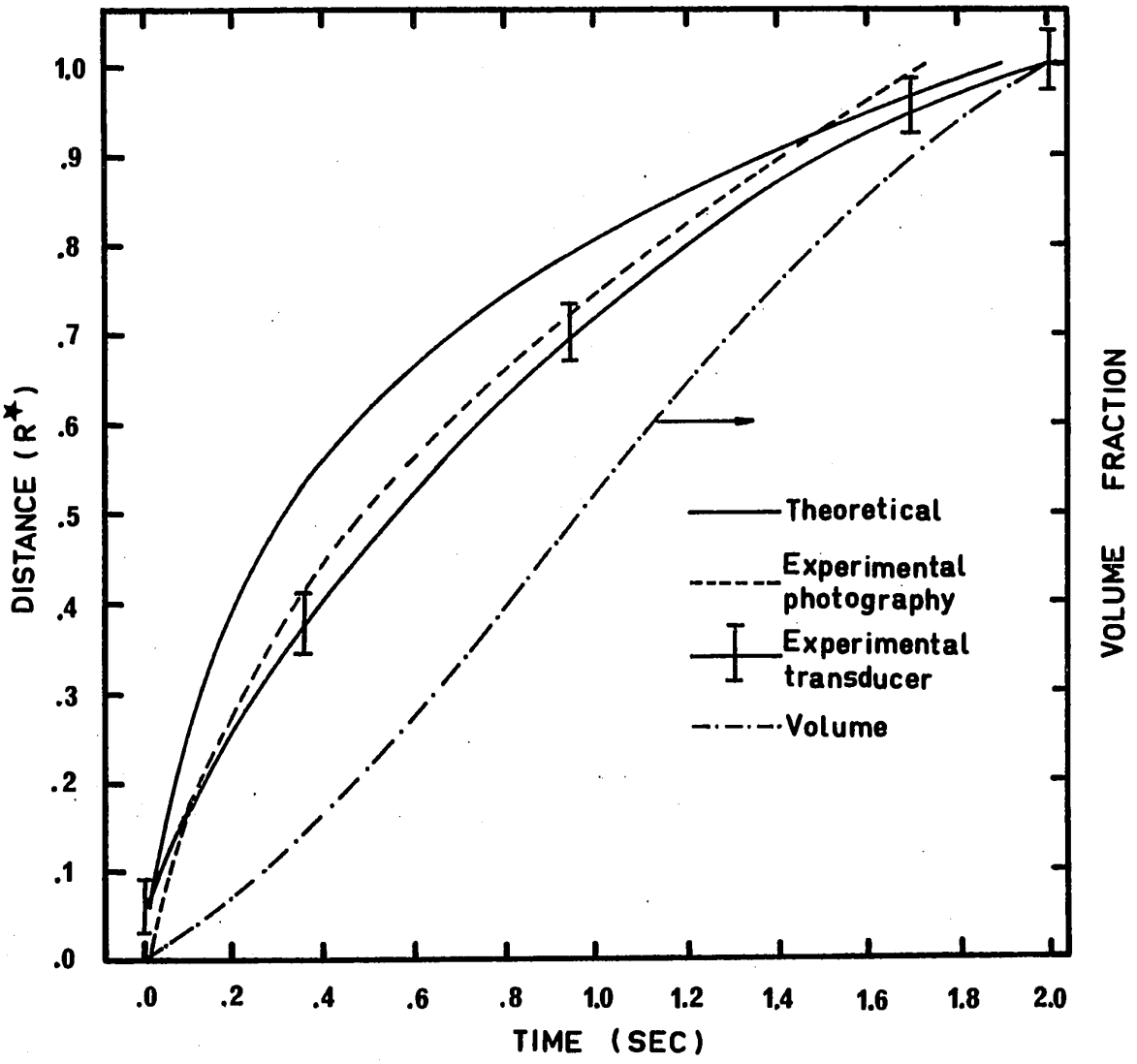

FIGURE 3-16

PROGRESSION OF MELT FRONT

CASE 10

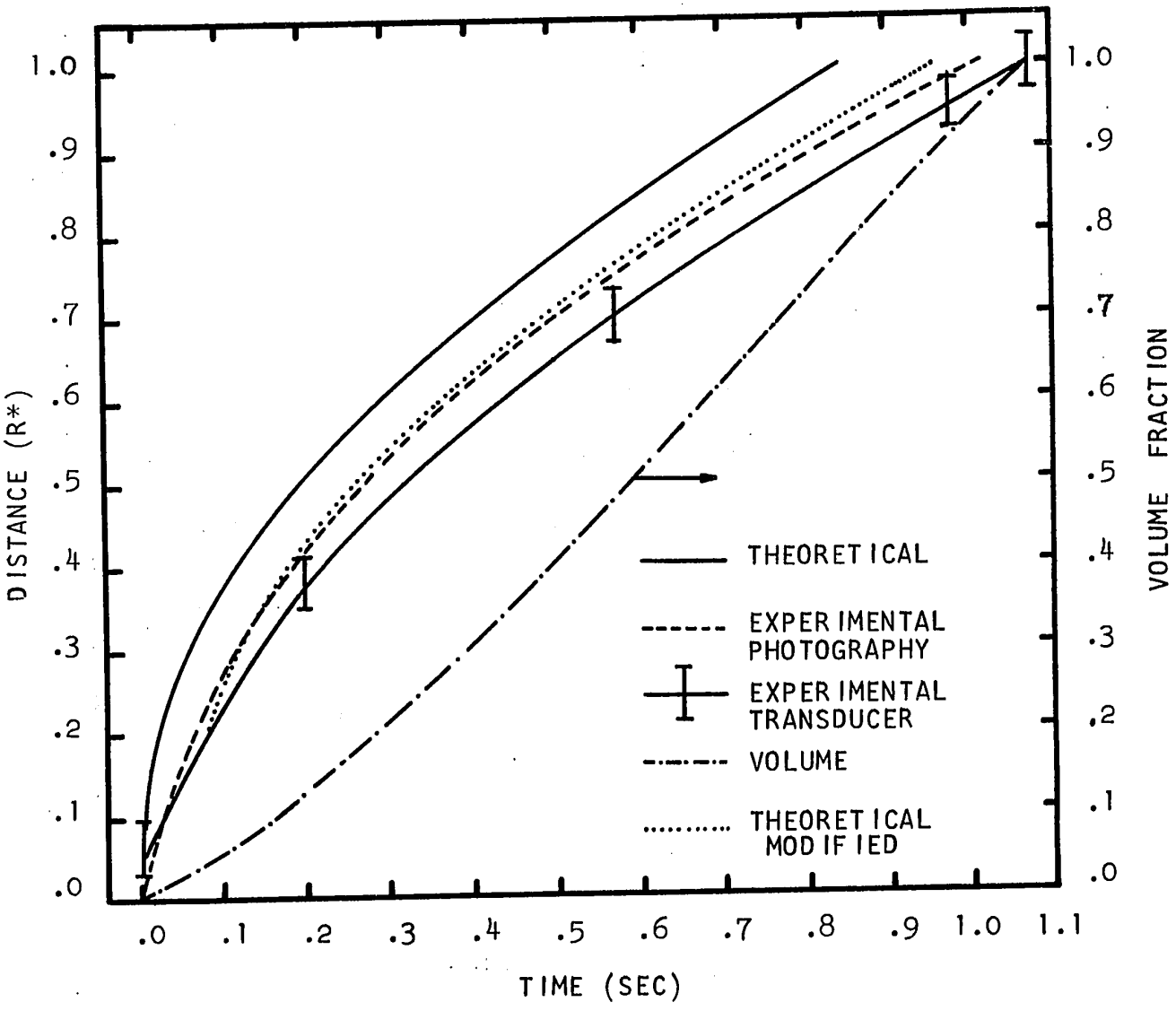

FIGURE 3-17

PROGRESSON OE MELT FRONT

CASE 11

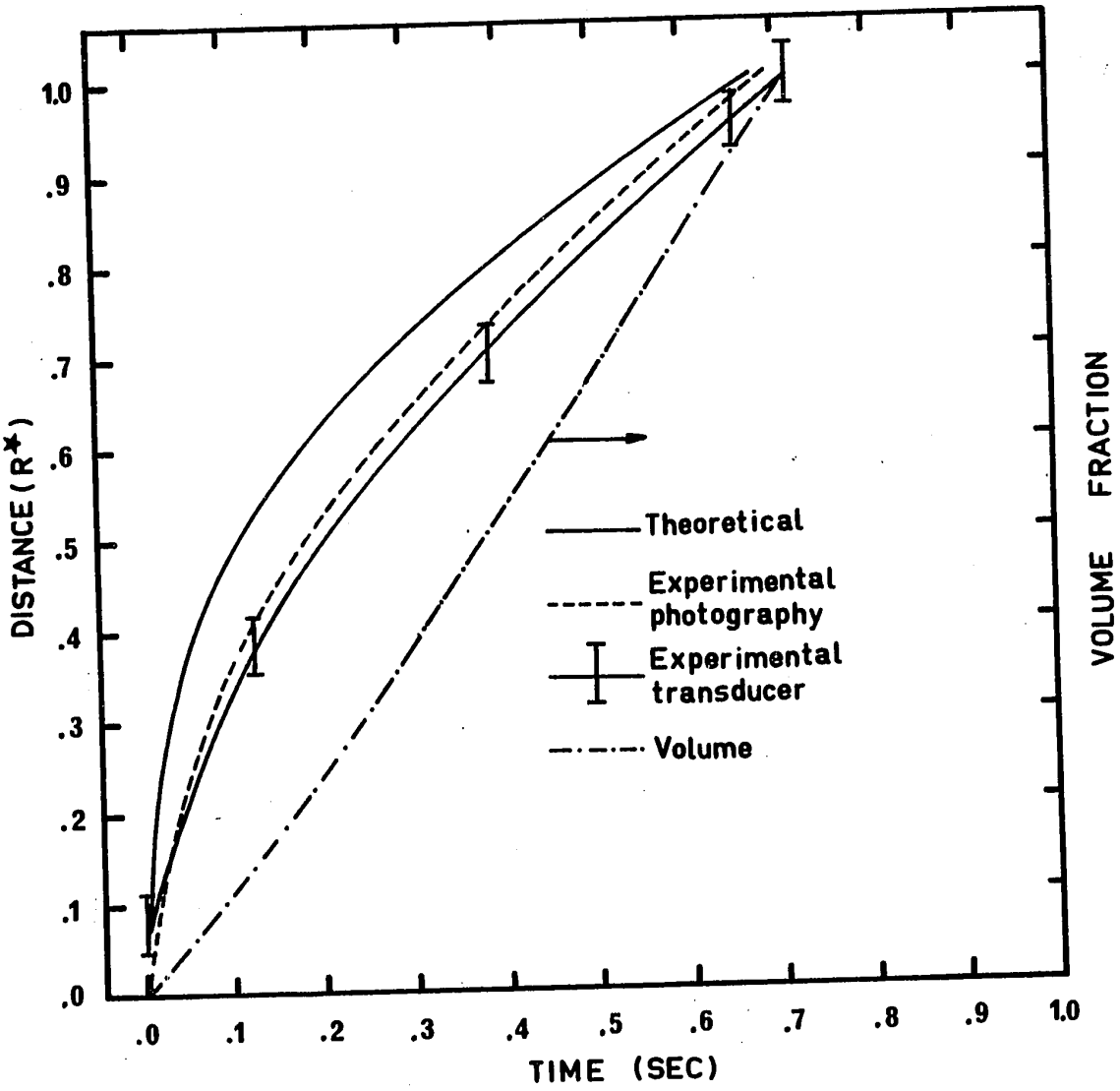

FIGURE 3-18

PROGRESSION OF MELT FRONT

CASE 12

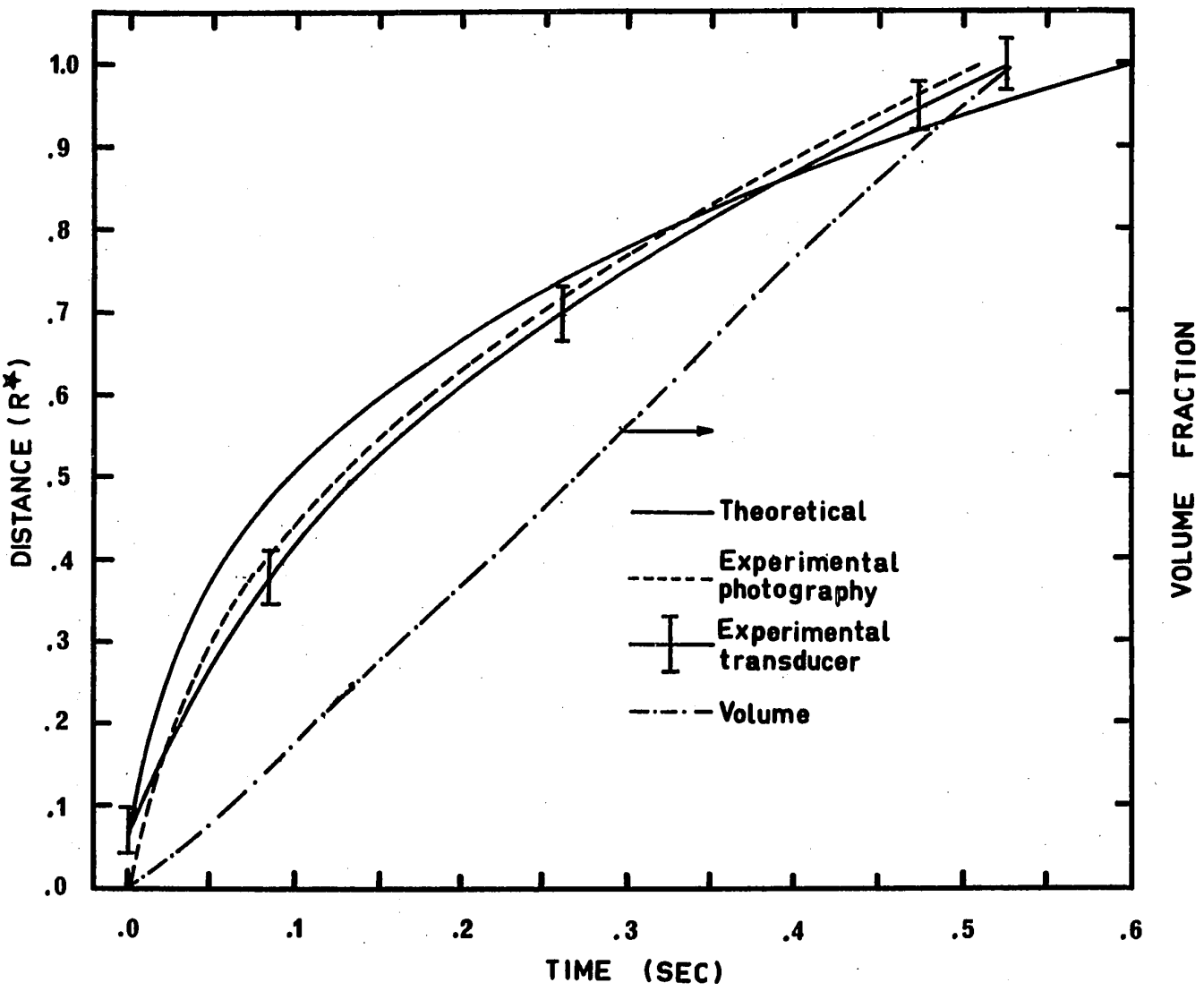

Some inaccuracies in the time-distance curves obtained by the pressure transducer are expected, since the active diameter of the transducer is about 6.3% of the cavity radius. Therefore, transducer data are reported in terms of a range of values rather than as discrete points.

A comparison between the experimental results and theoretical predictions shows that the proposed model can predict the obvious need for longer filling times as either the melt temperature or injection pressure is decreased. In most of the cases, both for polyethylene and polystyrene, the plot of volume fraction filled versus time shows a deflection point, which indicates a maximum in the flow rate. In general, this curve has an extended S shape. This is due to increasing pressure gradients in the cavity at the initial stages of filling, and to increasing difficulty in filling at later stages as a result of cooling and solidification.

All cases show a significant deviation between the predicted and experimental rates of filling during the early stages of filling. The deviation decreases as the melt progresses in the cavity. It is felt that the main source of error in the early stages is related to the sudden entry of the melt from the channel to the empty cavity, where factors like die swell and pressure loss due to the sudden change in cross sectional area for flow are very important.

In addition to that, as pointed out in section 3.1.1, the partial derivative of the radial velocity with respect to the radial direction times the velocity was neglected. The value of this term in the entrance region may be large and contribute to the deviations observed at the initial stages of filling (see Appendix 7). Accordingly, the calculation procedure has been modified, so that the very early stages of filling are ignored. In the new procedure, calculations start only after the front has reached the dimensionless radius of 0.2. The experimental measured time corresponding to this position is taken as the zero time for the momentum equation. The original zero time is used for the energy equation, in order to take into account the thermal effects from the beginning of filling. Figures 3-8 and 3-16, show that the agreement between the experimental and predicted modified results is better, for polyethylene and polystyrene, respectively.

Another factor which may account for the difference between the experimental and calculated results, is the pressure loss in radial flow due to the extensional stresses acting on the melt as it moves from smaller to larger radii. Cogswell and Lamb (48) have attempted to include this effect in the analysis of a simplified flow system where the conditions are assumed to be isothermal and the fluid obeys the Power Law. It can be shown, see Appendix 6, that the pressure gradient for the above conditions consists of two contributions: the shear contribution

$$\left(\frac{\partial P}{\partial r}\right)_s = M \times C_1 \times \frac{1}{r^n} \qquad \text{.....(3-60)}$$

where M is the consistency index and C_1 is a constant independent of r; and the hoop contribution

$$\left(\frac{\partial P}{\partial r}\right)_h = \lambda\, C_2\, \frac{1}{r^3} \qquad \text{.....(3-61)}$$

where λ is the constant extensional viscosity and C_2 a constant independent of r.

From equations (3-60) and (3-61), it can be seen that during the early stages of filling, when the radius of the melt is small, the pressure losses due to extension would be large compared to the shear losses. Thus the pressure which is utilized to advance the front (shear stress) in the radial direction would be lower, and consequently the melt would be slowed down. The relative importance of pressure losses due to viscous flow and to extension varies depending on the melt radius. The viscous loss becomes the dominating factor at large radii where the relative change in radius is smaller. The effect of the extensional losses (called sometimes also hoop losses) will be demonstrated once more, in the comparison between the experimental and theoretical pressure profiles. It is not possible to give an accurate treatment of extensional effects for the present flow system, due to lack of a satisfactory constitutive equation.

It is interesting to consider the effect of assuming constant polymer density (incompressibility) during the filling stage. The assumption of incompressibility is made by most workers in the field. Figures 3-19 and 3-20 show that the incompressible fluid gives shorter filling times than the corresponding compressible fluid. Thus the deviation from experimental results becomes larger with the assumption of incompressibility. This may be due to the presence of large temperature gradients in the cavity both in the radial and axial directions. Lower temperatures exist in the front regions, as will be shown later. The large temperature differences between the entrance and the melt front cause, at any instant, a difference between the volumetric flow rates in these regions. The volumetric flow rate at the front is lower than the corresponding flow rate at the entrance. Since the volumetric flow rate at the melt front is responsible for filling the empty part of the cavity, as given by equation (3-36), the compressible treatment results in slower filling rates than the treatment based on the assumption of incompressibility.

The effect of latent heat on the filling time, is given in Figure 3-19, for polyethylene. The comparison between the theoretical curves for the solution including latent heat and the one excluding this effect shows that the former case gives shorter filling time compared to the experi-

FIGURE 3-19

COMPARISON BETWEEN DIFFERENT SOLUTIONS
CASE 1

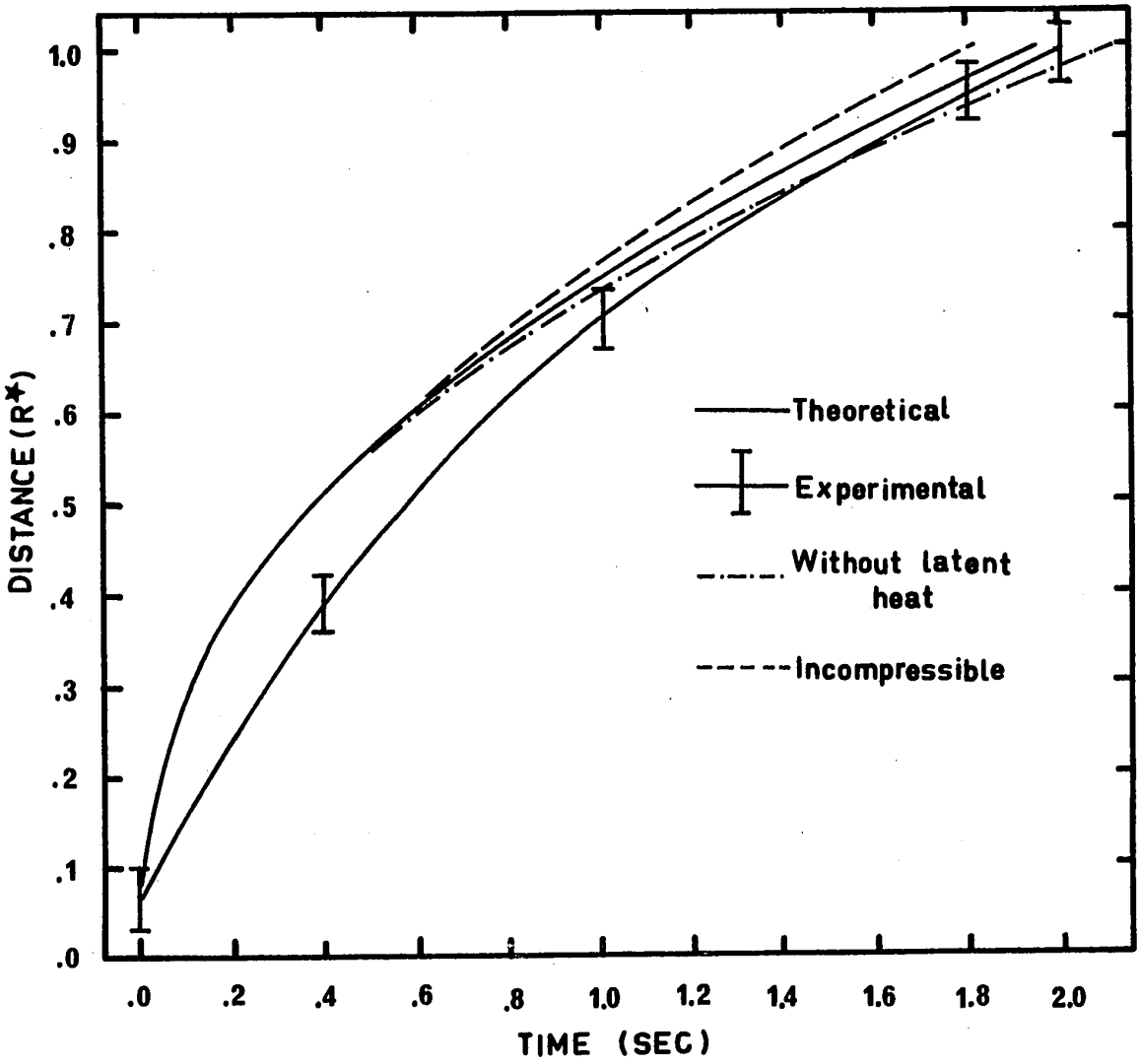

FIGURE 3-20

COMPARISON BETWEEN DIFFERENT SOLUTIONS

CASE 9

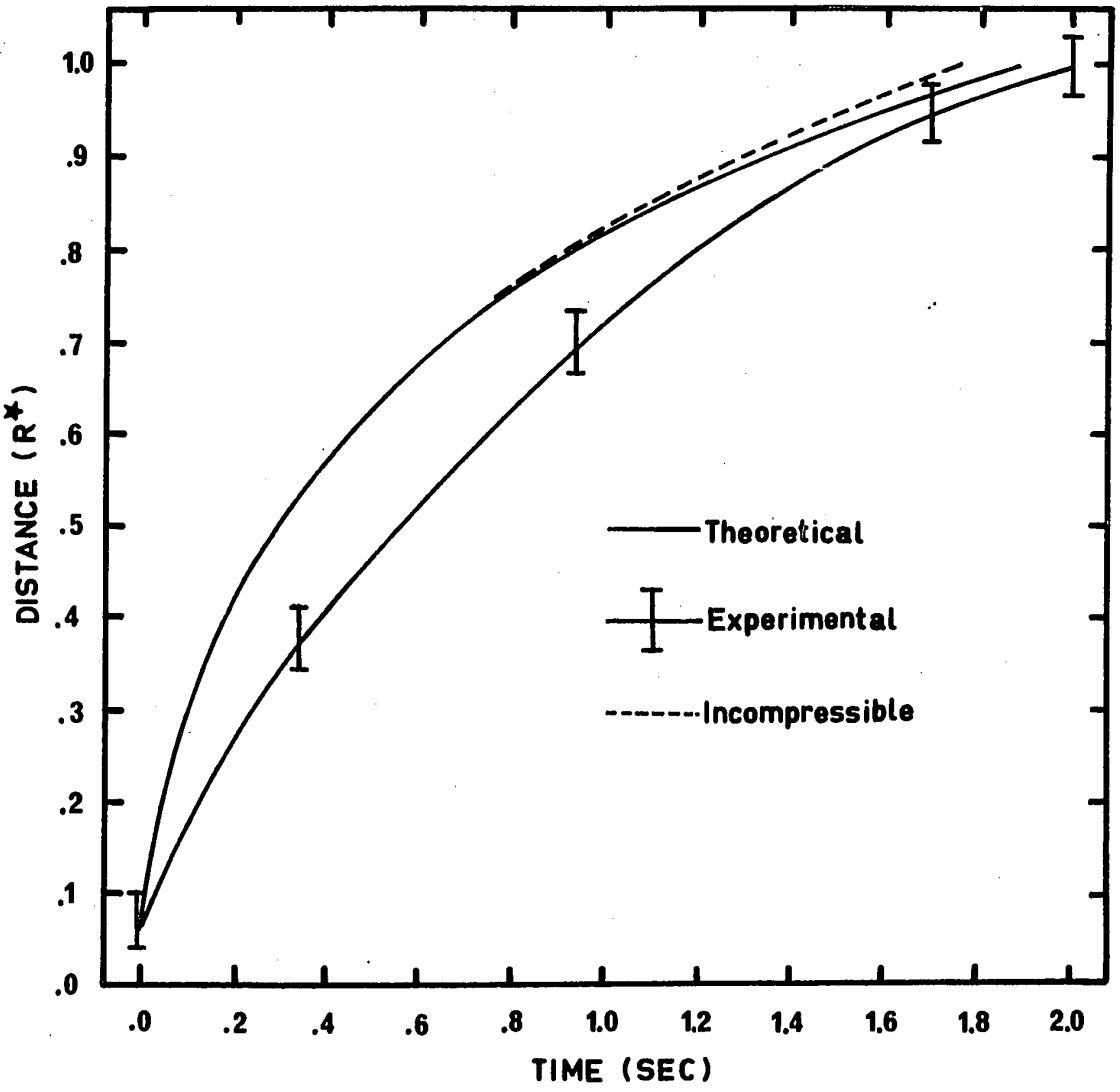

mental curve, due to higher temperatures and lower viscosities as a result of generation of heat during solidification. On the other hand, ignoring the latent heat yields a longer filling time than the experimental value.

3.2.4 Velocity Profiles

Figures 3-21 to 3-24 show the velocity profiles at $r^* = 0.20$ at different times during the filling stage, as defined by the position of the melt front R^*, for cases 1, 3, 6 and 8 respectively, for polyethylene, and Figures 3-25 and 3-26 for cases 10 and 12 respectively, for polystyrene. The main observation is that the velocity at a given point and consequently the flow rate, increase with increasing injection pressure and/or melt temperature. The calculated velocity profiles indicate that the flow rate decreases with time, due to decreasing pressure gradients and the rise in melt viscosity as a result of cooling, as the melt progresses in the cavity. All cases show an inflection point in the velocity profile, close to the cavity wall. This may be due to lower temperatures and high viscosities in this region. This phenomenon is more pronounced in the polystyrene cases, since the activation energy for viscosity is more than double than that of polyethylene, see Appendix 1, section 9.1. In addition, the velocity profiles are flatter, close to the centerline, for polystyrene, due to the lower value for the flow index, n, 0.368 for poly-

FIGURE 3-21

VELOCITY PROFILES AT $r^*=.20$

CASE 1

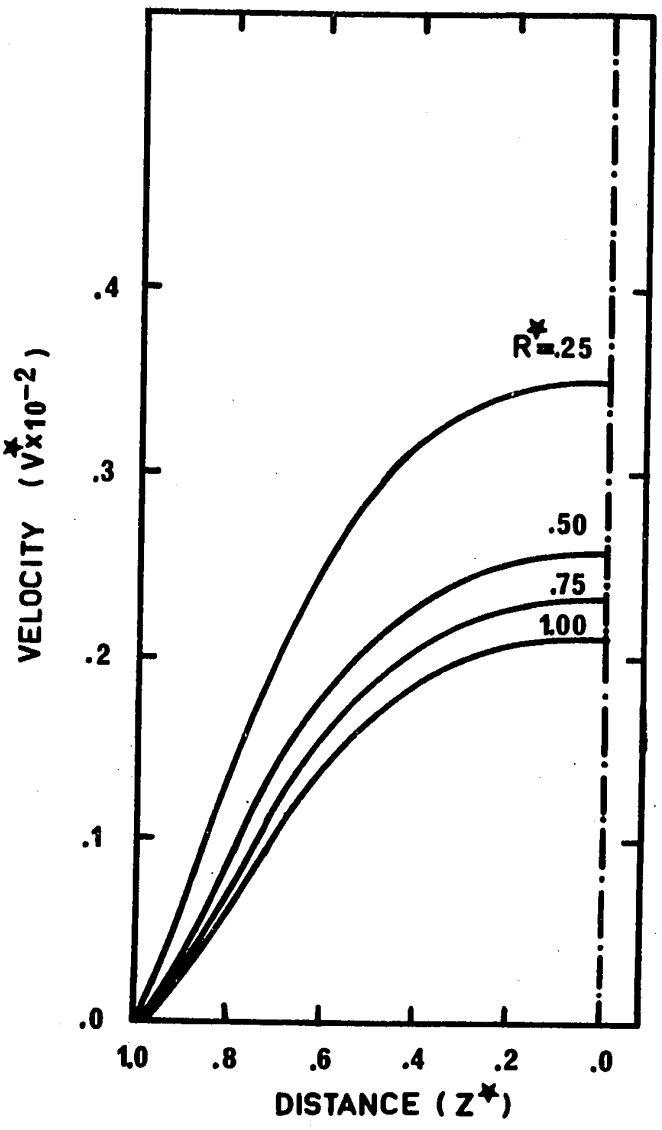

FIGURE 3-22

VELOCITY PROFILES AT r^*=.20
CASE 3

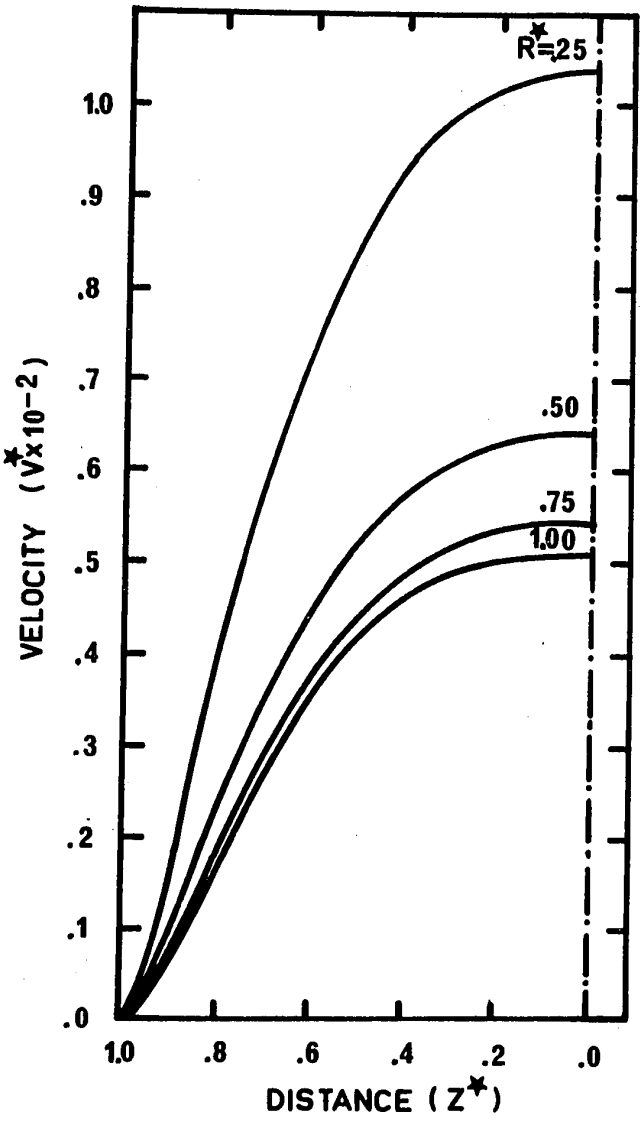

FIGURE 3-23

VELOCITY PROFILES AT r^*=.20

CASE 6

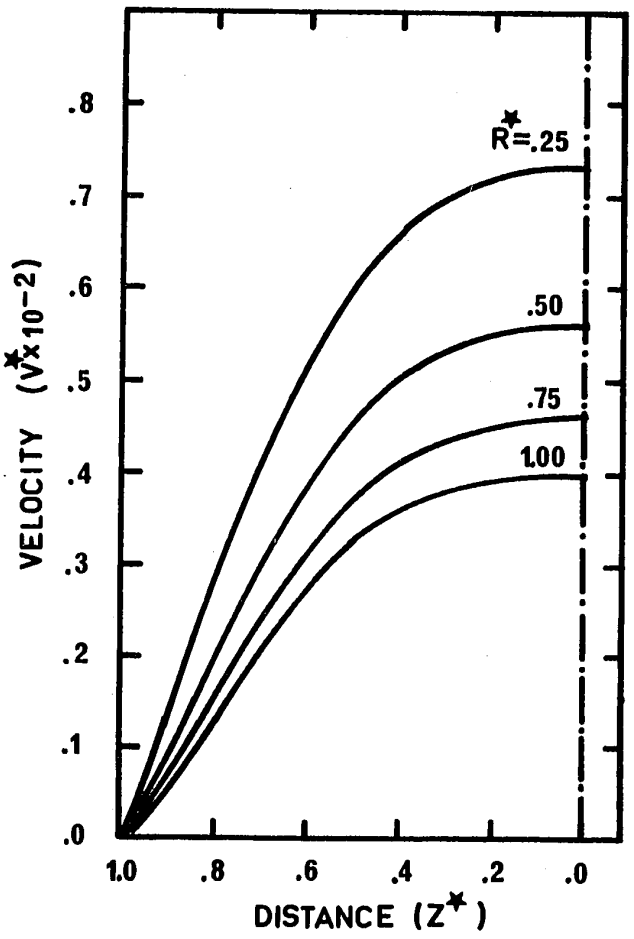

FIGURE 3-24

VELOCITY PROFILES AT $r^* = .20$

CASE 8

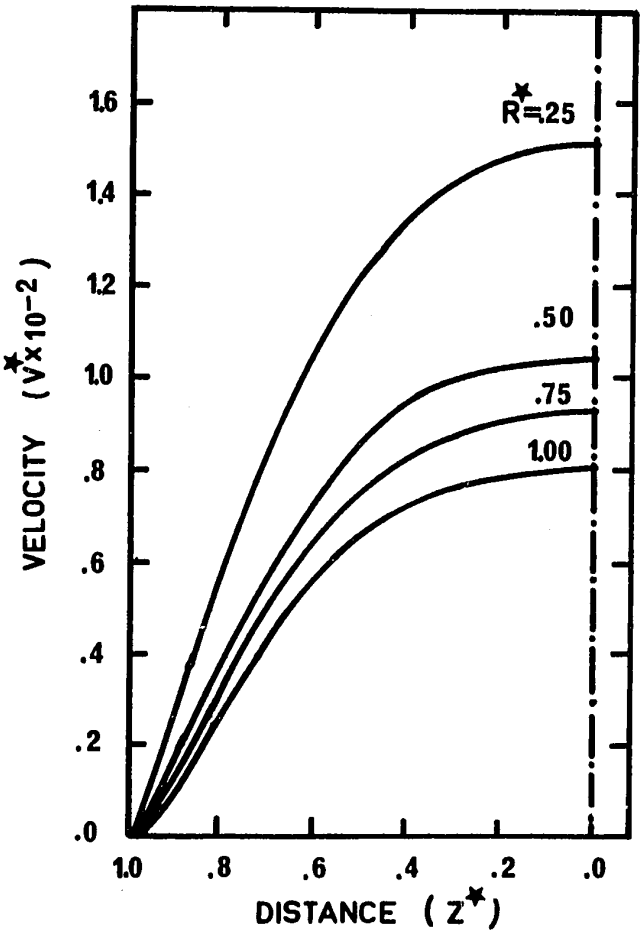

FIGURE 3-25

VELOCITY PROFILES AT r^*=.20

CASE 10

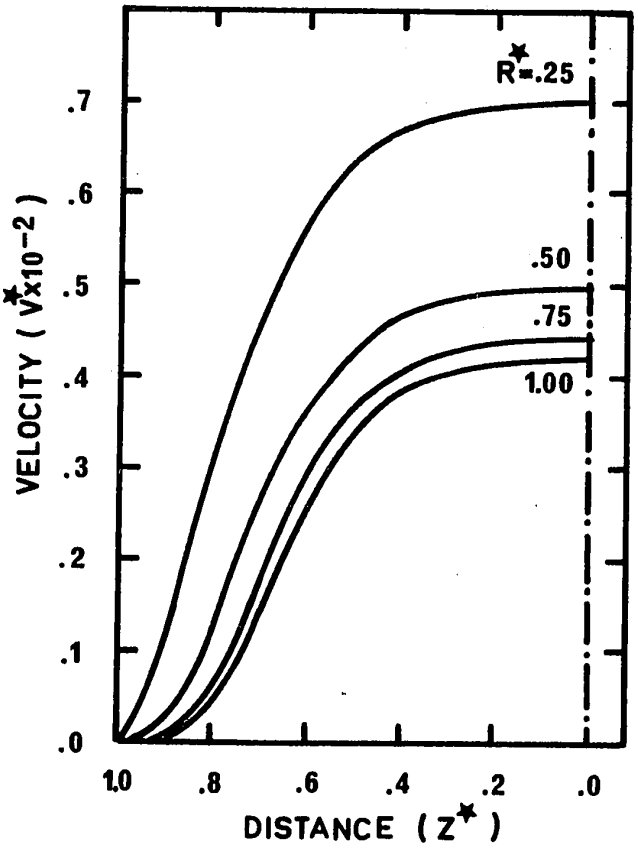

FIGURE 3-26

VELOCITY PROFILES AT r^*=.20

CASE 12

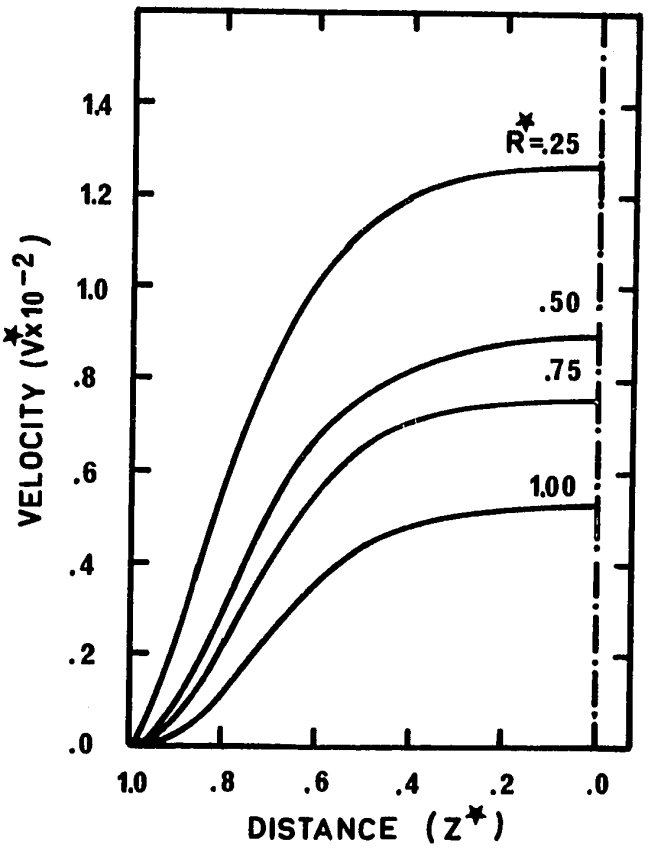

styrene compared to 0.594 for polyethylene.

3.2.5 Temperature Profiles

Figures 3-27 to 3-30 give the calculated temperature profiles at the end of filling for cases 2, 4, 5 and 7 respectively, for polyethylene and Figures 3-31 and 3-32 for cases 9 and 11, respectively for polystyrene. The temperature at the centerline of the cavity appears to be unaffected, except for relatively long filling times, cases 5 and 9 for polyethylene and polystyrene, respectively. Large temperature differences exist in the cavity, and are responsible, as mentioned earlier, for the differences between the compressible and incompressible solutions. With relatively long filling times, Figures 3-29 and 3-31, about 15% of the cross section is solidified during the filling stage. With shorter filling times obtained at higher injection pressure and temperature, viscous heating causes the temperature of the melt near the entrance to rise above the initial value as shown in Figure 3-28 for polyethylene. The viscous heating effect is apparently stronger in the case of polyethylene than in polystyrene, due to the lower flow index and lower velocity gradients close to the wall in the cases of polystyrene.

No temperature measurements have been conducted during the course of experiments, except for the wall temperature. Temperature profiles at the wall are given for a few

FIGURE 3-27

TEMPERATURE PROFILES AT THE END OF FILLING

CASE 2

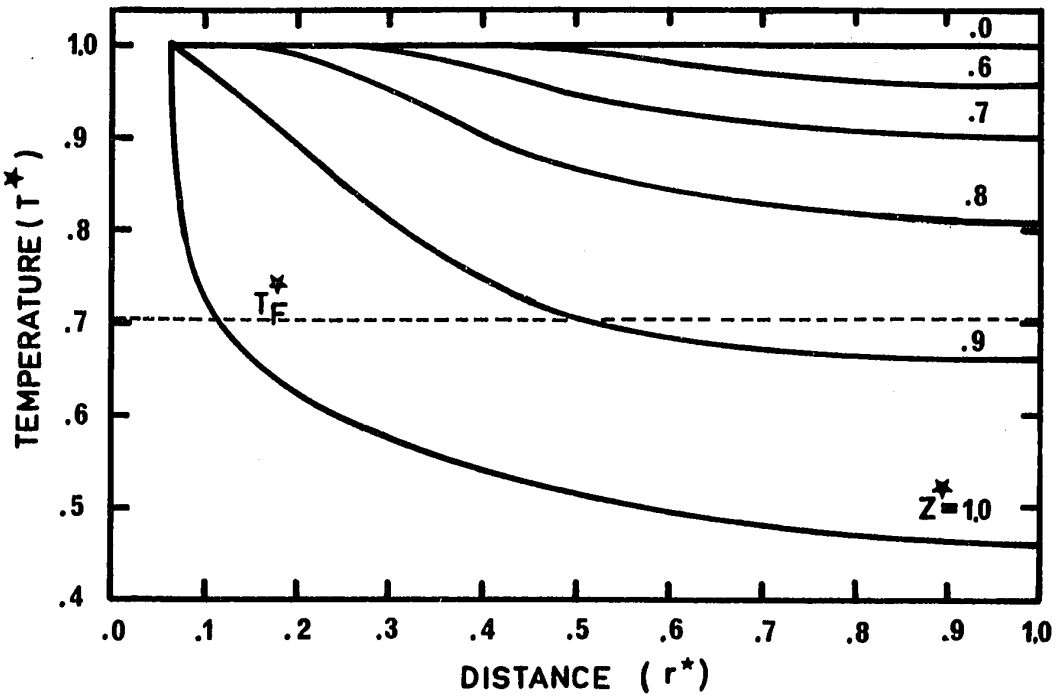

FIGURE 3-28

TEMPERATURE PROFILES AT THE END OF FILLING
CASE 4

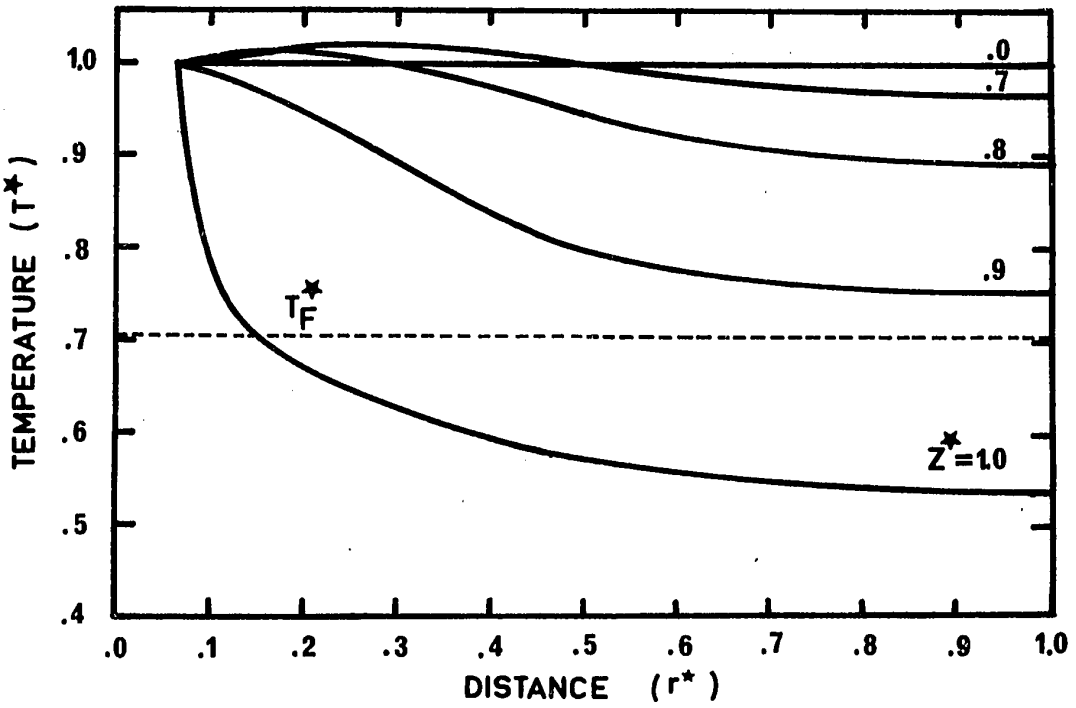

FIGURE 3-29

TEMPERATURE PROFILES AT THE END OF FILLING
CASE 5

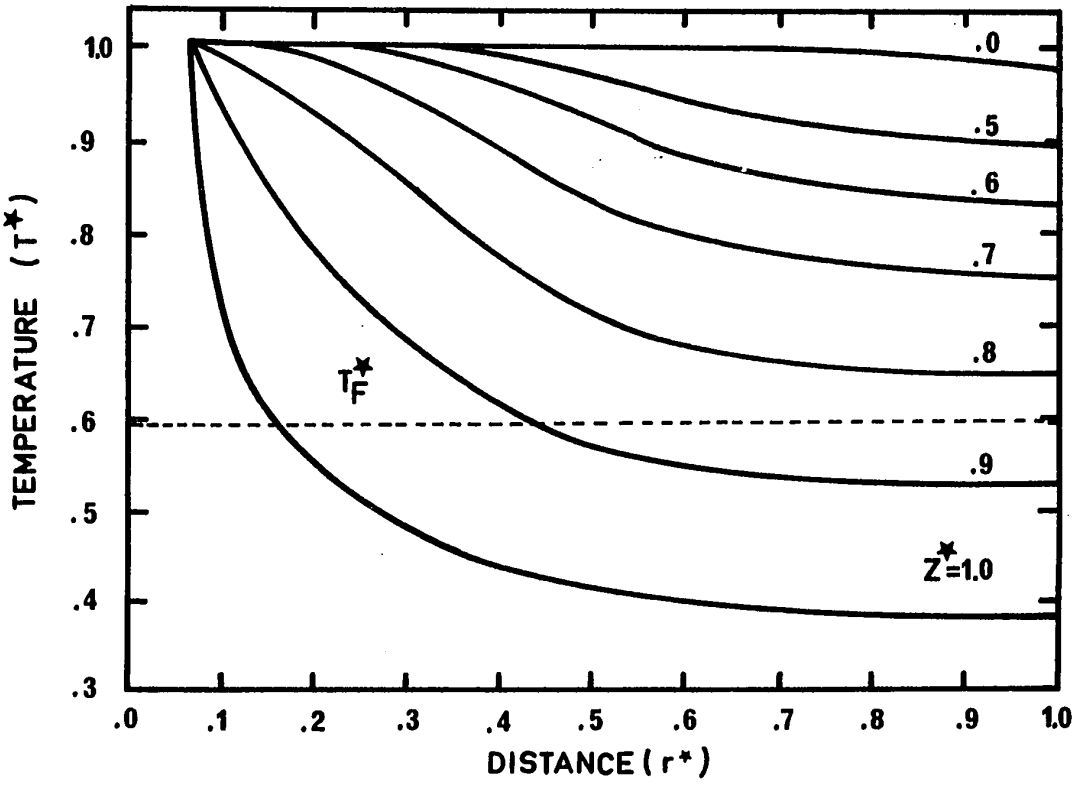

FIGURE 3-30

TEMPERATURE PROFILES AT THE END OF FILLING
CASE 7

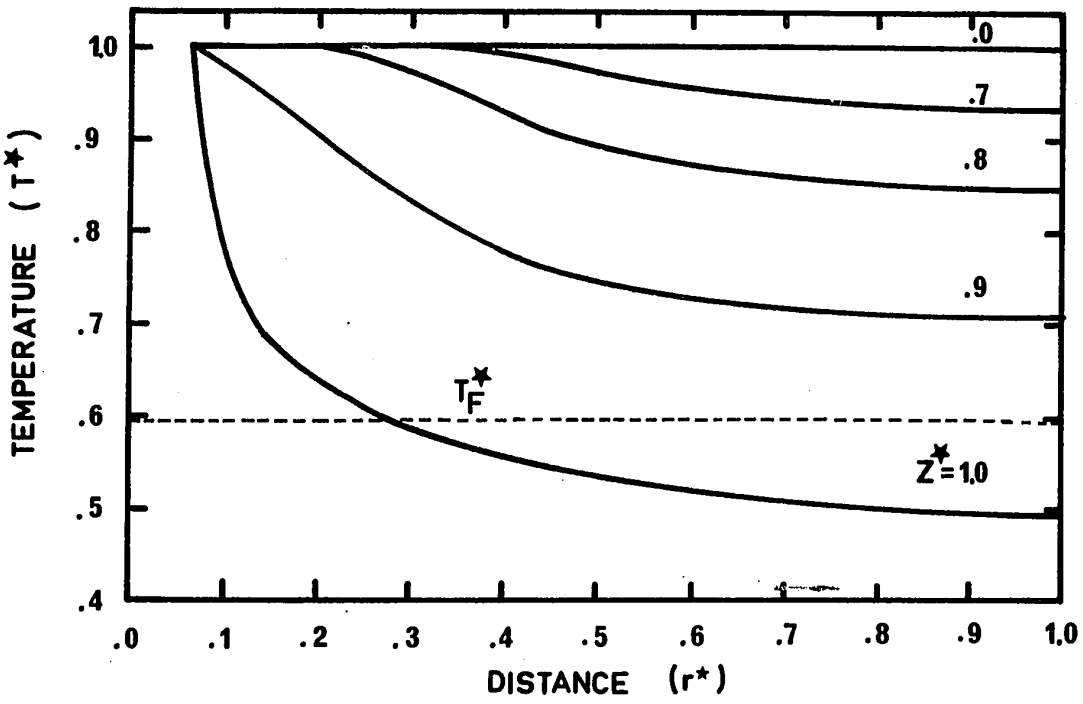

FIGURE 3-31

TEMPERATURE PROFILES AT THE END OF FILLING

CASE 9

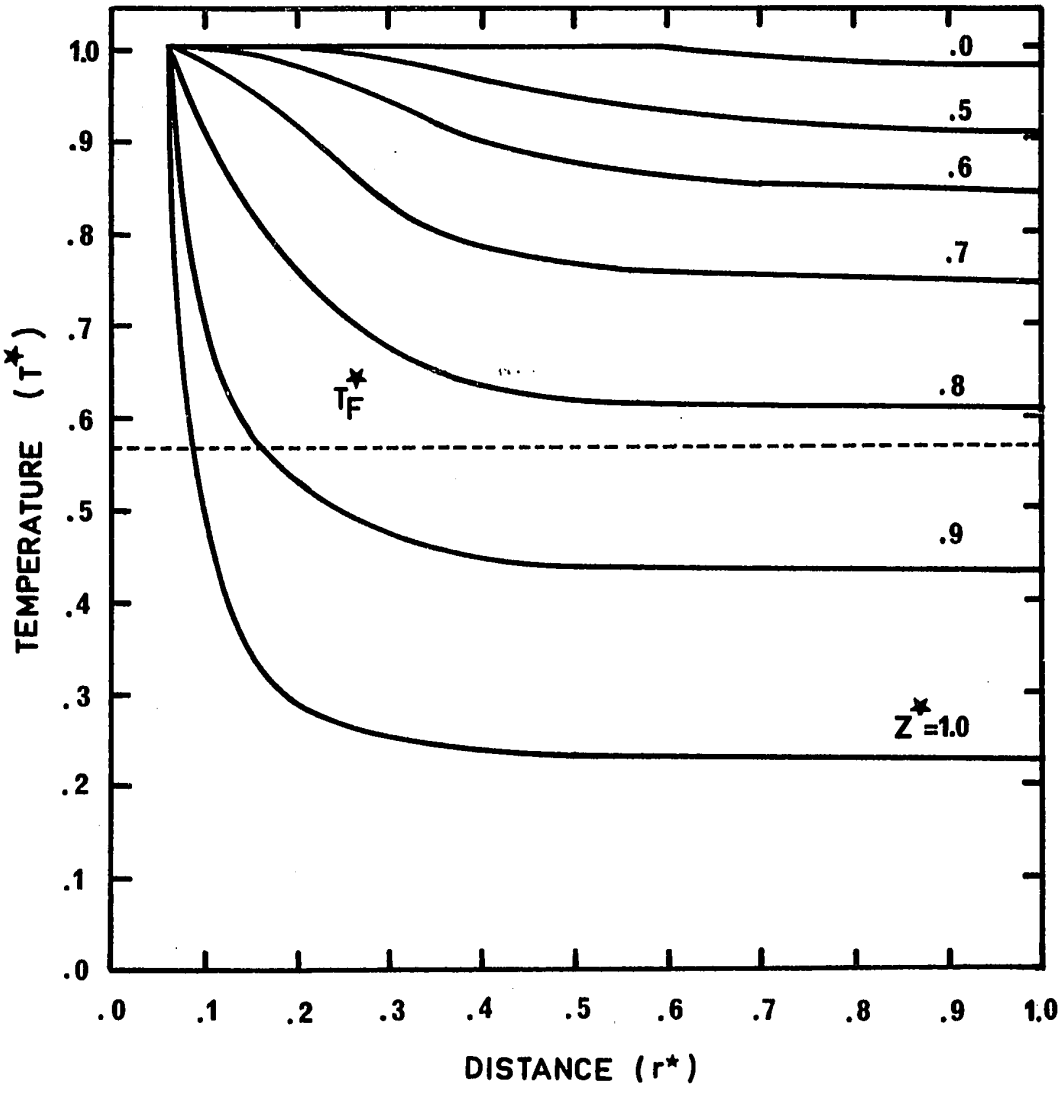

FIGURE 3-32

TEMPERATURE PROFILES AT THE END OF FILLING

CASE 11

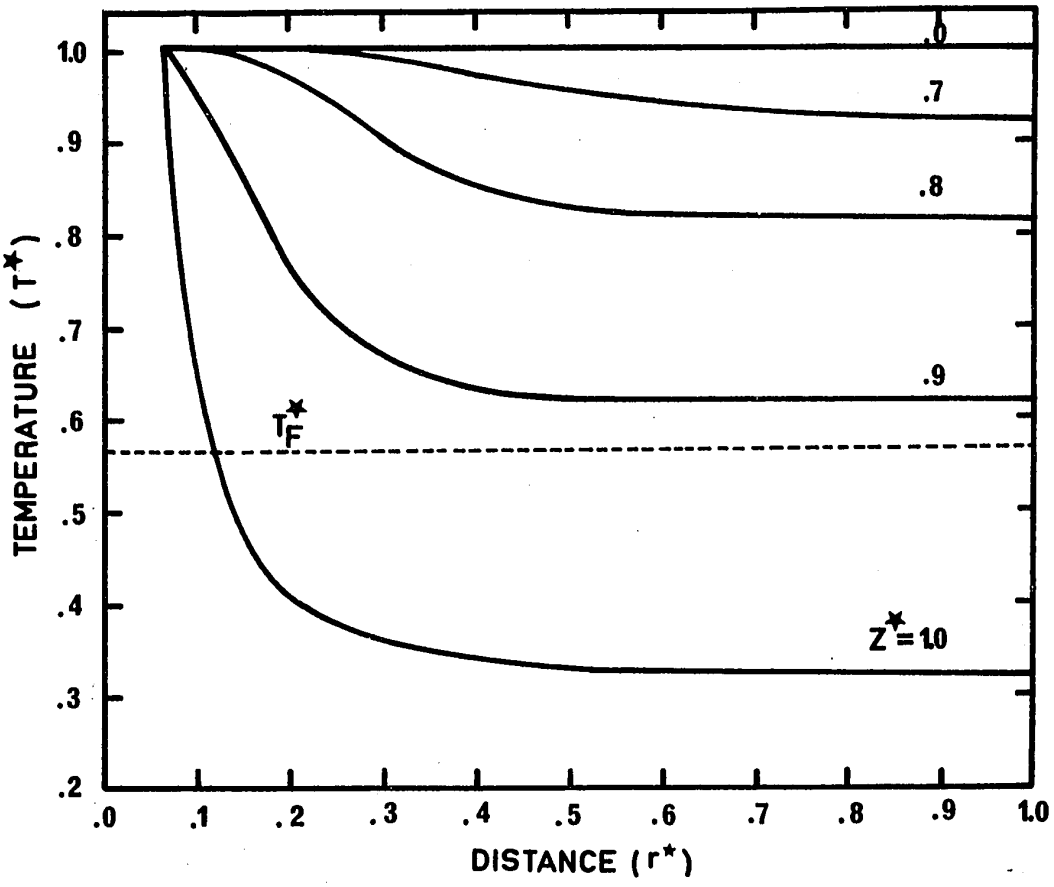

FIGURE 3-33

TEMPERATURE PROFILES AT THE WALL-CASE 2

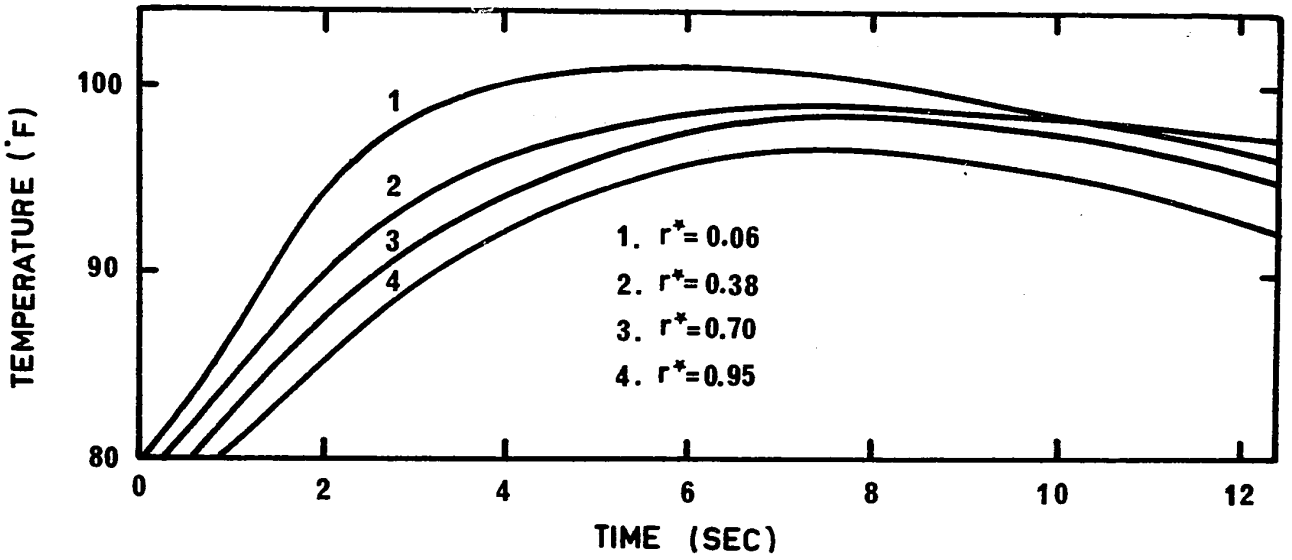

FIGURE 3-34

TEMPERATURE PROFILES AT THE WALL-CASE 6

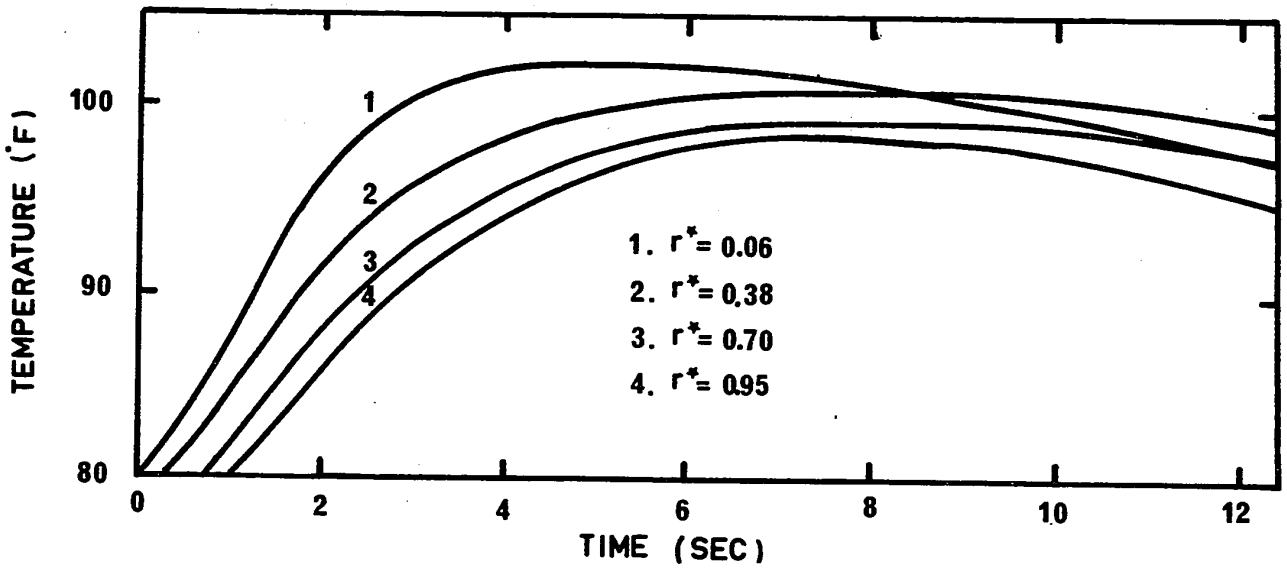

FIGURE 3-35

TEMPERATURE PROFILES AT THE WALL- CASE 10

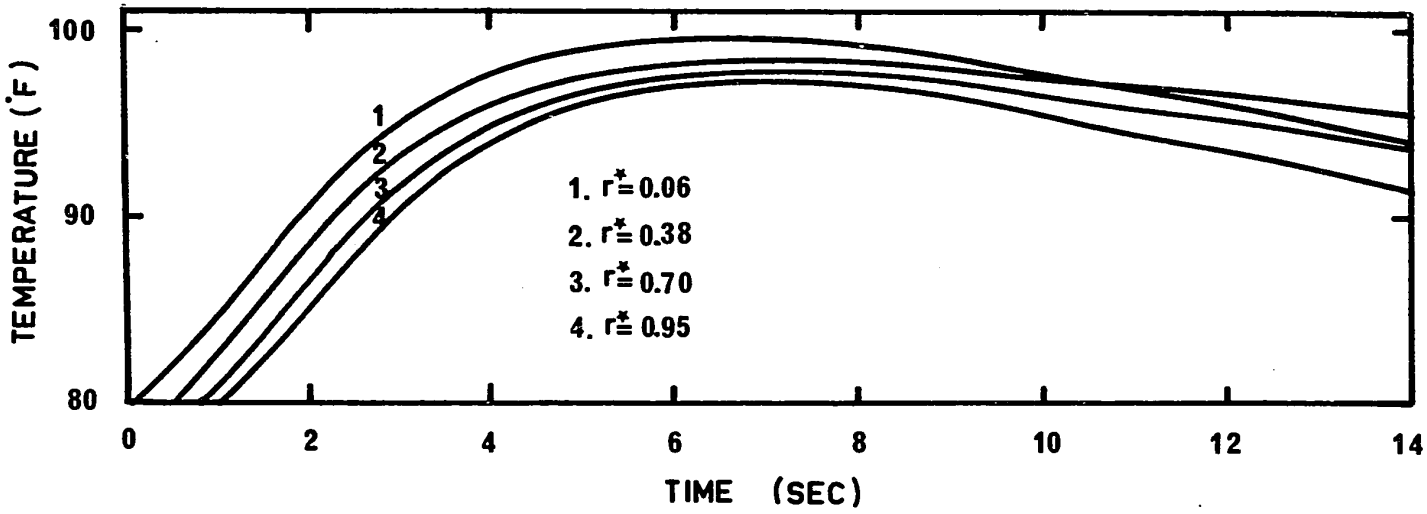

cases in Figures 3-33 to 3-35. The maximum temperature rise at the wall is about 20°F, a fact that could have a small effect on the filling stage, as discussed in Chapter 7.

Barrie (19) attempted to estimate the solid skin content of the polymer at the end of filling. He applied the heat conduction equation and obtained poor agreement between the experimental and calculated values, with the former being lower. As shown in the above discussion, viscous heating effects and convective heat transfer, should be taken into account. This may explain the lack of agreement in Barrie's approach.

3.2.6 Pressure Profiles

Figures 3-36 to 3-47 show the experimental values and calculated pressure profiles at the end of filling stage for polyethylene and polystyrene. The experimental measurements are subjected to errors due to the area of the pressure transducer, which accounts for 6.3% of the cavity radius, and to the non-isothermal conditions at the wall which are estimated at 1 psi/°F. The effects of these variables are discussed in detail in Chapter 7.

Generally, larger differences in temperature between the entrance and the front result in lower pressure gradients close to the entrance and greater ones close to the front, compared with the isothermal case. This is due

FIGURE 3-36

PRESSURE PROFILE AT THE END OF FILLING
CASE 1

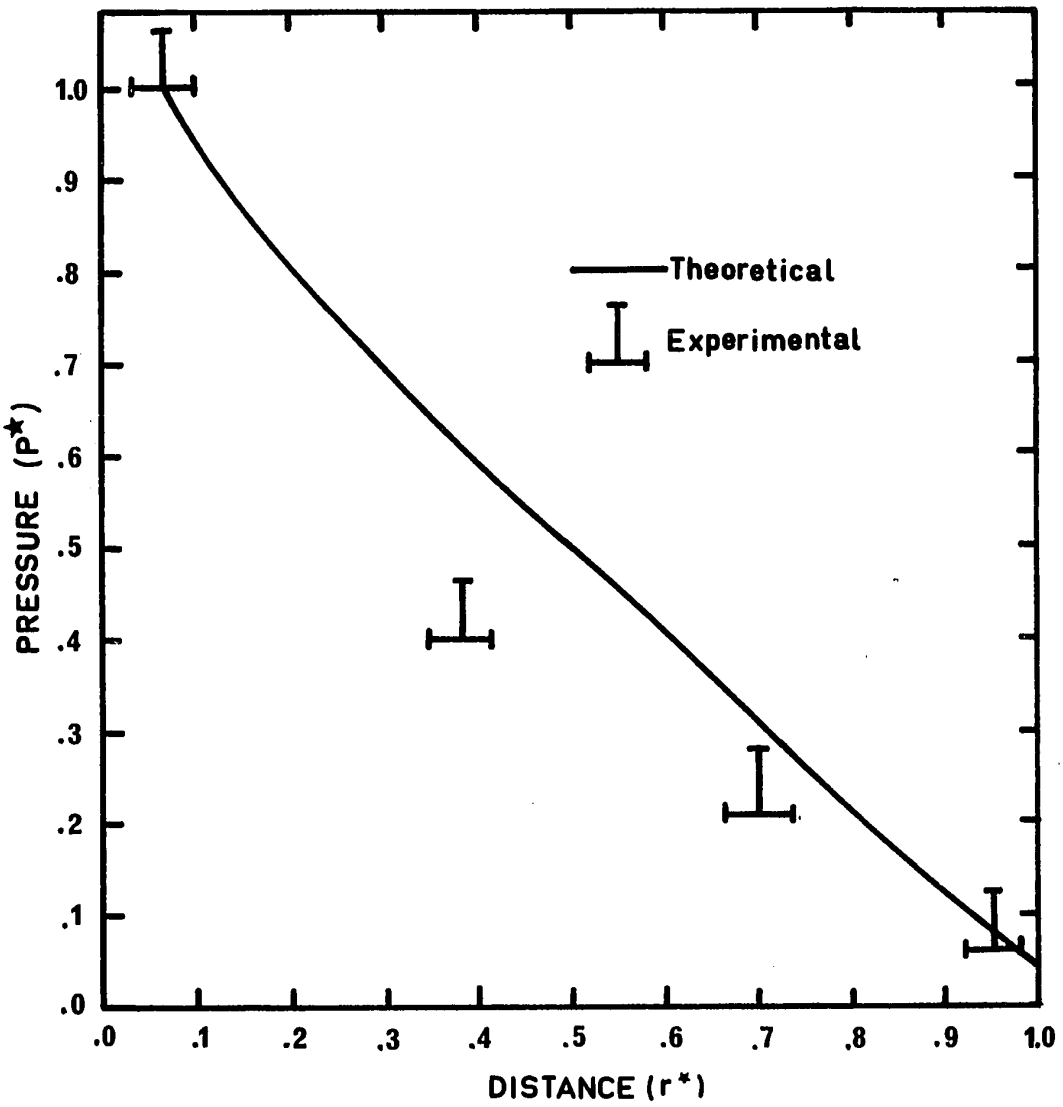

FIGURE 3-37

PRESSURE PROFILE AT THE END OF FILLING
CASE 2

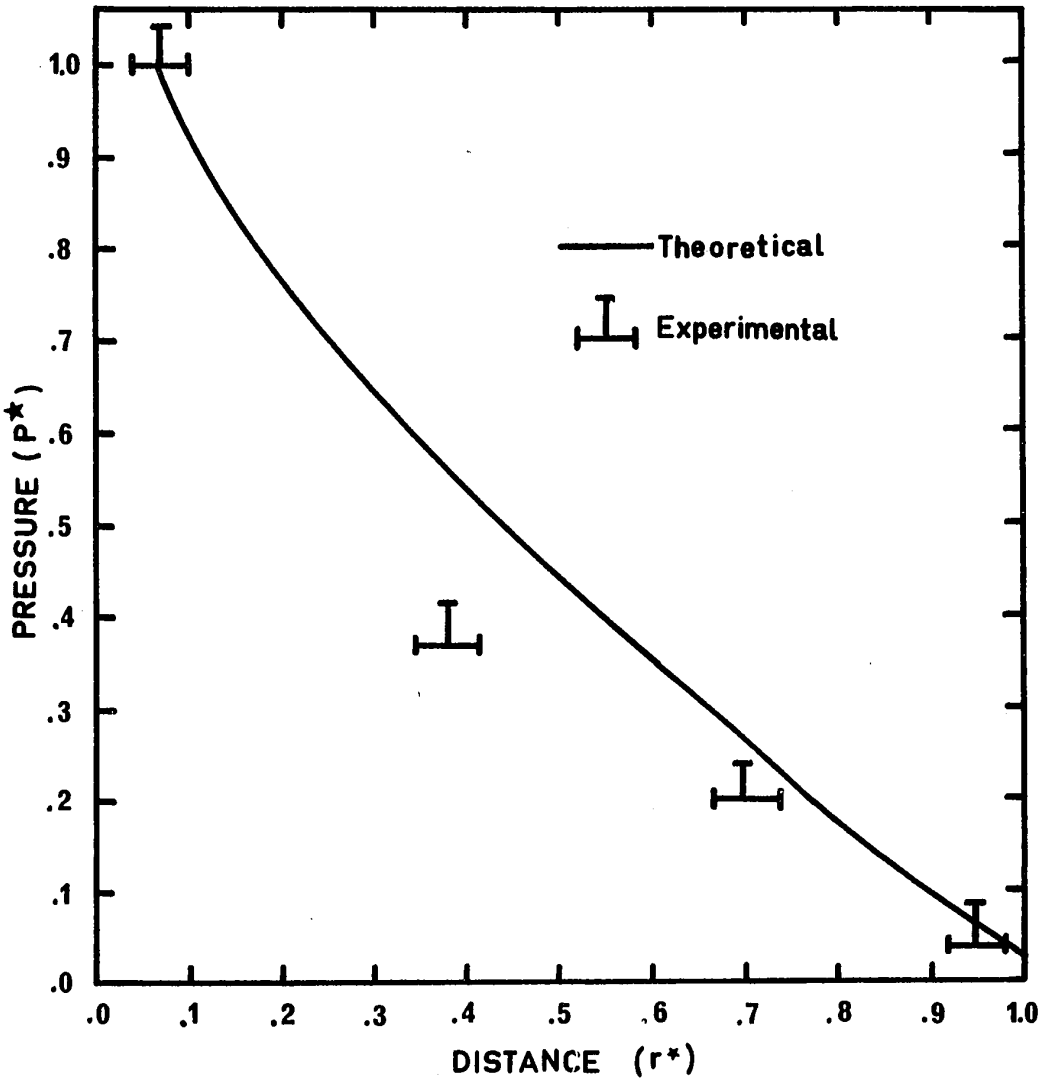

FIGURE 3-38

PRESSURE PROFILE AT THE END OF FILLING
CASE 3

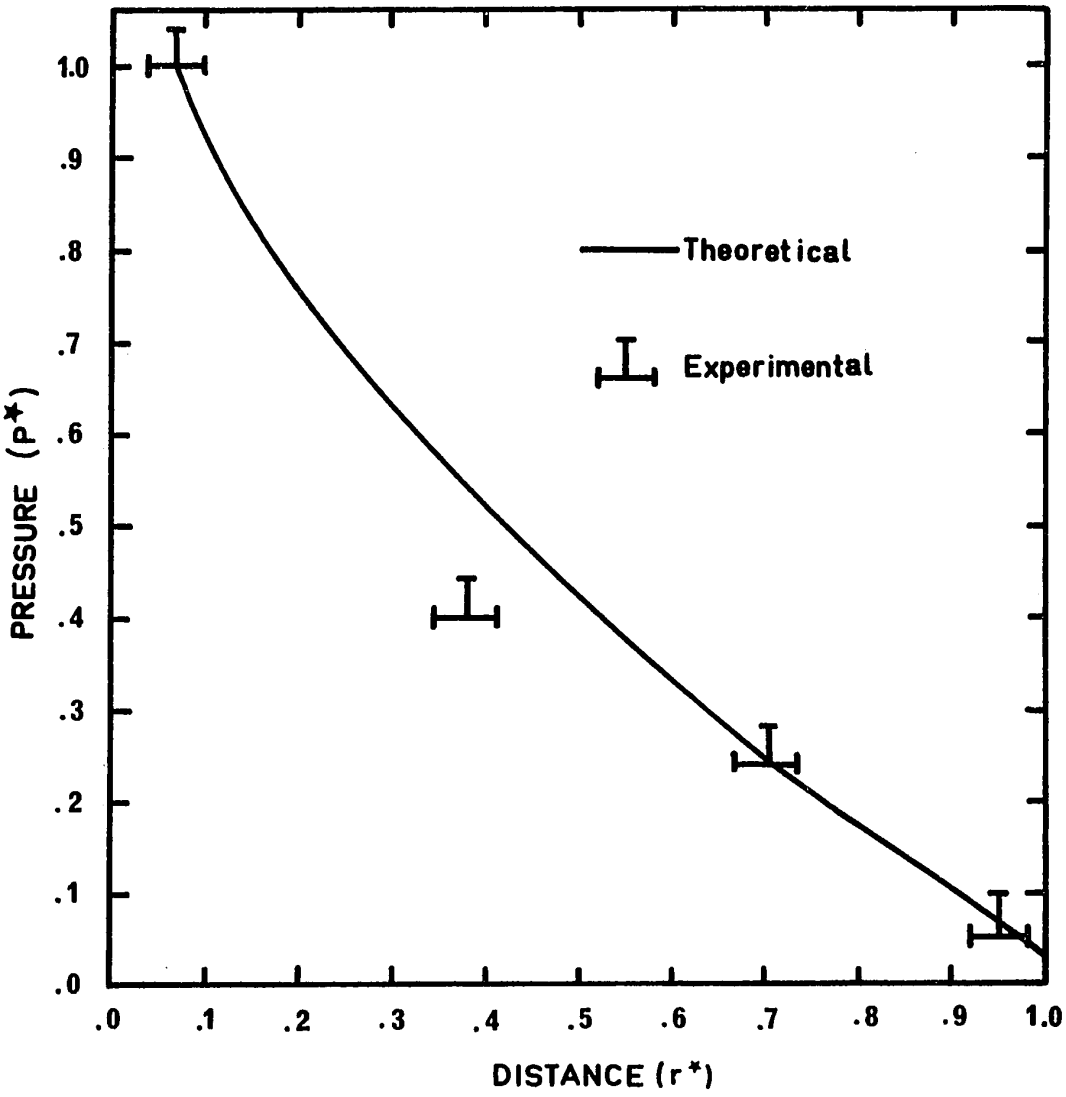

FIGURE 3-39

PRESSURE PROFILE AT THE END OF FILLING
CASE 4

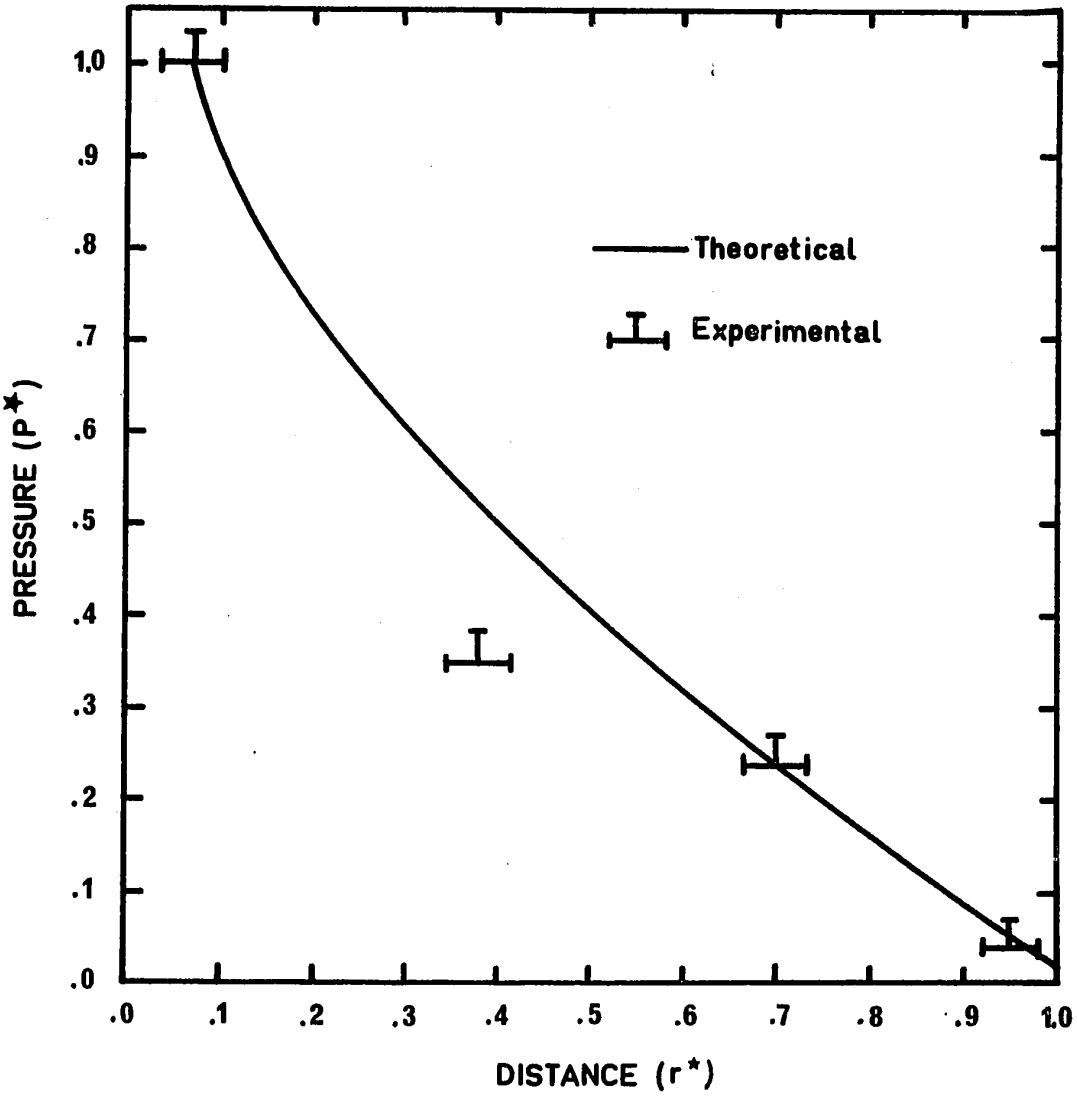

FIGURE 3-40

PRESSURE PROFILE AT THE END OF FILLING
CASE 5

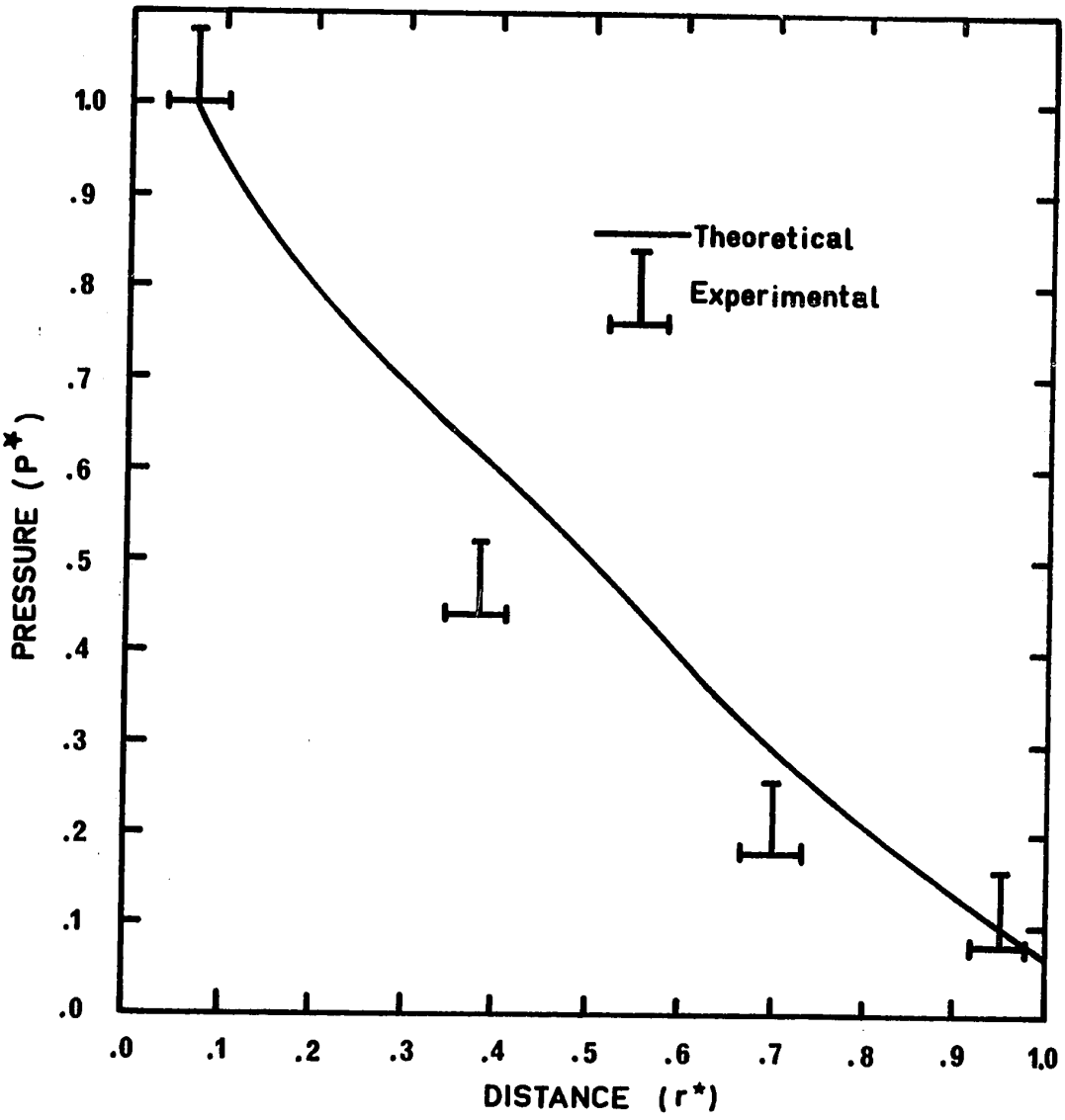

FIGURE 3-41

PRESSURE PROFILE AT THE END OF FILLING
CASE 6

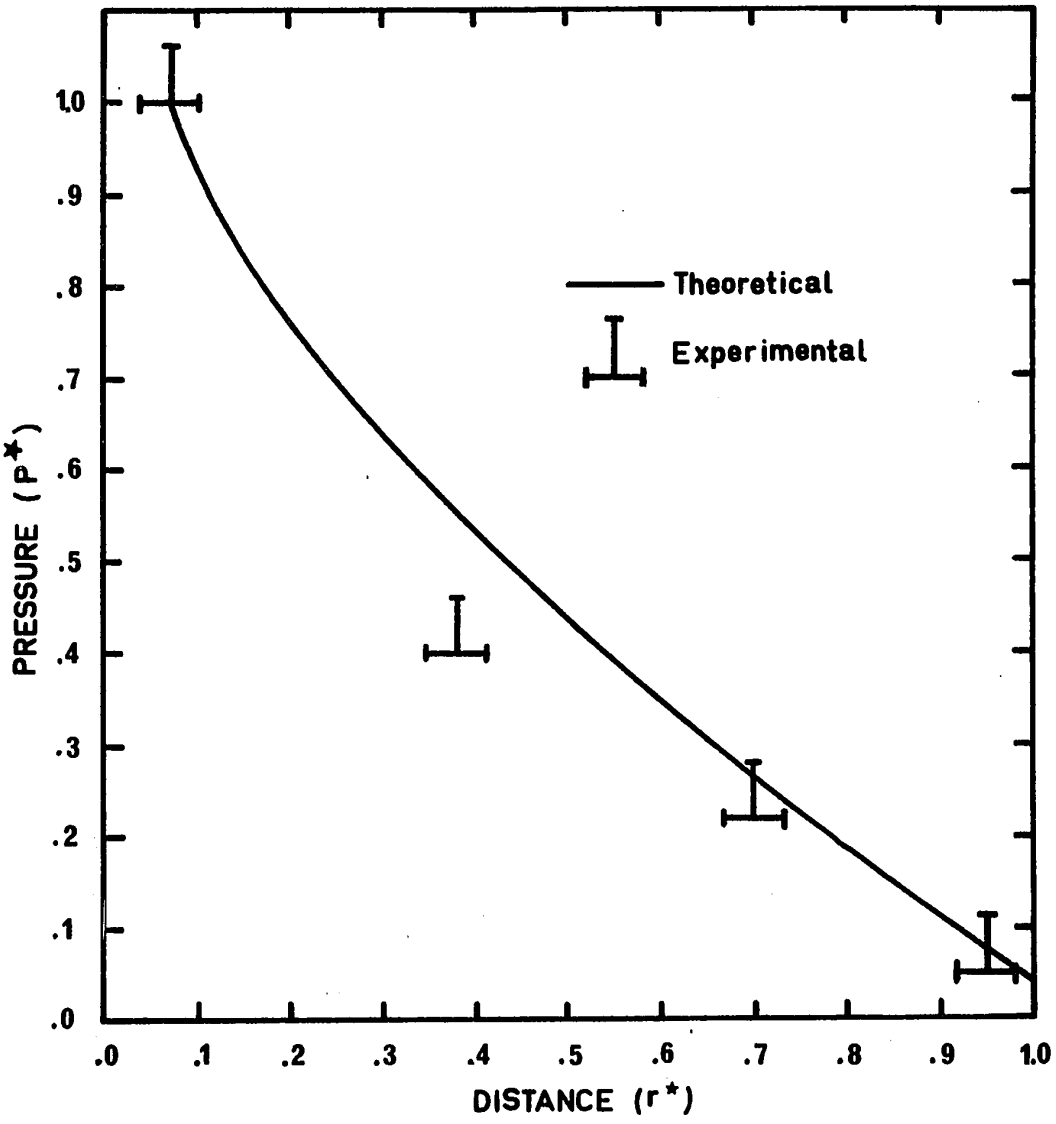

FIGURE 3-42

PRESSURE PROFILE AT THE END OF FILLING

CASE 7

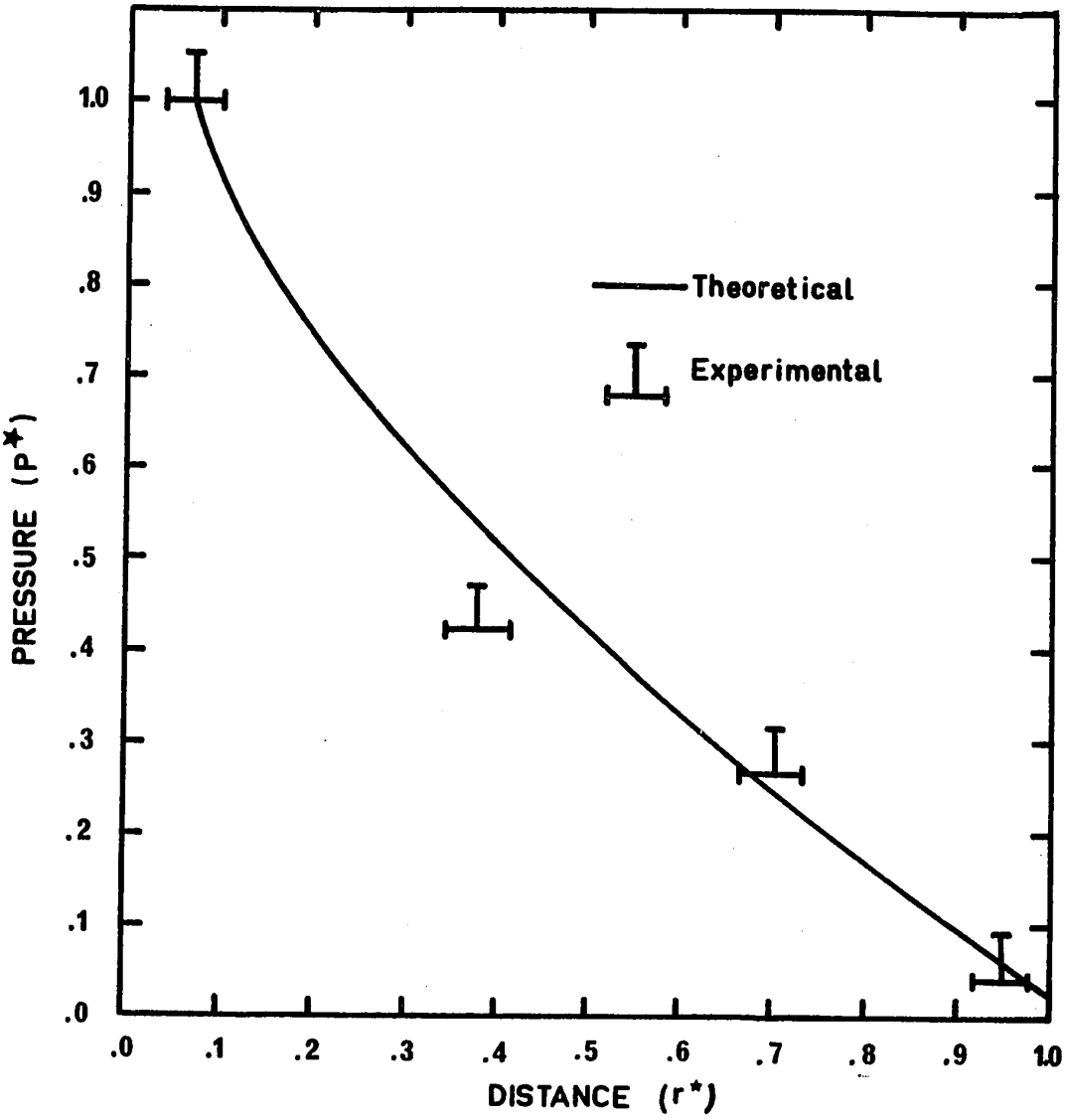

FIGURE 3-43

PRESSURE PROFILE AT THE END OF FILLING
CASE 8

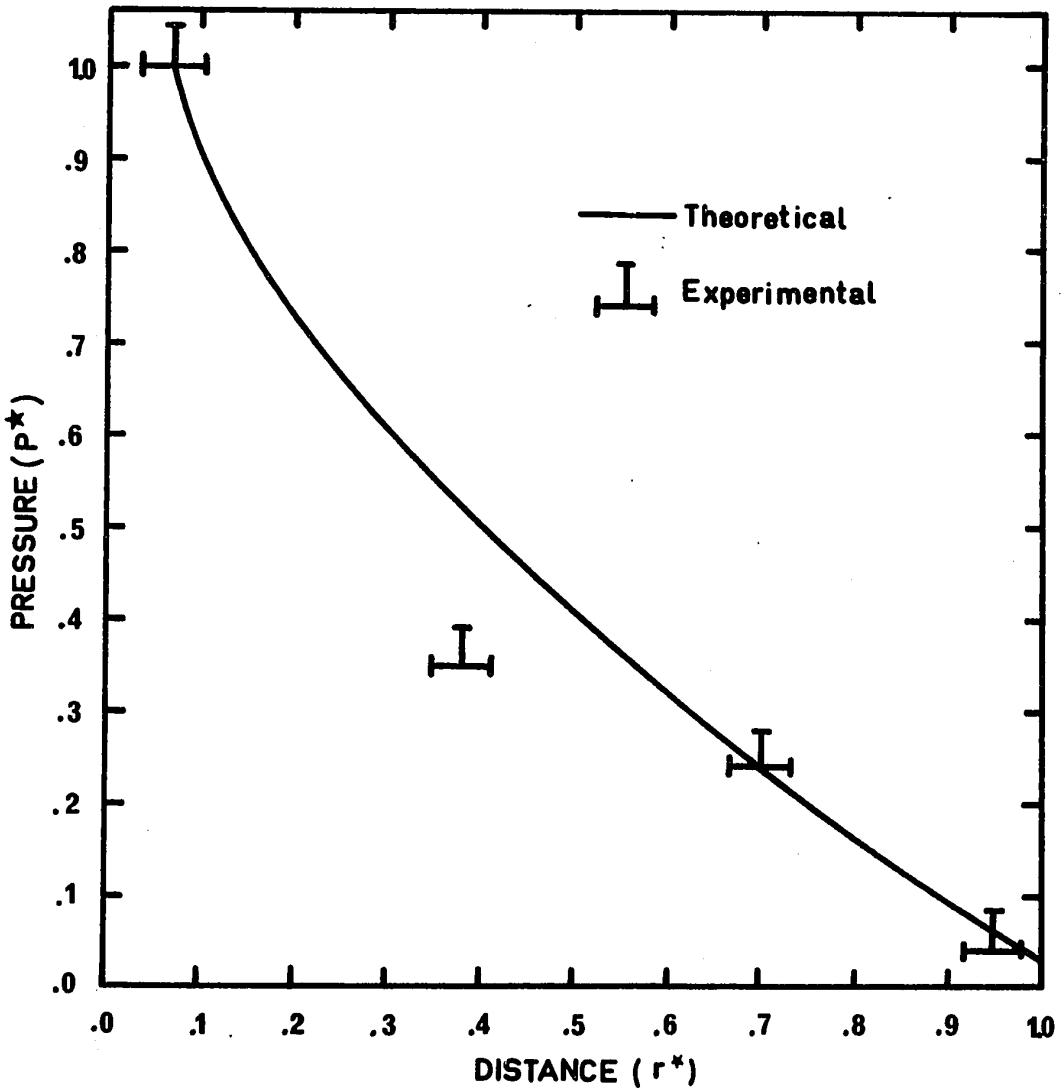

FIGURE 3-44

PRESSURE PROFILE AT THE END OF FILLING
CASE 9

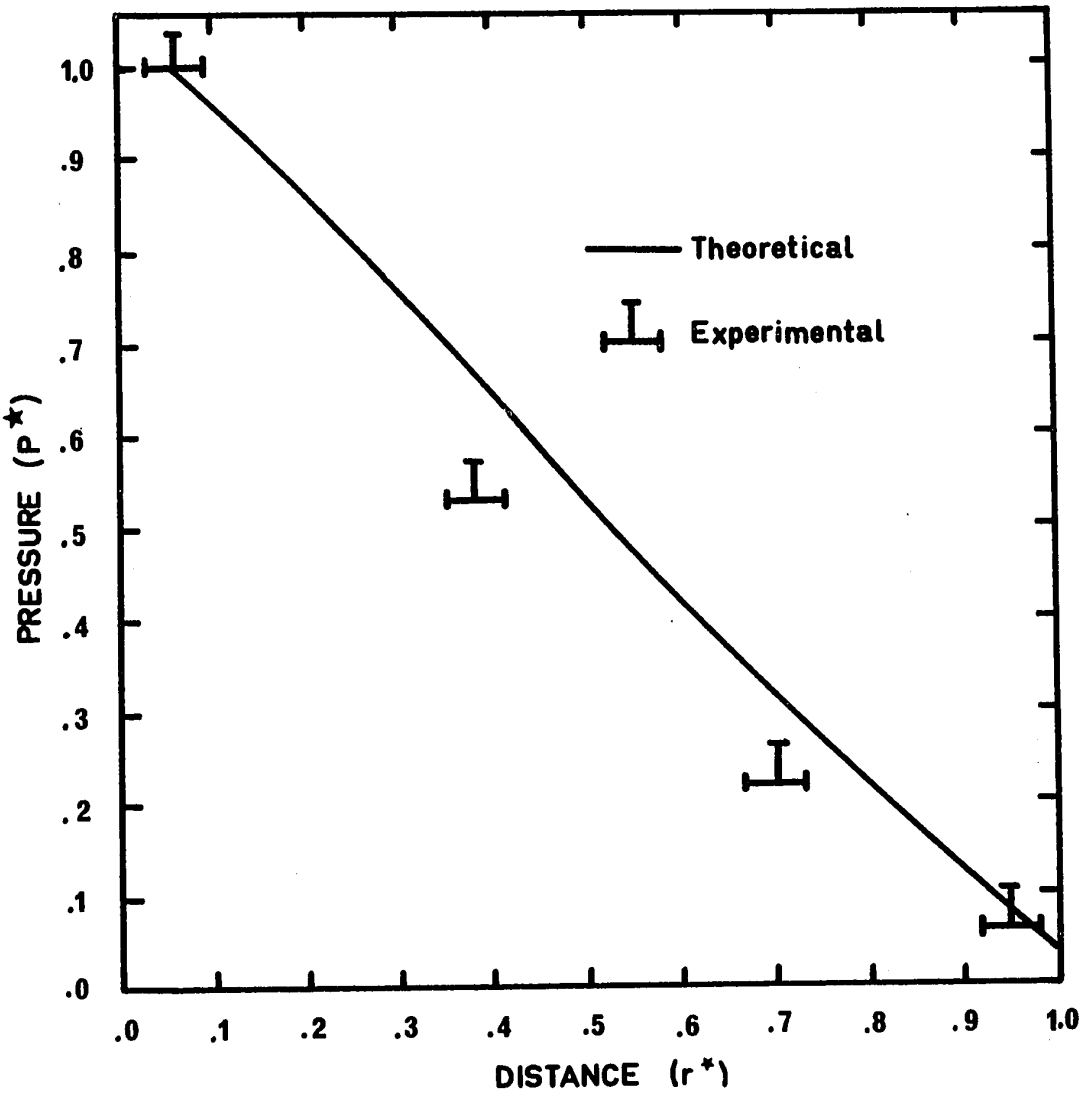

FIGURE 3-45

PRESSURE PROFILE AT THE END OF FILLING
CASE 10

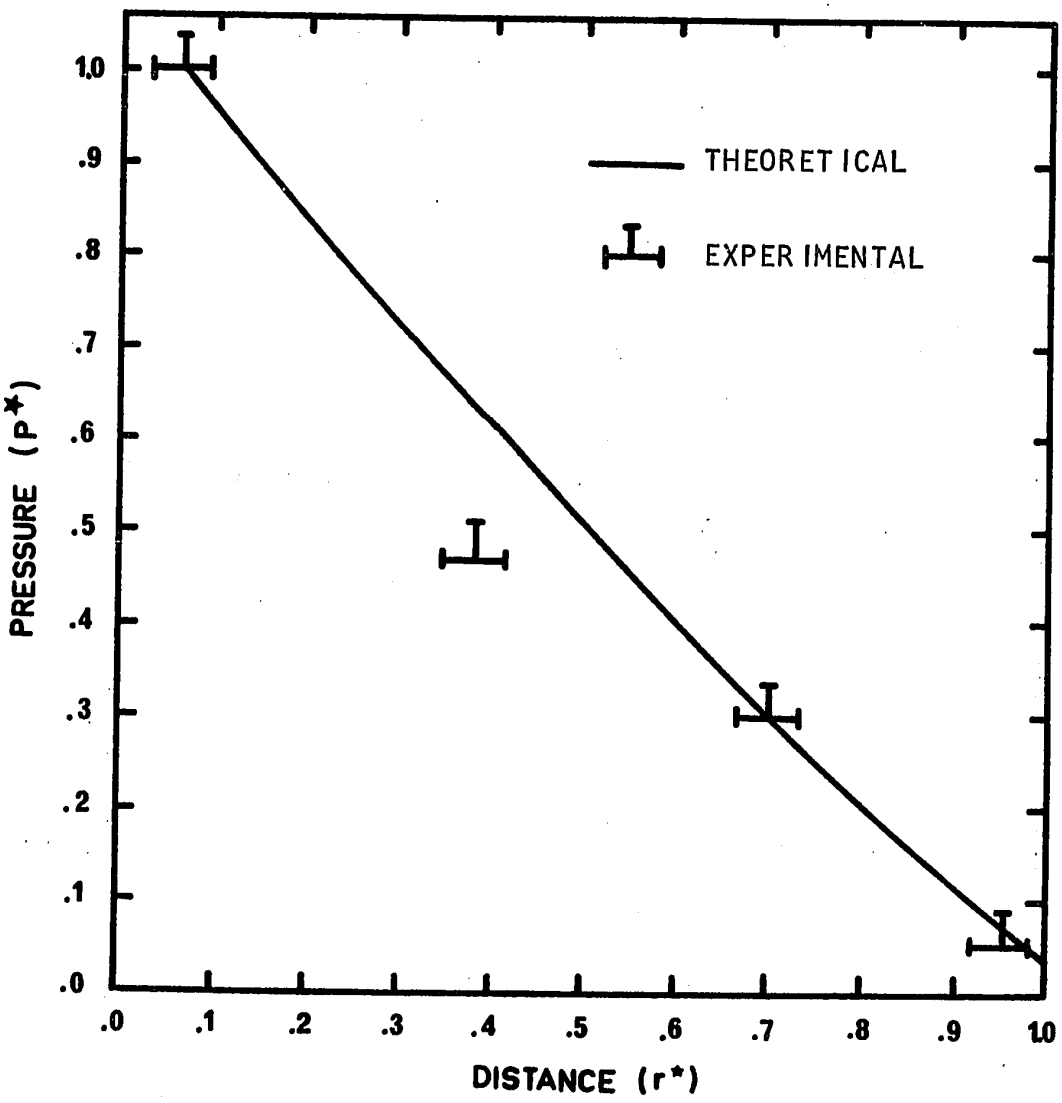

FIGURE 3-46

PRESSURE PROFILE AT THE END OF FILLING
CASE 11

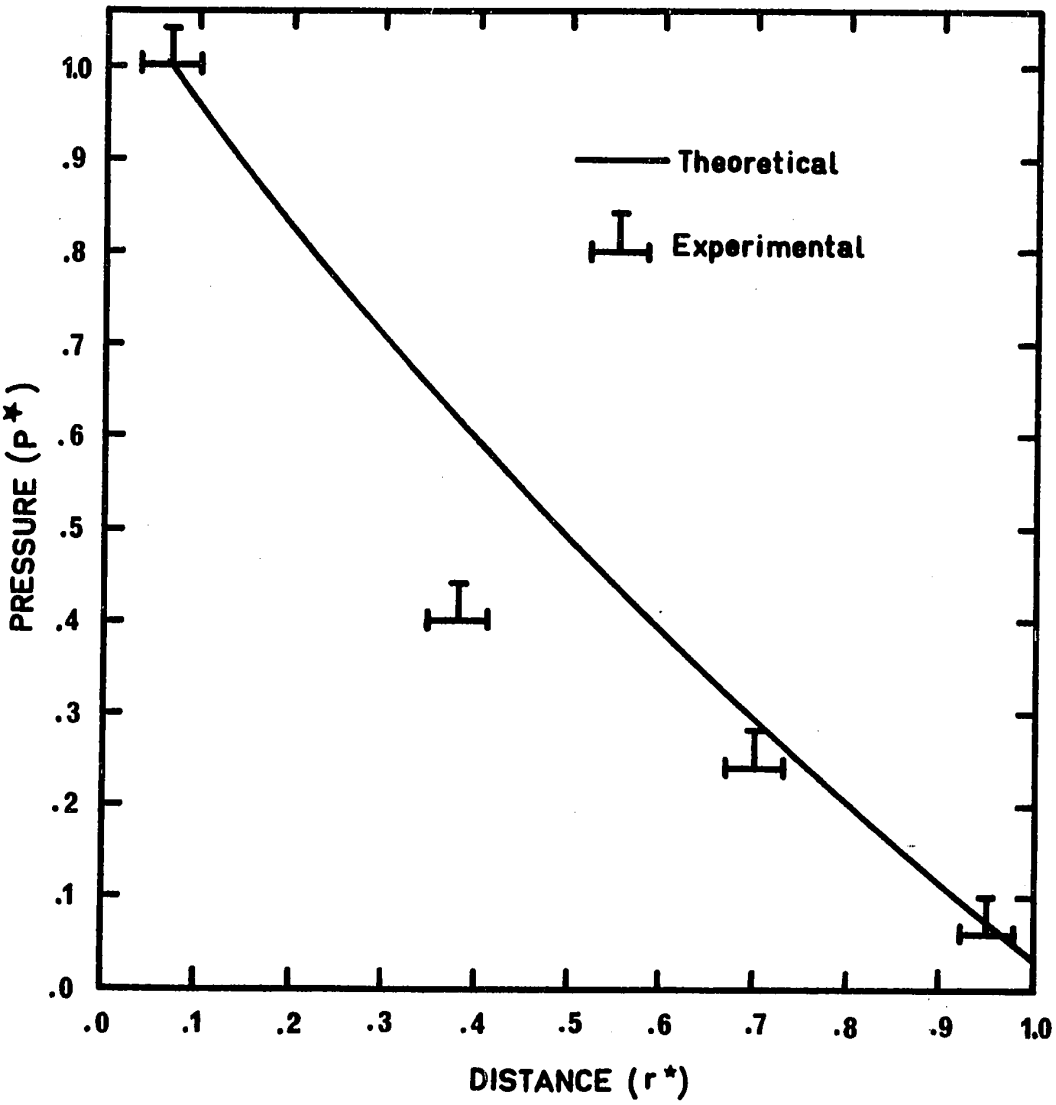

FIGURE 3-47

PRESSURE PROFILE AT THE END OF FILLING
CASE 12

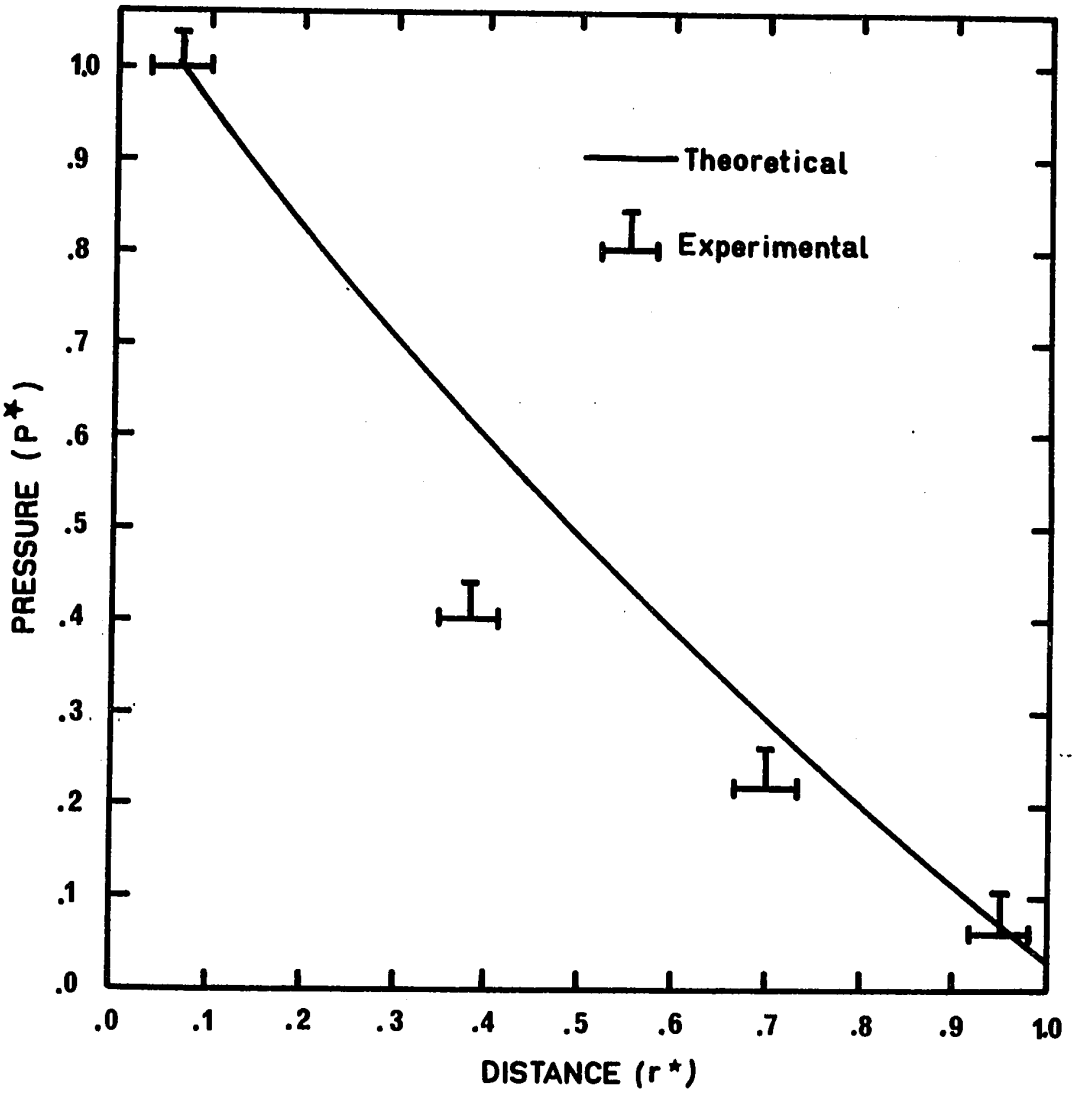

to higher viscosities in the low temperature regions. Temperature effects together with solidification that takes place close to the front, result in a deflection point in the pressure profile. This may be due to the large increase in the pressure drop as the front temperature and the cross section available for flow are decreased. These effects are larger for polystyrene cases due to the large activation energy for viscosity $\Delta E/R_g = 5910\ 1/K^o$ while that of polyethylene is only $2300\ 1/K^o$. A relatively small change in temperature would cause a large change in viscosity in the former case. The calculated pressure profiles for polystyrene exhibit less curvature than the corresponding profiles for polyethylene, due to the lower flow index in polystyrene cases. The effect of the melt flow index may be seen clearly in equation (3-58).

As can be seen from all the cases, the experimental values lie always below the calculated curve, and deviations are larger close to the entrance of the cavity. It is generally agreed that dissipative phenomena occur at the entrance, which may result in lower measured values. As mentioned before, the elimination of the extensional stresses and the non-linear term from the theoretical treatment may contribute to the large differences at small radii.

3.2.7 Short Shot

A partially filled cavity may be obtained at the end of the filling stage if low injection pressure and/or low melt temperature are employed. These conditions result in the solidification of the flowing melt before it reaches the boundary of the cavity.

The theoretical model for the filling stage was successful in predicting a short shot. Two short shots were performed experimentally: one for polyethylene and one for polystyrene.

Figures 3-48 and 3-49 give the calculated filling diagrams for the two cases, respectively. Experimentally, the short shot for polyethylene occurred after 18.5 seconds and the melt reached the radius of 2.5 inches (measured after cooling) while the calculated result gave 13.0 seconds and a radius of 2.1 inches. For polystyrene, the experimental short shot was obtained after 14.2 seconds at a radius of 2.9 inches, while calculations showed a short shot of 2.7 inches at a time of 9.9 seconds. The difference between the experimental and calculated results are reasonable considering the fact that slow filling, above 3 seconds, results in a rippled surface that may change the heat transfer conditions at the interface between the melt and the wall.

Figure 3-50 and 3-51 show the corresponding temperature profiles at the end of the short shot for polyethylene and polystyrene, respectively. As can be seen in Figure 3-50

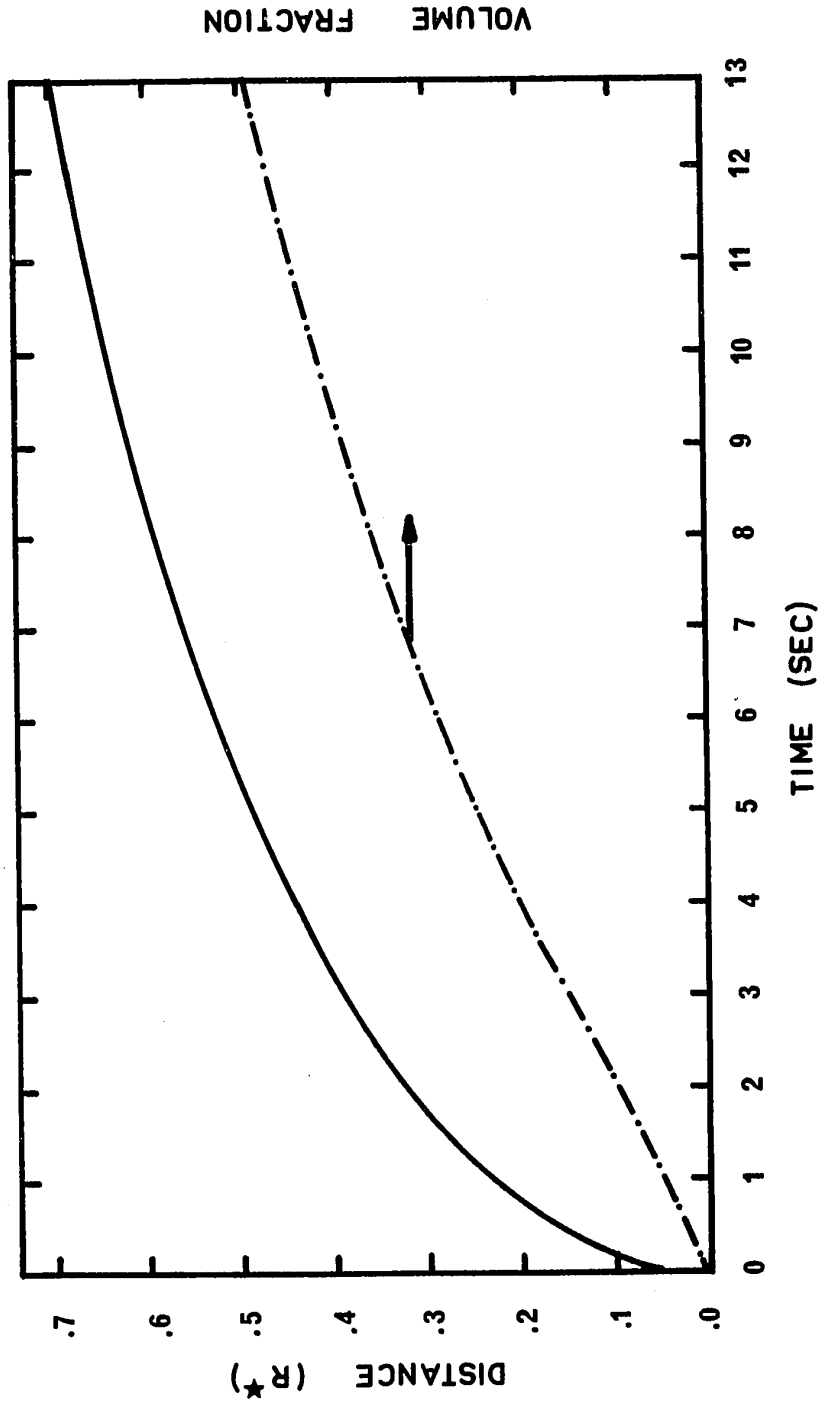

FIGURE 3-48
PROGRESSION OF MELT FRONT-SHORT SHOT
CASE 13

FIGURE 3-49

PROGRESSION OF MELT FRONT-SHORT SHOT
CASE 14

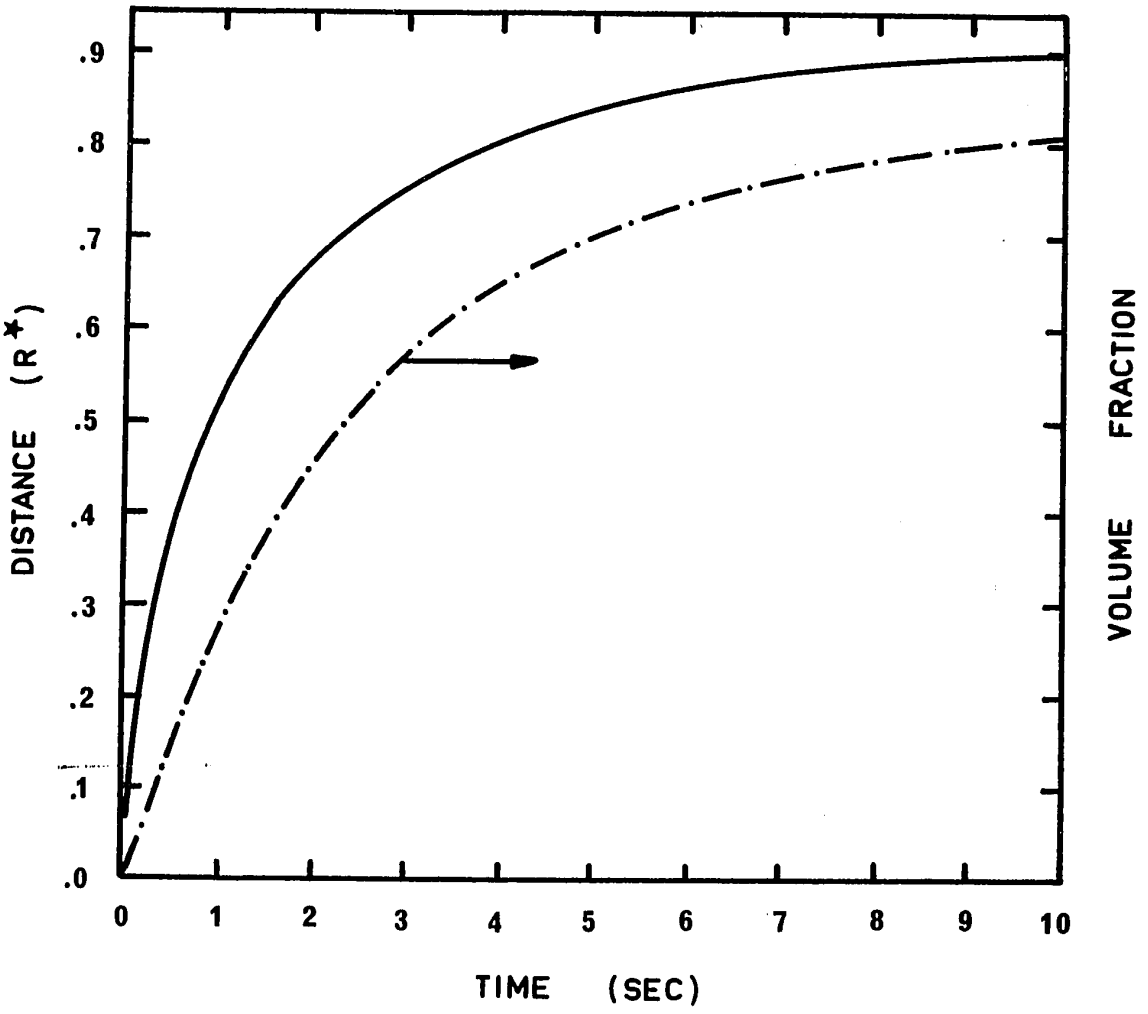

FIGURE 3-50

TEMPERATURE PROFILES AT THE END OF FILLING
CASE 13

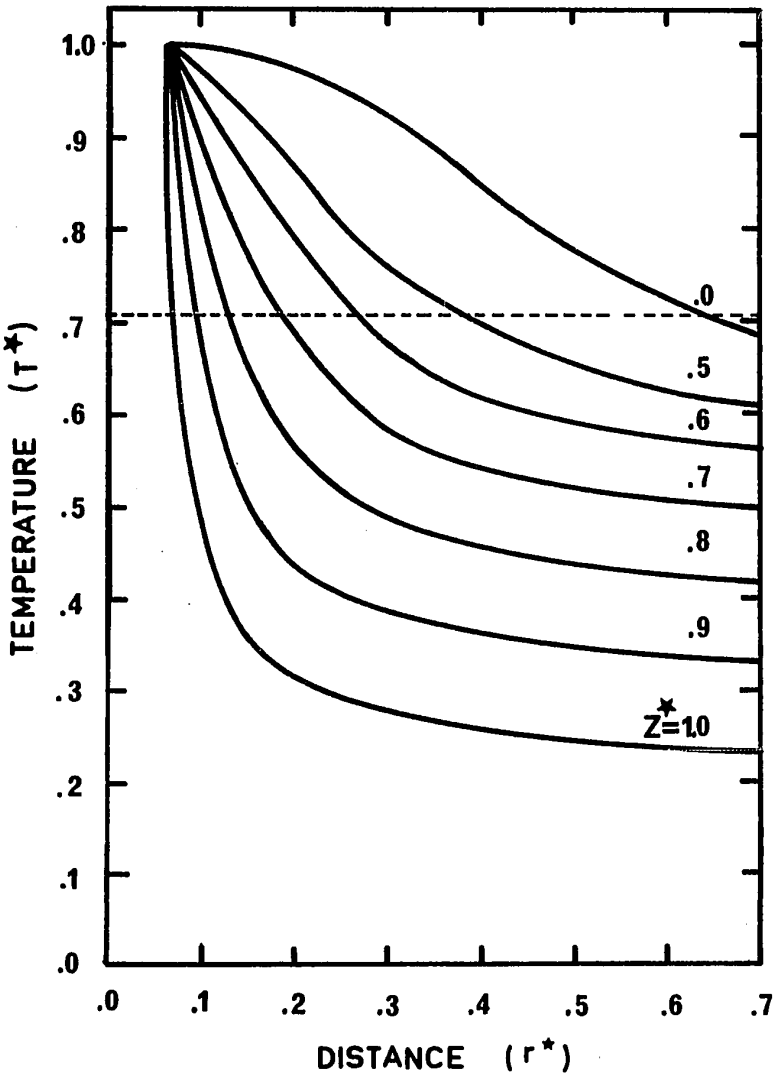

FIGURE 3-51

TEMPERATURE PROFILES AT THE END OF FILLING

CASE 14

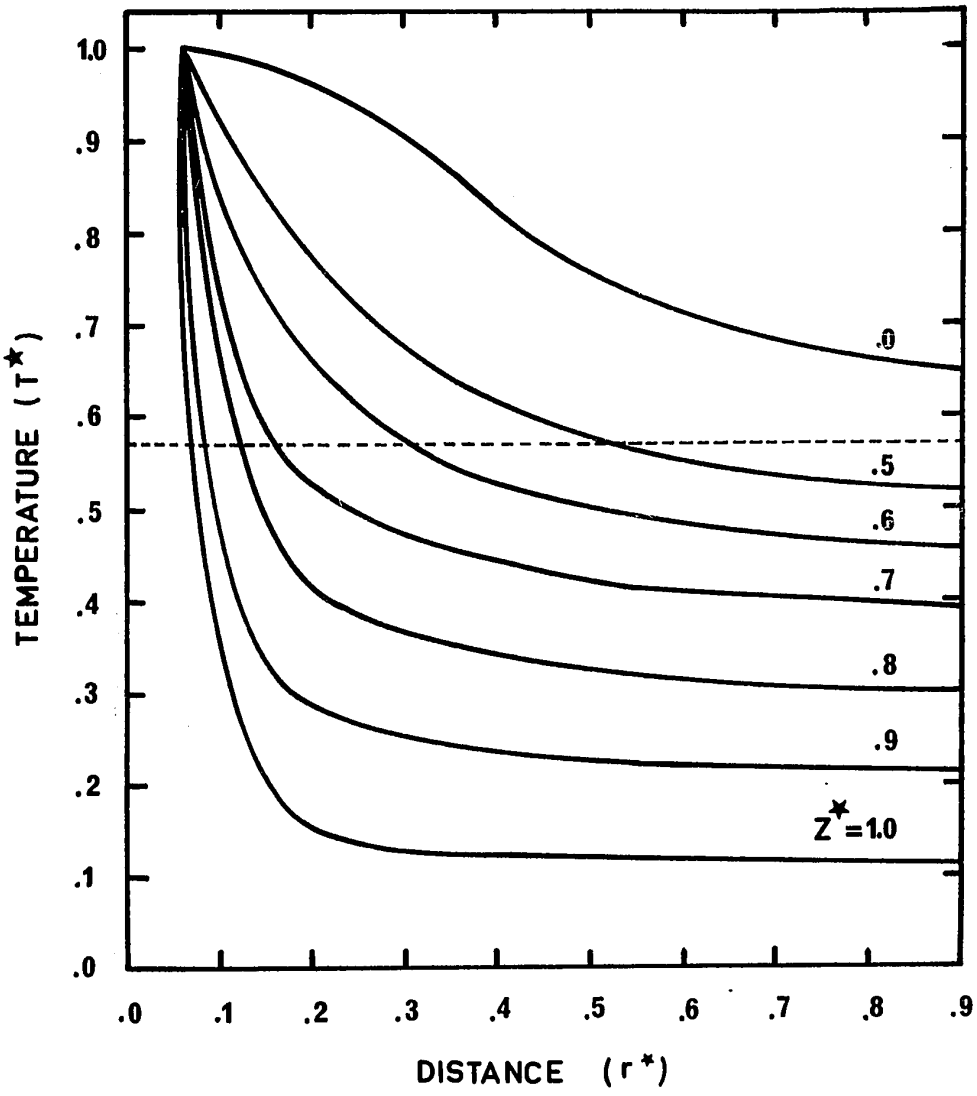

the centerline temperature lies below the freezing temperature of the resin and according to equation (3-13) filling is stopped at this point and a short shot is obtained. For polystyrene, Figure 3-51, the centerline temperature lies above the freezing temperature at the end of the predicted time for a short shot, as distinct from the former polyethylene case. This is due to the large viscosity activation energy for polystyrene. At the predicted time for the short shot the computer showed a very small flow rate that resulted in a very long time for advancement of the front to the next radial increment. This time exceeded half an hour. At this time the temperature would have dropped well below the freezing temperature.

3.2.8 Melt Fracture

As shown in Appendix 1, melt fracture for polystyrene occurred at 180°C at a relatively low shear rate (400 1/sec) in the Instron Capillary Rheometer. Similarly, melt fracture conditions were observed with polystyrene when it was injected to the cavity. Under these conditions, the pressure recorded at the entrance to the cavity showed fluctuations of about 150 psi. The recordings at the other three positions were smoother, but still some fluctuations could be detected. An attempt was made to "smooth" the pressure curve at the entrance and to solve for the filling stage,

but the deviations were large. For example, molding conditions that gave an experimental filling time of 0.7 seconds yielded a theoretical filling time of 2.1 seconds. However, an examination of the molded article did not reveal any irregularities in its appearance. On the other hand, examination of the high speed films produced under melt fracture conditions indicated irregular, interrupted flow at regions close to the entrance of the cavity, these disturbances vanished at larger radii. An attempt was made to develop still pictures from the movies, in order to demonstrate this phenomenon. However, the still pictures did not give a good representation of this effect which could be seen clearly from the continuous movies.

3.2.9 Summary

1. Spreading radial flow takes place in the parallel feed situation of this study.
2. Good agreement is obtained between experimental and theoretical filling times, except for deviations at the beginning of filling due mainly to extensional stresses and entrance effects.
3. Compressible fluid treatment of the melt, results in longer filling times compared with the incompressible treatment.

4. Elimination of latent heat of freezing in the case of crystalline polymers results in longer filling time compared with the solution that includes this effect.
5. Large temperature gradients exist in the cavity at the end of filling.
6. Good agreement is obtained between experimental and calculated pressure profiles, except near the entrance where large deviations are observed, due to the elimination of extensional stresses and entrance effects from the theoretical treatment.
7. The filling model is able to predict a short shot.
8. Melt fracture was observed both photographically and by pressure measurements.

4. PACKING STAGE

4.1 THEORETICAL ANALYSIS

4.1.1 Equations and Boundary Conditions

According to the proposed packing model, the polymer melt flows from the reservoir at the injection end through the nozzle and channel into the mold cavity by virtue of the difference in pressure between the cavity and the reservoir. Since the cavity is filled with polymer, the driving force for flow in the nozzle and channel is assumed to be the difference between the pressure in the reservoir and the average pressure in the cavity, Pa, the latter is defined by:

$$Pa(t) = \frac{1}{\pi R_o^2/2} \times \int_o^{R_o} P(r,t)\pi r dr \quad .....(4\text{-}1)$$

Where r is the radial distance from the entrance of the cavity to the point under consideration, R_o is the radius of the cavity; P is the pressure and t is the time elapsed from the beginning of packing.

At the beginning of the packing stage, the flow rate Q_o is assumed to be equal to that at the end of filling stage as given by the following equation:

$$Q_o = 2 \int_o^h \pi a v_r(a,z,o) dz \quad .....(4\text{-}2)$$

Where a corresponds to the radius of the entrance to the cavity, z is the height of the point under consideration above the mid-plane of the cavity, and h is the half thickness of the cavity. Subsequently, the flow rate Q_t at a given time t, is obtained by assuming that the melt obeys the Power Law. Thus

$$Q_t = Q_o \times \left(\frac{\Delta P_t}{\Delta P_o}\right)^{1/n} \qquad \text{.....(4-3)}$$

Where ΔP_o and ΔP_t are the differences between the pressure in the reservoir and the cavity at time zero and t, respectively, and n is the Power Law exponent for the melt.

Temperature profiles in the cavity are obtained from the heat conduction equations with phase transformation (for crystalline polymers only) neglecting convective heat transfer. It is assumed that heat is conducted only in the z direction since $R_o/h = 48$. However, temperature is different at different radial positions due to differences in temperature profiles at the end of filling stage. The polymer is assumed to have constant but different values for specific heat C_p, thermal conductivity k_t and density ρ, in the solid and melt regions, for purpose of solving the heat conduction equation.

Under the above assumption, heat conduction is described by the following equations:

In the solid region: $$\frac{\partial T_s}{\partial t} = \alpha_s \frac{\partial^2 T}{\partial z^2} \qquad \text{.....(4-4)}$$

In the melt region: $$\frac{\partial T_m}{\partial t} = \alpha_m \frac{\partial^2 T}{\partial z^2} \qquad \text{.....(4-5)}$$

Where s and m refer to solid and melt respectively, α is the thermal diffusivity, and T is the temperature.

Latent heat of freezing is taken into account by solving equations (3-14) and (3-15).

The following boundary conditions are assumed:

a) Temperature gradient at the centre of the cavity is zero:

$$\frac{\partial T}{\partial z}(r,o,t) = 0 \qquad \text{.....(4-6)}$$

b) Temperature at the mold surface is held at a constant value T_o, and a constant effective heat transfer coefficient, H, is assumed between the melt and the wall cavity:

$$k_t\left(\frac{\partial T}{\partial z}\right)_{z=\pm h} = H\,[T_o - T(r,\pm h,t)] \qquad \text{.....(4-7)}$$

The average temperature in the cavity, T_a, is defined as follows:

$$T_a(t) = \frac{2}{\pi R_o^2 \cdot h} \times \int_o^h \int_o^{R_o} T(r,z,t)\pi r\, dr dz \qquad \text{..(4-8)}$$

An average density ρ_a is calculated from the volume of the cavity and the mass of the polymer at each moment:

$$\rho_a = \rho_o + \frac{\int_0^t Q_t \times \rho_e (T_1, P_m) dt}{\pi R_o^2 h} \quad \ldots\ldots(4\text{-}9)$$

Where ρ_o is the initial density in the cavity at the beginning of packing stage, $\rho_e(T_1,P_m)$ is the density of the melt at the temperature and pressure prevailing before the melt enters the cavity.

The relation between the average pressure P_a, the average temperature T_a and the average density ρ_a is given by an equation of state, the same as equation (3-20). As a matter of fact, a P-V-T diagram was used instead, as in the filling stage (27,30).

4.1.2 Dimensional Analysis

For the sake of generality, a dimensional analysis is carried out. The following dimensionless variables are defined, the same as in the filling stage:

$$r^* = r/R_o \qquad P^* = P/P_f$$

$$z^* = z/h \qquad T^* = \frac{T - T_o}{T_1 - T_o}$$

$$t^* = \frac{t \cdot V_e}{h} \qquad Ar = h/R_o$$

$$V_e = \left(\frac{P_f}{\rho_m}\right)^{1/2} \qquad \rho^* = \rho/\rho_o$$

Where R_o is the radius of the cavity, h is half thickness of the cavity, P and T are the pressure and temperature of the melt, respectively. P_f is the injection pressure at the entrance to the cavity at the end of filling, ρ_m is a reference density, T_o and T_1 are the wall temperature and initial melt temperature, respectively.

Equations 4-1 to 4-9 take the following forms by introducing the above definitions:

$$P_a^*(t^*) = 2\int_0^1 P^*(r^*,t^*)\,r^*dr^* \qquad .....(4\text{-}10)$$

$$Q_o^* = 2\int_0^1 \pi a^* V^*(a^*,z^*,o)\,dz^* \qquad .....(4\text{-}11)$$

$$Q_t^* = Q_o^*\left(\frac{\Delta P_t^*}{\Delta P_o^*}\right)^{1/n} \qquad .....(4\text{-}12)$$

$$\frac{\partial T_s^*}{\partial t^*} = \frac{\alpha_s}{V_e \cdot h}\,\frac{\partial^2 T_s}{\partial z^{*2}} \qquad .....(4\text{-}13)$$

$$\frac{\partial T_m^*}{\partial t^*} = \frac{\alpha_m}{V_e \cdot h}\,\frac{\partial^2 T_m^*}{\partial z^{*2}} \qquad .....(4\text{-}14)$$

$$\frac{\partial T^*}{\partial z^*}(r^*,o,t^*) = 0 \qquad \text{.....(4-15)}$$

$$\left(\frac{\partial T^*}{\partial z^*}\right)_{z^*=\pm 1} = \frac{H \cdot h}{k_t}\left[- T^*(r^*,\pm 1,t^*)\right] \qquad \text{...(4-16)}$$

$$T_a^*(t^*) = 2\int_o^1\int_o^1 T^*(r^*,z^*,t^*)\,r^*dr^*dz^* \qquad \text{..(4-17)}$$

$$\rho_a^* = 1 + \frac{h}{\pi R_o}\int_o^{t^*} Q_t^*\,\rho_e^*\,dt^* \qquad \text{.....(4-18)}$$

Equations (3-14) and (3-15) take the following dimensionless form:

$$\left(\frac{\partial T_s^*}{\partial z^*}\right)_{z^*=\varepsilon} - \frac{k_m}{k_s}\left(\frac{\partial T_m^*}{\partial z^*}\right)_{z^*=\varepsilon} = \frac{\rho_s \cdot L \cdot V_e \cdot h}{k_s(T_1 - T_o)}\,\frac{d\varepsilon^*}{dt^*} \qquad \text{(4-19)}$$

$$T_s^* = T_m^* = T_F^* \quad \text{at} \quad z^* = \varepsilon^* \qquad \text{(4-20)}$$

And the equation of state (3-20):

$$P_a^* = \frac{T_a^*\,R_c(T_1 - T_o)}{\left(\frac{1}{\rho_a^* \cdot \rho_o} - b\right)} + \frac{R_c\,T_o}{P_f\left(\frac{1}{\rho_a^* \cdot \rho_o} - b\right)} - \frac{\omega}{P_f} \qquad \text{(4-21)}$$

4.1.3 Difference Equations

The set of equations (4-1)-(4-9) together with the latent heat equations (3-14) and (3-15) and an equation of state (3-20) are solved simultaneously by numerical techniques. The standard finite different representation is used.

By fixing the number of radial and axial increments to equal the numbers used in the filling state (I-1) and (J-1) respectively, a radial increment, Δr, and an axial increment, Δz, are defined. The difference equations are given in dimensional variables; however some results are also presented, later, in dimensionless form, using the above definitions in section 4.1.2.

All integrals appearing in equation (4-1), (4-2), (4-8) and (4-9) are solved by using the "Extended Trapazoidal Rule" (40).

The heat conduction equations are solved by using Saul'yev's explicit method, thus equations (4-4) and (4-5) are reduced to the following forms:

$$T_s(i,j,k+1) = T_s(i,j,k) \times \frac{1 - B_1}{1 + B_1} + [T_s(i,j-1,k+1) + T_s(i,j+1,k)] \times \frac{B_1}{1 + B_1} \qquad (4\text{-}22)$$

where $B_1 = \dfrac{\alpha_s \cdot \Delta t}{\Delta z^2}$

$$T_m(i,j,k+1) = T_m(i,j,k) \times \frac{1 - B_2}{1 + B_2} + [T_m(i,j-1,k+1) + T_m(i,j+1,k)] \times \frac{B_2}{1 + B_2} \qquad (4\text{-}23)$$

where $B_2 = \dfrac{\alpha_m \cdot \Delta t}{\Delta z^2}$

The finite difference form of equations (4-6) and (4-7) is:

$$T(i,1,k) = T(i,2,k) \qquad (4\text{-}24)$$

and

$$T_{(i,1)} = \frac{T_o \cdot A_1}{1 + A_1} + \frac{T_{i,2}}{1 + A_1} \qquad (4\text{-}25)$$

where $A_1 = \dfrac{H \cdot \Delta z}{k}$

Equations (3-14) and (3-15) are solved in the same modified conventional method, as outlined in Appendix 5.

4.1.4 Stability, Convergence and Uniqueness

The finite difference equations (4-22) and (4-23) and the numerical solution to equations (3-14) and (3-15) need to be evaluated with regard to stability, convergence and uniqueness. As in the filling stage, one seeks the available analytical solution to the closest physical problem. No analytical solutions are available for the case of unsteady heat conduction with phase transformation in confined spaces

like a slab, cylinder or sphere. The uniqueness of the numerical treatment of equations (3-14) and (3-15) has been tested in the case of a stationary cooling melt in a long cylinder, see reference (24).

In order to complete the test for stability, convergence and uniqueness of equations (4-22) and (4-23), an analytical solution (49) was compared for the numerical solution for the following problem: An infinite long slab at initial temperature T_I is subjected to a step change in temperature T_o, at time zero. The temperature profiles as function of time and axial position are compared for the analytical and numerical cases, see Figure 4-1. Different values for B_I were chosen 0.1, 0.5 and 0.7, but results are given only for $B_I = 0.1$. These results demonstrate that both convergence and uniqueness were achieved.

No additional problems would arise from the other integrals and algebraic equations which describe the packing stage. However, due to the high values of flow rate, especially at the beginning of packing, it was necessary to select a time increment smaller than that associated with convergence requirements for the heat conduction equations. A time increment of 0.005 sec gave the best convergence properties.

FIGURE 4-1

COMPARISON BETWEEN ANALYTICAL AND NUMERICAL SOLUTIONS TO HEAT CONDUCTION IN A SLAB

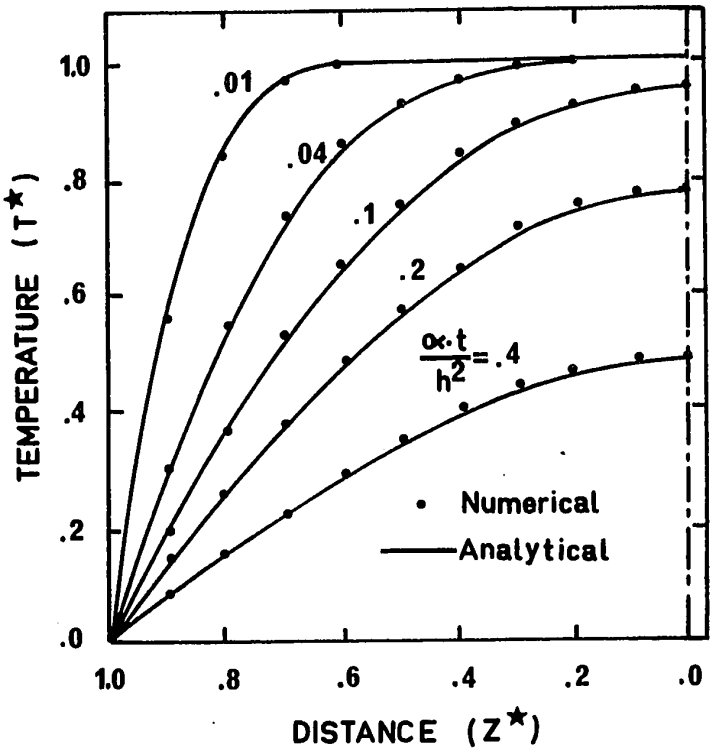

4.1.5 Numerical Procedure

A computer simulation of the packing stage was set up as outlined in Figure 4-2.

At the beginning of the packing stage, temperature and pressure profiles are the same as those prevailing at the end of the filling stage. Average temperature and pressure values are calculated by equations (4-8) and (4-1) respectively. The initial average density is calculated from the equation of state (3-20) by utilizing the initial average temperature and pressure in the cavity. In subsequent steps the average density is calculated from equation (4-9) and the average temperature (4-8) obtained from the temperature profile calculated from equations (4-4)-(4-7) and the numerical solution to equations (3-14) and (3-15). The average temperature and average density are employed in the equation of state (3-20) to yield the average pressure P_a. The latter is used in equation (4-3) to calculate the new flow rate. This cycle is repeated till the packing stage is terminated. Termination of the packing stage occurs when the new calculated pressure or density is equal to or smaller than the previous calculated pressure or density. The detailed computer program for the packing stage is given in Appendix 4 section 9.4.

FIGURE 4-2

COMPUTER FLOW DIAGRAM- PACKING STAGE

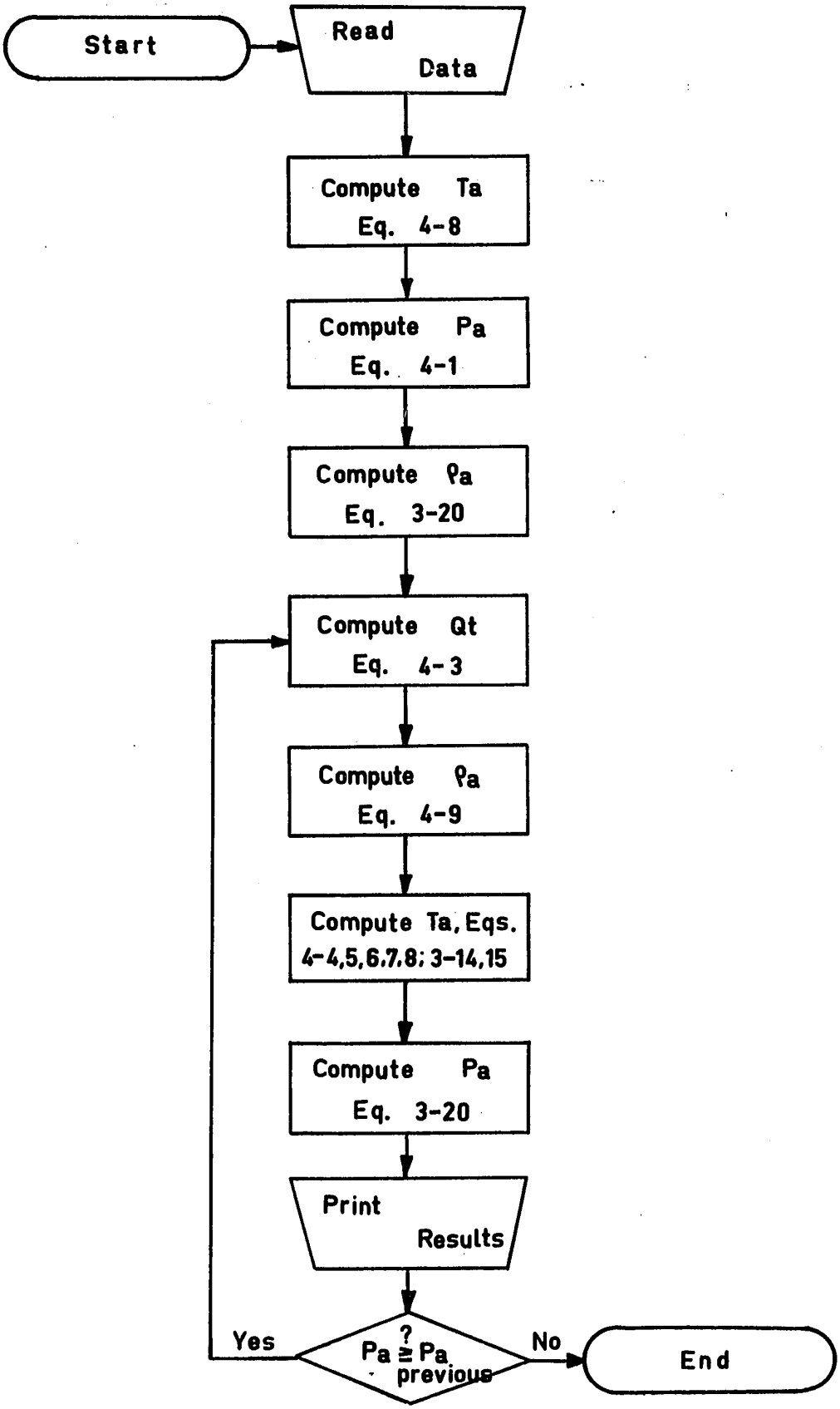

4.2 RESULTS AND DISCUSSION

Following the proposed model and numerical procedure for the packing stage, average pressures, flow rates and temperature profiles were calculated for the twelve cases discussed in the filling stage.

The maximum pressure that could be obtained at the end of the packing stage was limited, and depended on the maximum clamping force obtained from the twelve screws that held the two halves of the mold and the flow properties of the polymer. Pressures above 3500 psi and 5000 psi would cause flash to occur for polyethylene and polystyrene, respectively, in the temperature range used. Thus, the shot size and the holding pressure control valves were adjusted in order not to exceed these limits.

4.2.1 General

Since the pressure transducer was placed only in the cavity, it was not possible to obtain a dependable experimental value for the pressure at the injection end before the melt entered the channel. This pressure had to be at least equal to the pressure measured at the end of packing and possibly higher. In order to overcome this difficulty, a few alternative values were tested in the computational scheme. It was found that the best fit to the experimental curves could be obtained, when this pressure was taken to be 300 psi above

the maximum average cavity pressure recorded for polyethylene and 1100 psi above the maximum average pressure recorded for polystyrene. The maximum average pressure was obtained by averaging the maximum values recorded for the pressure at the four transducer locations. The extra pressure might be due to cooling of the melt and pressure loss as a result of the flow which takes place in the channel. The difference in the additional pressure needed for polyethylene and polystyrene, might be due to the difference between the viscosity activation energy for these two resins and the higher viscosities realized in the case of polystyrene (see Appendix 1).

The average initial density calculated from the average temperature and average pressure in the cavity at the end of the filling stage was compared with the average density calculated from the flow rates, filling time and volume of the cavity, as expressed in the following equation:

$$\rho_o = \frac{\int_0^t \rho_e (T_1, P_o(t)) \times Q_t \times dt}{\pi R_o^2 \times h} \qquad (4\text{-}26)$$

The average difference between values calculated from the P-V-T relation and equation (4-26) was less than 2%. In the above equation, t refers to the filling time.

4.2.2 Packing Profiles

Experimental and theoretical packing curves are given in Figures 4-3 to 4-10 for polyethylene for cases 1-8, respectively, and Figures 4-11 to 4-14 for polystyrene for cases 9-12, respectively. In general, good agreement is obtained between the experimental results and the predicted average values. At the initial stages of packing, the predicted rates of pressure buildup in the cavity are somewhat higher than the average experimental results. This may be due to the initial flow rate which has been employed in the computations. In most cases, the calculated initial flow rates are higher than the experimental ones, as can be seen from the slope of the distance-time curves at the end of filling, Figures 3-7 to 3-18.

It can be observed, in all cases for both polyethylene and polystyrene, that the rate of pressure rise and the maximum in pressure vary from one measuring position to another in the cavity. For polyethylene, the difference at the end of packing between the maximum and the minimum values measured is about 500 psi (for the same shot size), while for polystyrene the difference is about 1600 psi. These differences may be due to elastic and wave propagation effects in addition to back flow which may occur as a result of flow of the melt into the closed filled cavity, and density differences in the radial direction due to the temperature profiles realized.

FIGURE 4-3

PACKING CURVES

CASE 1

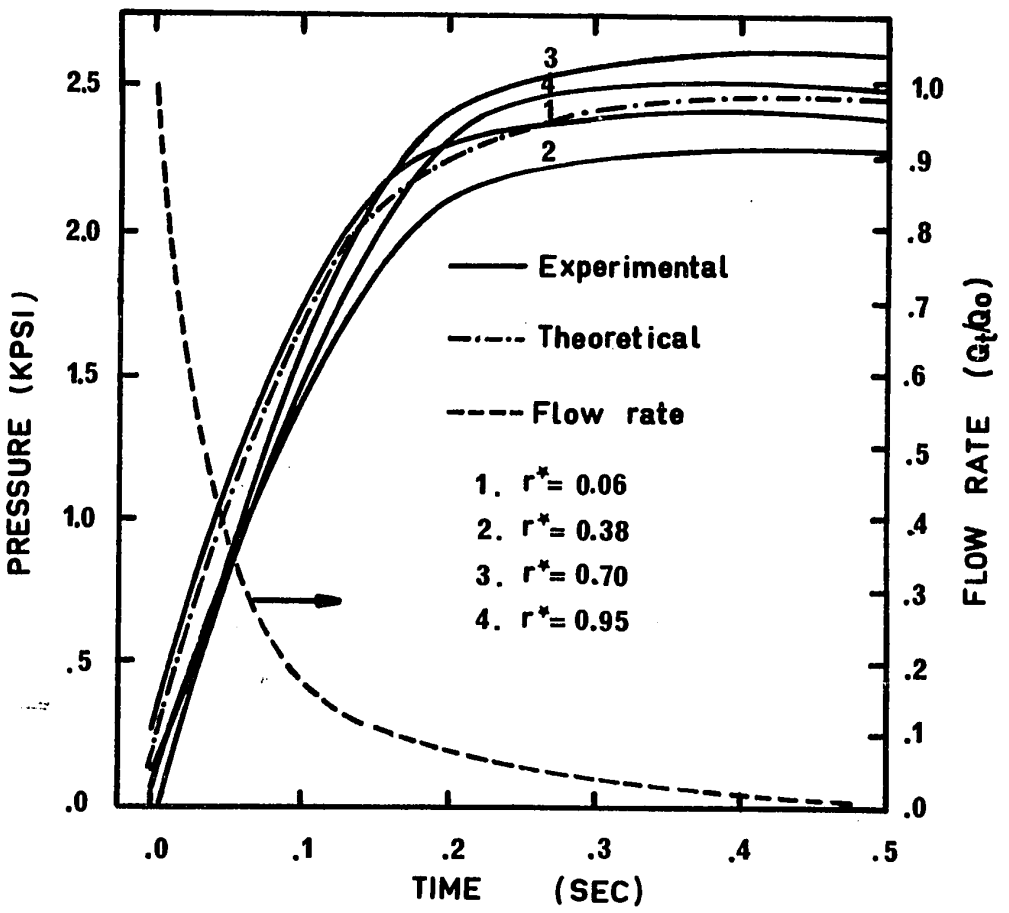

FIGURE 4-4

PACKING CURVES
CASE 2

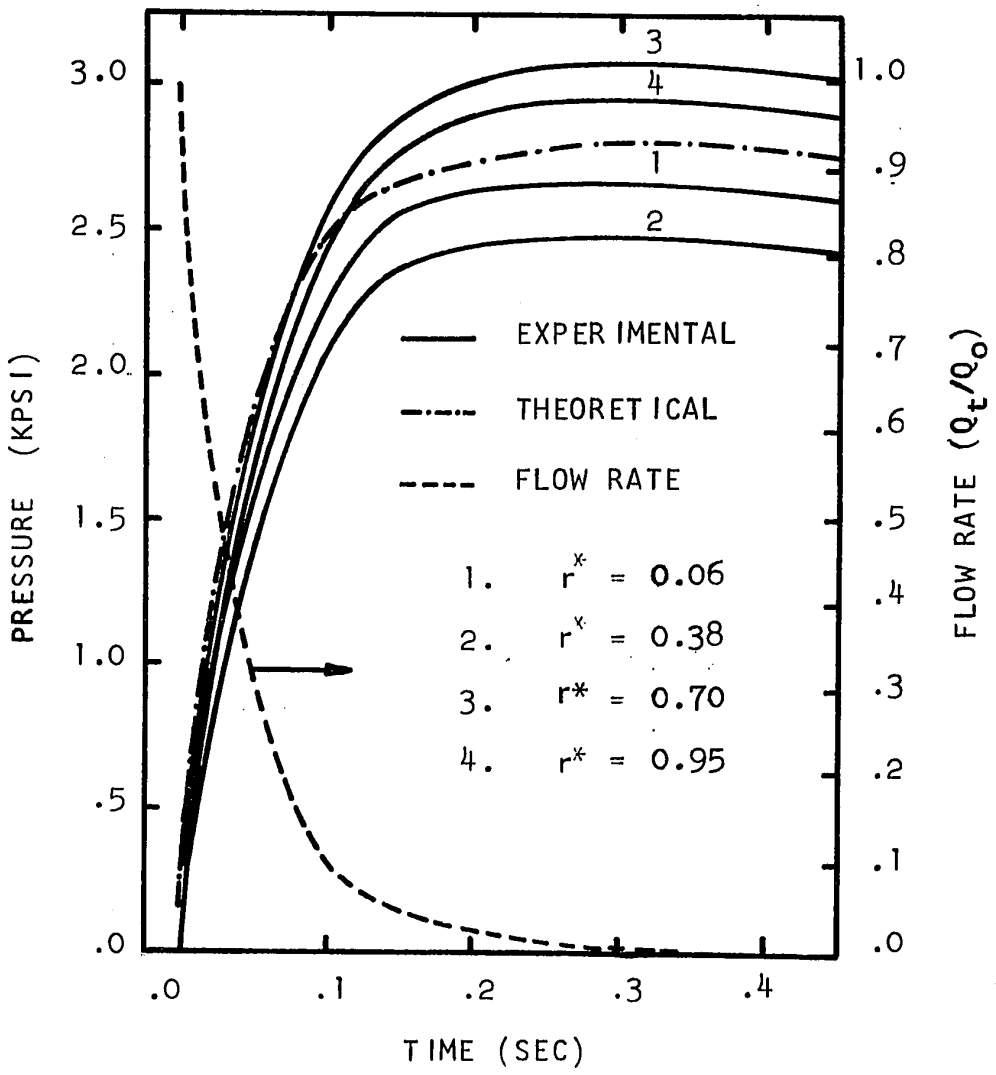

FIGURE 4-5

PACKING CURVES
CASE 3

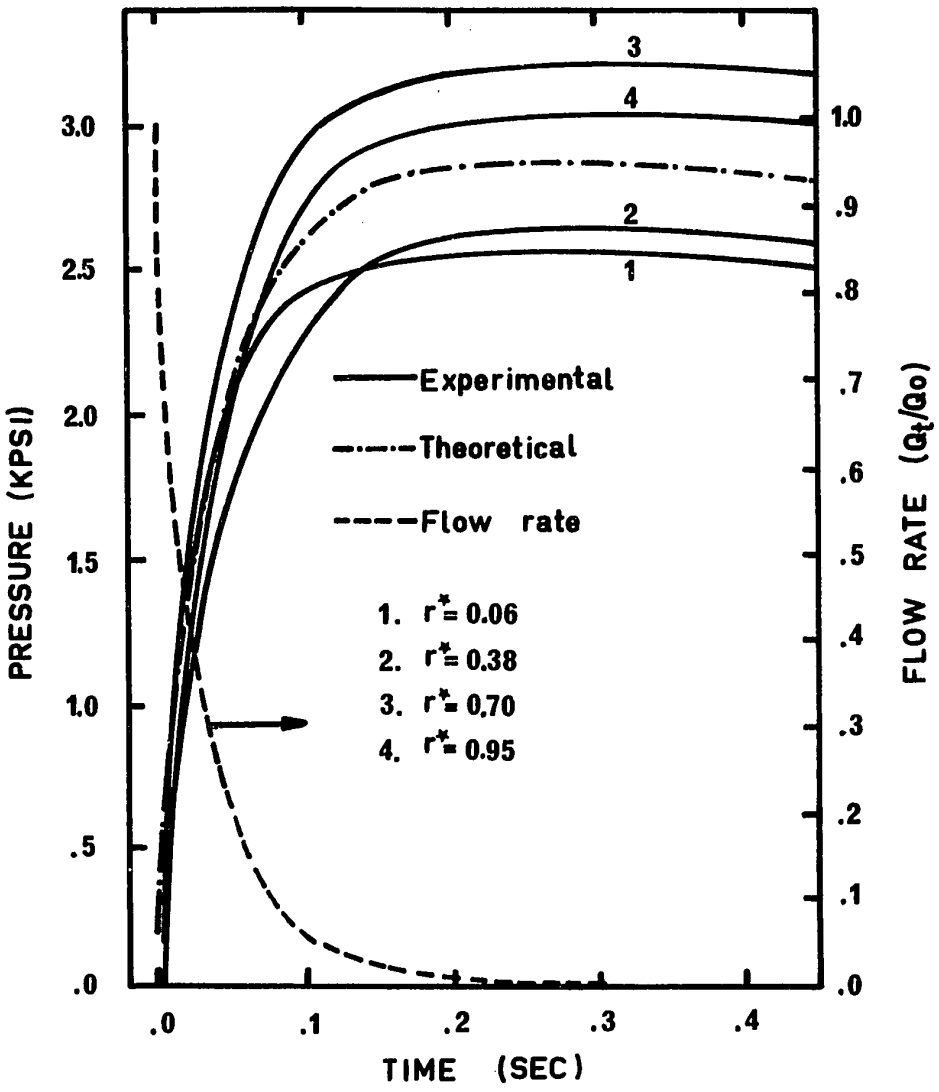

FIGURE 4-6

PACKING CURVES

CASE 4

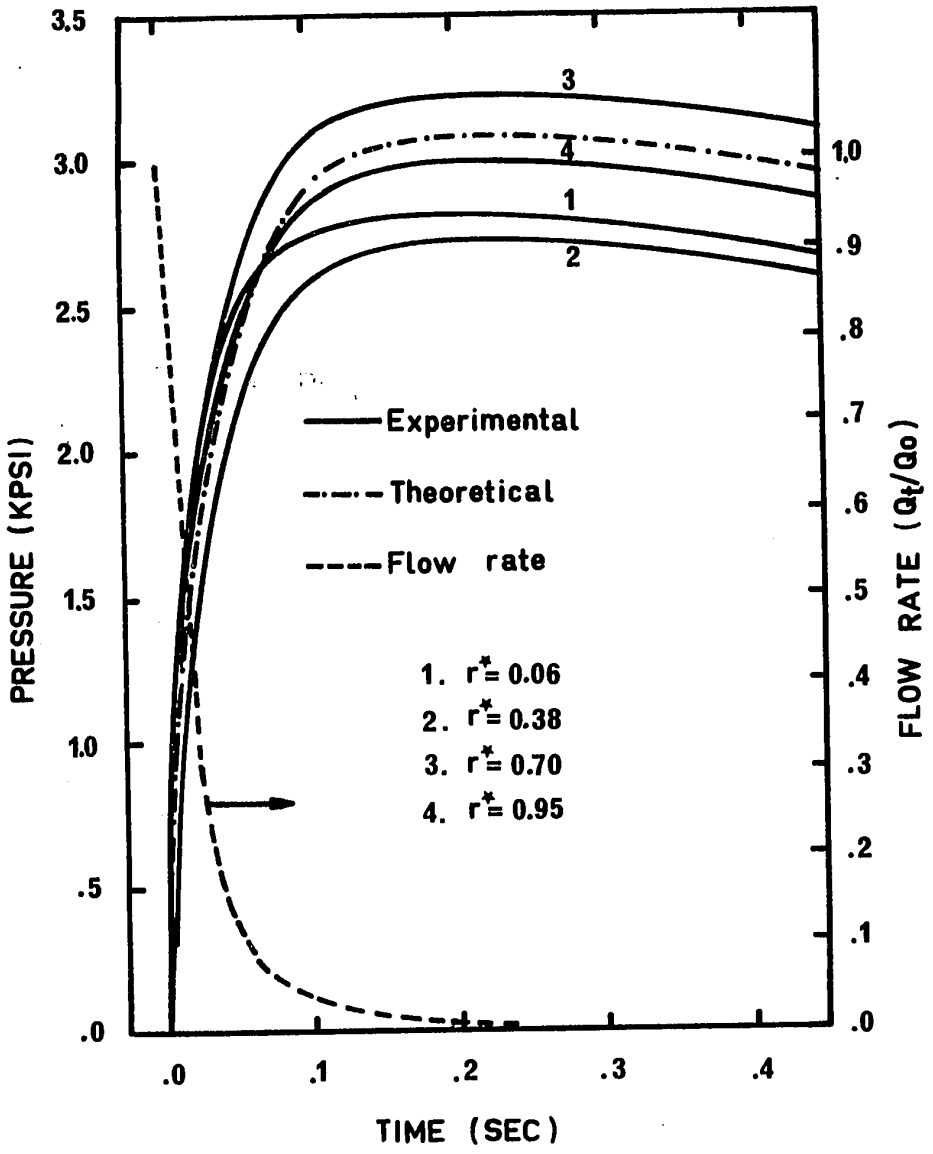

FIGURE 4-7

PACKING CURVES
CASE 5

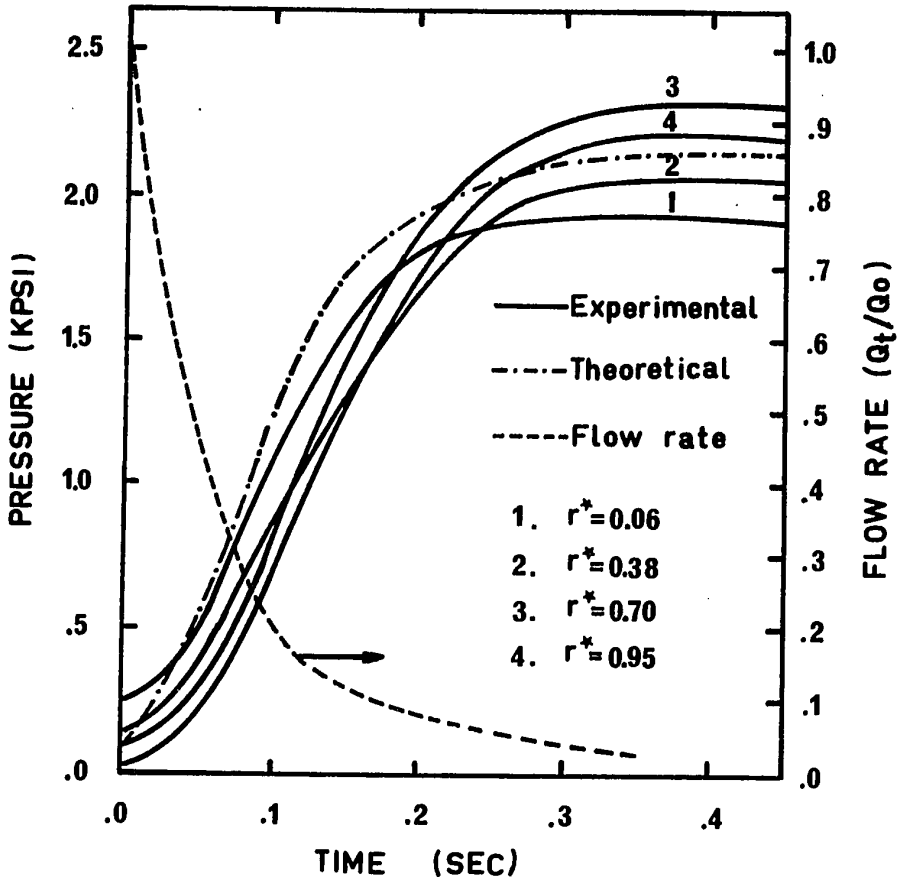

FIGURE 4-8

PACKING CURVES
CASE 6

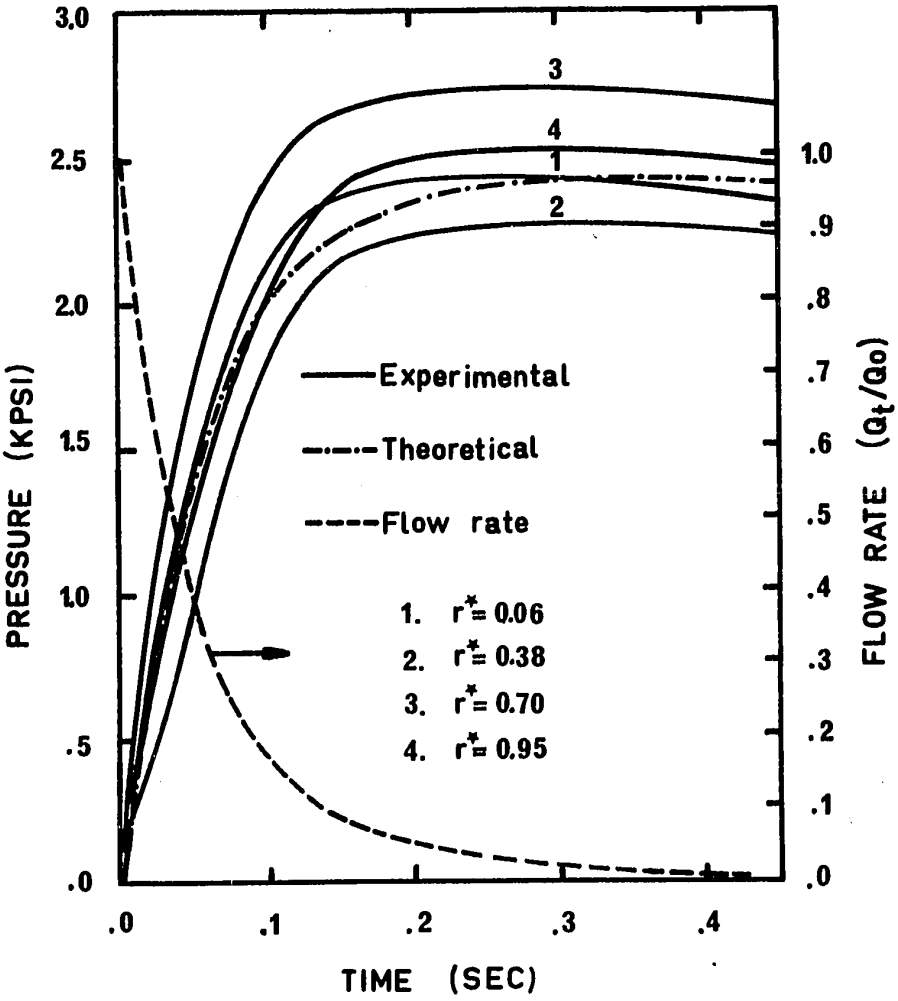

FIGURE 4-9

PACKING CURVES

CASE 7

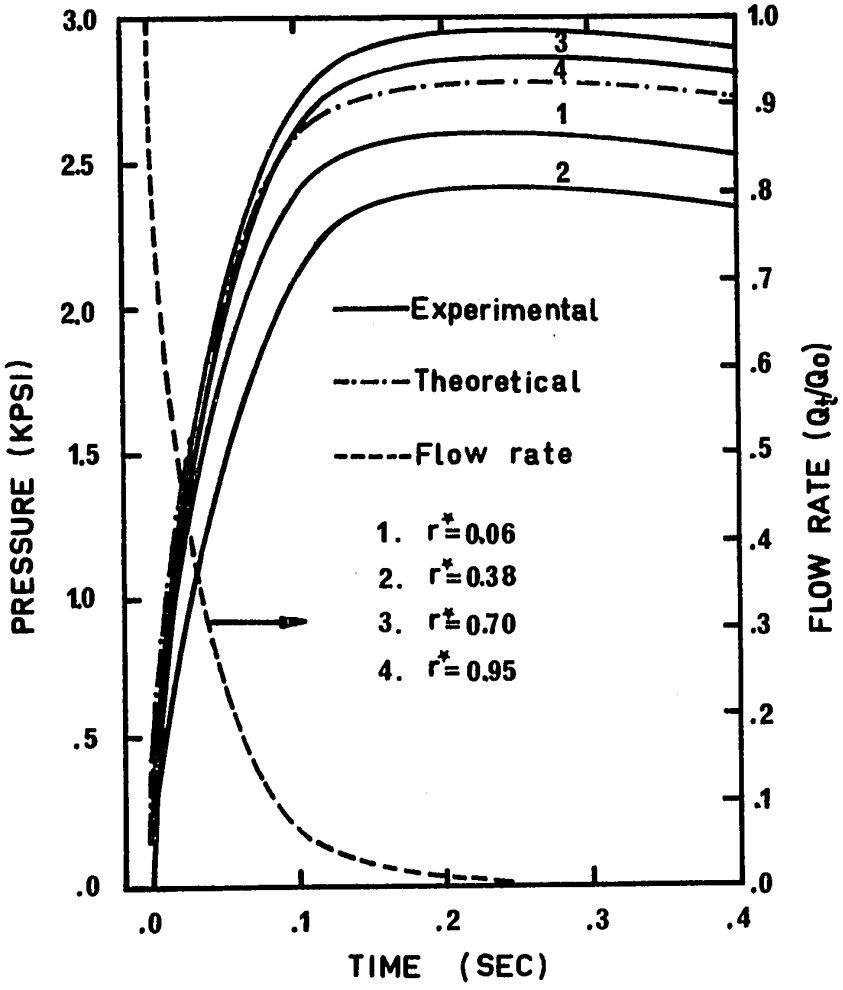

FIGURE 4-10

PACKING CURVES
CASE 8

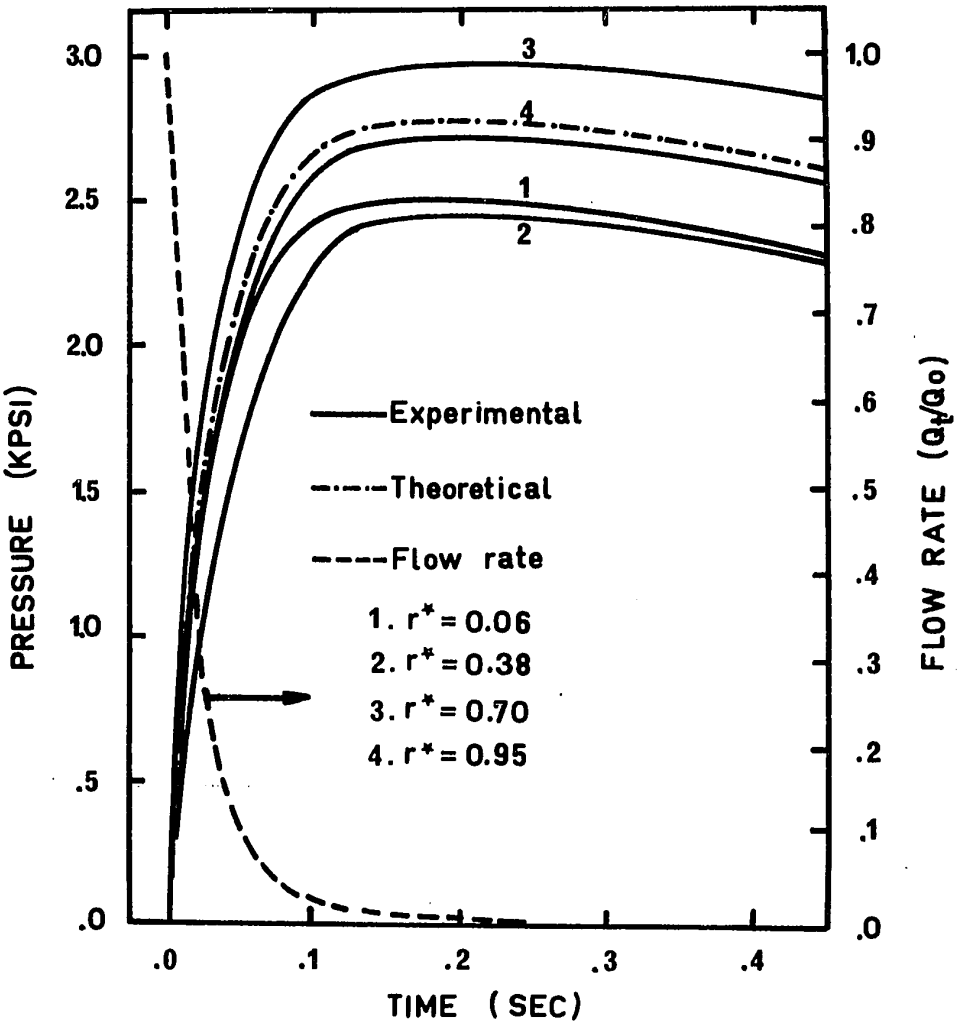

FIGURE 4-11

PACKING CURVES

CASE 9

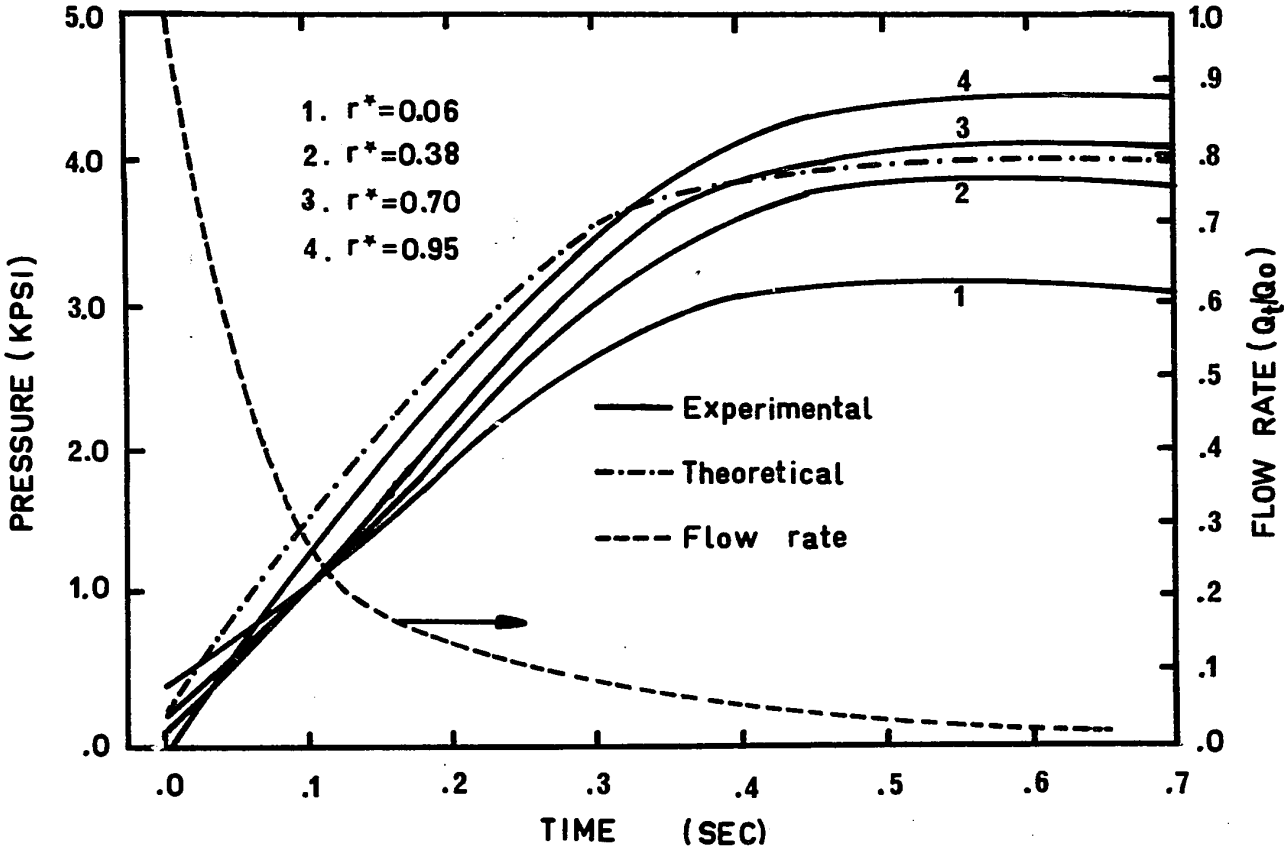

FIGURE 4-12

PACKING CURVES

CASE 10

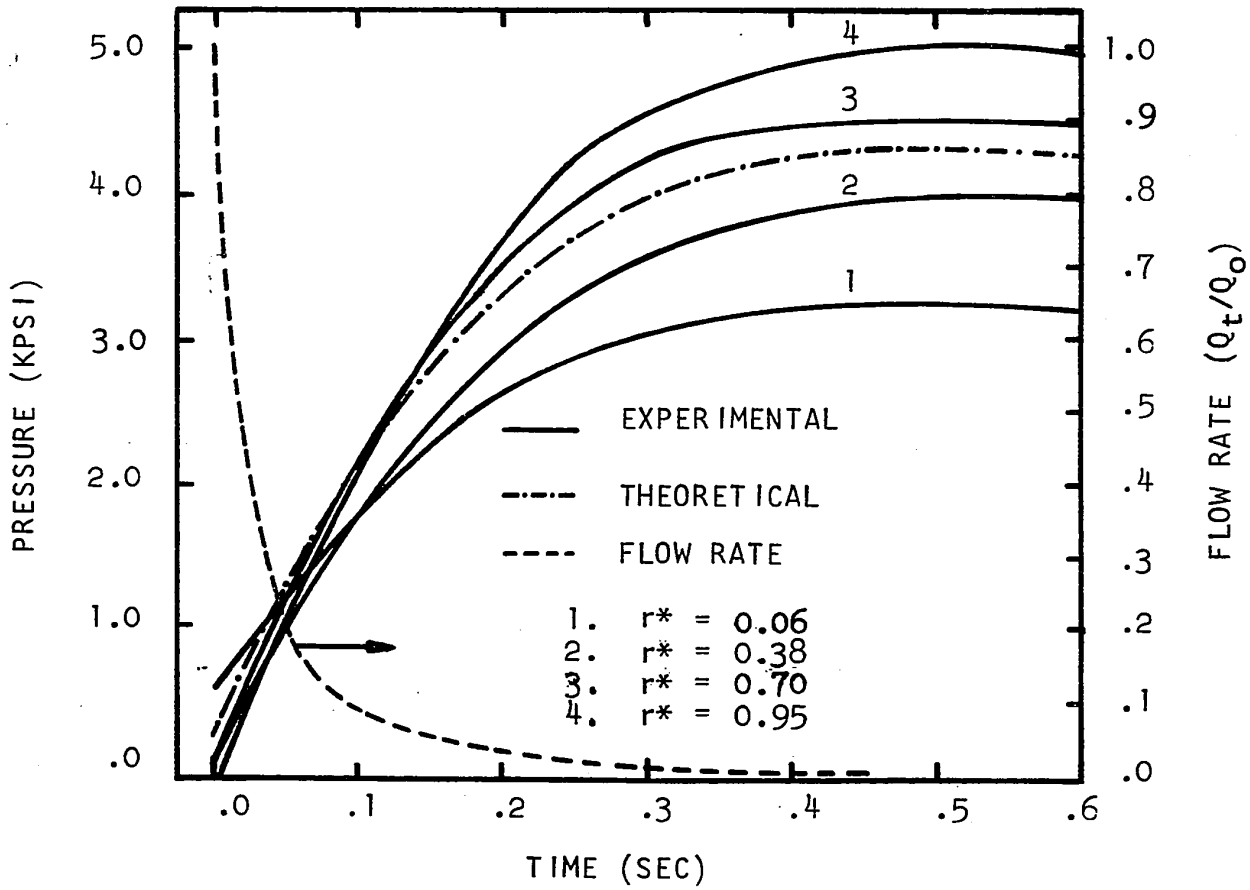

FIGURE 4-13

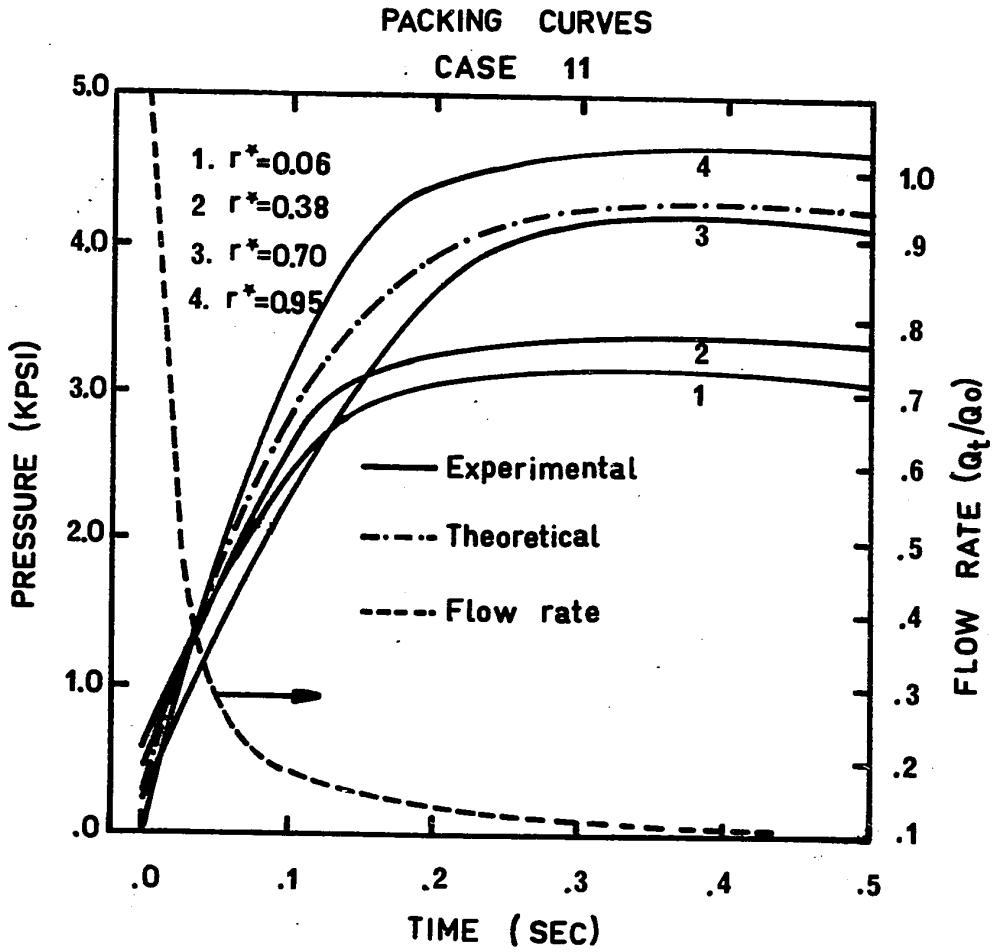
PACKING CURVES
CASE 11
1. r*=0.06
2 r*=0.38
3. r*=0.70
4. r*=0.95
Experimental
Theoretical
Flow rate
PRESSURE (KPSI)
FLOW RATE (Qt/Qo)
TIME (SEC)
5.0
4.0
3.0
2.0
1.0
.0
1.0
.9
.8
.7
.6
.5
.4
.3
.2
.1
.0
.1
.2
.3
.4
.5

FIGURE 4-14

PACKING CURVES

CASE 12

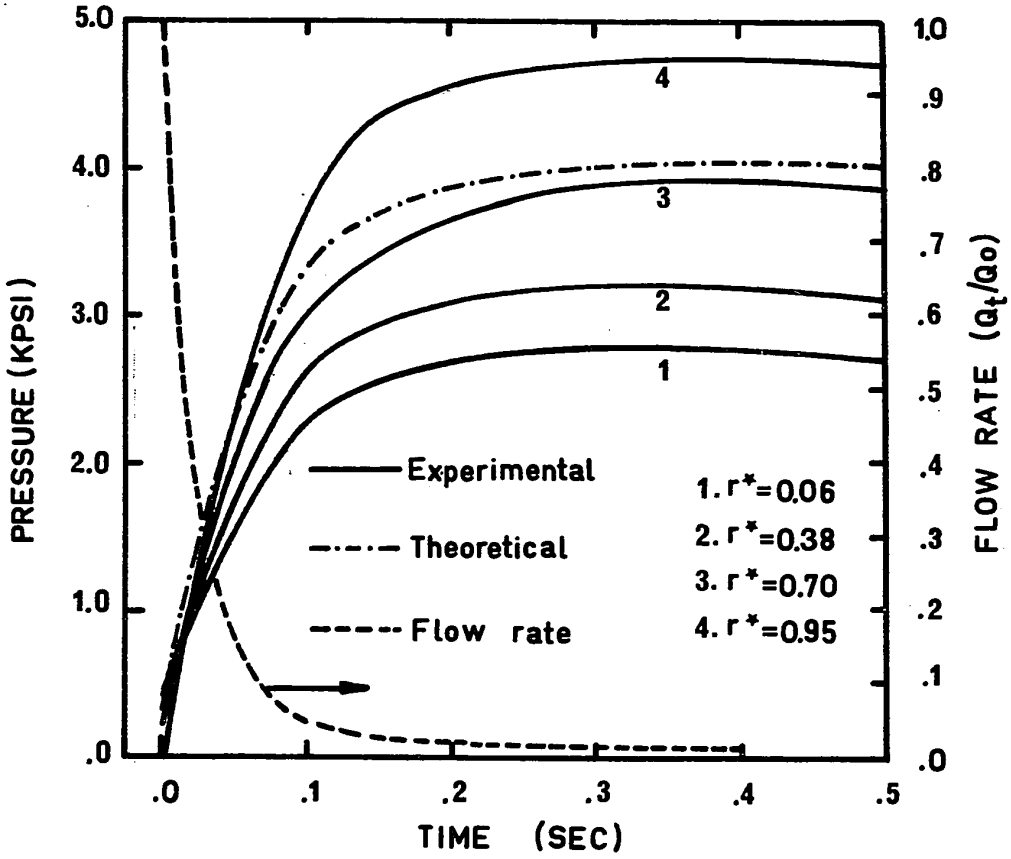

An attempt has been made to increase the shot size, for polyethylene, and thus obtain different packing curves for the same filling conditions. Figures 4-15 and 4-16 show results for cases 2 and 6, respectively. As the shot size increased, the difference between the measured minimum and maximum values increased to 900 psi from the former value of 500 psi. In addition by comparing Figures 4-4 and 4-8 to Figures 4-15 and 4-16, respectively, it is seen that the location of the maximum pressure in the cavity varies for the different shot sizes. As the shot size is increased, the location of the maximum pressure in the cavity moves from the third transducer position ($r^* = 0.70$) to the fourth transducer position ($r^* = 0.95$). Furthermore, the pressure profile in the cavity appears to depend on the shot size. These effects may be the result of combined backflow and elastic phenomena which tend to be more important as the shot size is increased. The four cases reported for polystyrene show that the pressure at the end of packing, increases from a minimum at the first position to a maximum at the fourth position. The pressure gradient which is established in the cavity indicates a situation in which back flow prevails.

Comparing Figures 4-4 and 4-8 to Figures 4-15 and 4-16 respectively, shows that a longer packing period is needed as the shot size is increased for the same filling time. This is confirmed both by the experimental and theoretical results.

FIGURE 4-15

PACKING CURVES
CASE 2

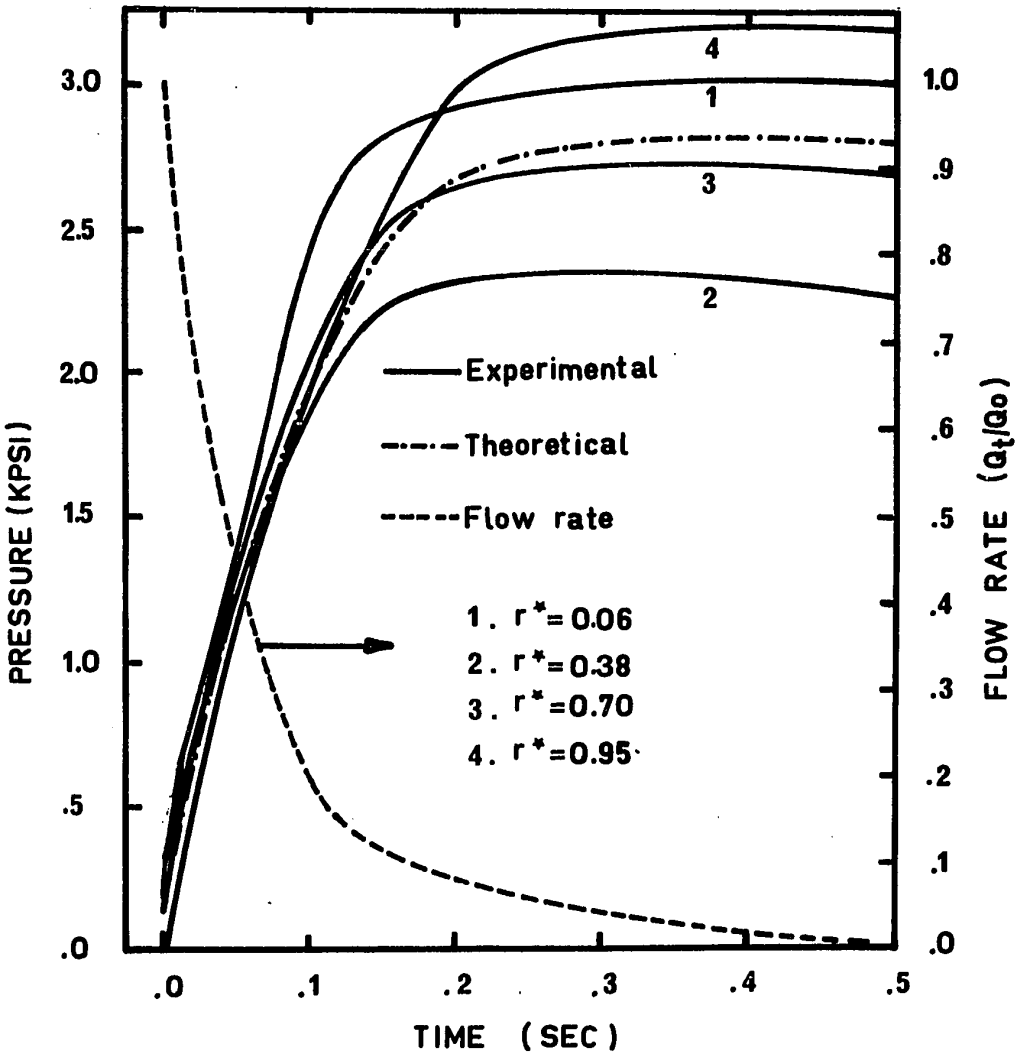

FIGURE 4-16

PACKING CURVES

CASE 6

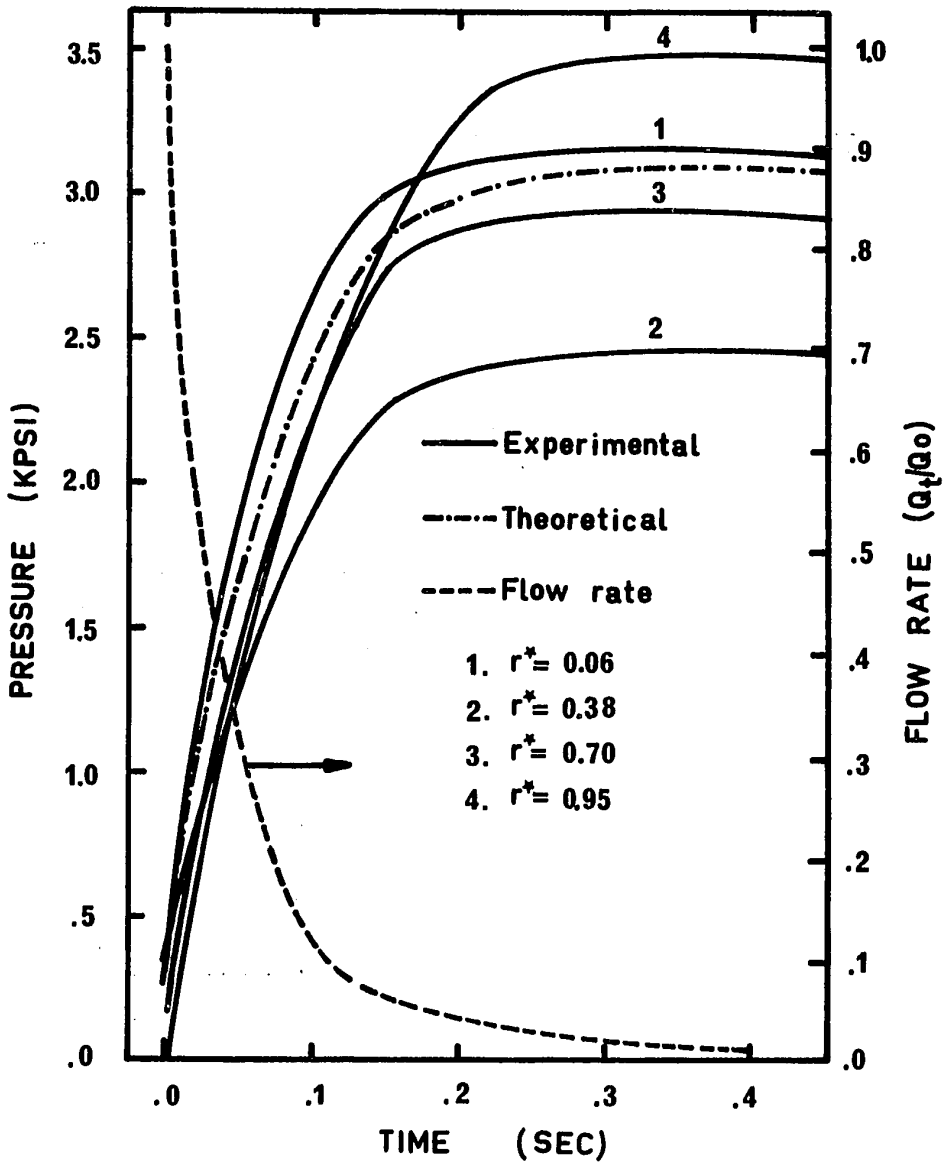

The rates of pressure rise are reduced as packing proceeds. As packing progresses, the pressure level in the cavity increases and thus the driving force for flow and packing decreases causing the latter stages of packing to be accomplished slowly.

4.2.3 Flow Rate Variation

Together with the rate of pressure rise in the cavity, the flow rate of material drops, as shown in Figures 4-3 to 4-10 for polyethylene and 4-11 to 4-14 for polystyrene. As the pressure rises sharply during the initial stages of packing, the flow rate is reduced due to the decrease in the driving force for flow, as can be seen clearly from equation (4-3).

There appears to be some correlation between the filling times and the corresponding packing times. A short filling time is associated always with a short packing time and visa versa. In general, packing time varies between 25-40% of the filling time for polyethylene and between 30-80% for polystyrene. The main contribution to the differences in packing times results from differences in the flow rate at the end of the filling stage which dominates the initial stages of packing. Also the temperature distribution in the cavity at the beginning of packing plays an important role.

FIGURE 4-17

TEMPERATURE PROFILES AT THE END OF PACKING
CASE 2

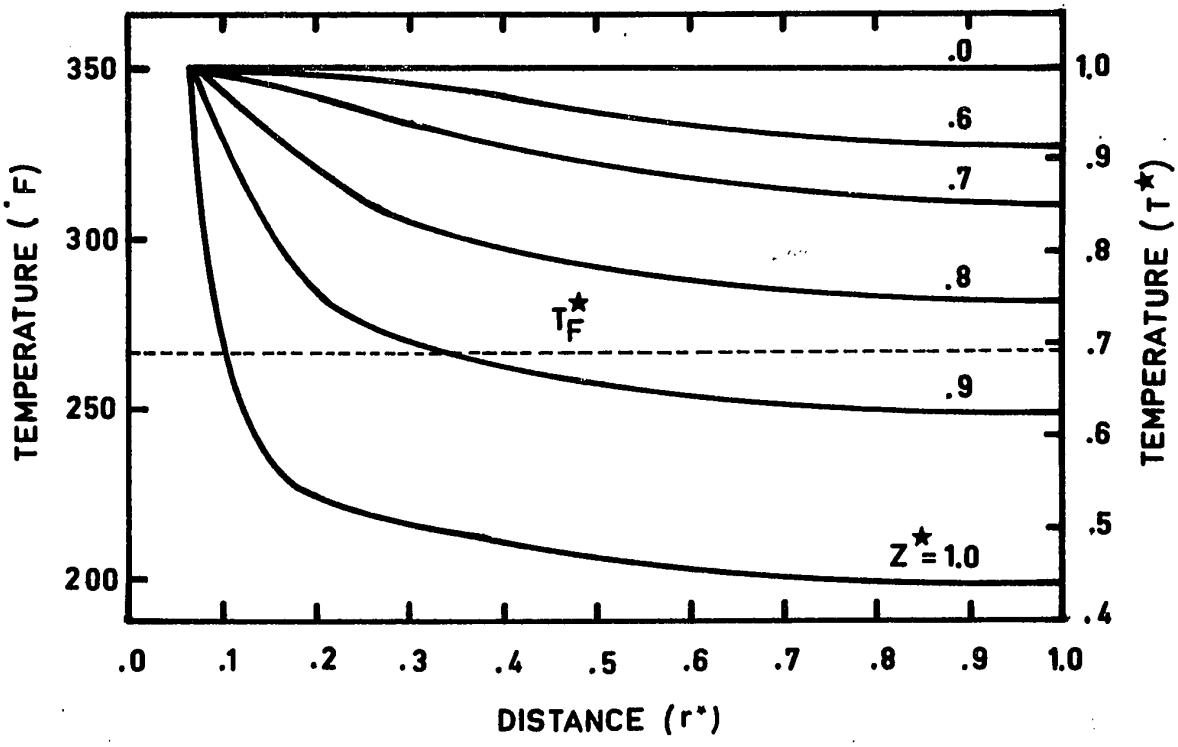

FIGURE 4-18

TEMPERATURE PROFILES AT THE END OF PACKING

CASE 4

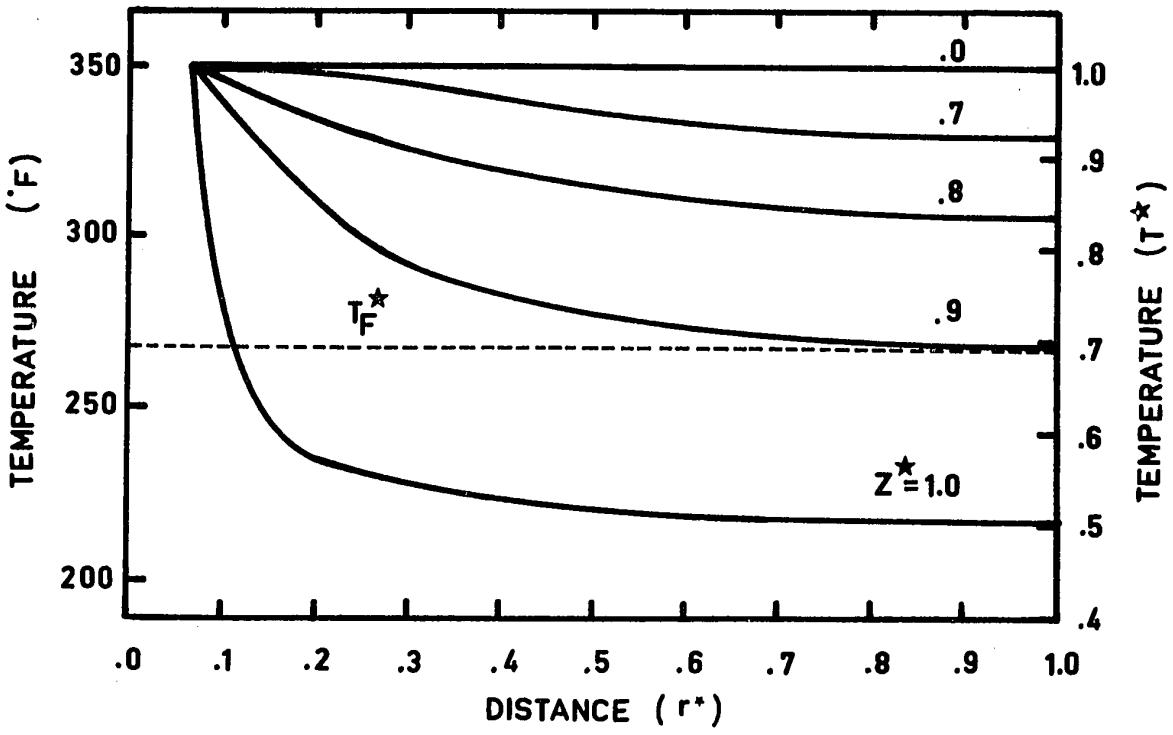

FIGURE 4-19

TEMPERATURE PROFILES AT THE END OF PACKING
CASE 5

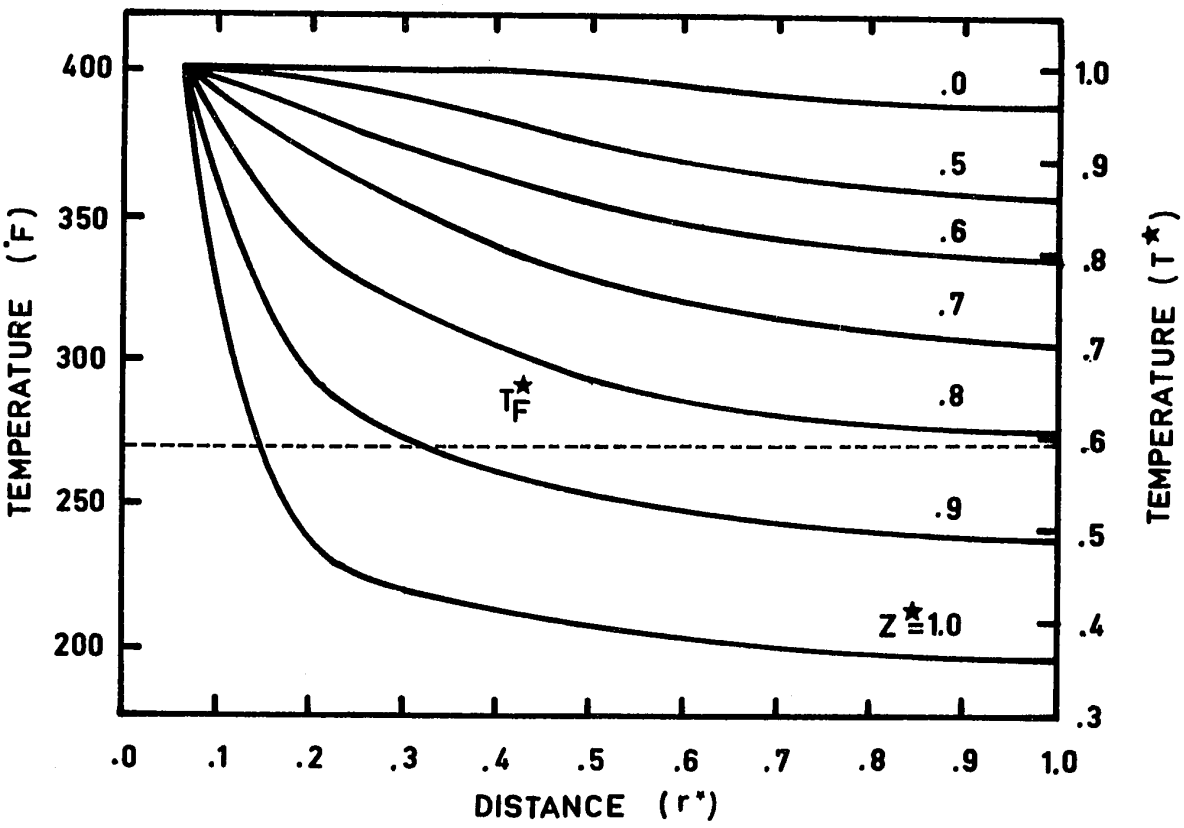

FIGURE 4-20

TEMPERATURE PROFILES AT THE END OF PACKING
CASE 7

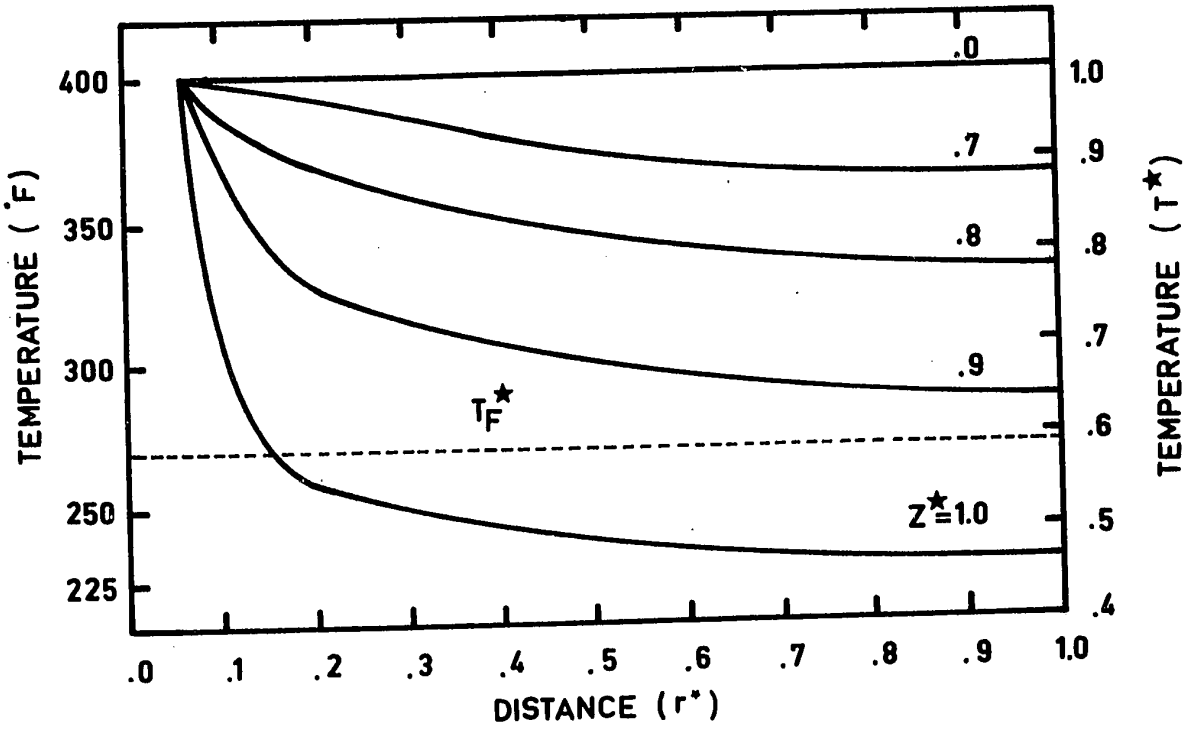

FIGURE 4-21

TEMPERATURE PROFILES AT THE END OF PACKING
CASE 9

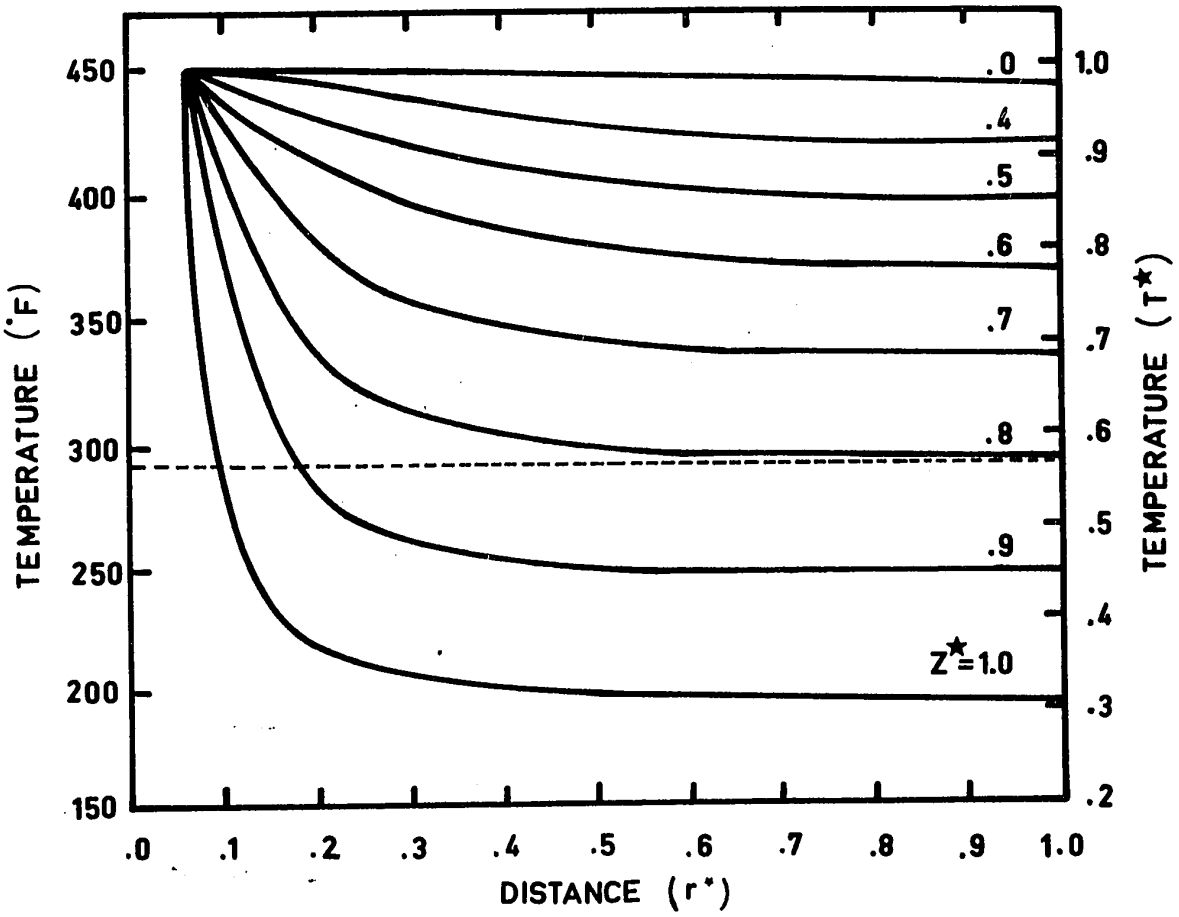

FIGURE 4-22

TEMPERATURE PROFILES AT THE END OF PACKING
CASE 11

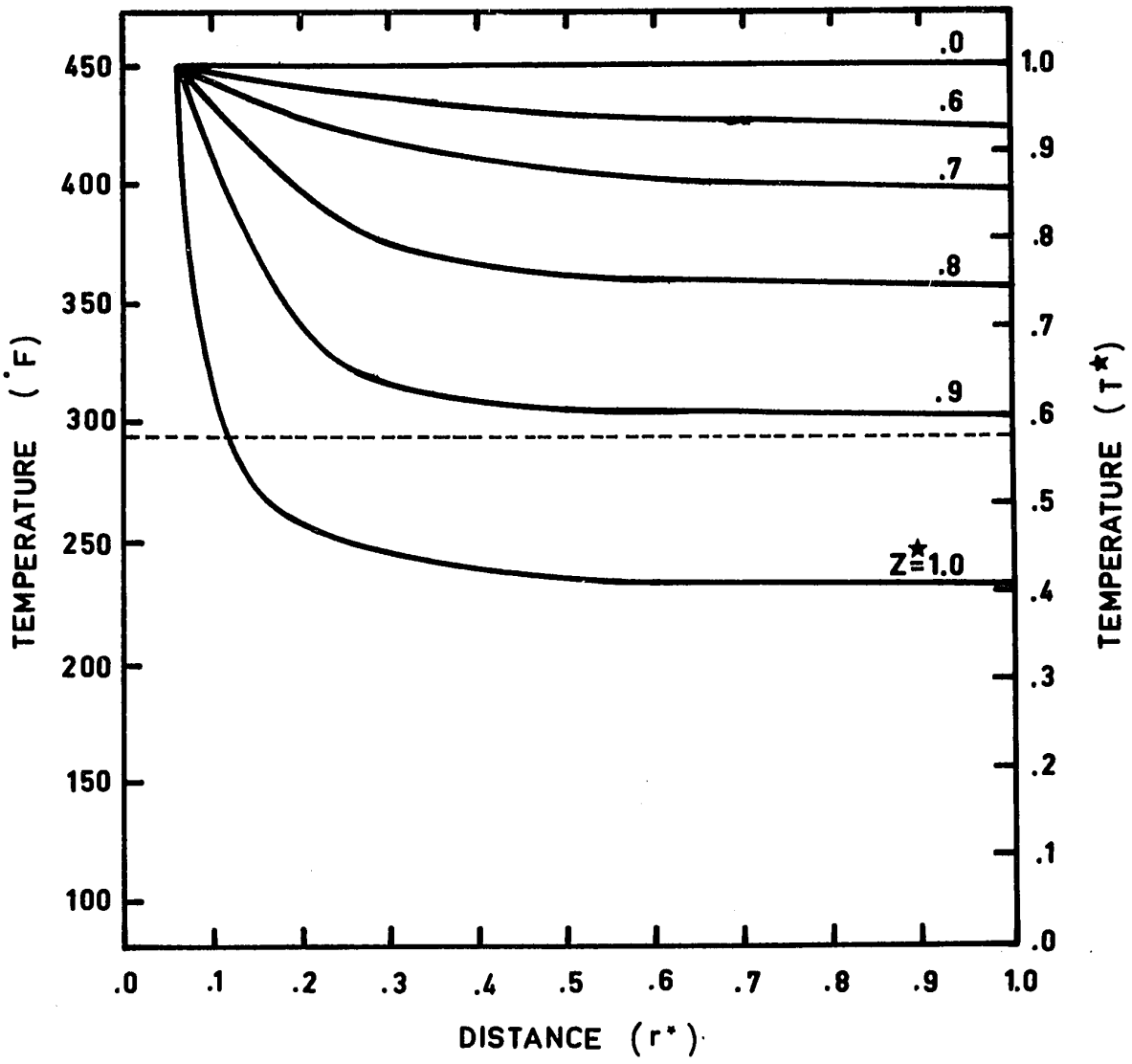

4.2.4 Temperature Profiles

Figure 4-17 to 4-22 give the calculated temperature profiles at the end of packing. The relatively short packing times seem to have a minor effect on the temperature profiles. However, some reduction in temperature and increase in the amount of solidified material may be noted.

The effect of the different parameters on the packing stage are discussed in Chapter 7.

4.2.5 Summary

1. Good agreement is obtained between experimental and calculated packing curves.
2. Pressure profiles exist in the cavity during the packing stage.
3. As the pressure rises in the cavity calculations show that the flow rate decreases.
4. A short filling time is associated with a short packing time and visa versa.

5. COOLING STAGE

5.1 THEORETICAL ANALYSIS AND COMPUTATIONAL PROCEDURE

In the cooling stage no flow takes place, cooling of the molded article proceeds and the pressure in the cavity drops as a result. From the computational point of view, this stage, is a particular case of the previous packing stage. The equations that are used in the cooling stage are : (4-1), (4-4), (4-5), (3-14), (3-15), (4-6), (4-7), (4-8). For each time increment, the temperature profile is computed by using equations (4-4) and (4-5) and boundary conditions (4-6) and (4-7). Latent heat is taken into consideration by equations (3-14) and (3-15).

Since flow ceases at the end of the packing stage, the density remains constant (unless pressure reaches the atmospheric level) at the same value as at the end of packing. Thus, pressure drop is found directly from the average temperature as defined by equation (4-8) and an equation of state (3-20) using the constant value for density. As in the other two stages, instead of an equation of state a P-V-T diagram was used in order to increase accuracy. In addition, the equation of state is valid only for the melt region, and the use of a tabulated P-V-T diagram allows the extension of the calculations to regions below the freezing temperature.

The same computer program was used for both the packing stage and the cooling stage. So that the temperature profile and the average pressure at the end of packing were automatically used as the initial temperature profile and average pressure, respectively, in the cooling stage.

5.2 RESULTS AND DISCUSSION

As indicated earlier, the cooling stage was followed experimentally only by the pressure transducer measurements. No temperature measurements inside the bulk of the polymer were conducted, in order to avoid interference of the temperature measuring elements with the flow in the cavity.

5.2.1 General

Since no flow takes place in the cooling stage, it is possible to simulate this stage by performing temperature measurements in static polymer systems under pressure. Such measurements have been conducted and reported by Kenig and Kamal (23,24) for the cooling and solidifcation of a polymer melt contained in a cylindrical cavity under varying combinations of initial temperature and pressure. These measurements give direct confirmation of the validity of the proposed model for the cooling stage in injection molding. Indirect evaluations of the proposed model for the cooling stage may be obtained by comparing the calculated and experimental values of pressure in the cavity, as functions of cooling time.

5.2.2 Pressure Variation

Figure 5-1 to 5-8 show the calculated average pressure and the experimental curves for polyethylene, and Figures 5-9 to 5-12 for polystyrene, for the twelve cases discussed in the filling and packing stages.

Cooling results show that the experimental pressure gradients, that are observed in the packing stage, persist during the cooling stage and that the cooling curves tend to intersect each other at later stages of cooling. In general, the time needed for the pressure to drop from its initial value to atmospheric is about twice longer for polystyrene than for polyethylene, as a result of the lower thermal diffusivity and the higher initial pressure realized in polystyrene cases.

The shapes of both the theoretical and experimental curves are different for polyethylene and polystyrene. While in polyethylene the rate of pressure drop is higher at longer cooling times, it is lower for polystyrene. This is due to the different types of phase transition that the two polymers undergo during cooling. Polyethylene undergoes a first order transition; as a result, its thermal conductivity, thermal diffusivity and density change to a large extent. The thermal properties change by 100%, as the density changes by about 20% in the solidification temperature region (see section 2.4). Polystyrene undergoes a second order transition, and thus its thermal properties change only slightly, as reported by Nagler

FIGURE 5-1

PRESSURE VARIATION DURING COOLING

CASE 1

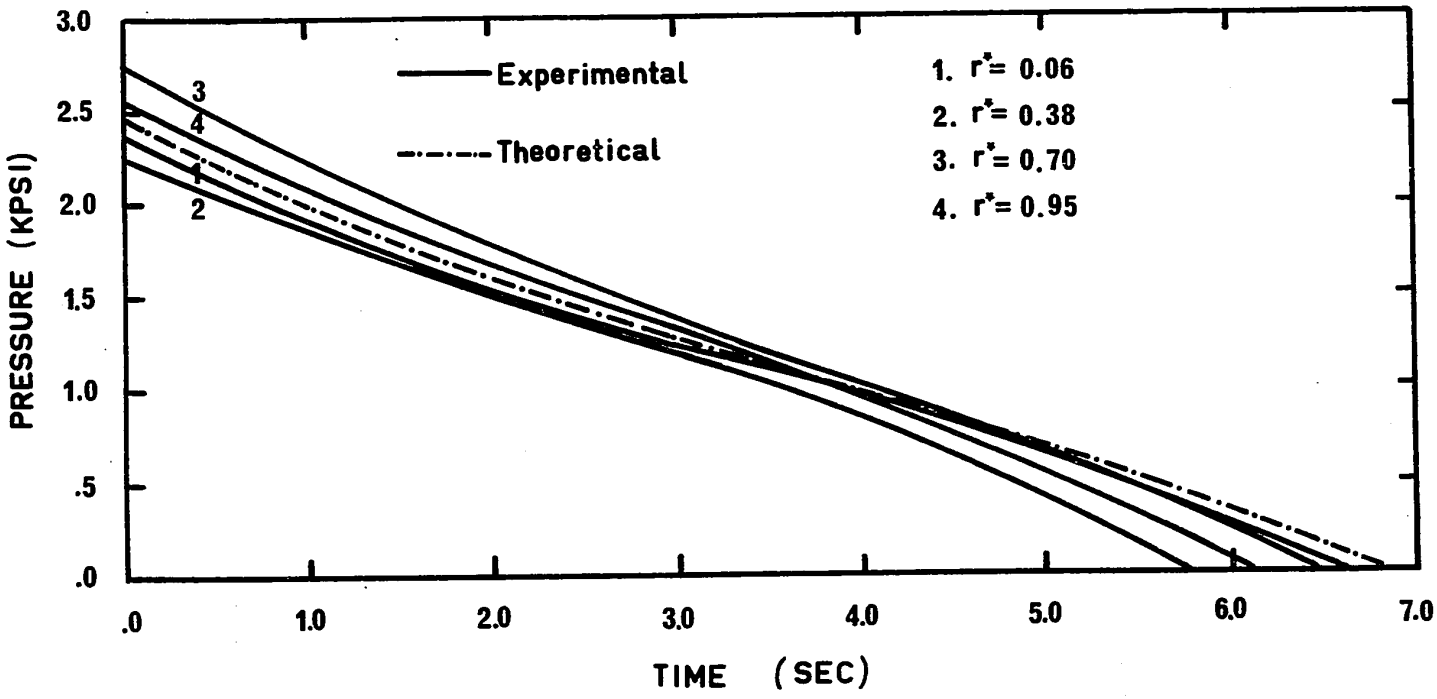

FIGURE 5-2

PRESSURE VARIATION DURING COOLING

CASE 2

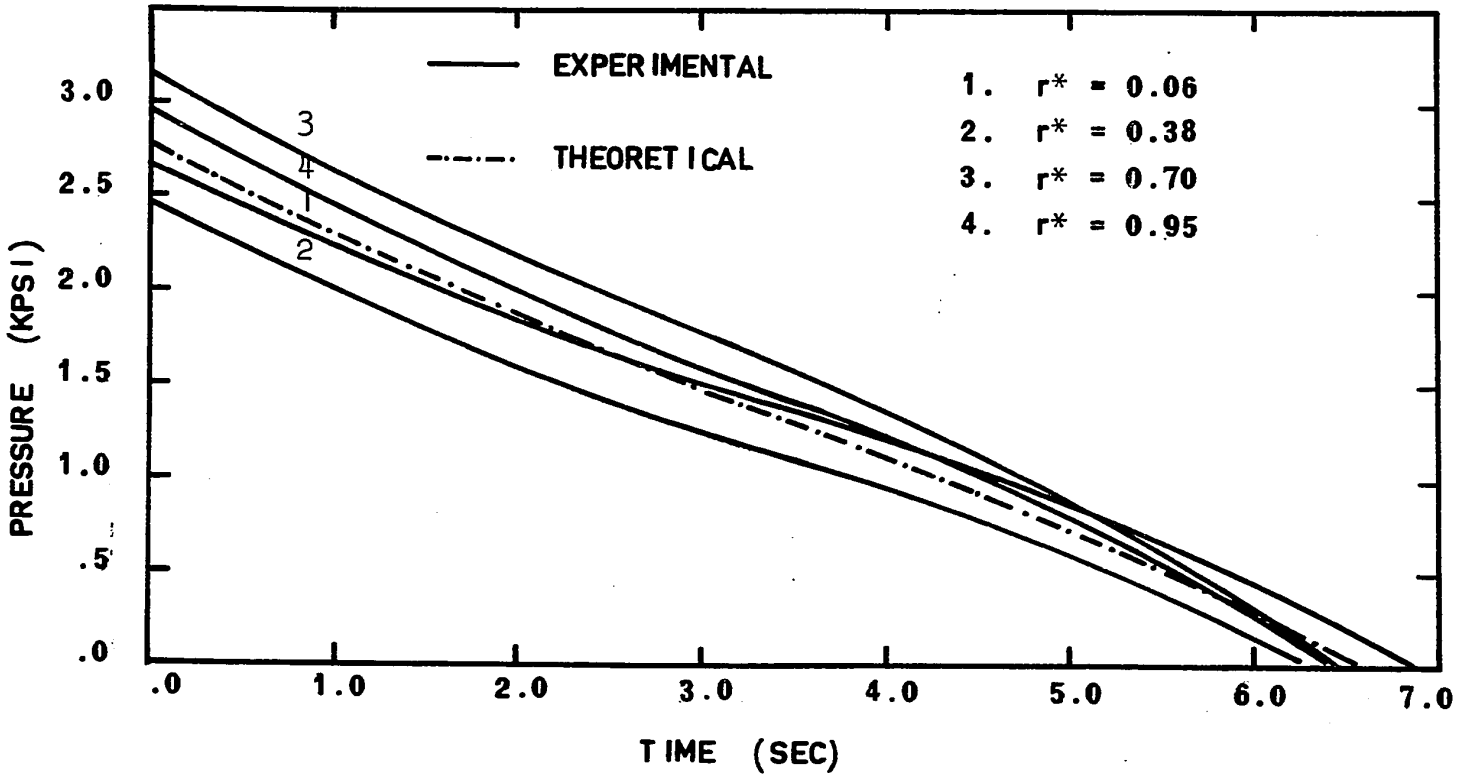

FIGURE 5-3

PRESSURE VARIATION DURING COOLING

CASE 3

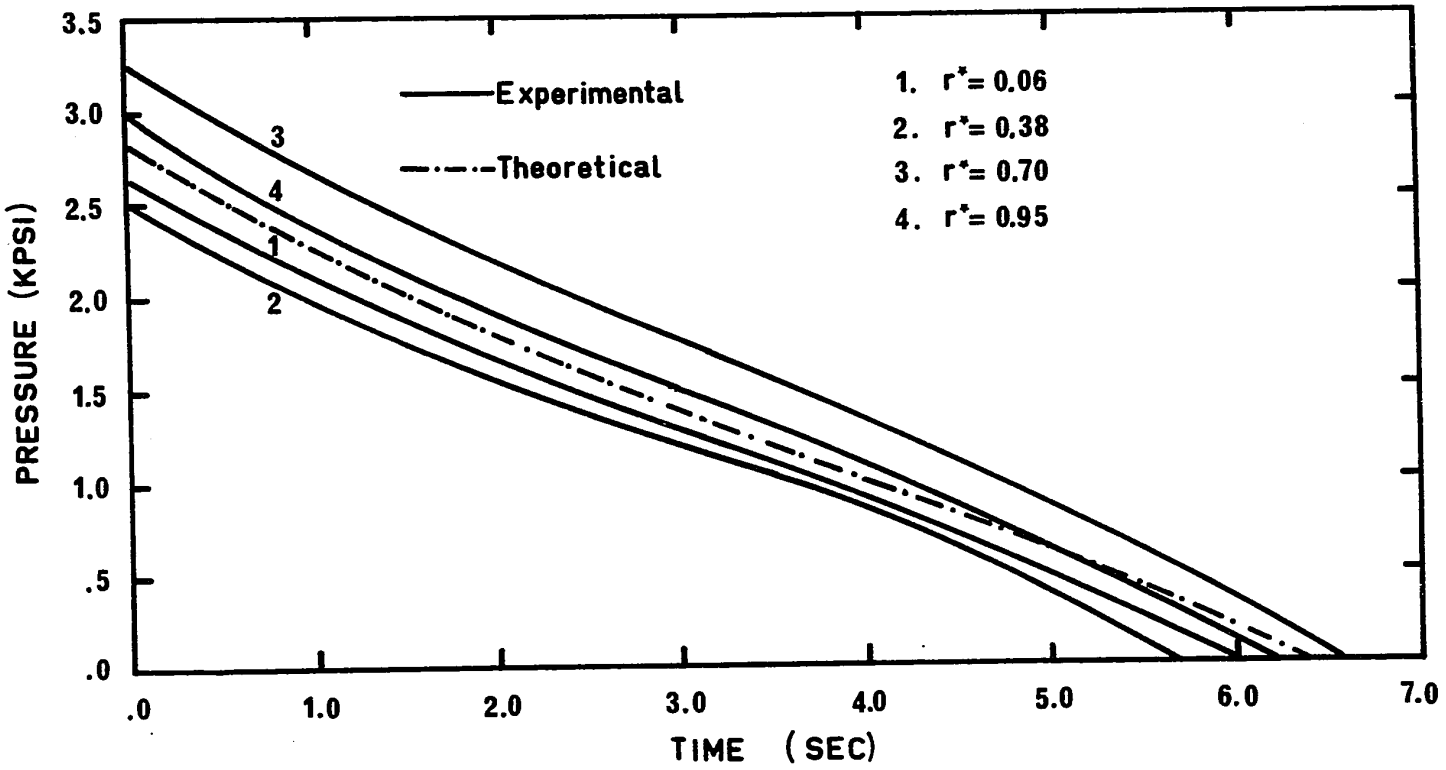

FIGURE 5-4

PRESSURE VARIATION DURING COOLING

CASE 4

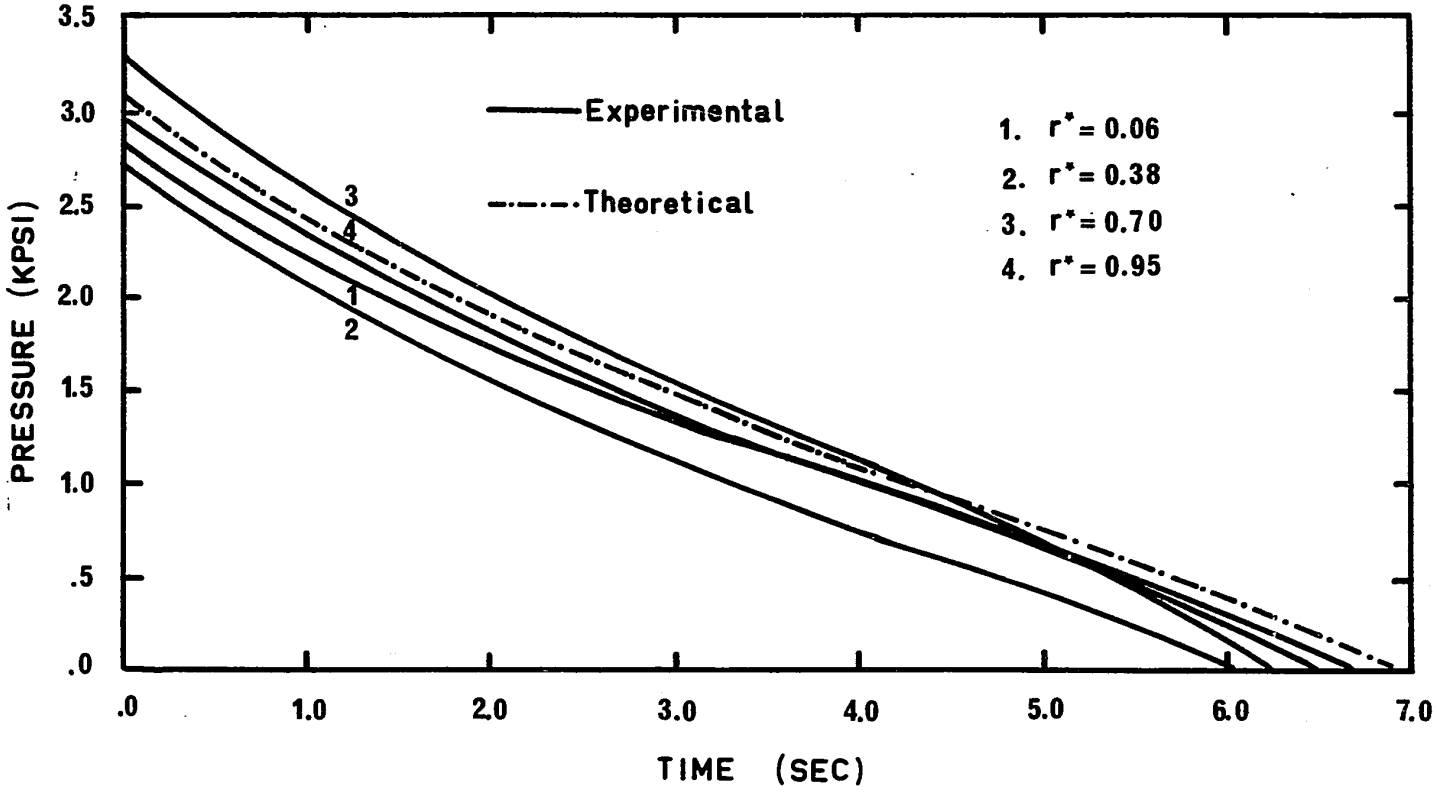

FIGURE 5-5

PRESSURE VARIATION DURING COOLING

CASE 5

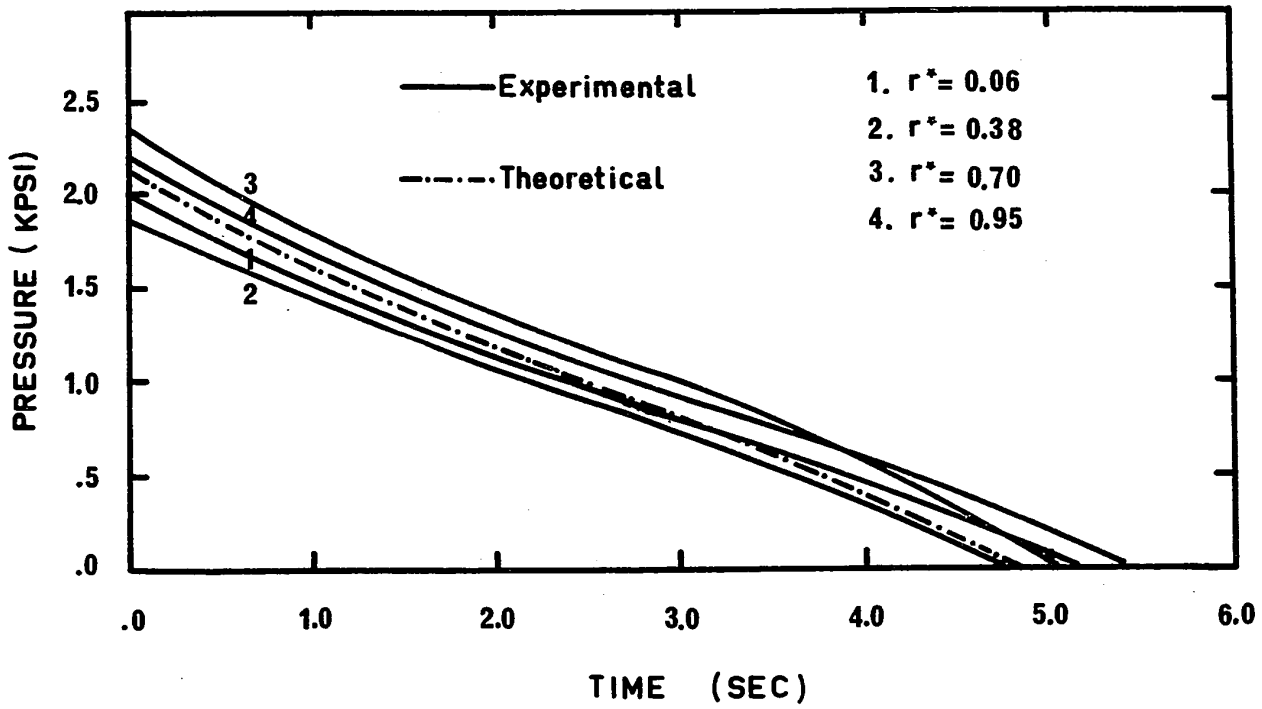

FIGURE 5-6

PRESSURE VARIATION DURING COOLING

CASE 6

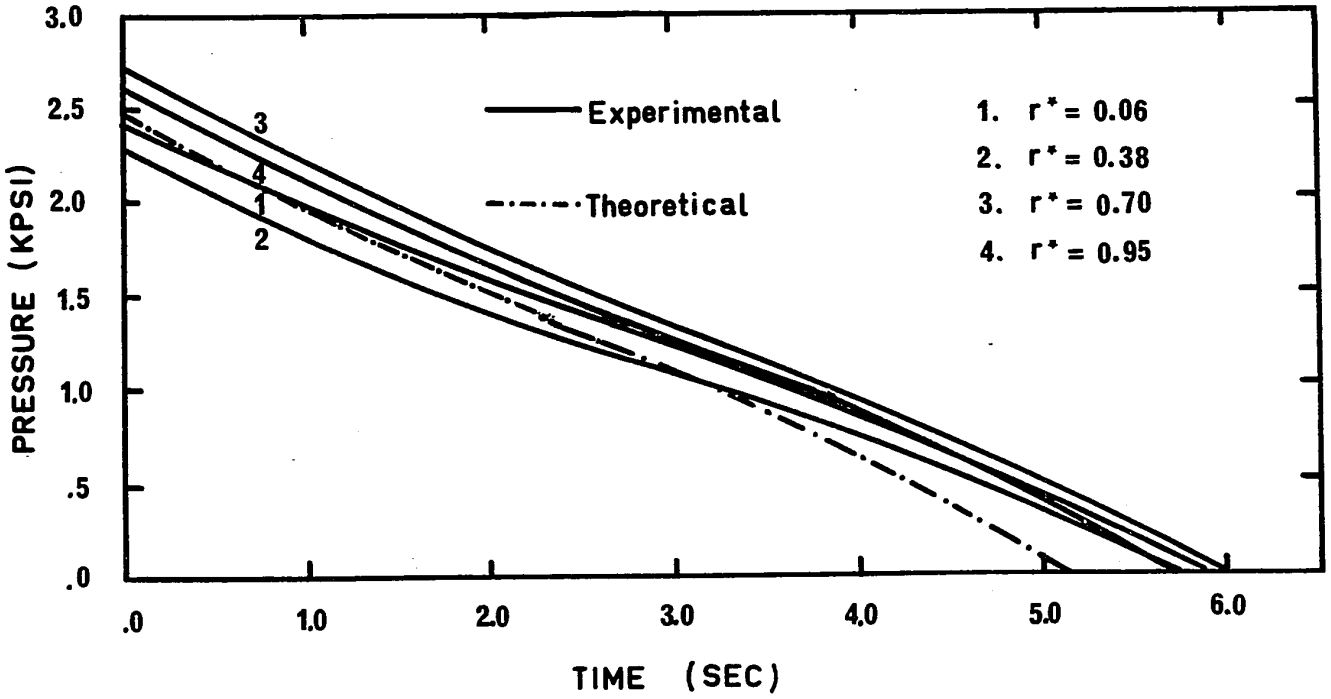

FIGURE 5-7

PRESSURE VARIATION DURING COOLING

CASE 7

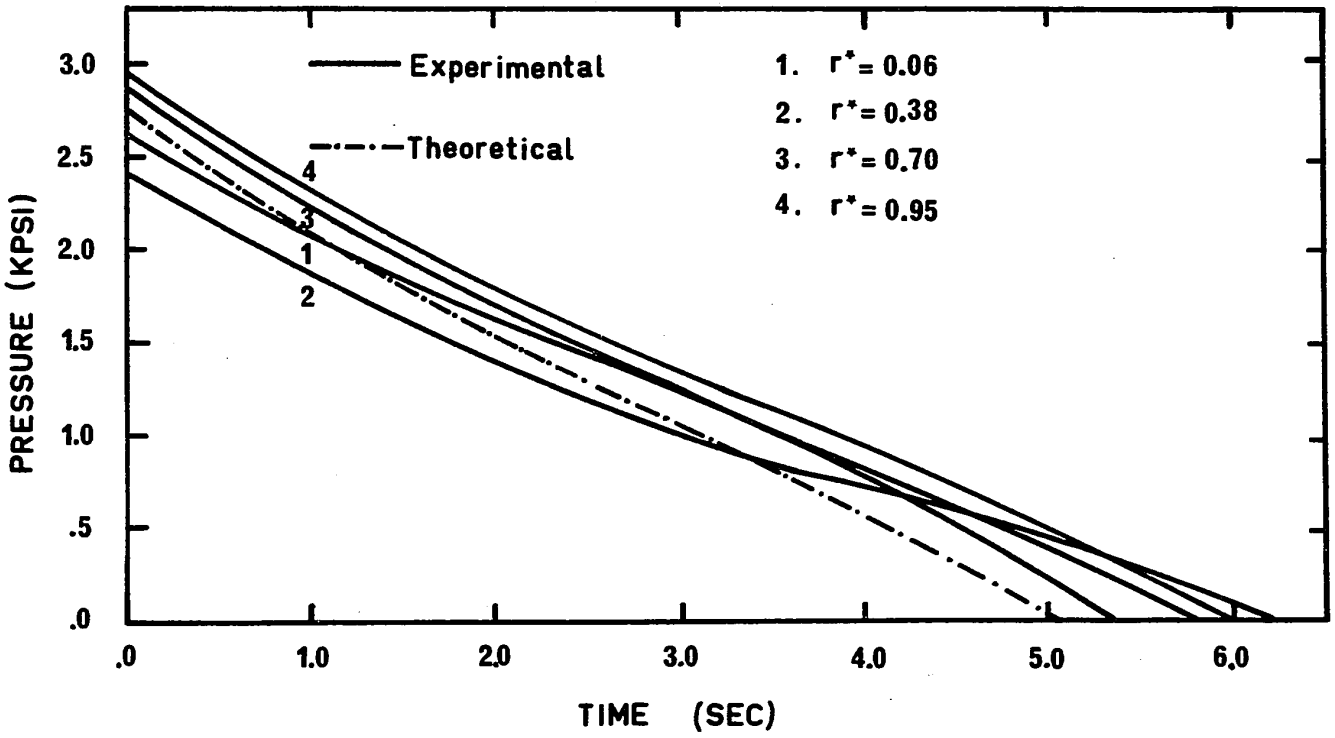

FIGURE 5-8

PRESSURE VARIATION DURING COOLING

CASE 8

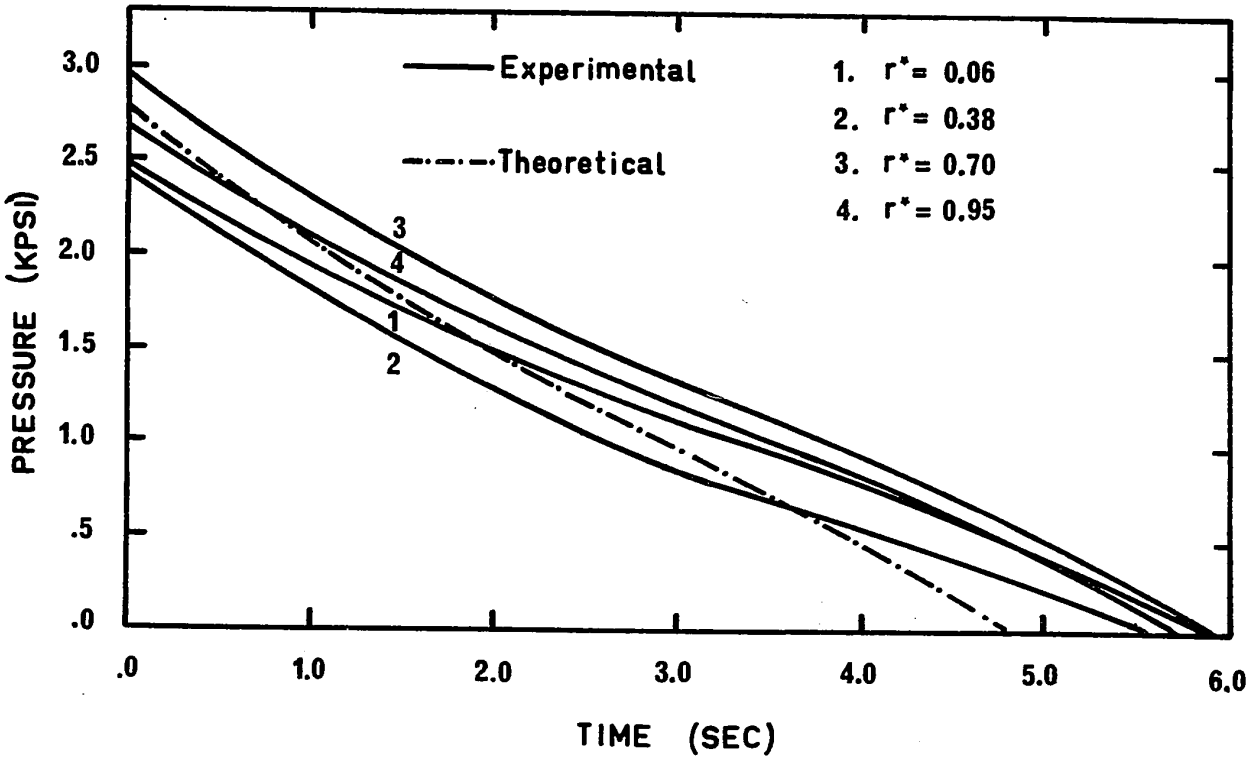

FIGURE 5-9

PRESSURE VARIATION DURING COOLING

CASE 9

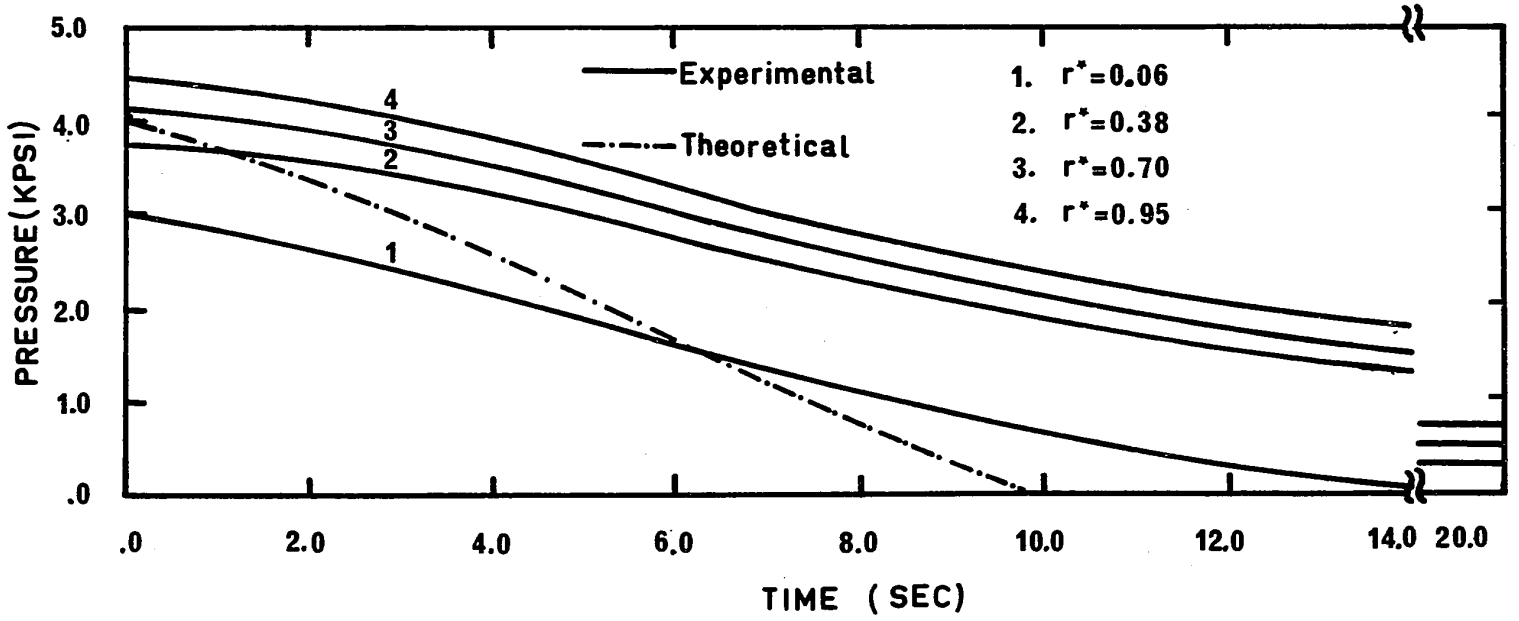

FIGURE 5-10

PRESSURE VARIATION DURING COOLING

CASE 10

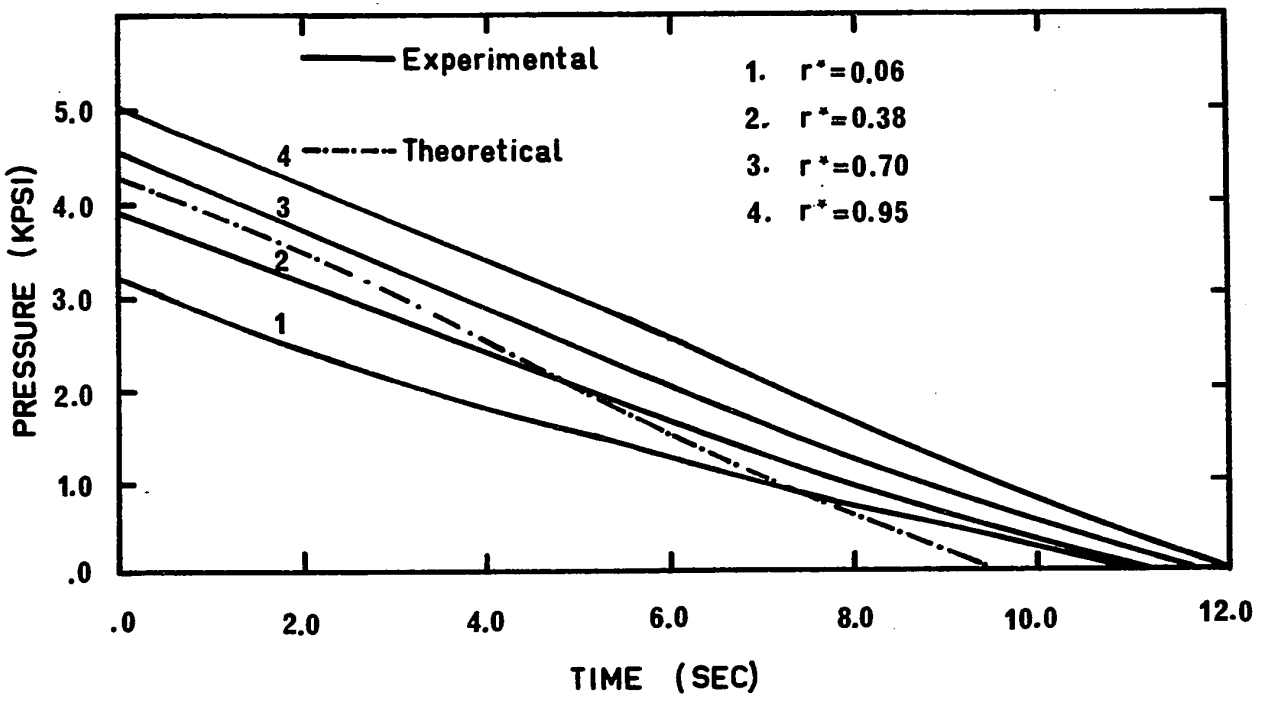

FIGURE 5-11

PRESSURE VARIATION DURING COOLING
CASE 11

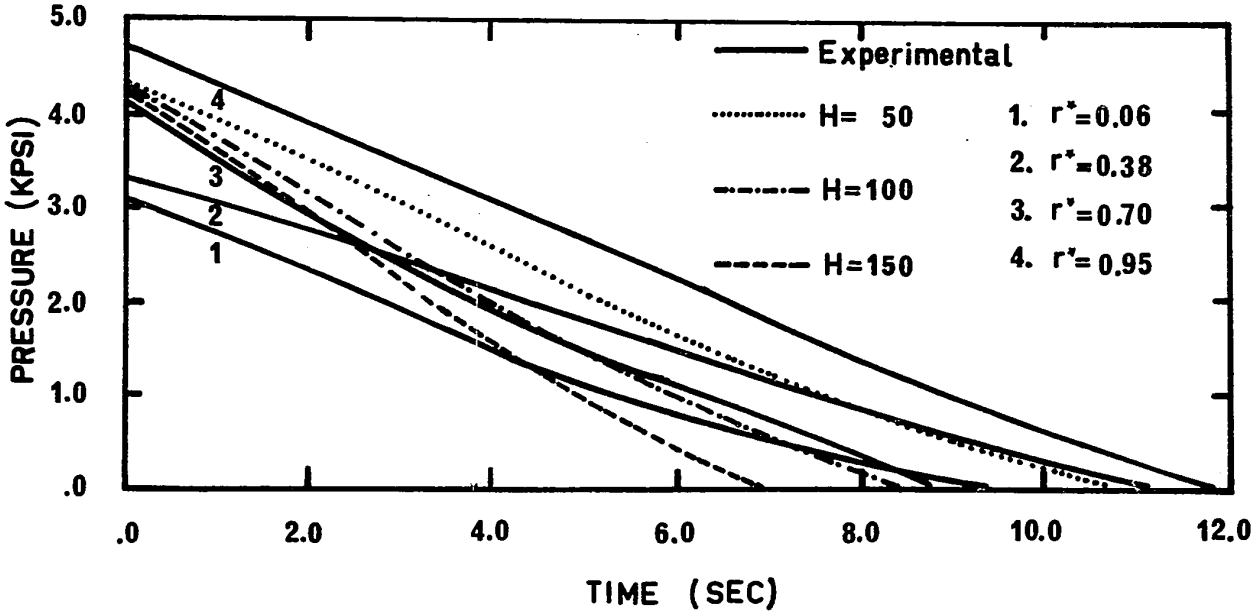

FIGURE 5-12

PRESSURE VARIATION DURING COOLING

CASE 12

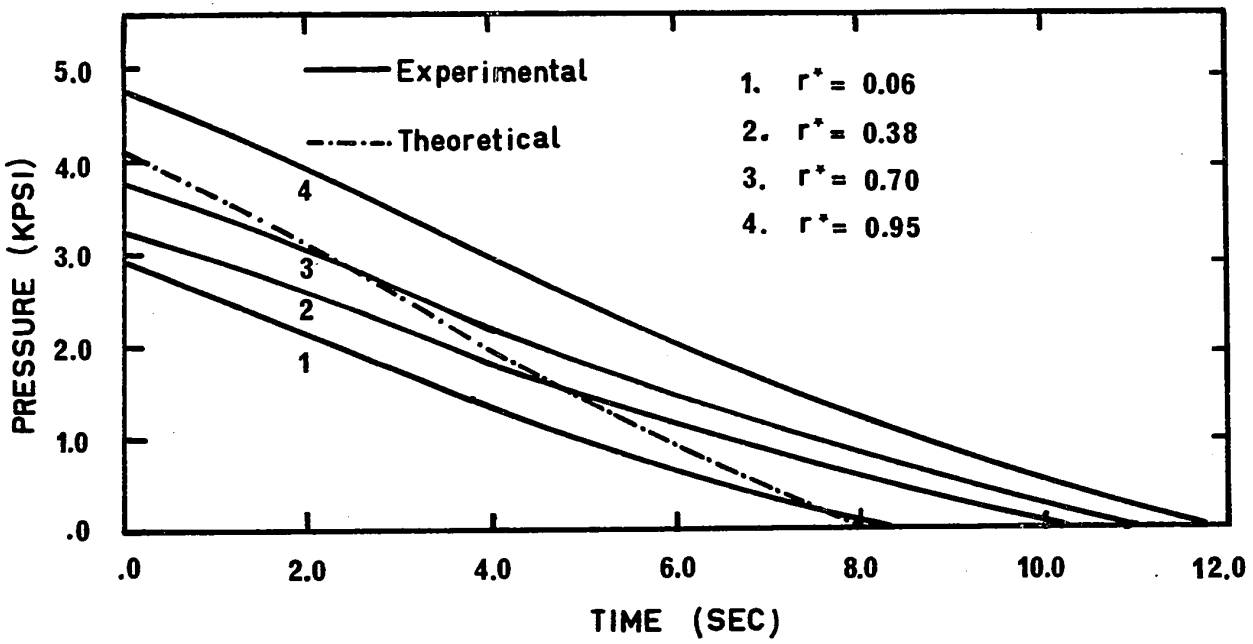

(26), while its density changes moderately. As cooling progresses, more of the polymer will solidify and thus, in the case of polyethylene, the temperature will decrease with an increased rate due to the solid layer. This leads to an inflection point in the pressure, time curve. Since, the thermal properties of polystyrene are practically constant, the rate of temperature drop will decrease at longer cooling times due to lower temperature gradients at these times. Consequently, the rate of pressure drop will decrease. The general shape of the pressure curve for polystyrene resembles the polyethylene curve at shorter times before the inflection point. The same general results are reported by Kenig and Kamal (23,24) for cooling both polyethylene and polystyrene.

As expected, the time required for the pressure to drop from its initial value to atmospheric is shorter for higher initial melt temperature, as can be seen in Figures 5-1 to 5-4 compared with Figures 5-5 to 5-8. This is due to the faster rates of cooling which are realized with higher initial temperatures. It takes 6-7 seconds for the pressure to reach the atmospheric level for polyethylene at the initial melt temperature of 350°F, and only 5-6 seconds at the initial temperature of 400°F.

The values which are assigned to the heat transfer coefficient between the polymer and the mold are crucial for the cooling stage, where most of the heat transfer takes place. While the value of 100 Btu/ft^2/hr/^{o}F gives satisfactory results for polyethylene at the initial melt temperature of 350^{o}F, there is less satisfactory agreement with experimental results, for the initial melt temperature of 400^{o}F. For polystyrene, deviations are larger. An attempt has been made to assign different values for the heat transfer coefficient in the range of 50-150 Btu/ft^2/hr/^{o}F (31,32). It can be seen in Figure 5-11 that better agreement between the experimental and predicted values is achieved when the value of the heat transfer coefficient, for polystyrene, is lowered to 50 Btu/ft^2/hr/^{o}F. A more detailed analysis of the effect of heat transfer coefficient is given in section 7.

5.2.3 Residual Pressure

In one case for polystyrene, Figure 5-9 for case 9, the pressure measurements detected a residual pressure in the cavity at the entrance to the cavity. Spencer and Gilmore (50) reported residual pressures for polystyrene, when the length of the packing stage exceeded a critical value. In the present case the sum of both the filling and packing stages was

about 2.65 seconds. The residual pressures might be attributed to the thermodynamic relation between the pressure, temperature and density. According to the P-V-T diagram (30) and Figure 2-11, a relatively low temperature combined with a high pressure at the beginning of cooling (or end of packing) would result in a residual pressure at room temperature. This was confirmed when the initial melt temperature of polystyrene was lowered to 400°F, where residual pressure were obtained for filling and packing times exceeding one second. In addition, when the shot size was decreased and consequently the maximum pressure at the end of packing did not exceed 3500 psi, no residual pressure were noticed at the initial melt temperature of 450°F. As the melt temperature was lowered to 400°F, residual pressures were detected when combined time for filling and packing exceeded 3 seconds. Manipulations of the calculation procedure as by lowering the heat transfer coefficient to 25 Btu/ft^2/hr/°F and increasing the initial pressure to the maximum pressure registered in curve 4 Figure 5-9, resulted only in increasing the cooling time to 20 seconds. It should be emphasized that Kenig and Kamal (24) did not observe residual pressures in the cooling of polystyrene from an initial pressure of 10,000 psi. In fact the reported experimental cooling times were even shorter than these predicted by calculations. The reason for the differences between experimental and calculated times was attributed

to end effects, since the ratio of the length to diameter was only 5.5.

The inability of the present theoretical calculations to predict the residual pressures may be a result of the time scale of the cooling stage. All thermodynamic relations between volume, pressure and temperature are applicable only under equilibrium conditions, relations would be true under unsteady conditions, only if the relaxation phenomena that take place in a dynamic process were negligible, in the sense that the time necessary for the polymer to readjust to time-varying conditions is much less than the time scale of the experiment. Since the relaxation time depends on the temperature and it increases as the temperature decreases, it seems that relaxation phenomena at low initial temperatures are not negligible when compared to the duration of cooling which is in order of ten seconds in the present case. These phenomena are not expected to be important when cooling times are more than ten minutes in the experiments conducted by Kenig and Kamal (24) in a two-inch diameter cylinder.

5.2.4 Temperature Profiles

Figures 5-13 to 5-16 give the calculated temperature profiles, at the end of cooling for polyethylene and Figures 5-17 and 5-18 for polystyrene for cases 2, 4, 5, 7, 9, 11 respectively. The main observation from these figures is that the temperature profiles are quite flat and that the temperature difference between the entrance and the cavity boundaries is about 20°F for any given axial distance. At the time when the average calculated pressure reaches the atmospheric level, about 40% of the cross section has solidified for polyethylene at the initial melt temperature of 350°F, while only about 30% has solidified when the initial melt temperature is 400°F. In the case 9 for polystyrene, more than 50% is below the defined freezing temperature (see section 9.1, Appendix 1), and about 25% below the glass transition temperature (220°F), and about 40% is below the freezing temperature for case 11.

5.2.5 Remarks on Pressure Measurement in the Cooling Stage

Some questions may arise in the cooling stage, as to the reliability of the pressure values measured by the pressure transducer. Since the pressure transducer is calibrated with a fluid (silicone oil) it may show different values for solids. Since in the cooling stage, solidification has reached high levels, it may introduce some errors in the experimental measurements. In principle, it is unimportant whether

FIGURE 5-13

TEMPERATURE PROFILES AT THE END OF COOLING
CASE 2

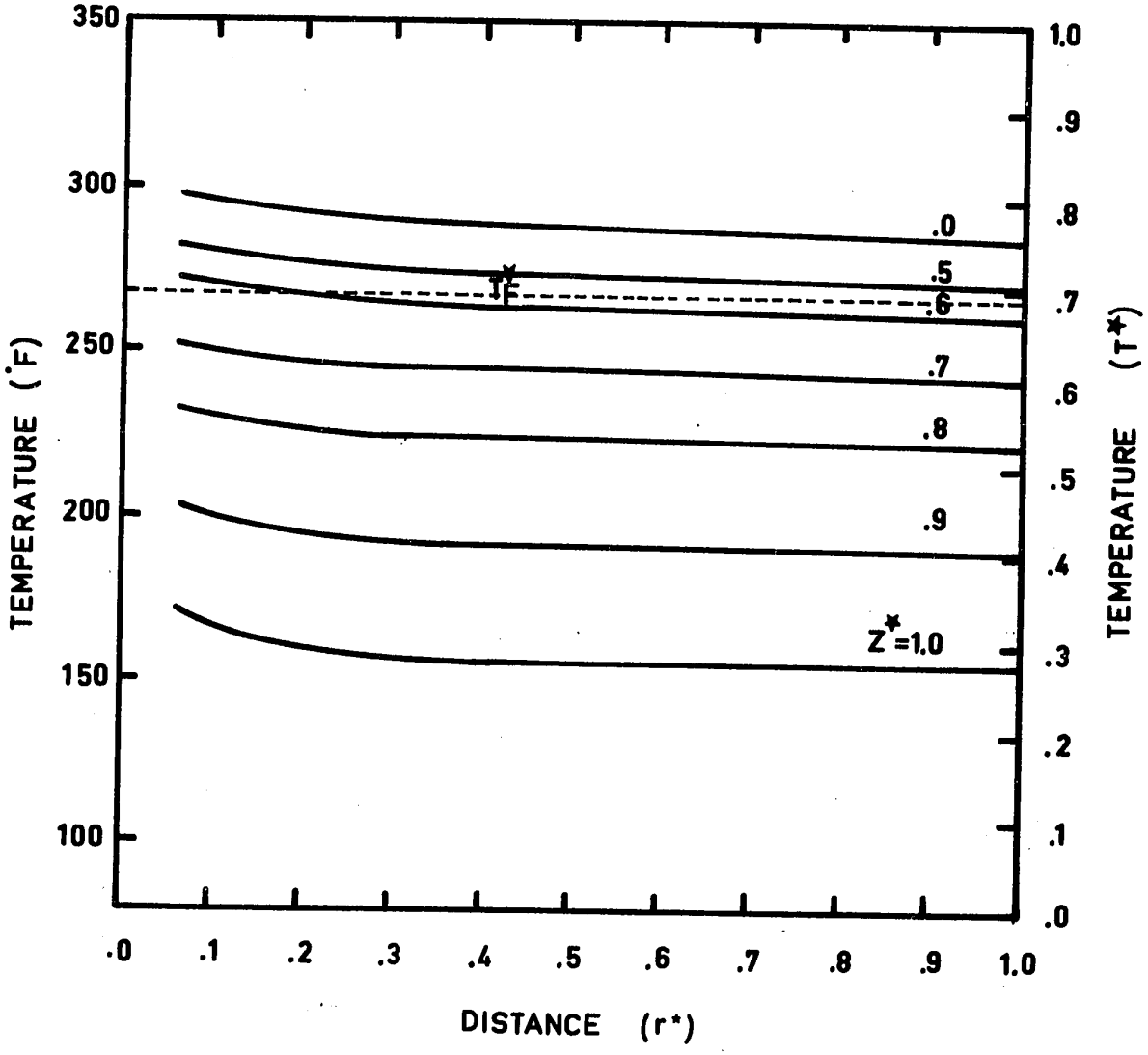

FIGURE 5-14

TEMPERATURE PROFILES AT THE END OF COOLING

CASE 4

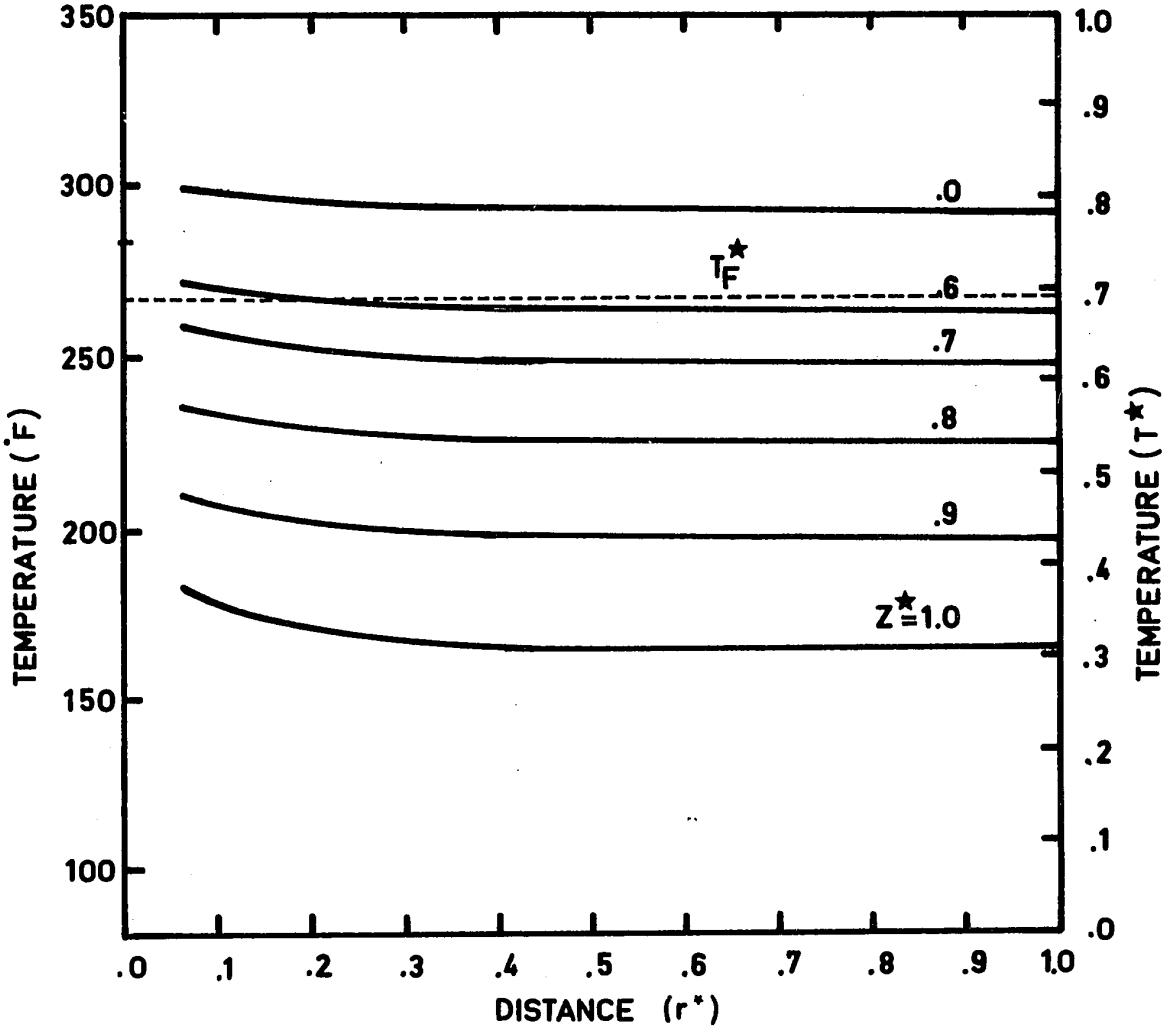

FIGURE 5-15

TEMPERATURE PROFILES AT THE END OF COOLING
CASE 5

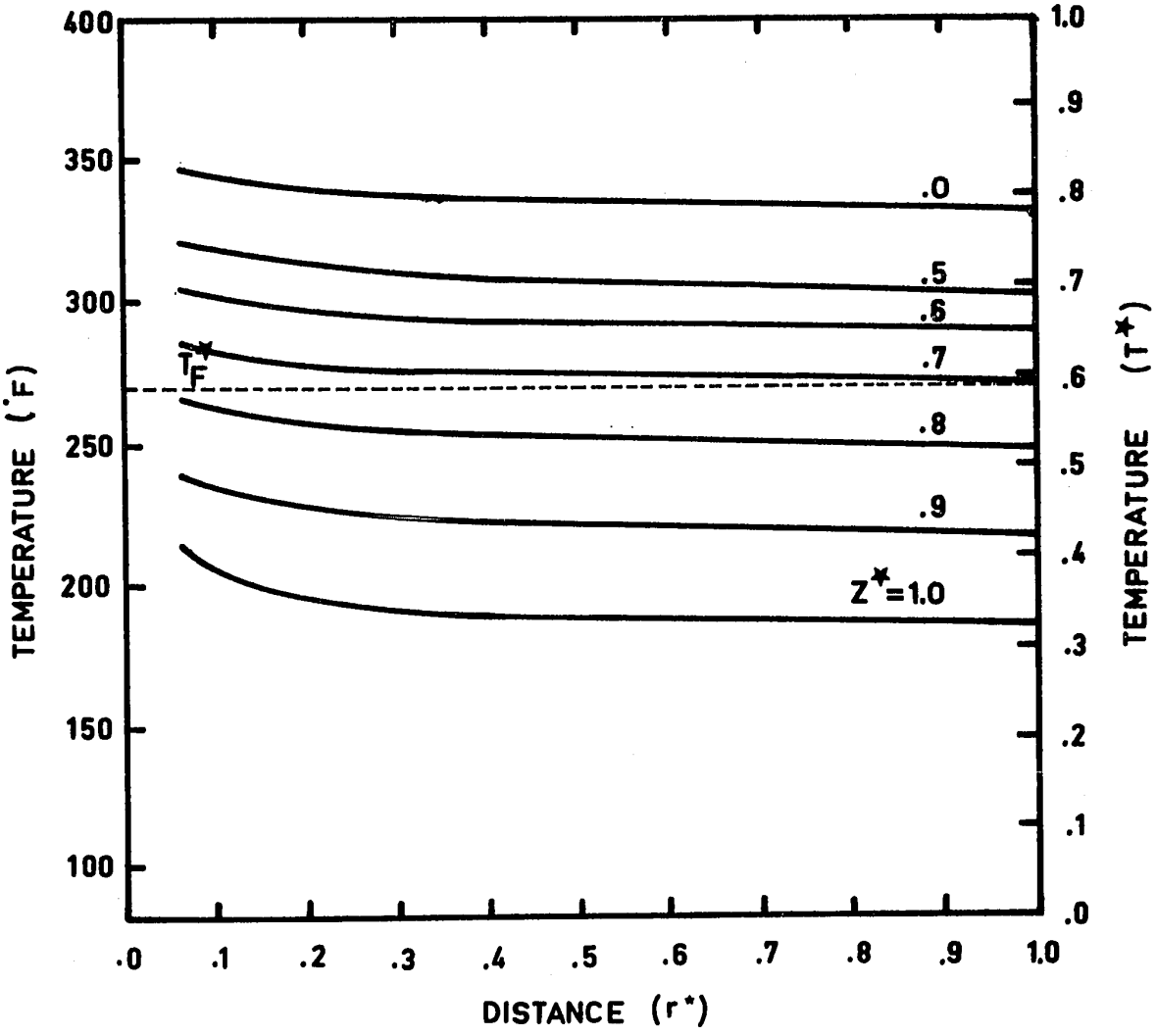

FIGURE 5-16

TEMPERATURE PROFILES AT THE END OF COOLING
CASE 7

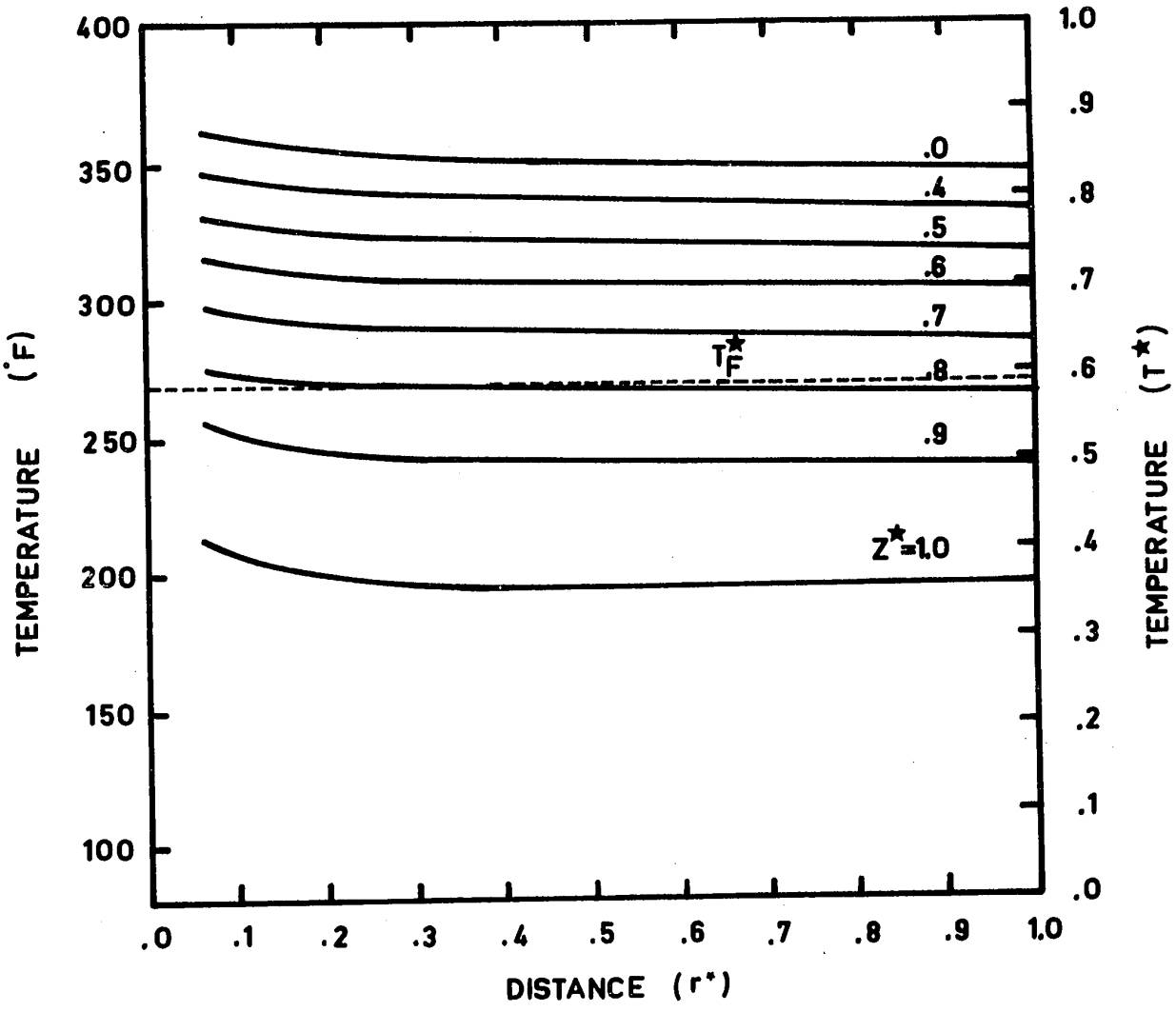

FIGURE 5-17

TEMPERATURE PROFILES AT THE END OF COOLING

CASE 9

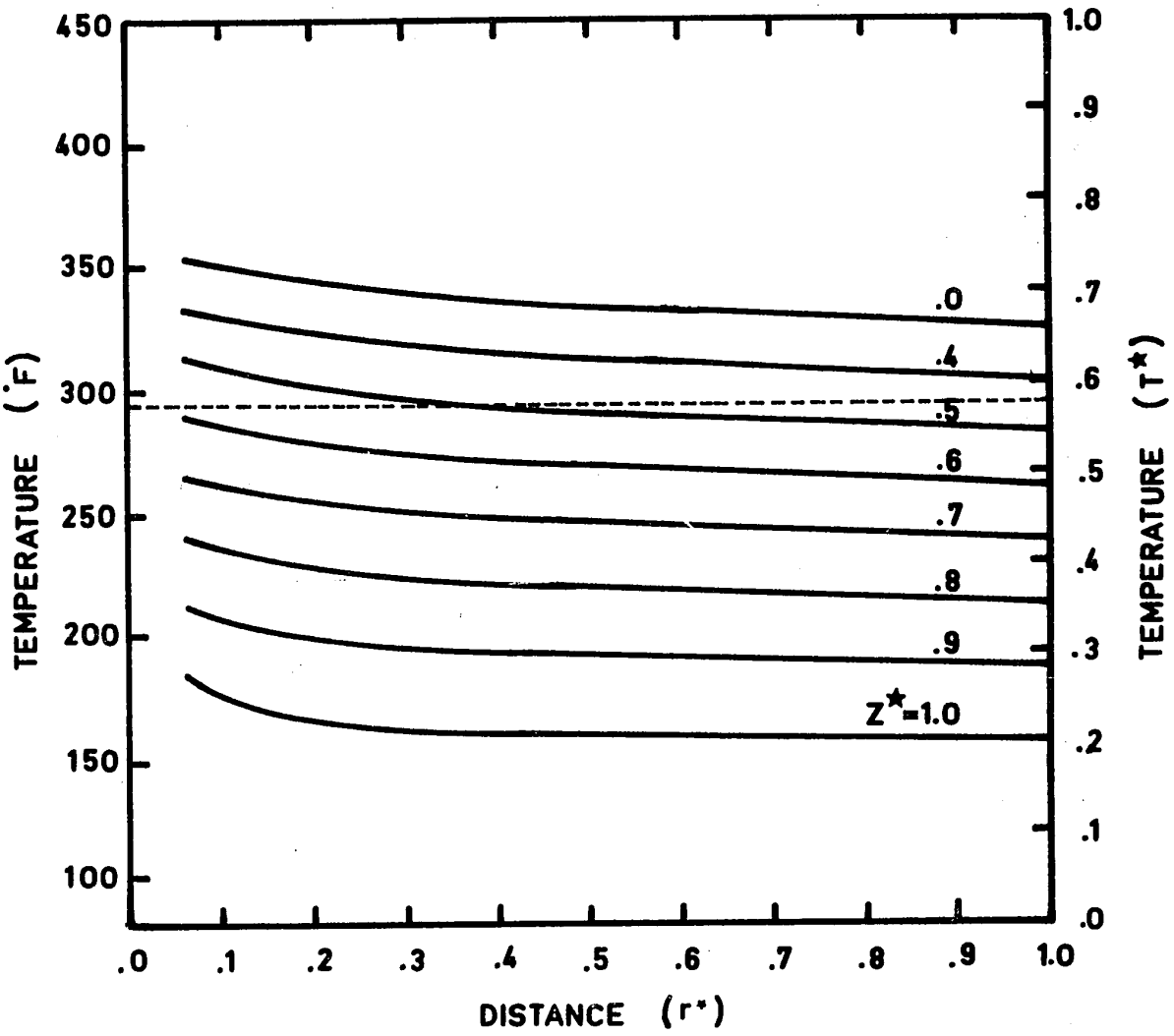

FIGURE 5-18

TEMPERATURE PROFILES AT THE END OF COOLING
CASE 11

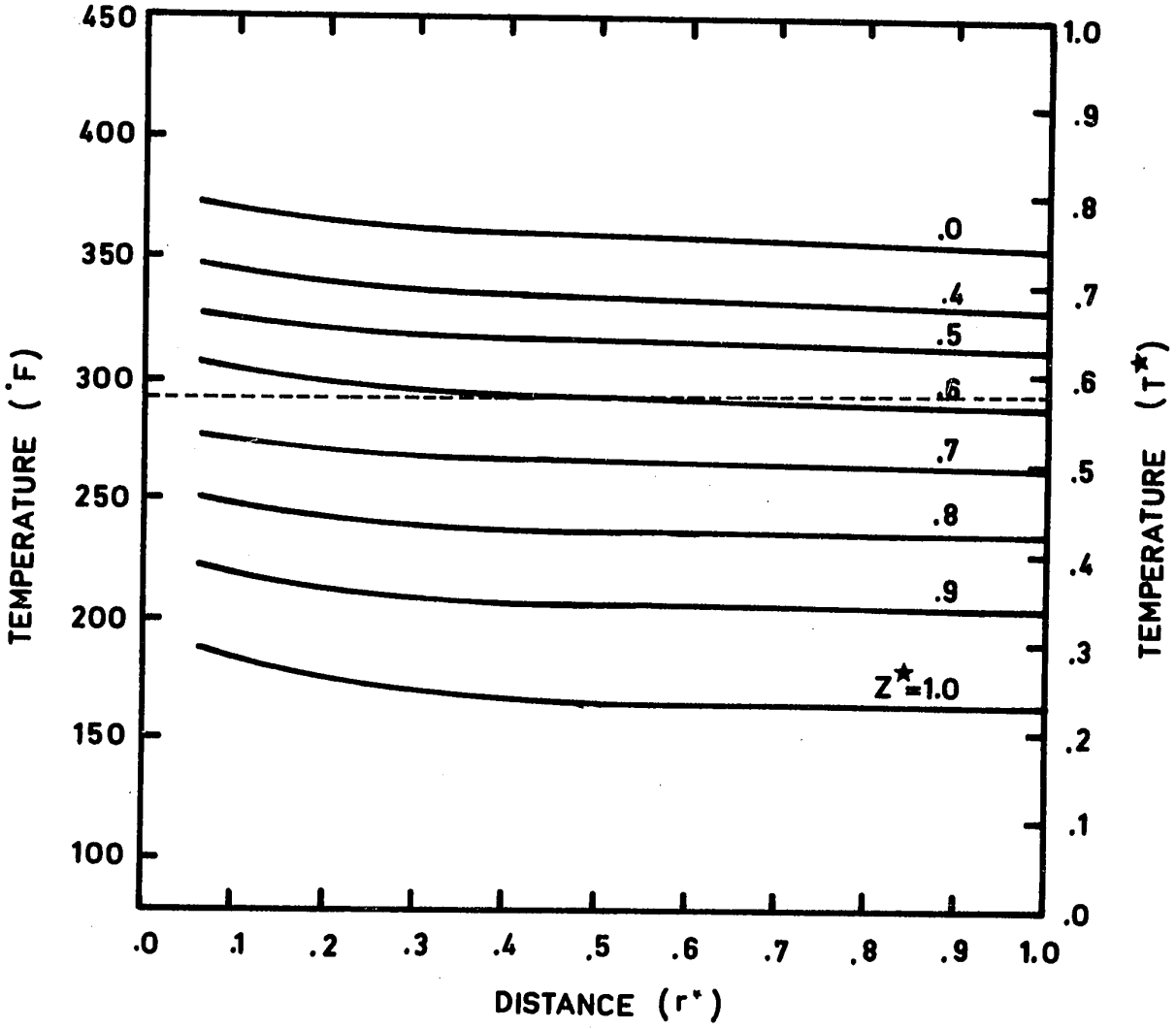

the load is transmitted to the diaphragm of the transducer by a melt or a solid, as long as perfect mechanical contact between the polymer and the diaphragm is ensured. As the main idea in molding is to produce an object which retains the dimensions of the cavity, this condition of a perfect mechanical contact is met till the molding shrinks away from the walls of the cavity, usually after the pressure reaches the atmospheric value. Evidence of good contact between the transducer and the polymer has been obtained by noting the mark left by the boundaries between the transducer and the cavity in the moldings.

5.2.6 Summary

1. Good agreement is obtained between experimental and calculated cooling times.
2. The shape of the pressure curves is different for polyethylene and polystyrene.
3. Pressure gradients are maintained in the cavity throughout the cooling stage.
4. The value assigned for the effective heat transfer coefficient is crucial. It seems that the coefficient for polystyrene is half that for polyethylene.
5. The cooling stage cannot predict residual pressure possibly due to the inadequacy of the equation of state for short cooling times.

6. COMPOSITE CYCLE

When the three parts of the pressure-time curve are combined, the composite curve for the overall injection molding cycle is obtained. Figures 6-1 and 6-2 give the calculated and experimental composite pressure-time curves for polyethylene and polystyrene for case 2 and case 10, respectively. The experimental values of pressure are the values recorded at the four transducer positions. The calculated values for the filling stage have been obtained to correspond to the four transducer positions. Since the packing stage is relatively short all experimental and theoretical lines collapse on a single line for the time scale employed in these graphs. It is obvious that both the theoretical and experimental curves conform to the standard forms reported in the injection molding literature (6,7,8). Furthermore, the general agreement between experimental and calculated results is good. Thus it may be concluded that the proposed computer simulation of the different stages of the injection molding process is realistic.

It can be seen from the composite curves that the cooling stage is four to five times longer than the filling and packing stages combined for case 2, and about seven times longer for case 10. As the filling stage becomes shorter (cases 3, 4, 7, 8, 11, 12) this ratio becomes larger,

FIGURE 6-1

COMPOSITE PRESSURE-TIME CURVE

CASE 2

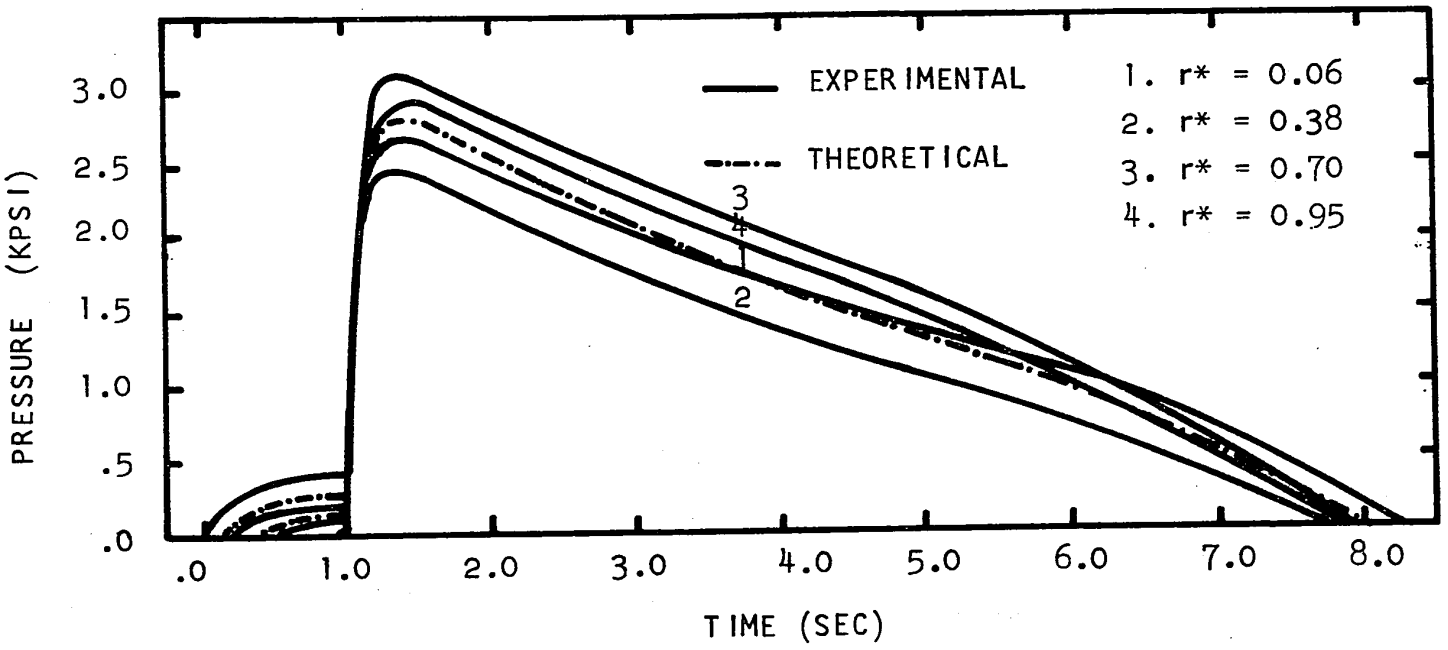

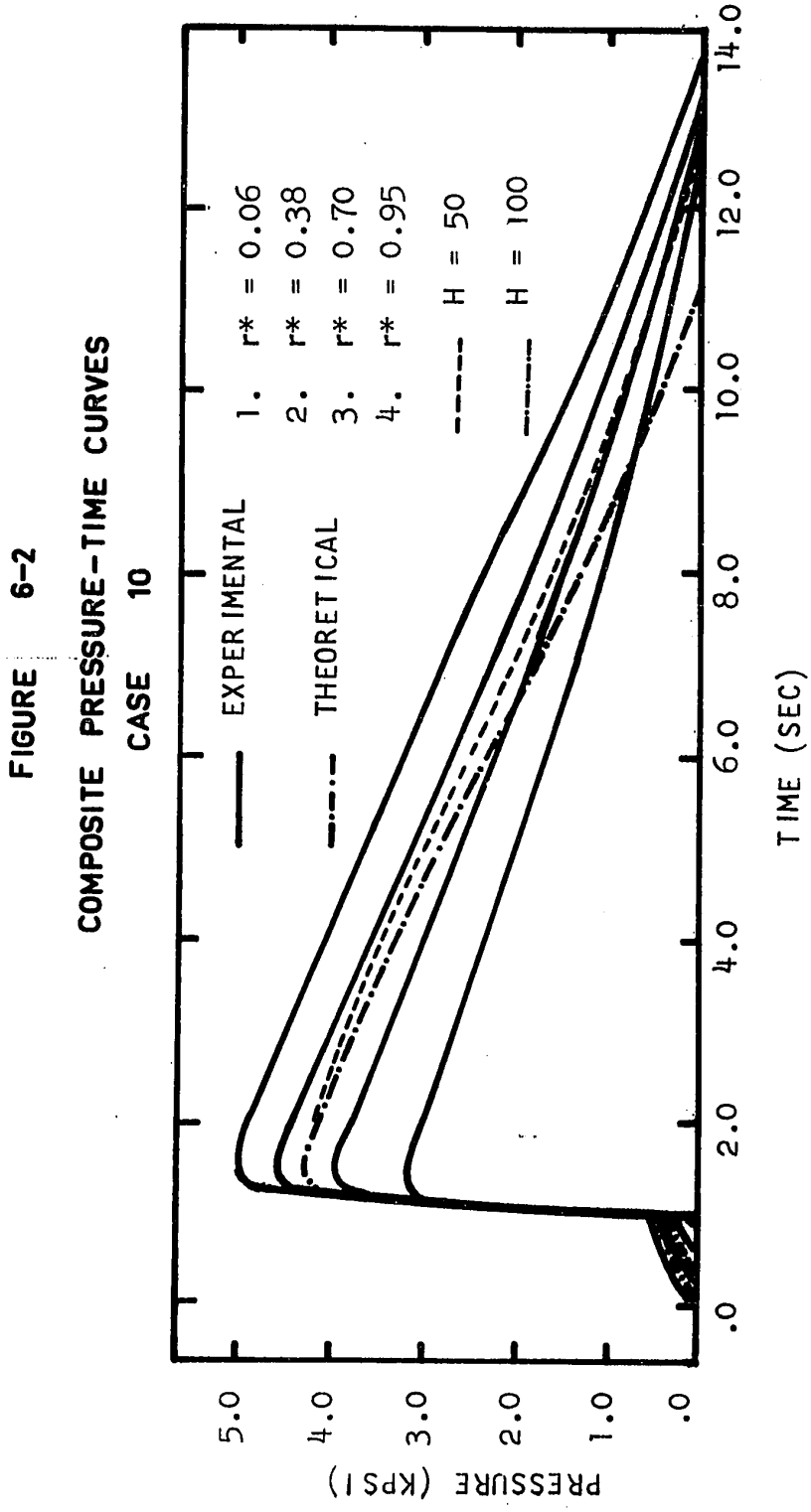

FIGURE 6-2

COMPOSITE PRESSURE-TIME CURVES

CASE 10

while for longer filling and packing times (cases 1, 5, 9) this ratio becomes smaller. Naturally, this ratio depends on the radius and thickness of the cavity. As the thickness of the cavity increases for the same length of flow, the cooling stage becomes more controlling. Furthermore, the injection conditions may be critical in some cases. For example, it is conceivable that filling and packing may be controlling for small thicknesses and long cavities.

7. REPRODUCIBILITY, ACCURACY AND ERROR ANALYSIS

Any attempt to compare the experimental and calculated results must consider the accuracy and reproducibility of the experimental measurements and the error which is introduced into the theoretical solution by the uncertainty of the material properties and processing conditions which are measured experimentally.

In order to check the overall reproducibility of the experimental set-up as described earlier, experimental measurements taken at different times in the same day, and in different days for the same processing conditions were compared. The different stages in the injection molding cycle were checked at different amplifications of the signal and different chart speeds. The difference between the maximum and minimum measured pressures and the maximum and minimum times did not exceed an average of 2% if taken at the same day. Measurements done at different days deviated up to an average of 5%. These differences can be attributed to the error introduced by the melt and mold temperature controllers with an accuracy level of $\pm 5^{\circ}F$ and the error in setting the pressure control valves. Naturally, differences were smaller for experiments at the same day. The performances of the

pressure transducer, the signal conditioning unit and the recorder were checked separately by following the calibration procedure at different days. Identical calibration curves were obtained, with deviations of less than one half a percent.

The main errors in the pressure-time measurements are attributed to the active area of the transducer which is 6.34% of the radius of the cavity, and the thermal error of the transducer (1 psi/^{o}F) which is estimated to be of a maximum value of 20-25 psi as a result of the temperature rise in the wall, equivalent to a maximum of 20-25^{o}F. These two errors are given graphically in the filling stage where they are most significant. Since very little flow takes place in the packing stage and no flow occurs in the cooling stage, the error due to the area of the transducer is negligible and the thermal error may be neglected except for the latter stages of cooling due to the low values of pressure in these stages.

In addition to the direct errors in pressure-temperature-time measurements, indirect errors may be attributed to viscometric measurements to evaluate the flow index n, the activation energy $\Delta E/R_g$ and the constant A_c in the Power Law for the melts (See Appendix 1, section 9.1). Furthermore, some uncertainty is introduced by the heat transfer coefficient between the polymer and the wall, since the two references consulted give a range of values (31,32).

In the following discussion an error analysis of the above uncertainties will be carried out. Since it is very expensive to check all the variables involved for all these stages in the twelve cases reported and thus obtain a complete statistical error analysis, two cases are followed thoroughly (case 3 and case 11) for polyethylene and polystyrene. The criterion for comparison of the different variables are the respective deviations of filling, packing and cooling times from the nominal values.

As can be seen from Table 7-1, 7-2 and 7-3, the highest deviations exist in the filling stage, where both momentum and heat transfer processes take place. Since these processes are time-dependent and coupled through the temperature dependence of viscosity, the effect of each variable is magnified in this stage. This explains also the higher deviation in the case of polystyrene where the activation energy for viscosity is higher than that of polyethylene.

The effects of the flow index, n, the activation energy, $\Delta E/R_g$, and the constant, A_c, that were evaluated by the double linear fitting (Appendix 1, section 9.1), are lumped into one variable, i.e. viscosity, the absolute average deviation of which was 7.2% for polyethylene and 13.6% for polystyrene. The variation of the wall temperature during the filling stage is estimated to be $10^{o}F$ due to the

TABLE 7-1

ERROR ANALYSIS: FILLING STAGE

	Polyethylene Case 3		Polystyrene Case 11	
	Filling Time (sec)	Deviation %	Filling Time (sec)	Deviation %
Nominal Value	.689	-	.674	-
$\eta + \Delta\eta$**	.788	+ 14.5	.982	+ 30.9
$\eta - \Delta\eta$**	.594	- 13.8	.492	- 27.1
T_o + 10°F	.676	- 1.9	.661	- 1.9
T_o - 10°F	.701	+ 1.7	.686	+ 1.8
T_1 + 10°F	.603	- 12.5	.532	- 21.1
T_1 - 10°F	.784	+ 13.8	.845	+ 25.4
P_f + 25 psi	.634	- 8.0	.584	- 13.3
P_f - 25 psi	.738	+ 7.1	.791	+ 15.9
H = 50*	.611	- 11.3	.573	- 15.0
H = 150*	.759	+ 10.2	.768	+ 14.0
H = ∞	.983	+ 30.0	1.080	+ 58.8

* Units: Btu/°F/hr/ft^2

** $\Delta\eta$ = 7% for polyethylene and 13% for polystyrene

TABLE 7-2

ERROR ANALYSIS: PACKING STAGE

	Polyethylene Case 3		Polystyrene Case 11	
	Packing Time (sec)	Deviation %	Packing Time (sec)	Deviation %
Nominal Value	.3153	-	.4250	-
n + 10%	.2802	- 11.2	.4350	- 1.1
n - 10%	.3503	+ 11.1	.4303	+ 2.4
P_a + 10%	.3102	- 1.6	.4203	- 1.1
P_a - 10%	.3195	+ 1.3	.4291	+ 1.0
Q_o + 10%	.3002	- 4.8	.4153	- 2.3
Q_o - 10%	.3353	+ 6.4	.4454	+ 4.8
T_o + 20°F	.3203	+ 1.6	.4303	+ 1.3
H = 50*	.3303	+ 4.8	.4454	+ 4.8
H = 150*	.3102	- 1.6	.4153	- 2.3
H = ∞	.3053	- 2.0	.4148	- 2.4

* Units: Btu/°F/hr/ft^2

TABLE 7-3

ERROR ANALYSIS: COOLING STAGE

	Polyethylene Case 3		Polystyrene Case 11	
	Cooling Time (sec)	Deviation %	Cooling Time (sec)	Deviation %
Nominal Value	6.35	-	8.40	-
n + 10%	6.35	-	8.40	-
n - 10%	6.35	-	8.40	-
Q_o + 10%	6.35	-	8.40	-
Q_o - 10%	6.35	-	8.40	-
P_a + 10%	6.35	-	8.40	-
P_a - 10%	6.35	-	8.40	-
T_o + 20°F	7.36	+ 15.9	8.83	+ 5.1
H = 50*	8.60	+ 35.4	11.09	+ 32.0
H = 150*	5.40	- 15.0	7.26	- 13.5
H = ∞	3.95	- 39.3	5.3	- 36.9

* Units: Btu/°F/ft^2/hr

temperature rise and is also bounded by a lower limit of $-10^{o}F$. However, these effects are shown to be small. The deviation of the melt temperature was estimated to be $\pm$ $10^{o}F$ due to the uncertainty introduced by the melt temperature controller ($\pm 5^{o}F$) and the cooling and/or viscous heating effects in the channel. The upper and the lower deviations for the injection pressure were estimated to be $\pm$ 5% due to the thermal effect on the pressture transducer. It should be emphasized that the values assigned to the heat transfer coefficient are very important, large deviation occur when perfect thermal contact ($H = \infty$) between the wall and the melt is assumed.

On the average, deviations in the packing stage are smaller than those in the filling stage, due to the fact that the duration of packing is shorter and thus temperature variations are relatively small. The error introduced into the packing stage by the preceding filling stage is represented by the deviations in the initial flow rate and the initial average pressure that are estimated not to exceed 10%. The average error in the evaluation of the flow index, n, has been found to be less than 10% for both resins. The rise of the wall temperature (a maximum of $20^{o}F$) does not seem to change the packing stage significantly, nor does the value assigned to the heat transfer coefficient.

Since the packing and cooling stages are solved by one computer program, the deviations introduced by the packing stage are carried over to the cooling stage. As can be seen from Table 7-3, the cooling stage is not affected by the previous errors in the filling and packing stages due to the fact that the only two variables that effect the cooling stage are the temperature and pressure at the end of packing and these do not change to a large extent, as a result of the errors in the previous two stages. Since cooling is predominantly a heat removal stage, the variables that affect the heat transfer process play the main role. A maximum increase in the wall temperature by $20^{o}F$ affects more the cooling time of polyethylene than that of polystyrene, due to the larger thermal diffusivity of the former resin. The main deviations in the cooling stage are related to the effective heat transfer coefficient between the polymer and the wall cavity. Since the cooling stage is usually the longest stage in the overall injection cycle, it would make the largest contribution to the total deviation.

8. CONCLUSION

8.1 CONCLUSIONS

The filling, packing and cooling stages in the injection molding of thermoplastics may be described adequately by models which permit quantitative treatment of the process through a numerical solution of the equations of continuity, motion and energy.

The filling stage model takes into consideration the non-Newtonian behaviour of the melt, the effect of temperature on density and viscosity, the latent heat of solidification (for crystalline polymers), and the difference in the thermal properties between the solid and the melt. In employing the proposed model, it is necessary to know the pressure-time variation at the entrance to the cavity. The complexity of the injection system, coupled with the lack of dependable data on viscoelastic and entrance-exit phenomena, prevents an accurate treatment based on the pressure-time variations at the injection end. The model gives the filling time, pressure, temperature and velocity profiles as well as flow rates during the filling stage. These results are in good agreement with experimental data for polyethylene and polystyrene.

The proposed model for the packing stage starts with the temperature and pressure profiles at the end of the filling stage, as calculated from the model for that stage. The packing model yields information on the pressure develop-

ment and the variations in temperature and flow rate during packing as functions of time. The model takes into account the non-Newtonian behaviour of the melt, latent heat effects, the difference of thermal properties between the solid and the melt, and the density dependence on both pressure and temperature. It is necessary to have a good estimate of the injection pressure of the melt prior to entering the channel. Calculated results based on the proposed model are in good agreement with experimental data both for polyethylene and polystyrene. These results show a pressure profile in the cavity throughout the packing stage. The profile is apparently due to elastic, wave propagation, back flow and density effects.

The proposed model for the cooling stage starts from the pressure and temperature conditions that exist in the cavity at the end of the packing stage. Although no direct confirmation has been obtained of the calculated temperature profiles, calculated results on the variation of pressure with time are in good agreement with experimental values for polyethylene. Good agreement for polystyrene is obtained when the effective heat transfer coefficient between the polymer and the wall is taken to be half that of polyethylene. Experimental data show that a pressure profile is maintained in the cavity, even at late stages of the cooling step. The cooling stage appears to be the controlling step for the geometry and dimensions of the cavity used in this study.

The composite calculated curves based on the proposed simulation of the overall injection molding process are in qualitative agreement with standard curves reported in the literature. The overall agreement between experimental and theoretical results is good.

8.2 RECOMMENDATIONS

As a result of the present study, the following is recommended:

1. To try to include the extensional stresses in the theoretical solution for the filling stage by using an appropriate constitutive equation for the melt.
2. To try to include in the theoretical solution for the filling stage the dependency of the flow index, n, and the activation energy, $\frac{\Delta E}{R_g}$, on shear rate and temperature.
3. To try and include in the solution for the filling stage the non-linear term $V_r \cdot \frac{\partial V_r}{\partial r}$.
4. To measure pressure at the injection end to confirm the validity of the assumptions made in the packing stage.
5. To use more than one transducer simultaneously in order to check the validity of the pressure profile in the packing and cooling stages.
6. To find a modified equation of state that will include also a time-dependent term; thus relaxation processes may be taken into account.

7. To use different channel geometries, other than sharp edges, to reduce die swell and entrance pressure losses.
8. To use different cavity dimensions in order to check the relative importance of the different stages.
9. To find experimentally the heat transfer coefficient between the polymer and the wall for the materials under study under different conditions.
10. To consider the applicability and extension of the proposed model to cavities of different geometry.

8.3 CLAIMS FOR ORIGINAL WORK

1. The present study is the first attempt to describe theoretically the complete injection molding cycle.
2. The "conventional" method for latent heat treatment has been modified for partially crystalline polymers and has been used throughout the injection molding cycle.
3. The first treatment of the filling stage for a compressible fluid is presented.
4. The experimental data reported in this work are the most complete and detailed data which are available on the filling of semicircular mold cavities by spreading radial flow.

5. The first attempt is made to obtain a quantitative treatment of the packing stage that includes both the thermodynamics and dynamics of the stage.
6. This study has shown for the first time that pressure profiles persist in the cavity during the packing and cooling stages.
7. The calculations presented in this study represent the first time that a short shot has been predicted by a filling stage model and confirmed experimentally.
8. The theoretical composite curves presented in Chapter 6 are the first curves to be calculated theoretically for describing the overall injection molding cycle.

LIST OF SYMBOLS

a	entrance radius
a^*	dimensionless entrance radius
A	dimensionless number = $\frac{\Delta t^*}{\Delta z^{*2} \times Pr \times Re}$
A_c	constant in the viscosity least square fitting
A_r	dimensionless number = h/R_o
A_1	dimensionless number = $\frac{H \times \Delta z}{k_t}$
b	constant in the equation of state
Br	Brinkman number
B_1	dimensionless number = $\frac{\alpha_s \times \Delta t}{\Delta z^2}$
B_2	dimensionless number = $\frac{\alpha_m \times \Delta t}{\Delta z^2}$
Cp	specific heat
Cp_a	average specific heat
C_1	constant independent on r
C_2	constant independent on r
D	diameter of capillary
D_1	constant coefficient
D_2	constant coefficient
D_3	constant coefficient

E	constant coefficient
F	constant coefficient
Fr	fraction
h	half thickness of the cavity
$h_{(j)}$	jth term in the Trapezoidal integration
H	heat transfer coefficient
H_{ℓ}	ℓth coefficient in infinite series
i	ith radial ring
I	number of radial rings
I_1	first integral
I_2	second integral
j	jth axial increment
J	number of axial increments
k	kth time increment
k_t	thermal conductivity
K	constant
ℓ	integer number
ℓ_1	integer number
L	latent heat of freezing
L_c	length of capillary
m	melt region
M	consistency index
n	flow index

N	dimensionless coefficient in the momentum equation
P	pressure
P^*	dimensionless pressure
P_a	average pressure
P_f	experimentally measured pressure at the entrance to the cavity at the end of filling
Pr	Prandtl number
P_o	experimental measured pressure at the entrance to the cavity
Q_m	mass flow rate
Q_t	volumetric flow rate
Q_T	heat conducted
Q_o	flow rate at the beginning of the packing stage
Q^*	dimensionless flow rate
r	radial co-ordinate
r^*	dimensionless radial co-ordinate
R	melt front location
R^*	dimensionless melt front location
R_c	constant in the equation of state
R_g	gas constant for polymer viscosity
R_o	radius of cavity
s	solid region

t	time
t^*	dimensionless time
T	temperature
T^*	dimensionless temperature
T_a	average temperature
T_d	delayed temperature
T_{eq}	equivalent temperature
T_F	freezing temperature
T_F^*	dimensionless freezing temperature
T_I	melt temperature at the cavity entrance
T_{LF}	lower limit of freezing range
T_u	undelayed temperature
V	specific volume
V_ℓ	equivalent velocity
V_r	radial velocity
V^*	dimensionless radial velocity
z	axial co-ordinate
z^*	dimensionless axail co-ordinate
Z	function dependent on z only

Greek Letters

α	thermal diffusivity
β	dimensionless number = $\frac{\Delta t^*}{\Delta z^{*2}}$
γ	dimensionless number = $\frac{\Delta t^*}{\Delta r^*}$
$\dot{\gamma}$	shear rate
$\dot{\gamma}_a$	apparent shear rate
$\dot{\gamma}_t$	true shear rate
ΔE	viscosity activation energy
ΔH_f	enthalpy of solidification
ΔP_d	deviation between the calculated pressure at the melt front and atmospheric pressure
ΔP_t	difference between the pressure in the reservoir and the cavity at time t
ΔP_o	difference between the pressure in the reservoir and the cavity at time zero
ΔP_{11}	assumed pressure drop during the first iteration
ΔP_{12}	assumed pressure drop during the second iteration
Δr	radial increment
Δr^*	dimensionless radial increment
Δt	time increment
Δt^*	dimensionless time increment
Δz	axial increment
Δz^*	dimensionless axial increment

$\underset{\approx}{\Delta}$	rate of deformation tensor
ϵ	axial co-ordinate of freezing front
ϵ^*	dimensionless axial co-ordinate of freezing front
η	non-Newtonian viscosity
η_a	apparent viscosity
η_t	true viscosity
θ	capillary entrance angle
λ	extensional viscosity
λ_1	constant
μ	Newtonian viscosity
ρ	density
ρ^*	dimensionless density
ρ_a	average density
ρ_e	melt density before entering the cavity
ρ_o	initial density in packing stage
τ	function dependent on t only
τ_{rr}	component of the stress tensor
τ_{rz}	component of the stress tensor
$\tau_{\theta\theta}$	component of the stress tensor
$\underset{\approx}{\pi}$	stress tensor
ϕ	function independent on $r (= V_r \times r)$
ϕ^*	dimensionless function independent on $r^* (= V_r^* \times r^*)$
ω	constant in the equation of state

REFERENCES

1. Z. Tadmor and I. Klein, "Engineering Principles of Plasticating Extrusion", Van Nostrand Reinhold Co., N.Y. (1970).

2. "Symposium on the Theory of Plastics Extrusion", Ind. Eng. Chem., 45, 969-993 (1953).

3. E.C. Bernhardt, "Processing of Thermoplastic Materials", pp. 154-307, Reinhold Pub. Co., N.Y. (1959).

4. J.M. McKelvey, "Polymer Processing", John Wiley and Sons Inc., N.Y., 228-298 (1962).

5. E.G. Fisher, "Extrusion of Plastics", Iliffe Book Ltd., London (1958).

6. C.E. Beyer and R.S. Spencer, "Rheology, Theory and Application", (F.R. Eirich Editor), 3, p. 510, Academic Press Inc. Pub., N.Y. (1960).

7. J.M. McKelvey, "Polymer Processing", p.340, John Wiley, New York, N.Y. (1962).

8. E.C. Bernhardt, "Processing of Thermoplastic Materials", p. 308, Reinhold Pub. Corp. N.Y. (1959).

9. J.R.A. Pearson, "Mechanical Principles of Polymer Melt Processing", p. 128, Pergamen Press, New York (1966).

10. J.L. Berger and C.G. Gogos, S.P.E. Technical Papers, 17, 1 (1971).

11. _____, Canadian Plastics, (2), 23 (1971).

12. _____, Modern Plastics, 48(1), 65 (1972).

13. R.L. Ballman, T. Shusman and H.L. Toor, Ind. Eng. Chem., 51(7), 847 (1959).

14. Y.N. Kazankov and N.I. Basov, Mech. Polim., 1, 157 (1968) Russ.

15. V.N. Grinblat, Penerbatka Plasticheskish Mass., 28 (1968) Russ.

16. R.S. Spencer and G,D. Gilmore, J. Coll. Sci., 6(2), 118 (1951).

17. W. Bauer, Kunststoffe, 53, 210 (1963) Ger.

18. I.T. Barrie, Plastics and Polymers, 37, 463 (1969).

19. I.T. Barrie, Plastics and Polymers, 38, 47 (1970).

20. D.H. Harry and R.G. Parrott, S.P.E. Technical Papers, 15, 448 (1969).

21. D.H. Harry and R.G. Parrott, Polym. Eng. Sci., 10(4), 209 (1970).

22. W.Z. Gloor, S.P.E., Transactions, 3, 270 (1963).

23. S. Kenig and M.R. Kamal, S.P.E. Journal, 26(7), 50 (1970).

24. S. Kenig and M.R. Kamal, Can. J. Chem. Eng., 49, 210 (1971).

25. D.D. Perlmutter, "Introduction to Chemical Process Control", p. 7, John Wiley and Sons Inc., N.Y. (1965).

26. R.G. Nagler, J. Appl. Polym. Sci., 9, 811 (1965).

27. E.C. Bernhardt, Editor, "Processing of Thermoplastic Materials", p. 594, Reinhold Pub. Corp., N.Y. (1959).

28. E. Baer and J.L. Karados, J. Polym. Sci., 3, 2827 (1965).

29. R.H. Shoulberg, J. App. Polym. Sci., 7, 1597 (1963).

30. E.C. Bernhardt, Editor, "Processing of Thermoplastic Materials", p. 630, Reinhold Pub. Corp., N.Y. (1959).

31. C.H. Jepson, Ind. Eng. Chem., 45(5), 992 (1953).

32. F. Carley, Polym. Eng. Sci., 6(2), 158 (1966).

33. R.B. Bird, W.E. Stewart and E.N. Lightfoot, "Transport Phenomena", p. 83-85, John Wiley and Sons Inc., N.Y. (1966).

34. Ibid., p. 318.

35. H.S. Carslaw and J.C. Jaeger, "Conduction of Heat in Solids",pp. 282-298, 2nd Ed., Oxford University Press (1959).

36. R.S. Spencer and R.D. Gilmore, J. Appl. Phys., 20, 502 (1949).

37. B. Carnaham, H.A. Luther and J.O. Wilkes, "Applied Numerical Methods", pp. 432-448, John Wiley, New York, N.Y. (1969).

38. G.D. Smith, "Numerical Solution of Partial Differential Equations", Oxford University Press, London (1965).

39. B. Carnaham, H.A. Luther and J.O. Wilkes, "Applied Numerical Methods", p. 451, John Wiley, New York, N.Y. (1969).

40. M. Abramovitz and L.A. Stegum, Editors, "Hand Book of Mathematical Functions", p. 885, National Bureau of Standards (1968).

41. R.E. Gee and J.B. Lyon, Ind. Eng. Chem., 49(6), 956 (1957).

42. G.D. Smith, "Numerical Solution of Partial Differential Equations", p. 24, Oxford University Press, London (1965).

43. S.W. Churchill, Chem. Eng. Prog., 66(7), 86 (1970).

44. B. Carnaham, H.A. Luther and J.O. Wilkes, "Applied Numerical Methods", pp. 474-481, John Wiley, New York, N.Y. (1969).

45. I.T. Barrie, S.P.E. Technical Papers, 17, 251 (1971).

46. S.L. Hoyt, Editor, "ASME Handbook - Material Properties", p. 71, McGraw-Hill Book Company, N.Y. (1954).

47. D.F. Miner and J.B. Seastone, Editors, "Handbook of Engineering Materials", p. 4-144, John Wiley and Sons Inc., London (1955).

48. F.N. Cogswell and P. Lamb, Plastics and Polymers, 38, 331 (1970).

49. R.B. Bird, W.E. Stewart and E.N. Lightfoot, "Transport Phenomena", p. 356, John Wiley and Sons Inc., N.Y. (1966).

50. R.S. Spencer and R.D. Gilmore, Modern Plastics, 27, 143 (1950).

51. R.B. Bird, W.E. Stewart and E.N. Lightfoot, "Transport Phenomena", p. 103, John Wiley and Sons Inc., N.Y. (1966).

52. I. Klein and D.I. Marshall, Editors, "Computer Programs for Plastic Engineers", pp. 73-92, Reinhold Book Corp., N.Y. (1968).

53. R.A. Mandelson, Polym. Eng. Sci., 9(5), 350 (1969).

54. M.D. Murray and F. Landis, Trans. ASME 81C, 106 (1959).

55. P.H. Price and M.R. Slack, Brit. J. Appl. Phys. 5, 285 (1954).

56. J.M. Dealy, Polym. Eng. Sci., 11(6), 433 (1971).

9. APPENDICES

9.1 APPENDIX 1: CONSTITUTIVE EQUATION AND VISCOSITY

In order to solve the equations of change (3-2) and (3-3) a rheological equation of state, which relates the stress tensor to the velocity field, is required.

A large volume of data available in the literature indicate that the "Power-Law" model is successful in describing the stress-rate of strain relationship in the polymer melts, especially in narrow shear rate ranges. The general form of this model is given by (51).

$$\underline{\underline{\tau}} = -\left\{M \left| \left[1/2\ (\underline{\underline{\Delta}}:\underline{\underline{\Delta}})\right]^{1/2}\right|^{n-1}\right\}\underline{\underline{\Delta}} \qquad \ldots\ldots(9\text{-}1)$$

Where $\underline{\underline{\tau}}$ and $\underline{\underline{\Delta}}$ are the deviative stress tensor and the rate of deformation tensor, respectively; M and n are constants. The non-vanishing components of the stress tensor, for the radial flow case are:

$$\tau_{rr} = -2\left\{M \left| \left[1/2(\underline{\underline{\Delta}}:\underline{\underline{\Delta}})\right]^{1/2}\right|^{n-1}\right\}\frac{\partial V_r}{\partial r} \qquad \ldots\ldots(9\text{-}2)$$

$$\tau_{\theta\theta} = -2\left\{M \left| \left[1/2(\underline{\underline{\Delta}}:\underline{\underline{\Delta}})\right]^{1/2}\right|^{n-1}\right\}\frac{V_r}{r} \qquad \ldots\ldots(9\text{-}3)$$

$$\tau_{rz} = \tau_{zr} = -\left\{M \left| \left[1/2(\underline{\underline{\Delta}}:\underline{\underline{\Delta}})\right]^{1/2}\right|^{n-1}\right\}\frac{\partial V_r}{\partial z} \qquad \ldots(9\text{-}4)$$

Where $1/2(\underline{\underline{\Delta}}:\underline{\underline{\Delta}}) = 2(\frac{\partial V_r}{\partial r})^2 + 2(\frac{V_r}{r})^2 + (\frac{\partial V_r}{\partial z})^2$ .....(9-5)

The mathematical complexity inherent in this formulation makes the solution of the boundary value problem equations (3-1), (3-2) and (3-3) almost impossible. Thus, further simplification is needed. It is assumed that the rate of change of the velocity V_r with respect to the radial direction, r, is much smaller then its rate of change in the z-direction (For relative magnitudes see Appendix 7, section 9.7). As a result:

$$\tau_{rr} = \tau_{\theta\theta} = 0 \qquad .....(9-6)$$

and

$$\tau_{rz} = -M(\frac{\partial V_r}{\partial z})^n \qquad .....(9-7)$$

Equations (9-6) and (9-7) describe a "Simple Shear Flow". However, the above simplifications and assumptions can lead to inaccuracies in the final solution, especially in the regions close to the entrance to the cavity, where the velocity gradient in the radial direction cannot be neglected (see Appendix 7, section 9.7). In addition, the extensional stress $\tau_{\theta\theta}$ may play an important role in the entrance regions (48). The latter problem can be solved by using a constitutive equation which relates the extensional stresses to the velocity field. Since it is very difficult to find such an equation for

polymer melts, this approach is abandoned in the present work. As a result some deviations are anticipated in the entrance region in the mold cavity.

Equation (9-7) can be expressed in terms of the apparent viscosity by

$$\eta_a = M \left|\dot{\gamma}_a\right|^{n-1} \qquad \text{.....(9-8)}$$

and by assuming an Ahrenius-type dependence on temperature

$$\eta_a = A_c \ell^{\Delta E/RgT} \left|\dot{\gamma}_a\right|^{n-1} \qquad \text{.....(9-9)}$$

where $\dot{\gamma}_a = \frac{\partial V_r}{\partial z}$, A_c is a constant independent of temperature and $\Delta E/R_g$ is the activation energy for viscosity. In order to evaluate the constants in equation (9-9), viscometric measurements were made on the materials under study with the aid of the Instron Capillary Rheometer. In these measurements two capillaries were used:

1. D = 0.052 inch and L_c = 1.04 inch (L_c/D = 20) entrance angle $\theta = 90^o$.
2. D = 0.052 inch and L_c = 3.12 inch (L_c/D = 60) entrance angle $\theta = 90^o$.

Where L_c is the length and D is the diameter of the capillary. Measurements were taken for Dow Chemicals polyethylene E.P. 245 in the temperature range of 130-190°C and for Dow Chemicals polystyrene Styren 683 in the temperature range 160-230°C.

The lower limit indicates the temperature below which the viscosities are too high to be measured and these were the freezing temperatures employed in equation (3-13).

The Rabinowitsch-Mooney-Weissenberg Correction was applied and thus true viscosity values were obtained (52). The use of the true shear rate and true viscosity was very important since the viscometric measurements were conducted in a capillary where axial flow exists for utilization in a radial flow system. No Bagley corrections were needed (52) since measurements were taken with high L_c/D ratios.

Figure 9-1 shows the viscosity as function of shear rate for different temperatures for polyethylene based on 161 measured values (not all of them shown). Figure 9-2 shows the same representation for polystyrene based on 111 measured values (not all of them shown). From the diagrams, it is apparent that the curves are not linear. Thus a single n cannot describe the flow behaviour of the melt in the entire temperature-shear rate range. A careful analysis shows that n and $\Delta E/R_g$ are functions of both shear rate and temperature. From the results, it seems unlikely that a single shift factor would be satisfactory to superpose all the different temperature curves to a single master curve, as reported by some workers (53). However, in order to simplify the computational procedures, it is desirable that a single n and a single $\Delta E/R_g$ describe the flow behaviour. Taking n and $\Delta E/Rg$ to be

FIGURE 9-1

VISCOSITY AS FUNCTION OF SHEAR RATE AND TEMPERATURE
POLYETHYLENE E.P. 245

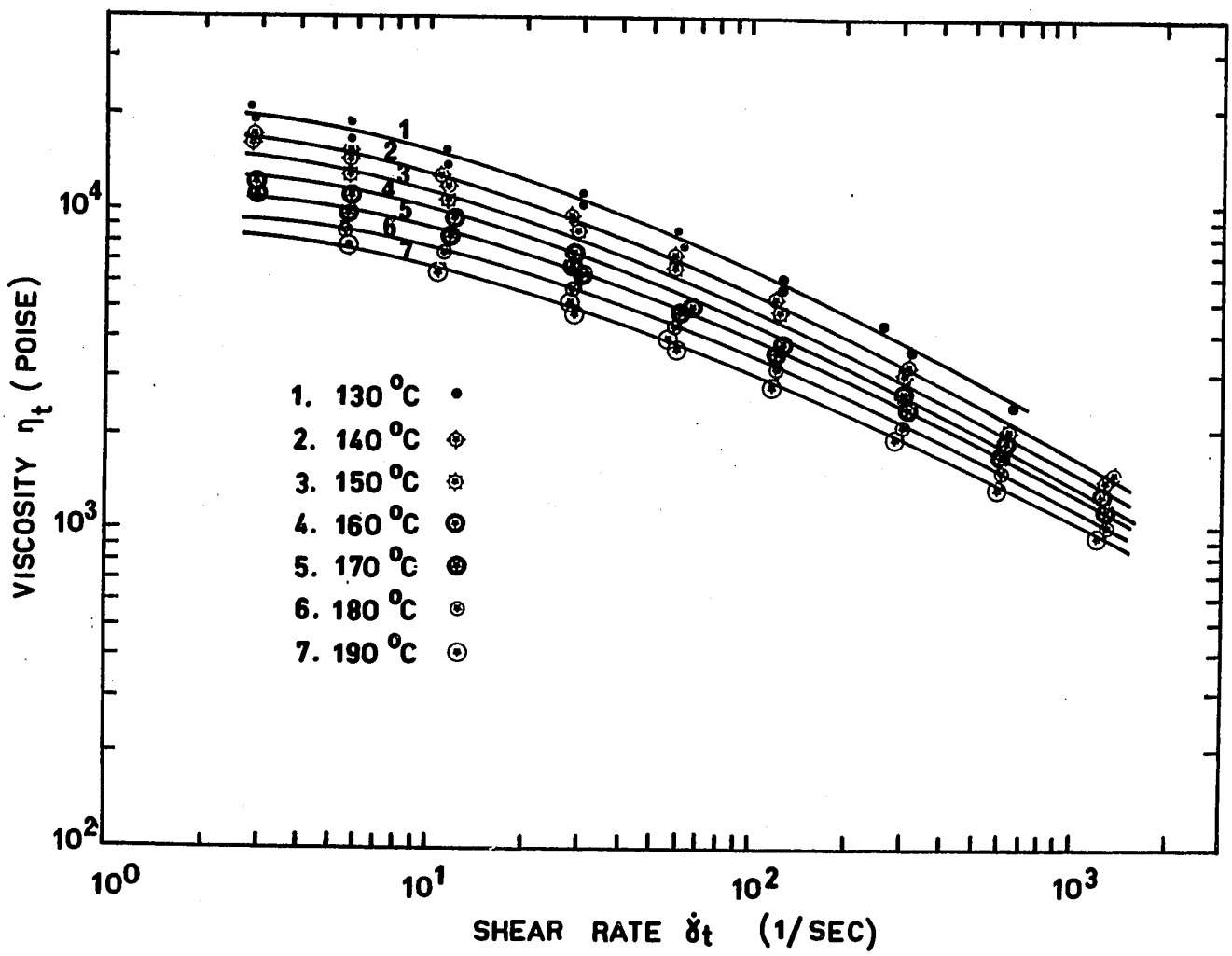

FIGURE 9-2

VISCOSITY AS FUNCTION OF SHEAR RATE AND TEMPERATURE
POLYSTYRENE STYRON 683

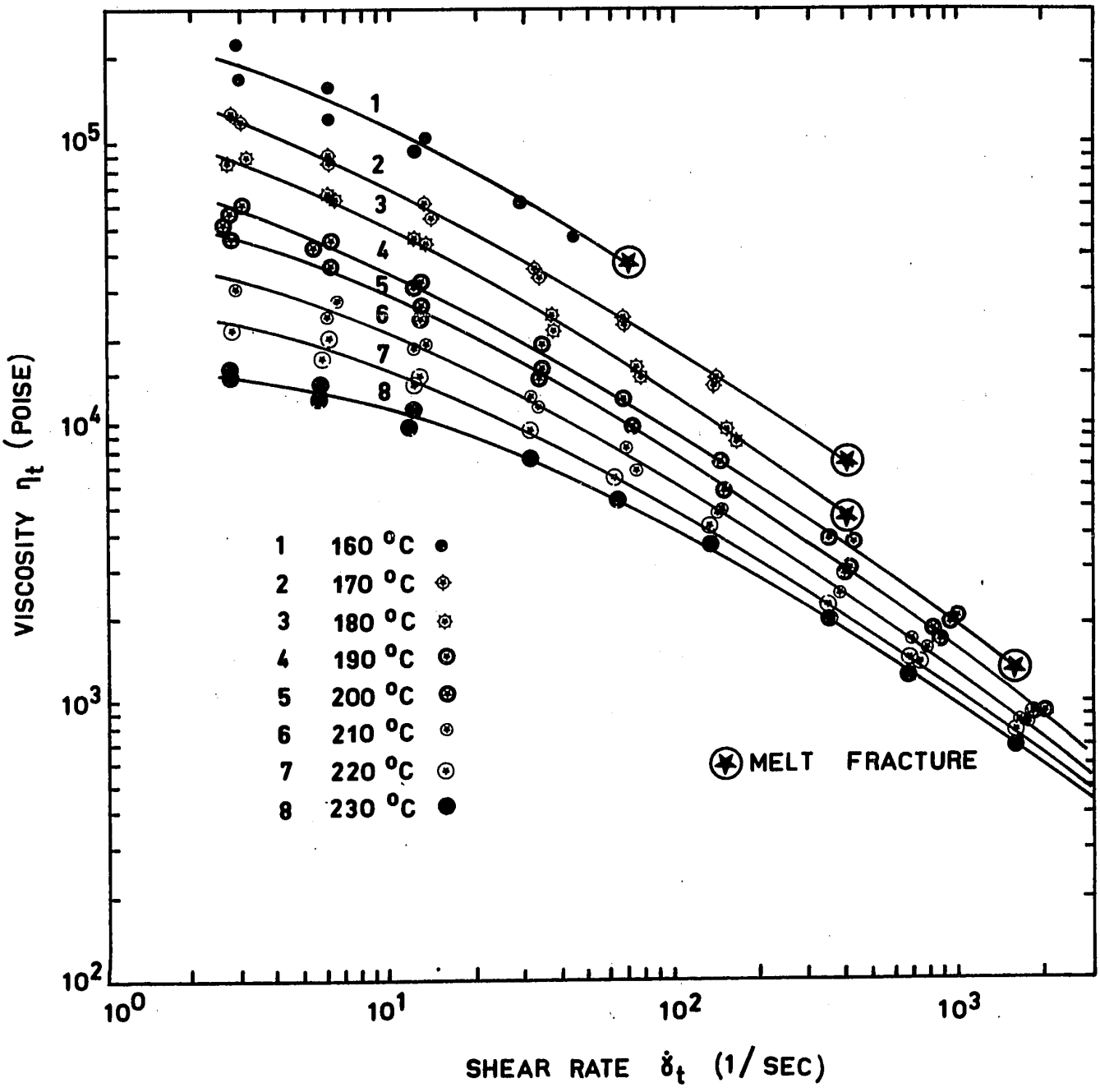

functions of both shear rate and temperature would result in an iteration at each radial position for the computation of the velocity profile.

In order to find the best single n, the viscosity data for log η_t vs. log $\dot{\gamma}_t$ were fitted by linear least squares using all 161 points for polyethylene and 111 points for polystyrene. The result for polyethylene was n = 0.594 and for polystyrene n = 0.368. From equation (9-8), it follows that a plot of [log η_t - (n - 1) log $\dot{\gamma}_t$] vs. 1/T would give $\Delta E/R_g$ from the slope, and A_c from the intercept. Thus a second linear least squares fitting was carried out using all measured values. For polyethylene the result was: $\Delta E/R_g$ = 2300 $1/^oK$ and $A_c = 8.53 \times 10^5$ lb/ft/hr^{n-2}. For polystyrene $\Delta E/R_g$ = 5910 $1/^oK$ and $A_c = 2.14 \times 10^4$ in the same units as above.

The resultant equations are:

For polyethyelen: $$\eta_t = 8.53 \times 10^5 \times \exp(2300/T) \times \dot{\gamma}_t^{(-0.406)} \quad \text{.....(9-10)}$$

For polystyrene: $$\eta_t = 2.14 \times 10^4 \times \exp(5910/T) \times \dot{\gamma}_t^{(-0.632)} \quad \text{.....(9-11)}$$

Where η_t is in units of lb/ft/hr, T in ^oK and $\dot{\gamma}_t$ in hr^{-1}.

In order to find the standard deviation, the average deviation and the mean, the experimental shear rates at each temperature were substituted into equations (9-10) and (9-11) for polyethylene and polystyrene, respectively, and the

calculated viscosities were compared with the corresponding experimental ones. The mean of population for polyethylene 1.59×10^6 lb/ft/hr with a standard deviation over the mean of 1.51% and an average deviation over the mean of 7.2%. For polystyrene the mean was 6.44×10^6 lb/ft/hr with a standard deviation of 3.81% and an average deviation of 13.6%.

9.2 APPENDIX 2: ANALYTICAL SOLUTION OF A SIMPLIFIED RADIAL FLOW PROBLEM

As indicated earlier, the fact that the equations of change are coupled and need to be solved simultaneously makes the analytical solution of the present problem impossible. However, if one considers the isothermal flow of an incompressible Newtonian fluid, which is contained between semi-circular plates, the continuity and momentum equations may be solved analytically to give expressions for the pressure and velocity profiles as functions of time and distance resulting from a constant pressure applied to the entrance at time zero. This analytical solution is equivalent to one step in the filling of a circular cavity, and thus will be helpful in demonstrating the fact that the establishment of steady-state in momentum transfer is very fast compared with the duraction of filling.

The equations to be solved are:

Continuity: $$\frac{\partial}{\partial r^*}\left(r^* \times V_r^*\right) = 0 \qquad \text{.....(9-12)}$$

Momentum: $$\frac{\partial V_r^*}{\partial t^*} = -\frac{\partial P^*}{\partial r^*} A_r + \frac{1}{Re}\frac{\partial^2 V_r^*}{\partial z^{*2}} \qquad \text{.....(9-13)}$$

Where $Re = \frac{V_e \times \rho_m \times h}{\mu}$, μ is the Newtonian viscosity and ρ_m is a reference density.

With the following boundary and initial conditions:

$$V_r^* (r^*, \pm 1, t^*) = 0 \quad \text{.....(9-14)}$$

$$\frac{\partial V_r^*}{\partial z^*} (r^*, 0, t^*) = 0 \quad \text{.....(9-15)}$$

$$V_r^* (a^*, z^*, 0) = 0 \quad \text{.....(9-16)}$$

$$P^* (a^*, t^*) = 1 \quad \text{.....(9-17)}$$

$$P^* (1, t^*) = 0 \quad \text{.....(9-18)}$$

By integration of (9-12) we obtain:

$$V_r^* \cdot r^* = \phi^* = \text{constant} \quad \text{.....(9-19)}$$

and

$$V_r^* = \frac{\phi^*}{r^*} \quad \text{.....(9-20)}$$

Substituting (9-19) and (9-20) into (9-13) yields:

$$\frac{1}{r^*} \frac{\partial \phi^*}{\partial t^*} = - \frac{\partial P^*}{\partial r^*} A_r + \frac{1}{Re \times r^*} \frac{\partial^2 \phi^*}{\partial z^{*2}} \quad \text{.....(9-21)}$$

Integrating (9-21) with respect to r* (ϕ^* = const.):

$$- A_r = \left(\frac{1}{Re} \frac{\partial^2 \phi^*}{\partial z^{*2}} - \frac{\partial \phi^*}{\partial t^*}\right) \times \ell n \left(\frac{R_o}{a}\right) \qquad \ldots\ldots\ldots(9\text{-}22)$$

$$\frac{\partial \phi^*}{\partial t^*} - \frac{1}{Re} \frac{\partial^2 \phi^*}{\partial z^{*2}} = \frac{A_r}{\ell n \frac{R_o}{a}} = K \qquad \ldots\ldots\ldots(9\text{-}23)$$

The equation to solve is:

$$\frac{\partial \phi^*}{\partial t^*} = \frac{1}{Re} \frac{\partial^2 \phi^*}{\partial z^{*2}} + K \qquad \ldots\ldots\ldots(9\text{-}24)$$

Assuming that:

$$\phi^*(z^*, t^*) = \phi^*_\infty - \phi^*_t(t^*, z^*) \qquad \ldots\ldots\ldots(9\text{-}25)$$

a. $$t^* \to \infty \to \phi^*_\infty \to \frac{\partial \phi^*}{\partial t^*} = 0 \qquad \ldots\ldots\ldots(9\text{-}26)$$

(9-23) and (9-24) give:

$$0 = \frac{1}{Re} \frac{\partial^2 \phi^*_\infty}{\partial z^{*2}} + K \qquad \ldots\ldots\ldots(9\text{-}27)$$

$$\frac{\partial \phi^*_\infty}{\partial z^*} = - K \times Re \times z^* + D_1 \qquad \ldots\ldots\ldots(9\text{-}28)$$

Boundary conditions (9-15) $\to D_1 = 0$ $\qquad \ldots\ldots\ldots(9\text{-}29)$

$$\phi^*_\infty = - \frac{K\, Re\, z^{*2}}{2} + D_2 \qquad \ldots\ldots\ldots(9\text{-}30)$$

Boundary condition (9-14) $\rightarrow D_2 = \frac{K \cdot Re}{2}$ .....(9-31)

$$\phi^*_\infty = \frac{K \cdot Re}{2} (1 - z^{*2}) \quad .....(9\text{-}32)$$

Substituting (9-32) into (9-25) and then into (9-24):

b. $$\frac{\partial \phi^*_t}{\partial t^*} (t^*, z^*) = \frac{1}{Re} \frac{\partial^2 \phi^*_t}{\partial z^{*2}} \quad .....(9\text{-}33)$$

Using the method of separation of variables:

$$\phi^*_t = \tau \cdot Z \quad .....(9\text{-}34)$$

Substituting into (9-33) and dividing by $\tau \times Z$:

$$\frac{1}{\tau} \frac{\partial \tau}{\partial t^*} = \frac{1}{Re} \frac{1}{Z} \frac{\partial^2 Z}{\partial z^{*2}} = -\lambda_1^2 \quad .....(9\text{-}35)$$

I. Left hand side $\rightarrow$ $\tau = D_3 \times \exp(-\lambda_1^2 \times t^*)$ .....(9-36)

II. Right hand side $\rightarrow$ $Z = E \sin(\lambda_1 Re^{\frac{1}{2}} z^*) + F \cos(\lambda_1 Re^{\frac{1}{2}} z^*)$

.....(9-37)

Boundary condition (9-15) $\rightarrow E = 0$

Boundary condition (9-14) $\rightarrow 0 = F \cos(\lambda_1 Re^{\frac{1}{2}})$ .....(9-38)

From equation (9-38): $\cos(\lambda_1 Re^{\frac{1}{2}}) = 0 \rightarrow \lambda_1 Re^{\frac{1}{2}} = (\ell + \frac{1}{2}) \times \pi$

.....(9-39)

From equation (9-39): $\lambda_1 = \frac{(\ell + \frac{1}{2})\pi}{Re^{\frac{1}{2}}}$ $\ell = 0, 1, 2, \ldots,$ (9-40)

(9-34), (9-35), (9-36) and (9-40) give:

$$\phi_t^* = \sum_{\ell=0}^{\infty} H_\ell \exp\left[-(\ell + \tfrac{1}{2})^2 \frac{\pi^2}{Re} \times t^*\right]$$

$$\times \cos\left[(\ell + \tfrac{1}{2}) \times \pi \times z^*\right] \qquad \ldots\ldots\ldots(9\text{-}41)$$

Where $H_\ell = D_\ell \times F_\ell$

From the initial condition (9-16) (at $t^* = 0 \rightarrow \phi_t^*(z^*, t^*) = \phi_\infty^*$ so that $\phi^* = 0$)

$$\frac{K \times Re}{2}[(1 - z^{*2})] = \sum_{\ell=0}^{\infty} H_\ell \cos[(\ell + \tfrac{1}{2}) \times \pi \times z^*]$$

$\ldots\ldots\ldots(9\text{-}42)$

Multiplying both sides by $\cos[(\ell_1 + \frac{1}{2}) \times \pi \times z^*]$ and integrating between -1 and +1:

$$\text{Right hand side} = H_\ell \left[\frac{\frac{1}{2}(\ell_1+\frac{1}{2})\pi z^* + \frac{1}{4}\sin(\ell_1+\frac{1}{2})2\pi z^*}{(\ell_1 + \frac{1}{2})\pi}\right]_{z^*=-1}^{z^*=+1}$$

$\ldots\ldots\ldots(9\text{-}43)$

$$\text{Left hand side} = \int_{-1}^{+1} \frac{KRe}{2}[(1 - z^{*2})] \times \cos[(\ell_1 + \tfrac{1}{2})\pi z^*]dz^*$$

$$= \frac{K \cdot Re}{2}\left(-\frac{2}{(\ell_1+\frac{1}{2})\pi} + \frac{4}{(\ell_1+\frac{1}{2})^3\pi^3} + \frac{2}{(\ell_1+\frac{1}{2})\pi}\right)$$

$\ldots\ldots\ldots(9\text{-}44)$

Equations (9-44) and (9-43) give:

$$H_\ell = \frac{K\,Re}{2} \times \frac{4(-1)^\ell}{(\ell + \frac{1}{2})^3 \pi^3} \qquad \text{.....(9-45)}$$

Substituting all above coefficients and results into (9-25);

$$\phi^* = \frac{KRe}{2}\left\{[1-z^{*2}] - \sum_{\ell=0}^{\infty} 4 \times \frac{(-1)^\ell}{(\ell + \frac{1}{2})^3 \pi^3}\right.$$

$$\times \exp[-(\ell + \tfrac{1}{2})^2 \times \frac{\pi^2}{Re} \times t^*]$$

$$\left. \times \cos[(\ell + \tfrac{1}{2})\,\pi\, z^*]\right\} \qquad \text{.....(9-46)}$$

Rearranging equation (9-13):

$$\frac{dP^*}{dr^*} A_r = \frac{1}{Re} \frac{1}{r^*} \frac{\partial^2 \phi^*}{\partial z^{*2}} - \frac{1}{r^*} \frac{\partial \phi^*}{\partial t^*} \qquad \text{.....(9-47)}$$

Substituting the appropriate expressions for the partial derivatives according to (9-46) gives the simple result:

$$\frac{dP^*}{dr^*} = -\frac{1}{\ell n\,(\frac{R_o}{a})} \times \frac{1}{r^*} \qquad \text{.....(9-48)}$$

Integrating (9-48) gives:

$$1 - P^*_{(r^*)} = \ell n\,(\frac{r^*}{a^*}) / \ell n\,(\frac{R_o^*}{a^*}) \qquad \text{.....(9-49)}$$

FIGURE 9-3

UNSTEADY STATE VELOCITY PROFILES
FOR ANALYTICAL SOLUTION

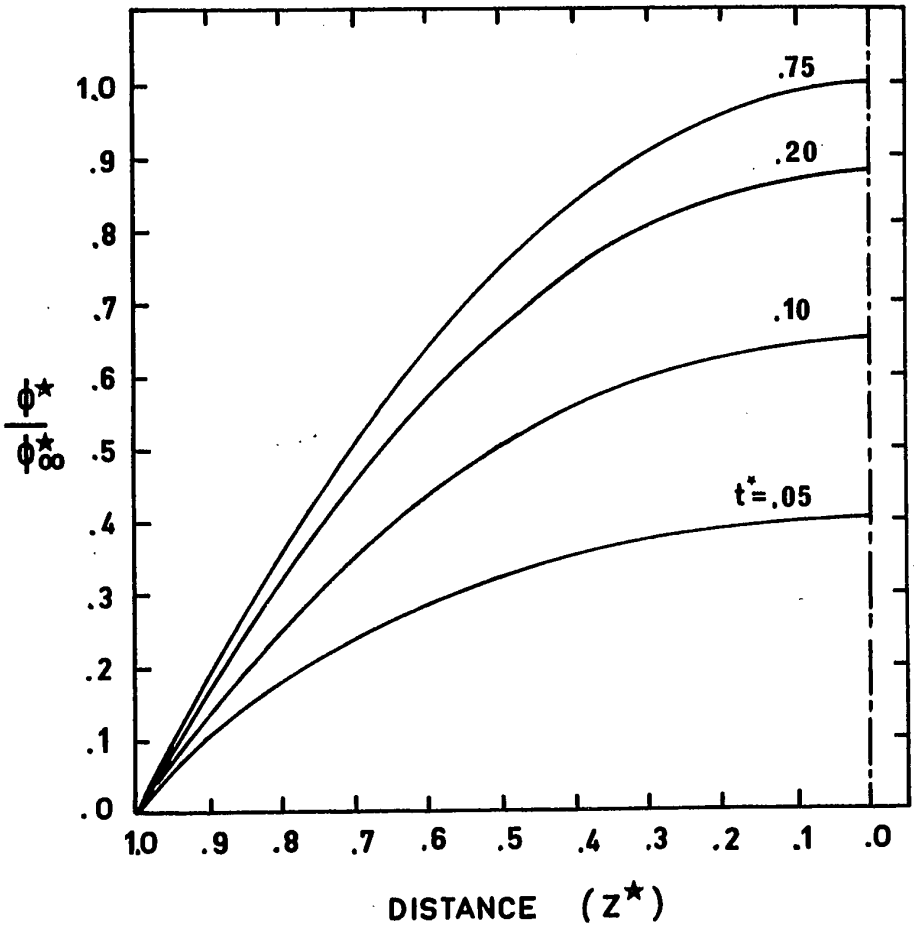

The analysis of the above solution results in the following conclusions:

1. Pressure is not a function of time but only of the radial position in the cavity.
2. Steady state is achieved very quickly and is a function of Re number (see equation (9-46)). Figure 9-3 gives the unsteady-state velocity profile development for the case of 500 psi injection pressure, for the dimensions of the experimental cavity and a Newtonian viscosity 8.53×10^5 lb/ft/hr (3500 poise). As can be seen from Figure 9-3 steady-state is achieved after 0.75 dimensionless time units which corresponds to about 5×10^{-9} hr.

9.3 APPENDIX 3: COMPUTER PROGRAM - FILLING STAGE

The following symbols are used in the computer program.

AR	dimensionless number = h/R_o
B	dimensionless number in the energy equation
B1	coefficient in the energy equation
CP	specific heat
COEF	dimensionless number for heat transfer at the wall
DELTP	pressure gradient in the entrance ring
DELTP1	pressure gradient for the first iteration
DELTP2	pressure gradient for the second iteration
DELTP3	pressure gradient for the third iteration
DELTP4	pressure gradient for the fourth iteration
DENS	density
DENSTP(T,P)	subroutine for calculation of density as a function of temperature and pressure
DENS1	density array for 0 psig
DENS2	density array for 5000 psig
DR	dimensionless radial increment
DT1	time increment
DZ	dimensionless axial increment
ETHA(I,J)	viscosity array
FH(I,J)	latent heat of freezing array
FT(I,J)	previous cycle temperature array

H	heat transfer coefficient at the cavity wall
HT	thickness of the cavity
I	ith radial increment
ID	radial increment where the melt front is located
IDF	previous cycle value of ID
J	jth axial increment
K	integer number of repeated time increment
KX	integer number for control purposes
NM	integer number for control purposes
NX	integer number for control purposes
N1	the third radial ring
P(I)	dimensionless pressure array
PATM	dimensionless atmospheric pressure
PK	pressure
PMAX	maximum pressure at the end of filling
PR1	pressure at the melt front as calculated in the first iteration
PR2	pressure at the melt front as calculated in the second iteration
PR3	pressure at the melt front as calculated in the third iteration
PR4	pressure at the melt front as calculated in the fourth iteration
PX(I)	array for dimensionless experimental measured pressure at the entrance to the cavity
Q1(I)	summation of the second integral
QT	volumetric flow rate

R	dimensionless radius of melt front
RO	radius of mold cavity
SUM	summation of the first integral
T(I,J)	dimensionless temperature array
TEMPD1	temperature array for density at 0 psig
TEMPD2	temperature array for density at 5000 psig
TERM1	a term in the first integral
TERM2	a term in the second integral
TF	dimensionless freezing temperature
TFO	freezing temperature
TI	initial melt temperature
TIME	time elapsed from the beginning of filling
TIMET1	time increment calculated from flow rate
TIMET2	time increment as calculated from stability requirements for energy equation
TIMET	time increment used in the energy equation
TK	temperature
TO	wall temperature
V(I,J)	dimensionless velocity array
VEQ	equivalent velocity
VI	coefficient in the energy equation
X	constant coefficient in the momentum equation
XK	thermal conductivity
XKP	thermal conductivity
XLF	dimensionless freezing enthalpy

```
$WATFIV CE20001_682705_KENIG
C     ***********************************************
C     APPENDIX  3: COMPUTER PROGRAM_FILLING  STAGE
C     ***********************************************
      DIMENSION V(21,11),T(21,11),FT(21,11),P(21),PX(21),SUM(21,11),
     1TERM1(21,11),TERM2(21,11),ETHA(21,11),QI(21),TEMPD1(12),DENS1(12),
     2TEMPD2(11),DENS2(11),FH(21,11)
      COMMON TEMPD1,DENS1,TEMPD2,DENS2,TI,TO,PMAX
C     READ  DATA
      READ(5,1)DR,DZ,DT1,TI,TO,TFO,H,XKP,RO,QT,PMAX,HT
    1 FORMAT(2F8.0,E8.2,3F5.1,F5.1,F5.3,E8.2,F5.1,F7.1,E8.2)
      WRITE(6,29)DR,DZ,DT1,TI,TO,TFO,H,XKP,RO,QT,PMAX,HT
   29 FORMAT(3E10.3,3F10.1,F10.3,E10.2,F10.3,F10.1,E10.2,F10.3)
      READ(5,75)(TEMPD1(I),I=1,12),(DENS1(I),I=1,12)
     1,(TEMPD2(I),I=1,11),(DENS2(I),I=1,11)
   75 FORMAT(12F5.0/12F5.0/11F5.0/11F5.0)
      WRITE(6,301)(TEMPD1(I),I=1,12),(DENS1(I),I=1,12)
     1,(TEMPD2(I),I=1,11),(DENS2(I),I=1,11)
  301 FORMAT(2(12F8.1/), 2(11F8.1/))
      READ(5,3)(PX(I),I=1,21)
    3 FORMAT (16F5.0/5F5.0)
      WRITE(6,9)(PX(I),I=1,21)
    9 FORMAT(21F6.3)
      PATH=14.7/PMAX
      XLF=130.0/0.625/(TI-TO)
      TF=(TFO-TO)/(TI-TO)
      VEQ=SQRT(PMAX*32.2/46.0)*3600*12
      X=(HT/2.0)**0.594*VEQ**(2.0-0.594)
      AR=1.0/48.0
C     INITIAL  CONDITIONS
      DO 2 J=1,11
      T(1,J)=1.0
      T(2,J)=1.0
      T(3,J)=1.0
      T(4,J)=1.0
    2 CONTINUE
      DO 14 I=3,21
      DO 14 J=1,11
      FH(I,J)=0.0
   14 CONTINUE
      ID=4
      R=0.15
      L=1
      TIME=0.0
      DO 15 I=2,ID
      P(I)  =PX(ID)-PX(ID)*(I-2)/(ID-2)
   15 CONTINUE
   10 L=L+1
C     MELT ADVANCES TO NEXT INCEMENT
      IDF=ID
      ID=ID+1
      R=R+DR
      DO 51 J=1,11
      T(ID,J)=T(IDF,J)
      P(ID)=P(IDF)
   51 CONTINUE
      DO 52 J=1,11
      T(2,J)=1.0
   52 CONTINUE
      IF(R.GE.1.0)GO TO 13
```

```
      N1=3
      DELTP1=0.0
      DELTP2=0.0
      DELTP3=0.0
      IF(L.EQ.2)DELTP=0.2
      NM=0
      WRITE(6,39) DELTP,ID,DELTP1,DELTP2,DELTP3,P(ID)
   39 FORMAT(' ',6X,E10.2,I4,4E10.2)
C     CALCULATE FIRST INTEGRAL
      DO 5 I=N1,ID
      SUM (I,1)=0.0
      DO 5 J=1,11
      ETHA(I,J)=8.53E+5*EXP(2300.0/((T(I,J)*(TI-T0)+T0-32.0)*5.0/9.0
     1+273.0))
      TERM1(I,J)=((11-J)*DZ*46.0*X*AR/ETHA(I,J))**(1.0/0.594)*DZ/2.0
      IF(J.EQ.1) GO TO 12
      SUM(I,J)=SUM(I,J-1)+TERM1(I,J-1)+TERM1(I,J)
   12 IF(T(I,J).LT.TF)SUM(I,J)=0.0
    5 CONTINUE
C     CALCULATE SECOND INTEGRAL
      DO 6 I=N1,ID
      QI(I)=0.0
      TERM2(I,1)=0.0
      DO 6 J=2,11
      Y=1.0
      IF(J.EQ.11)Y=0.5
      TERM2(I,J)=DENSTP(T(I,J),P(I))*2.0*3.14159*(I-1)*DR*DZ  *SUM(I,J)
      QI(I)=QI(I)+TERM2(I,J)*Y
    6 CONTINUE
C     CALCULATE PRESSURE PROFILE
  906 P(3)=PX(ID)-DELTP
      P(2)=PX(ID)
      DO 7 I=4,ID
      P(I)=P(I-1)-DELTP/0.75/2.0*((QI(3)/QI(I))**0.594+(QI(3)/QI(I-1))**
     10.594)
    7 CONTINUE
      WRITE(6,11)(P(I),I=3,ID)
   11 FORMAT(20F5.3)
      IF(ID.EQ.N1) GO TO 909
C     ITERATE FOR PRESSURE
      IF(P(ID)  .LT.1.5*PATM.AND.P(ID)  .GT.0.5*PATM)GO TO 909
      NM=NM+1
      IF(NM.EQ.1)DELTP1=DELTP
      IF(NM.EQ.1)PR1=P(ID)
       IF(NM.EQ.2)DELTP2=DELTP
       IF(NM.EQ.2)PR2=P(ID)
      IF(NM.GE.2) GO TO 65
      IF(P(ID)   -PATM  )61,61,62
   61 F=(PATM  -P(ID)  )**3
      F=-F
      GO TO 63
   62 F=(P(ID)  -PATM  )**3
   63 DELTP=DELTP+F
      IF(ABS(DELTP).GT.1.0)DELTP=0.5
      IF(NM.EQ.1)  GO TO 69
      IF(PR1.EQ.PR2)GO TO 909
   65  IF(NM.GE.3) GO TO 66
      IF(NM.EQ.2)DELTP=DELTP2+(DELTP1-DELTP2)/(PR2-PR1)*(PR2-PATM  )
      GO TO 69
   66 IF(NM.EQ.3)DELTP3=DELTP
```

```
      IF(NM.EQ.3)PR3=P(ID)
      IF(NM.GE.4) GO TO 67
      DELTP=(PATM  -PR2)*(PATM  -PR3)/(PR1-PR2)/(PR1-PR3)*DELTP1
     2+(PATM  -PR1)*(PATM  -PR3)/(PR2-PR1)/(PR2-PR3)*DELTP2
     3+(PATM  -PR1)*(PATM  -PR2)/(PR3-PR1)/(PR3-PR2)*DELTP3
      GO TO 69
  67  IF(P(ID)  .LE.PATM  )DELTP2=DELTP
      IF(P(ID)  .LE.PATM  )PR2=P(ID)
      IF(P(ID)  .GT.PATM  )DELTP1=DELTP
      IF(P(ID)  .GT.PATM  )PR1=P(ID)
      DELTP=(PATM  -PR2)*(PATM  -PR3)/(PR1-PR2)/(PR1-PR3)*DELTP1
     2+(PATM  -PR1)*(PATM  -PR3)/(PR2-PR1)/(PR2-PR3)*DELTP2
     3+(PATM  -PR1)*(PATM  -PR2)/(PR3-PR1)/(PR3-PR2)*DELTP3
  69  WRITE(6,39) DELTP,ID,DELTP1,DELTP2,DELTP3,P(ID)
      GO TO 906
C     CALCULATE VELOCITIES
 909  DO 8 I=N1,ID
      DO 8 J=1,11
      IF(I.EQ.ID) GO TO 16
      YP=1.0
      IF(I.EQ.N1)YP=0.875
      V(I,J)=SUM(I,J)*((P(I-1)-P(I+1))/(2.0*DR*YP))**(1.0/0.594)
  16  IF(I.EQ.ID)V(I,J)=SUM(I,J)*((P(I-1)-P(I))/DR)**(1.0/0.594)
   8  CONTINUE
C     CALCULATE FLOW RATE
      QT=0.0
      DO 93 J=2,10
      QT=QT+V(ID-1,J)*2.0*3.14159*DR*(ID-2)*DZ
  93  CONTINUE
      QT=QT+V(ID-1, 1)*2.0*3.14159*DR*(ID-2)*DZ/2.0
      QT=QT+V(ID-1,11)*2.0*3.14159*DR*(ID-2)*DZ/2.0
      XP=1.0
      TIMET1=2.0*3.14159*(((ID-1)*DR)**2-((ID-2)*DR*XP)**2)/(2.0*QT)*1.0
     1/AR
      TIME=TIME+TIMET1
      IF(L.EQ.2)TIMET1=TIME
      IF(L.EQ.2)TIMET1=TIME
      NX=0
C     CHECK FOR STABILITY
      TIMET2=DR/(AR*V(3,10))
      IF(TIMET2.LE.0.65E+4) GO TO 81
      IF(TIMET1.LE.0.65E+4)NX=1
      IF(TIMET1.LE.0.65E+4)TIMET=TIMET1
      IF((TIMET1-0.65E+4))71,71,72
  72  K=TIMET1/0.65E+4
      TIMET=0.65E+4
      GO TO 91
  81  IF(TIMET1.LE.TIMET2)NX=1
      IF(TIMET1.LE.TIMET2)TIMET=TIMET1
      IF((TIMET1-TIMET2))71,71,82
  82  K=TIMET1/TIMET2
      TIMET=TIMET2
      GO TO 91
  91  KX=0
  73  KX=KX+1
      IF(KX.EQ.(K+1))TIMET=TIMET1-TIMET*K
      IF(KX.GT.(K+1))GO TO 74
C     CALCULATE TEMPERATURE PROFILE
  71  DO 910 I=N1,ID
      DO 910 J=1,11
```

```
      FT(I,J)=T(I,J)
      FT(2,J)=T(2,J)
      V(2,J)=V(3,J)
      IF(J.EQ.11) GO TO 22
      IF(T(I,J).LT.TF)DENS=57.0
      IF(T(I,J).GE.TF)DENS=46.0
      IF(T(I,J).LT.TF)XK=0.26
      IF(T(I,J).LT.TF)CP=0.55
      IF(T(I,J).GE.TF)XK=0.130
      IF(T(I,J).GE.TF)CP=0.70
      COEF=DZ*H*HT/2.0/XK
      IF(J.EQ.1) GO TO  21
      B=TIMET/(DZ*DZ*VEQ*HT/2.0 )*XK/DENS/CP
      VI=8.53E+5*EXP(2300/((T(I,J)*(T1-T0)+T0-32.0)*5/9+273.0))
      B1=VI*VEQ**0.594/((TI-T0)*(HT/2.0)**0.594*CP*DENS*32.2*778*3600*
     13600*(1+B))*TIMET
      T(I,J)=T(I,J)*(1-B)/(1+B)-TIMET /DR/(1+B)*(V(I,J)+V(I-1,J))/2.0
     1*(T(I,J)-FT(I-1,J))*AR+B/(1+B)*(T(I,J-1)+T(I,J+1))+(B1*((V(I,J+1)
     2-V(I,J-1))/2.0/DZ)**(1.0+0.594))
C     LATENT HEAT EFFECT
      IF(V(I,J).EQ.0.0.AND.FH(I,J).LT.XLF)FH(I,J)=FH(I,J)+FT(I,J)-T(I,J)
      IF(V(I,J).EQ.0.0.AND.FH(I,J).LT.XLF)T(I,J)=FT(I,J)-(FT(I,J)-T(I,J)
     1)*0.28
 21   IF(J.EQ.1)T(I,J)=T(I,J+1)/(1.0+COEF)
  22  IF(J.EQ.11)T(I,J)=T(I,J-1)
 910  CONTINUE
      IF(NX.EQ.0)GO TO 73
C     PRINT RESULTS
 74   DO 911 I=N1,ID
      DO 911 J=1,11
      WRITE(6,20)P(I),V(I,J),T(I,J),R,TIME,I,J,B1,QT
 20   FORMAT(' ',3E10.3,F8.3,E10.3,2I3,2E10.3)
 911  CONTINUE
      GO TO 10
  13  WRITE(6,23)((FH(I,J),J=1,11),I=2,21)
 23   FORMAT(20(11F11.3/))
      STOP
      END


      FUNCTION  DENSTP(T,P)
      DIMENSION TEMPD1(12),DENS1(12),TEMPD2(11),DENS2(11)
      COMMON TEMPD1,DENS1,TEMPD2,DENS2,TI,TO,PMAX
      TK=T*(TI-TO)+TO
      PK=P*PMAX
      IF(PK.LT.14.7)PK=14.7
      DENSTP=DENSP1(TK)+(DENSP2(TK)-DENSP1(TK))/5000*PK
      RETURN
      END


      FUNCTION DENSP1(TK)
      DIMENSION TEMPD1(12),DENS1(12),TEMPD2(11),DENS2(11)
      COMMON TEMPD1,DENS1,TEMPD2,DENS2,TI,TO,PMAX
      INTEGER Z
      IF(TK.LE.240.0)GO TO 100
      DENSP1 =50.0-4.8*(TK-240.0)/160.0
      RETURN
  100 Z=1
  110 IF(TK-TEMPD1(Z))101,102,103
```

```
103   Z=Z+1
      GO TO 110
 102   DENSP1=DENS1(Z)
      RETURN
101   DENSP1=DENS1(Z-1)+(DENS1(Z)-DENS1(Z-1))/(TEMPD1(Z)-TEMPD1(Z-1))*
     1(TK-TEMPD1(Z-1))
      RETURN
       END


       FUNCTION DENSP2(TK)
      DIMENSION TEMPD1(12),DENS1(12),TEMPD2(11),DENS2(11)
      COMMON TEMPD1,DENS1,TEMPD2,DENS2,TI,TO,PMAX
      INTEGER  Z
      IF(TK.LE.225)GO TO 130
      DENSP2=52.3-3.4*(TK-255)/145
      RETURN
 130  Z=1
 140  IF(TK-TEMPD2(Z))141,142,143
 143  Z=Z+1
      GO TO 140
 142  DENSP2=DENS2(Z)
      RETURN
 141  DENSP2=DENS2(Z-1)+(DENS2(Z)-DENS2(Z-1))/(TEMPD2(Z)-TEMPD2(Z-1))*
     1(TK-TEMPD2(Z-1))
      RETURN
      END
```

9.4 APPENDIX 4: COMPUTER PROGRAM - PACKING STAGE

The following symbols are used in the computer program.

B	dimensionless coefficient
COEF	dimensionless number for heat transfer at the wall
CP	specific heat
DAVT	average density
DENS	density
DENSTP(T,P)	subroutine for calculating density as a function of temperature and pressure
DENSP1(T)	subroutine for calculating density as a function of temperature at 0 psig
DENSP2(T)	subroutine for calculating density as a function of temperature at 5000 psig
DENSP3(T)	subroutine for calculating density as a function of temperature at 10000 psig
DENSP4(T)	subroutine for calculating density as a function of temperature at 15000 psig
DENS1	density array for 0 psig
DENS2	density array for 5000 psig
DENS3	density array for 10000 psig
DENS4	density array for 15000 psig
DPT	difference between the pressure at the injection end and the average pressure in the cavity
DPT1	value of DPT in previous cycle

DR	radial increment
DT	time increment
DZ	axial increment
FH(I,J)	array for latent heat of freezing
FT(I,J)	array for previous cycle temperatures
HT	thickness of the cavity
I	ith radial ring
J	jth axial increment
M	integer number for control purposes
NM	integer number for control purposes
P(I)	pressure array
PAV	average pressure
PMAX	pressure at the injection end
PR(D,T)	subroutine for calculating pressure from average density and temperature
PO	difference between the pressure at the injection end and the average pressure in the cavity at zero time
QT	flow rate at time t
QO	initial flow rate
RO	radius of cavity
T(I,J)	temperature array
TEMPD1	temperature array for density at 0 psig
TEMPD2	temperature array for density at 5000 psig
TEMPD3	temperature array for density at 10000 psig
TEMPD4	temperature array for density at 15000 psig

TF	freezing temperature
TI	initial melt temperature
TIME	time elapsed from the beginning of packing
TO	wall temperature
VOL	volume introduced into the cavity during time increment DT
XMAV	polymer mass in the cavity
XK	thermal conductivity

```
$WATFIV CE20001_682705_KENIG
C     ******************************************************
C     APPENDIX  4:  COMPUTER  PROGRAM_PACKING+COOLING  STAGES
C     ******************************************************
      DIMENSION        P(11),TEMPD1(12),TEMPD2(11),TEMPD3(12),T(11,11),
     1TEMPD4(12),DENS1(12),DENS2(11),DENS3(12),DENS4(12),FH(11,11),FT(11
     1,11)
      COMMON TEMPD1,DENS1,TEMPD2,DENS2,TEMPD3,DENS3,TEMPD4,DENS4,TF,I,J
  302 FORMAT(11(11E11.3/))
C     READ DATA
      READ(5,70) ((T(I,J),J=1,11),I=1,11),(P(I),I=1,11)
   70 FORMAT(7(16F5.0/),9F5.0/11F5.0)
      READ(5,71)(TEMPD1(I),I=1,12),(TEMPD2(I),I=1,11),(TEMPD3(I),I=1,12)
     1,(TEMPD4(I),I=1,12),(DENS1(I),I=1,12),(DENS2(I),I=1,11),(DENS3(I),
     2I=1,12),(DENS4(I),I=1,12)
   71 FORMAT (12F5.0/11F5.0/12F5.0/12F5.0/12F5.0/11F5.0/12F5.0/12F5.0)
      READ(5,72)PMAX,RO,HT,DT,DR,DZ,TO,TI  ,XKP ,TF,QO
   72 FORMAT(10E8.2/F5.0)
      DO 303 I=1,11
      WRITE(6,304)(T(I,J),J=1,11)
  304 FORMAT(11E11.3 )
  303 CONTINUE
      WRITE(6,301)                                (P(I),I=1,11),(TEMPD1(I),I=1
     1,12),(DENS1(I),I=1,12),(TEMPD2(I),I=1,11),(DENS2(I),I=1,11),(TEMPD
     23(I),I=1,12),(DENS3(I),I=1,12),(TEMPD4(I),I=1,12),(DENS4(I),I=1,12
     3),PMAX,RO,HT,DT,DR,DZ,TO,TI,TF,XKP
  301 FORMAT(              11E11.3/,2(12F8.1/),2(11F8.1/),4(12F8.1/),10E1
     10.3///)
      NM=0
      PX=0.0
      TIME=0.0
      DPT=1000.0
      M=0
C     CALCULATE AVERAGE PRESSURE
      PAV=0.0
      DO 103 I=2,10
      PAV=PAV+     3.14159*(I-1)*DR*DR*P(I)
  103 CONTINUE
      PAV=PAV+3.14159*DR*DR*P(11)*10.0/2.0
      PAV=PAV+3.14159*DR*DR*P(2) /2.0
      PAV=PAV/(3.14159*RO*RO/2.0)
      WRITE(6,305)         PAV
  305 FORMAT(F9.2)
      PO=PMAX-PAV
      DO 150 I=1,11
      DO 150 J=1,11
      FH(I,J)=0.0
  150 CONTINUE
   99 IF(NM.EQ.1)GO TO 2
      DPT1=DPT
      DPT=PMAX-PAV
      M=M+1
C     CALCULATE FLOW RATE
      QT=QO*(DPT/PO)**(1.0/0.594)
      IF(ABS(DPT1-DPT).LT.1.5)QT=0.0
      IF(ABS(DPT1-DPT).LT.1.5)NM=1
      IF(ABS(DPT1-DPT).LT.1.5)
     1WRITE(6,302)((T(I,J),J=1,11),I=1,11)
    2 IF(TIME.GT.0.50) DT=0.70E-4
      VOL=QT*DT
```

```
 1      TIME=TIME+DT*3600
C       CALCULATE AVERAGE TEMPERATURE
        TAV=0.0
        DO 100 I=2,10
        DO 100 J=2,10
        TAV=TAV+  2*3.14159*(I-1)*DR*DR*DZ*T(I,J)
  100 CONTINUE
        DO 101 I=2,10
        TAV=TAV+  3.14159*(I-1)*DR*DR*DZ*T(I,11)
        TAV=TAV+  3.14159*(I-1)*DR*DR*DZ*T(I,1)
  101 CONTINUE
        DO 102 J=2,10
        TAV=TAV+  2*3.14159*10*DR*DR*DZ/2*T(11,J)
        TAV=TAV+  2*3.14159*1 *DR*DR*DZ/2*T( 1,J)
  102 CONTINUE
        TAV=TAV+  3.14159*10*DR*DR/2*DZ*T(11,11)
        TAV=TAV+  3.14159*10*DR*DR/2*DZ*T(11,1)
        TAV=TAV+  3.14159*1 *DR*DR/2*DZ*T( 1,1)
        TAV=TAV+  3.14159*1 *DR*DR/2*DZ*T( 1,11)
        TAVT=TAV/(3.14159*(R0*R0)*HT/2)
C       CALCULATE AVERAGE DENSITY
        IF(M.EQ.1)XMAV=DENSTP(TAVT,PAV)*3.14159*R0*R0*HT/2.0
        XMAV=XMAV+QT*DT*DENSTP(TI,PMAX)
        DAVT=XMAV/(3.14159*R0*R0*HT/2.0)
C       CALCULATE NEW AVERAGE PRESSURE
        PAV=PR(DAVT,TAVT)
        IF(PAV.EQ.14.70)
       1WRITE(6,302)((T(I,J),J=1,11),I=1,11)
C       CALCULATE TEMPERATURE PROFILE
        DO 97 I=1,11
        DO 97 J=1,11
        FT(I,J)=T(I,J)
        IF(J.EQ.11)GO TO 81
        IF(T(I,J).GT.TF      )XK=0.130
        IF(T(I,J).GT.TF      )DENS=46.0
        IF(T(I,J).GT.TF      )CP=0.70
        IF(T(I,J).LT.TF      )XK=0.260
        IF(T(I,J).LT.TF      )DENS=57.0
        IF(T(I,J).LT.TF      )CP=0.55
        COEF=100.0*DZ/XK
        IF(J.EQ.1)GO TO 80
        B=XK/DENS/CP*DT/DZ/DZ
        T(I,J)=T(I,J)*(1-B)/(1+B)+B/(1+B)*(T(I,J-1)+T(I,J+1))
        GO TO 82
 80     T(I,1)=T0*COEF/(1+COEF)+T(I,2)/(1+COEF)
        GO TO 82
   81 T(I,J)=T(I,J-1)
C       LATENT HEAT EFFECT
   82 IF(T(I,J).LT.TF      .AND.FH(I,J).LT.130)FH(I,J)=FH(I,J)+0.625*(FT(
      1I,J)-T(I,J))
        IF(T(I,J).LT.TF      .AND.FH(I,J).LT.130)T(I,J)=FT(I,J)-(FT(I,J)-T(
      1I,J))*0.28
 98     IF(NM.EQ.0)T(1,J)=TI
   97 CONTINUE
C       PRINT RESULTS
  201 WRITE(6,300)QT,DT,TIME,DPT     ,TAV,PAV,DAVT,TAVT
  300 FORMAT(9E13.4)
        IF(PAV.GT.PMAX)GO TO 113
        IF(PAV.LE.14.7)GO TO 113
        IF(TIME.GT.9.1) GO TO 113
```

```
      GO TO 99
  113 STOP
      END


      FUNCTION  DENSTP(T,P)
      DIMENSION TEMPD1(12),DENS1(12),TEMPD2(11),DENS2(11),TEMPD3(12),DENS3(12)
     1S3(12),TEMPD4(12),DENS4(12)
      COMMON TEMPD1,DENS1,TEMPD2,DENS2,TEMPD3,DENS3,TEMPD4,DENS4,TF,I,J
      IF(P.LT.14.7)P=14.7
      IF(P-10000)31,32,33
   31 IF(P-5000)34,35,36
   32 DENSTP=DENSP3(T)
      RETURN
   33 DENSTP=DENSP3(T)+(DENSP4(T)-DENSP3(T))/5000*(P-10000)
      RETURN
   34 DENSTP=DENSP1(T)+(DENSP2(T)-DENSP1(T))/5000*P
      RETURN
   35 DENSTP=DENSP2(T)
      RETURN
   36 DENSTP=DENSP2(T)+(DENSP3(T)-DENSP2(T))/5000*(P-5000)
      RETURN
      END


      FUNCTION DENSP1(T)
      DIMENSION TEMPD1(12),DENS1(12),TEMPD2(11),DENS2(11),TEMPD3(12),DENS3(12)
     1S3(12),TEMPD4(12),DENS4(12)
      COMMON TEMPD1,DENS1,TEMPD2,DENS2,TEMPD3,DENS3,TEMPD4,DENS4,TF,I,J
      INTEGER Z
      IF(T.LE.220)GO TO 100
      DENSP1=50.0-3.7*(T-240)/160.0
      RETURN
  100 Z=1
  110 IF(T-TEMPD1(Z))101,102,103
  103 Z=Z+1
      GO TO 110
  102 DENSP1=DENS1(Z)
      RETURN
  101 DENSP1=DENS1(Z-1)+(DENS1(Z)-DENS1(Z-1))/(TEMPD1(Z)-TEMPD1(Z-1))*
     1(T-TEMPD1(Z-1))
      RETURN
      END


      FUNCTION DENSP2(T)
      DIMENSION TEMPD1(12),DENS1(12),TEMPD2(11),DENS2(11),TEMPD3(12),DEN
     1S3(12),TEMPD4(12),DENS4(12)
      COMMON TEMPD1,DENS1,TEMPD2,DENS2,TEMPD3,DENS3,TEMPD4,DENS4,TF,I,J
      INTEGER  Z
      IF(T.LE.225)GO TO 130
      DENSP2=52.3-3.4*(T-255)/145
      RETURN
  130 Z=1
  140 IF(T-TEMPD2(Z))141,142,143
  143 Z=Z+1
      GO TO 140
  142 DENSP2=DENS2(Z)
      RETURN
  141 DENSP2=DENS2(Z-1)+(DENS2(Z)-DENS2(Z-1))/(TEMPD2(Z)-TEMPD2(Z-1))*
```

```
     1(T-TEMPD2(Z-1))
      RETURN
      END


      FUNCTION DENSP3(T)
      DIMENSION TEMPD1(12),DENS1(12),TEMPD2(11),DENS2(11),TEMPD3(12),DEN
     1S3(12),TEMPD4(12),DENS4(12)
      COMMON TEMPD1,DENS1,TEMPD2,DENS2,TEMPD3,DENS3,TEMPD4,DENS4,TF,I,J
      INTEGER Z
      IF(T.LE.265)GO TO 150
      DENSP3=54.2-3.2*(T-265)/135
      RETURN
  150 Z=1
  160 IF(T-TEMPD3(Z))161,162,163
  163 Z=Z+1
      GO TO 160
  162 DENSP3=DENS3(Z)
      RETURN
  161 DENSP3=DENS3(Z-1)+(DENS3(Z)-DENS3(Z-1))/(TEMPD3(Z)-TEMPD3(Z-1))*
     1(T-TEMPD3(Z-1))
      RETURN
      END


      FUNCTION DENSP4(T)
      DIMENSION TEMPD1(12),DENS1(12),TEMPD2(11),DENS2(11),TEMPD3(12),DEN
     1S3(12),TEMPD4(12),DENS4(12)
      COMMON TEMPD1,DENS1,TEMPD2,DENS2,TEMPD3,DENS3,TEMPD4,DENS4,TF,I,J
      INTEGER Z
      IF(T.LE.275)GO TO 170
      DENSP4=56.0-2.8*(T-275)/125
      RETURN
  170 Z=1
  180 IF(T-TEMPD4(Z))181,182,183
  183 Z=Z+1
      GO TO 180
  182 DENSP4=DENS4(Z)
      RETURN
  181 DENSP4=DENS4(Z-1)+(DENS4(Z)-DENS4(Z-1))/(TEMPD4(Z)-TEMPD4(Z-1))*
     1(T-TEMPD4(Z-1))
      RETURN
      END


       FUNCTION PR(D,T)
      DIMENSION TEMPD1(12),DENS1(12),TEMPD2(11),DENS2(11),TEMPD3(12),DEN
     1S3(12),TEMPD4(12),DENS4(12)
      DIMENSION DE(4)
      COMMON TEMPD1,DENS1,TEMPD2,DENS2,TEMPD3,DENS3,TEMPD4,DENS4,TF,I,J
      DE(1)=DENSP1(T)
      DE(2)=DENSP2(T)
      DE(3)=DENSP3(T)
      DE(4)=DENSP4(T)
      IF(DE(1)-D)1,2,2
    1 IF(DE(2)-D)4,5,6
    4 IF(DE(3)-D)7,8,9
    2 PR=14.7
      RETURN
    5 PR=5000
```

```
      RETURN
    6 PR=5000/(DE(2)-DE(1))*(D-DE(1))
      RETURN
    7 PR=10000+5000/(DE(4)-DE(3))*(D-DE(3))
      RETURN
    8 PR=10000
      RETURN
    9 PR=5000+5000/(DE(3)-DE(2))*(D-DE(2))
      RETURN
      END
```

9.5 APPENDIX 5: NUMERICAL TREATMENT OF LATENT HEAT

When latent heat of freezing is involved during phase transformation, as in the case of crystalline polymers, equations (3-14) and (3-15) for the generation of latent heat in the solidifying layer need to be solved.

A few methods are suggested in the literature for solving equations similar to (3-14) and (3-15) for the case of stationary systems and sharp transition temperatures (54,22). The "conventional" method is the simplest, from the computational point of view. In this method, the solution to equations (3-14) and (3-15) is indirect. Instead of dealing with latent heat, one deals with an equivalent temperature defined by $T_{eq} = L/Cp$ where L is the latent heat of freezing and Cp is the specific heat. When the solidification temperature is reached at a given mesh point during computation, further reduction in temperature (as a result of cooling) at this point is delayed until the equivalent temperature is achieved.

In this work, the "conventional" method has been modified for applications involving partially crystalline materials (like polyethylene) which exhibit a freezing range. Instead of a complete delay of temperature when the upper limit of the freezing range T_{uF} is reached at a given mesh point, only a partial delay is applied. The partial delay is based on a fraction F_r, defined as follows:

$$Fr = \frac{\Delta H_f - Cp_a\,(T_{uF} - T_{LF})}{\Delta H_f} \qquad \text{.....(9-50)}$$

Where ΔH_f is the enthalpy of solidification and Cp_a is the weighted average specific heat for the partially crystalline polymer. Thus a fraction (1 - Fr) of the heat which is conducted at any lump of the difference scheme is utilized to lower the temperature of the lump as sensible heat, while the other fraction Fr, is utilized in freezing the crystalline part as latent heat. The partial reduction is terminated when the lower limit of the freezing range T_{LF} is reached. The value T_{LF} is obtained from the following definition.

$$\Delta H_f = \sum_{T_{uF}}^{T_{LF}} Q_T = \int_{Td=T_{uF}}^{Td=T_{LF}} Cp_a\, dTu \qquad \text{.....(9-51)}$$

Where Q_T is the amount of heat conducted across the freezing boundary when its temperature equals T. Td and Tu refer to delayed and undelayed temperature values as obtained in the computational scheme.

In the literature, it is emphasized (54,55) that, since one deals with space and time increments, the conventional method fails to describe the travel of the freezing front continuously and to give a precise temperature near the freezing line. Furthermore, it is possible for the front to

remain at one mesh point so long (as a result of large latent hear or small specific heat) that the constant temperature which pertains at the solidifying layer eventually may cause the calculated temperature profile to reach a steady-state situation. In the modified proposed method for partially crystalline polymers, this risk of reaching a steady state and inaccurate temperature near the freezing front are eliminated by partial delay. A steady state is not achieved since the temperature decreases due to the amorphous portion. The modified "conventional" method would fail to represent temperature profiles near the phase change boundary in the case of highly crystalline polymers like Nylon. In these extreme cases, one has always the choice to go to the more sophisticated methods outlined by Murray and Landis (54).

This method was first tested and used in the case of cooling polymer melts in a long cylinder (24).

9.6 APPENDIX 6: EXTENSIONAL STRESSES

For the isothermal flow of an incompressible fluid, one may include the extensional viscosity in the momentum equation. The momentum equation, after eliminating the unsteady, the nonlinear term, and τ_{rr}, takes the following form:

$$\frac{\partial P}{\partial r} = \frac{\tau_{\theta\theta}}{r} - \frac{\partial \tau_{rz}}{\partial r} \qquad \text{.....(9-52)}$$

Assuming that:

$$\tau_{\theta\theta} = -\lambda \frac{V_r}{r} \qquad \text{.....(9-53)}$$

and

$$\tau_{rz} = -M \left(\frac{\partial V_r}{\partial z}\right)^n \qquad \text{.....(9-54)}$$

where λ is the constant extensional viscosity.
Substituting of (9-53) and (9-54) into (9-52) gives:

$$\frac{\partial P}{\partial r} = -\lambda \frac{V_r}{r^2} + M \frac{\partial}{\partial z}\left[\left(\frac{\partial V_r}{\partial z}\right)^n\right] \qquad \text{.....(9-55)}$$

From continuity (3-1):

$$V_r \times r = \phi(z) = \text{constant} \qquad \text{.....(9-56)}$$

Substitution of (9-56) into (9-55) yields:

$$\frac{\partial P}{\partial r} = -\lambda \frac{\phi}{r^3} + M \frac{1}{r^n} \frac{\partial}{\partial z}\left[\left(\frac{\partial \phi}{\partial z}\right)^n\right] \qquad \text{.....(9-57)}$$

The total pressure loss as expressed in equation (9-57) can be divided into two contributions. The shear contribution

$$\left(\frac{\partial P}{\partial r}\right)_s = M \frac{1}{r^n} \frac{\partial}{\partial z}\left[\left(\frac{\partial \phi}{\partial z}\right)^n\right] \qquad \text{.....(9-58)}$$

and the hoop contribution:

$$\left(\frac{\partial P}{\partial r}\right)_h = -\lambda \frac{\phi}{r^3} \qquad \text{.....(9-59)}$$

It can be seen from equations (9-58) and (9-59) that the hoop loss is large especially at small radii. The relative magnitude of the shear loss and the hoop loss depends on the shear rate, the magnitude of the extensional viscosity, the consistency index and the radial co-ordinate of the point under consideration.

In an oversimplification of the problem, Cogswell and Lamb (48) separated the shear loss and the hoop loss then integrated each term separately with respect to the radial direction and added up the two losses. Furthermore in the integration of the hoop loss they assumed a plug flow situation. As a result of the above simplifications they obtained the following expression for the pressure loss:

$$P = \frac{\lambda Q}{4\pi h}\left(\frac{1}{a^2} - \frac{1}{R_o^2}\right) + \frac{2M}{h^{1+2n}} \times \left(\frac{6Q}{2\pi}\right)^n \times \frac{1}{1-n} \times \left(R_o^{1-n} - a^{1-n}\right) \qquad \text{.....(9-60)}$$

Equation (9-60) gives the total pressure loss and shows that part of this loss is contributed to the extensional stresses.

The simplifications and assumptions made by Cogswell et al (48) can be avoided for the case of a steady radial flow of a Newtonian incompressible fluid, and an analytical solution can be obtained.

Starting from equation (9-52) and assuming the following constitutive equations:

$$\tau_{\theta\theta} = -\lambda \frac{V_r}{r} \qquad \text{.....(9-61)}$$

$$\tau_{rz} = -\mu \frac{\partial V_r}{\partial r} \qquad \text{.....(9-62)}$$

Substituting (9-61) and (9-62) into (9-52) gives:

$$\frac{\partial P}{\partial r} = -\lambda \frac{V_r}{r^2} + \mu \frac{\partial^2 V_r}{\partial z^2} \qquad \text{.....(9-63)}$$

Expressing all variables in the same dimensionless variables as in Chapter 3.1.2 results in:

$$\frac{\partial P^*}{\partial r^*} = -\frac{1}{Re_2} A_r \frac{V^*}{r^{*2}} + \frac{1}{Re_1 A_r} \frac{\partial^2 V^*}{\partial z^{*2}} \qquad \text{....(9-64)}$$

Where:

$$Re_1 = \frac{V_e \cdot \rho_m \cdot h}{\mu}$$

$$Re_2 = \frac{V_e \cdot \rho_m \cdot h}{\lambda}$$

Using the continuity equation:

$$V^* \times r^* = \phi^* \qquad \text{.....(9-65)}$$

Substituting (9-65) into (9-64) gives:

$$\frac{\partial P^*}{\partial r^*} = -\frac{1}{Re_2} A_r \frac{\phi^*}{r^{*3}} + \frac{1}{Re_1 A_r} \frac{1}{r^*} \frac{\partial^2 \phi^*}{\partial z^{*2}} \qquad \text{.....(9-66)}$$

Integrating with respect to r* and using boundary conditions (9-17) and (9-18) yields:

$$\frac{d^2\phi^*}{dz^{*2}} - \phi^* \frac{A_r^2 Re_1}{2Re_2 \ell n(\frac{R_o}{a})} \times (\frac{1}{a^{*2}} - 1) = -\frac{Re_1 A_r}{\ell n(\frac{R_o}{a})} \qquad \text{.....(9-67)}$$

Equation (9-67) is an ordinary differential equation the solution of which is given by:

$$\phi^* = \frac{K}{c^2} (1 - \frac{\ell^{cz^*} + \ell^{-cz^*}}{\ell^c + \ell^{-c}}) \qquad \text{.....(9-68)}$$

Where:

$$K = \frac{Re_1 A_r}{\ell n(\frac{R_o}{a})}$$

and

$$c^2 = \frac{A_r^2 \cdot Re_1}{2 \cdot Re_2 \cdot \ell n(\frac{R_o}{a})} \times (\frac{1}{a^{*2}} - 1)$$

Substituting (9-68) into (9-66) and solving for $P^*(r^*)$ yields:

$$P^*(r^*) = 1 - a^{*2}\left(\frac{1}{a^{*2}} - \frac{1}{r^{*2}}\right)\left(1 - \frac{\ell^{cz^*} + \ell^{-cz^*}}{\ell^{c} + \ell^{-c}}\right)$$

$$- \frac{\ell n\left(\frac{r^*}{a^*}\right)}{\ell n\left(\frac{R_o}{a}\right)} \times \left(\frac{\ell^{cz^*} + \ell^{-cz^*}}{\ell^{c} + \ell^{-c}}\right) \quad .....(9\text{-}69)$$

The solution for the same problem excluding the extensional stress is given by:

$$P^*(r^*) = 1 - \frac{\ell n\left(\frac{r^*}{a^*}\right)}{\ell n\left(\frac{R_o}{a}\right)} \quad .....(9\text{-}70)$$

It can be seen from equations (9-69) and (9-70) that the pressure will vary with the axial direction z^*. The same pressure will be obtained only for $z^* = 1$ (at the wall); at all other positions the pressure will differ from the Newtonian case. Assuming that the extensional viscosity is three times the Newtonian one (56) and for the dimensions of the cavity in the present study, the pressure values computed at the wall are higher by more than 10% from the ones computed at the centerline.

Although an analytical solution is impossible for a Power Law fluid, a similar result can be expected. Thus, the hoop and shear losses cannot be separated and integrated separately as done by Cogswell et al (48).

9.7 APPENDIX 7: ESTIMATE OF DIFFERENT TERMS IN THE MOMENTUM EQUATION

An estimate of the relative magnitudes of the different terms in the momentum equation is very important in assessing the validity of eliminating a few of these terms for the sake of simplicity of the calculation procedure.

Tables 9-1 and 9-2 compare the magnitudes of the derivative of the radial velocity with respect to the axial distance and with respect to the radial direction, for polyethylene and polystyrene for cases 3 and 11, respectively. The latter derivative also gives a good estimate of the ratio between the velocity and the radial position $(\frac{V_r}{r})$, as may be deduced from the continuity equation (3-1) for an incompressible fluid. Both $\frac{\partial V_r}{\partial r}$ and $\frac{V_r}{r}$ were neglected in order to simplify the rheological equation of stage and to use the data obtained from the capillary rheometer.

Tables 9-1 and 9-2 also compare the magnitude of the rate of change of the shear stress with respect to the axial direction (which is constant for isothermal flow) and the magnitude of the nonlinear term in the momentum equation that was eliminated in order to simplify the calculation of the velocity profile at each radial position. Keeping the last term in the equation would have demanded an iteration procedure for its calculation. All values are given at three different positions (R* = 0.2, 0.5, 1.0) and both at the wall and the centre of the cavity, in addition to the entrance and melt front regions.

TABLE 9-1

MAGNITUDES OF DIFFERENT TERMS IN THE MOMENTUM EQUATION

POLYETHYLENE CASE 3

	R* = 0.20 Entrance		R* = 0.50 Entrance		R* = 0.50 Melt Front		R* = 1.00 Entrance		R* = 1.00 Melt Front	
	Wall	Centre	Wall	Centre	Wall	Centre	Wall	Centre	Wall	Centre
1. $\frac{\partial V_r}{\partial z}$ *	1.7×10^{3}	0	7.3×10^{2}	0	2.2×10^{2}	0	5.6×10^{2}	0	6.6×10^{1}	0
2. $\frac{\partial V_r}{\partial r}=(-\frac{V_r}{r})$ *	1.8×10^{1}	1.6×10^{2}	8.2	7.9	6.8×10^{-1}	2.5×10^{1}	6.8	6.2×10^{1}	2.2×10^{-1}	1.0×10^{1}
3. $\rho_m V_r \frac{\partial V_r}{\partial r}$ **	8.2×10^{2}	1.37×10^{4}	1.25×10^{2}	3.9×10^{3}	3.1	1.33×10^{2}	7.8×10^{1}	2.5×10^{3}	3.1×10^{-1}	9.4
4. $M\frac{\partial}{\partial z}[(\frac{\partial V_r}{\partial z})^n]$ **	7.5×10^{8}		8.25×10^{7}		7.8×10^{7}		3.14×10^{7}		5.3×10^{6}	

* Units: 1/sec

** Units: $lb/ft^2/sec^2$

TABLE 9-2

MAGNITUDES OF DIFFERENT TERMS IN THE MOMENTUM EQUATION

POLYSTYRENE CASE 11

	R* = 0.20 Entrance		R* = 0.50 Entrance		R* = 0.50 Melt Front		R* = 1.00 Entrance		R* = 1.00 Melt Front	
	Wall	Centre	Wall	Centre	Wall	Centre	Wall	Centre	Wall	Centre
1. $\frac{\partial V_r}{\partial z}$ *	4.6×10^{3}	0	6.6×10^{2}	0	1.8×10^{2}	0	3.3×10^{2}	0	1.1×10^{1}	0
2. $\frac{\partial V_r}{\partial r}=(-\frac{V_r}{r})$ *	5.0×10^{1}	1.6×10^{3}	8.0	4.3×10^{1}	3.3×10^{-1}	4.6	6.2×10^{1}	3.1×10^{1}	1.7×10^{-3}	8.0×10^{-1}
3. $\rho_m V_r \cdot \frac{\partial V_r}{\partial r}$ **	8.2×10^{3}	7.9×10^{4}	9.7×10^{1}	4.9×10^{3}	9.1×10^{-1}	1.8×10^{2}	2.1×10^{1}	2.6×10^{3}	5.5×10^{-4}	1.2×10^{1}
4. $M\frac{\partial}{\partial z}[(\frac{\partial V_r}{\partial z})^n]$**	4.0×10^{9}		3.4×10^{9}		3.12×10^{9}		4.11×10^{9}		4.21×10^{9}	

* Units: 1/sec

** Units: $lb/ft^2/sec^2$

It can be noticed from both tables, that the change of velocity with respect to the radial direction is negligible at all front positions near the wall. At the mid-plane of the cavity the magnitude of $\frac{\partial V_r}{\partial r}$ reaches its maximum value and $\frac{\partial V_r}{\partial z}$ is zero, as follows from boundary conditions (3-8). However, the value of $\frac{\partial V_r}{\partial r}$ even in the centre region is less than 10%, in average, compared with the value of $\frac{\partial V_r}{\partial z}$ close to the wall.

The comparison of the magnitude of terms 3 and 4 in Tables 9-1 and 9-2 shows that in all given regions and positions the elimination of the nonlinear term is justifiable.

An attempt was made to include the nonlinear term $V_r \frac{\partial V_r}{\partial r}$ in the solution to the filling stage for an isothermal system. A different numerical procedure was used to achieve it, as follows. The velocity profile was calculated for the first radial ring using equation (3-22) and assuming a pressure gradient in the same way as described in Chapter 3.1.4. Velocity profiles down stream to the melt front were calculated by using the continuity equation (3-21). The calculated velocity profiles were substituted in the momentum equation, including the nonlinear term, to calculate the corresponding pressure profile. The test for atmospheric pressure at the melt front and the iteration procedure for the pressure correction were identical to the ones described in Chapter 3.1.4. The pressure profiles obtained by this procedure were compared with the same problem excluding the non-

linear term. Results showed that the pressure profiles and filling times were different only in the third decimal place. The solution to the former case gave higher values for pressure at the entrance by 1% compared with the latter case. In the above procedure, the nonlinear term $V_r \times \frac{\partial V_r}{\partial r}$ was taken into account in all regions except at the entrance ring, and was shown to be of minor importance.

It should be emphasized that the magnitudes of the terms in Table 9-1 and 9-2 have been evaluated from the numerical solution of the equations of change that have already neglected a few of these terms, as pointed out in section 3.1.1 and Appendix 1. Thus, the above values can serve only as a first approximation and do not represent the true values.